FY02 Highlight:

ISTC Target Complex TC-1 being unloaded at the University of Nevada Las Vegas (May 2002), shipped from the International Science and Technology Centre in Moscow.

Los Alamos National Laboratory, Argonne National Laboratory
Oak Ridge National Laboratory, Pacific Northwest National Laboratory
Brookhaven National Laboratory, Lawrence Livermore National Laboratory
Idaho National Engineering and Environmental Laboratory, Idaho Accelerator Center
University of Nevada, University of Michigan, University of California, University of Texas
Burns & Roe, Enterprises, Inc., General Atomics, Westinghouse Savannah River Company

Blank Page

AFC/AAA Technical Quarterly Report
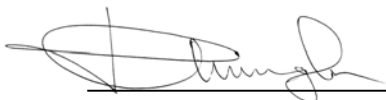## July - Sept 2002
LA-UR-02-7220

Approvals

_____

Date_____11/15/02_____

Michael Cappiello, AFC Director
for Transmutation Engineering

_____

Date_____11/15/02_____

Kemal Pasamehmetglu, AFC National Director
for Fuels Development

_____

Date_____11/15/02_____

Jim Laidler, AFC National Director
for Separations

Blank Page

Table of Contents

Major Contributors

Fuels Development:	D. Crawford (ANL)
	K. Chidester (LANL)
	M. Meyer (ANL)
	S. Hayes (ANL)
	R. Margevicius (LANL)
	K. McClellan (LANL)
Separations Technology:	J. Laidler (ANL)
Transmutation Science:	K. Pasamehmetoglu (LANL)
	E. Pitcher (LANL)
	L. Waters (LANL)
	M. James (LANL)
	M. Chadwick (LANL)
	N. Li (LANL)
	V. Tcharnotskaia (LANL)
	S. Wender (LANL)
	S. Maloy (LANL)
	B. Haight (LANL)
	G. Morgan (LANL)
	S. Lillard (LANL)
	R. Klann (ANL)
	G. Palmiotti (ANL)
	K. Woloshun (LANL)
Systems Technologies:	M. Cappiello (LANL)
	S. McConnell (LANL)
	K. Pasamehmetoglu (LANL)
	J. Roglans (ANL)
	R. Guffee (LANL)
	H. Cohen (BREI/GA)
	J. Herceg (ANL)
	W. Chaves (LANL)
	G. Willcutt (LANL)
	J. Elson (LANL)
	H. Ludewig (BNL)
	M. Todosow (BNL)
Project Integration:	R. Krakowski (LANL)
	C. Bathke (LANL)
	D. Beller (LANL)
	A. Hechanova (UNLV)
	J. Lee (Univ Michigan)
	E. Greenspan (UC Berkeley)
	W. Charlton (UT Austin)

Acronyms and Symbols

AAA	Advanced Accelerator Applications
AC	Accelerating cavities
ADS	Accelerator-Driven System
ADTF	Accelerator-Driven Test Facility
ADMAB	Accelerator-Driven Minor Actinide Burner
AES	Advanced Energy Systems (formerly Northrup-Grumman Corp.)
AET	Ability Engineering Technology
AFCI	Advanced (Nuclear) Fuel Cycle Initiative
AFM	Atomic Force Microscopy
A•h	Ampere-Hour
AHA	Acetohydroxamic acid
Am	Americium
AMUSE	Argonne Model for Universal Solvent Extraction, the generic TRUEX model expanded to include UREX and PUREX processing
ANL	Argonne National Laboratory (Chicago)
ANL-W	Argonne National Laboratory-West (Idaho Falls)
ANRC	Amarillo National Research Center
ANS	American Nuclear Society
ANSYS	structural analysis modeling code
appm	atomic parts per million
APT	Accelerator Production of Tritium
ASME	American Society of Mechanical Engineers
ATR	Advanced Test Reactor (INEEL)
ATW	Accelerator Transmutation of Waste
Ba	Barium
BCM	Beam-Current Monitor
BCP	Baseline Change Proposal
BCP	Buffered Chemical Polishing
Be	Beryllium
Beta (β)	Ratio to the speed of light
Bi	Bismuth
BISTRO	Two-Dimensional Discrete Ordinates Code
BNFL	British Nuclear Fuels, Ltd
BNL	Brookhaven National Laboratory
BOF	Balance of Facility
BOL	Beginning of Life
BOP	Balance of Plant
BOR-60	Sodium-Cooled Fast Reactor (Dmitrovgrad, Russia)
BPM	Beam-Position Monitor
BSE	backscattered electron (images)
CCDTL	Coupled-Cavity Drift-Tube Linac
CCL	Coupled-Cavity Linac
Ce	Cerium
CEA	Commissariat l Energie Atomique (France)
CEM	Cascade Exciton Model code (Model-based Monte-Carlo particle transport code)
CERCA	Compagnie Pour L'Etude Et La Realisation De Combustibles Atomiques
cercer	Ceramic-Ceramic
cermet	Ceramic-Metal
CFD	Computational Fluid Dynamics
CINDER90	Computer Code
CLWR	Commercial Light-Water Reactor
Cm	Curium

CMPO	Neutral Extractant
CMR	Chemistry and Metallurgy Research (facility at LANL)
CONCERT	COmbined Neutron Center for European Research and Technology
Cs	Cesium
Cu	Copper
CVD	Chemical Vapor Deposition
cw	Continuous Wave (100% duty factor)
DACS	Data Acquisition and Control System
DAS	Data Acquisition System
DBTT	Ductile-To-Brittle Transition Temperature
DCR	Design Change Request
DDN	Design Data Need
DIAMEX	Aqueous Solvent Extraction Process for TRU Recovery
DOE	Department of Energy
dpa	Displacements per Atom
EBR	Experimental Breeder Reactor
ED&D	Engineering Development and Demonstration
EDS	Energy Dispersive Spectrometry
EFPD	Effective Full-Power Day
EFTTRA-T4	Radiation Test Sponsored by the European Union
EIS	Electrochemical Impedance Spectroscopy
EIS	Environmental Impact Statement
ENDF	Evaluated Nuclear Data File — Evaluations that can be used in MCNPX for more accurate predictions of fission, criticality, transport, and radiation damage
EOI	End of Irradiation
EOL	End of Life
EPICS	Experimental Physics and Industrial Control System
ERANOS	Computer modeling code
ERC	External Review Committee
ES&H	Environmental, Safety, and Health
ESS	European Spallation Source
ESSAB	Energy System Acquisition Advisory Board (DOE)
Eu	Europium
FDD	Facility Design Description
Fe	Iron
FFTF	Fast Flux Test Facility
FMF	Fuel Manufacturing Facility
FODO	Focus-Drift-Defocus-Drift
FPY	Full-Power Year
FWHM	Full Width Half Maximum
FZJ	Forschungs Zentrum J lich (German Laboratory)
FZK	Forschungs Zentrum Karlsruhe (German Laboratory)
g/L	Grams per Liter
GA	General Atomics Inc.
GNASH	Nuclear Reaction Code
GSI	Gesellschaft f r Schwerionenforschung (Darmstadt, Germany)
GT-MHR	Gas Turbine Modular Helium Reactor
H	Hydrogen
HAN	Hydroxylamine
HCP	Hazard Control Plan
He	Helium
HEBT	High-Energy Beam Transport
HEU	Highly enriched uranium
Hf	Hafnium
HFIR	High Flux Isotope Reactor (ORNL)
HFR	High Flux Reactor (Petten, Netherlands)

Hg	Mercury
HIP	Hot Isostatic Process (for bonding materials)
HM	Heavy metal
HPRF	High-Power Radio Frequency
HS/WS	Halo-Scraper/Wire-Scanner (diagnostic device)
HX	Heat exchanger
I&C	Instrumentation and Control
IAC	Idaho Accelerator Center
IAEA	International Atomic Energy Association (Vienna, Austria)
ICP-MS	Inductively Coupled Plasma-Mass Spectrometry
ICS	Integrated Control System
IFMIF	International Fusion Materials Irradiation Facility
IFR	Integral Fast Reactor
IHX	Intermediate Heat Exchanger
IMS	Information Management System
INEEL	Idaho National Engineering and Environmental Laboratory
IPBT	In-Pile Beam Tube
IPPE	Institute of Physics and Power Engineering, Obninsk, Russia.
ISABEL	Physics Modeling Code
ISTC	International Science and Technology Centre (Moscow)
ITER	International Thermonuclear Experimental Reactor
ITU	Institute for Transuranium Elements (Karlsruhe, Germany)
JAERI	Japan Atomic Energy Research Institute
JCNNM	Johnson Controls Northern New Mexico
JLAB	Jefferson Laboratory (VA)
K	Potassium
KAERI	Korean Atomic Energy Research Institute
KEK	National Laboratory for High-Energy Physics (Tsukuba, Japan)
keV	Kiloelectron Volt
LA150n	Los Alamos generated nuclear data library, extending up to 150 MeV
LAHET	Los Alamos High-Energy Transport
LANL	Los Alamos National Laboratory
LANSCE	Los Alamos Neutron Science Center
LBE	Lead-bismuth eutectic
LBHM	Low-β Hot Model
L/d	Length-to-diameter ratio
L/hr	Liter per hour
LEBT	Low-Energy Beam Transport
LEDA	Low-Energy Demonstration Accelerator
LHGR	linear heat generation rate
LINAC	A computer code based on PARMILA that has been modified to include CCDTL and SCRF elliptical cavities as options
LLFP	Long-lived fission product
LLNL	Lawrence Livermore National Laboratory
LLRF	Low-level radio frequency
LME	Liquid-metal embrittlement
LMR	Liquid-metal reactor
LWR	Light-water reactor
M	Molar
MA	Minor actinide
mb	Millibarn
MCA	Multi-criteria analysis
mCi	Millicurie
MCNP	Monte Carlo N-Particle Transport Code
MCNPX	Merged code Los Alamos High-Energy Transport (LAHET) and Monte Carlo N-Particle Codes (MCNP)

MCWO	MCNP Coupling With ORIGEN2 (burnup calculation code)
MDD	Modified Direct Denitration
MEAM	Molecular Embedded Atom Method
MEGAPIE	Megawatt Pilot Experiment
MFM	Magnetic Flow Meter
MIT	Massachusetts Institute of Technology
mL	Milliliter
Mo	Molybdenum
MOX	Mixed oxide fuel
mR	Millirad (a measure of radiation)
MT	Metric Ton
MTL	Materials Test Loop
MUSE	CEA-Cadarache Zero-Power Subcritical Experiments
MW	Megawatt
MWD/T	Megawatt Days per Ton (standard unit for burnup)
MWth	Megawatt thermal
N	Nickel or nitride
Np	Neptunium
n/p	Neutrons per proton
NDA	Nondestructive analyses
NEA	Nuclear Energy Agency (Paris)
NEPA	National Environmental Protection Agency
NERAC	Nuclear Energy Research Advisory Committee
NERI	Nuclear Energy Research Initiative
NFC	Nuclear Fuel Cycle
NFF	Nonfertile Fuel
O	Oxygen or Oxide
O&M	Operations and Maintenance
OECD	Organization for Economic Cooperation and Development (Paris)
ORIGEN	A computer code system for calculating the buildup, decay, and processing of radioactive materials
ORNL	Oak Ridge National Laboratory
P&ID	Piping and Instrumentation Diagram
P&T	Partitioning and transmutation
PACS	Personnel Access Control System
PARMTEQM	RFQ simulation code
Pb	Lead
PCM	Pulse Control Modulation
Pd	Paladium
PFD	Process Flow Diagram
PHA	Preliminary Hazards Assessment
PHENIX	Fast Reactor in France
PIE	Post-irradiation examination
PNNL	Pacific Northwest National Laboratory
POP	Proof of Performance, Proof of Principle
PRAD	Proton Radiography
PRISM	Power Reactor Innovative Small Module
PSAR	Preliminary Safety Analysis Report
PSS	Personnel Safety System
PSI	Paul Scherrer Institute (Switzerland)
Pu	Plutonium
PUREX	Plutonium-Uranium Extraction
PWR	Pressurized Water Reactor
PYRO	Pyrochemical process
Q	Quality factor
QA	Quality Assurance

QAC	Quick ATW Costing
R	Rad (a measure of radiation)
RAMI	Reliability, Availability, Maintainability, and Inspectability
RBS	Rutherford Backscattering Spectrometry
RERTR	Reduced Enrichment for Research and Test Reactors program
RF	Radio Frequency
RFQ	Radio-Frequency Quadrupole
RCCS	Resonance-Control Cooling System
RIA	Rare Isotope Accelerator
RIAR	Russian Institute of Atomic Reactors
rms	root mean square
RRR	Residual Resistance Ratio
RSICC	Radiation Safety Information Computational Center
RTD	Surface Temperature Detector
RTH	Royal Institute of Technology (Stockholm, Sweden)
Ru	Ruthenium
SAA	Systems Approaches Analysis
SANEX	Aqueous Solvent Extraction Process for Am and Cm Recovery
SAR	Safety Analysis Report
SC	Superconducting
SCM	Subcritical Multiplier
SCRF	Superconducting RF
SDD	System Design Description
SEM	Scanning Electron Microscopy
SFT	Stacking-Fault Tetrahedral
SHR	shutdown heat-removal
SINQ	Spallation Neutron Source at Paul Scherrer Institute (Switzerland)
SNF	Spent Nuclear Fuel
SNL	Sandia National Laboratory
SRS	Savannah River Site
SRTC	Savannah River Technology Center
Star-CD	Computational fluid dynamics code
STAYSL	A computer code to analyze results of activation foil measurements
STAYSL2	A computer code to analyze results of activation foil measurements in both a proton and neutron flux
STP	Standard Temperature and Pressure
STIP	Spallation Target Irradiation Program (at PSI)
T/p	Tritons (nucleii of tritium atoms) per Proton
T/B	Target / Blanket
Ta	Tantalum
TBP	Tri-*n*-butyl Phosphate or Tributylphosphate
Tc	Technitium
TEM	Transmission Electron Microscopy
TESLA	International Collaboration on a TeV Superconducting Linear Accelerator
TGA	Thermal Gravimetric Analysis
TJNAF	Thomas Jefferson National Accelerator Facility
TMT	Target and Materials Test Station
TRAC	Transient Reactor Analysis Code
TRACE 3-D	Interactive computer code that calculates the envelopes of a bunched beam through a user-defined transport system
TREACS	TReat Experiment for ACcelerator-driven Systems
TREAT	Transient Reactor Test Facility
TRISO	Tri-isotropic, referring to a multi-layered fuel-particle coating consisting of pyrolytic carbon and silicon carbide
TRADE	TRIGA Accelerator Driven Experiment
TRIGA	Small Reactor Type

TRISPAL	Refers to the French APT Program
TRL	Technical Readiness Level
TRU	Transuranics (americium, curium, neptunium, and plutonium)
TRUEX	Aqueous solvent extraction process for TRU recovery
U	Uranium
UFP	University Fellowship Program
UNLV	University of Nevada Las Vegas
UPP	University Participation Program
UREX	Uranium Extraction (an aqueous partitioning process)
URA	University Research Alliance
URP	University Research Program
USQD	Unreviewed Safety Question Determination
V	Vanadium
VPS	Vapor Plasma Spray
VARIANT	Three-Dimensional Nodal Transport Code
W	Tungsten
WBS	Work Breakdown Structure
WNR	Weapons Neutron Research (facility at LANL)
WPPT	Working Party on Partitioning and Transmutation
WSRC	Westinghouse Savannah River Company
Xe	Xenon
XRD	X-ray Diffraction
Y	Yttrium
ZPPR	Zero Power Physics Reactor
Zr	Zirconium

Advanced Fuel Cycle Initiative

Advanced Accelerator Applications

Quarterly Report

July - September 2002

I. INTRODUCTION

The Advanced Accelerator Applications (AAA) Program was a Department of Energy (DOE) program commissioned by Congress in FY2000, constituting a national effort by DOE laboratories (Los Alamos, Argonne, Savannah River, Livermore, and Oak Ridge), industry (Burns and Roe Engineering Inc, General Atomics) and universities (UC-Berkeley, Texas-Austin, Michigan, Nevada) to address pressing nuclear issues facing the United States. The primary mission of the Program was to develop the technology base for the transmutation of nuclear waste and to demonstrate its practicality and value for long-term waste management. The AAA Program was initiated by combining two earlier programs: the Accelerator Production of Tritium (APT) Program and the Accelerator Transmutation of Waste (ATW) Program.

On October 1, 2002, the AAA Program was transitioned into the Advanced Fuel Cycle (AFC) Initiative, with a more immediate focus on completing and closing the nuclear fuel cycle, but still maintaining the long-range focus of transmutation of nuclear waste. In addition to the primary mission of closing the nuclear fuel cycle with more emphasis and focus on the development of fuels and separations technologies, the AFC Program will continue to evaluate the effectiveness of transmutation of spent nuclear fuel against the following important criteria:

(1) Reduce the long-term radiological impact of waste;
(2) Enable development of a simpler, cheaper repository;
(3) Reduce proliferation risk; and
(4) Improve long-term prospects for nuclear power.

Improving the long-term prospects for nuclear power includes not only closing the fuel cycle, but also demonstrating through proof-of-performance the practicality of the transmutation of nuclear waste and its meaningful impact on nuclear materials, waste management, and economics. It also means defining and executing activities designed to support the country's nuclear science and engineering infrastructure.

Program efforts are currently focused on the following activities:

(1) Developing separations technologies to partition long-lived radioactive waste from reusable nuclear material;

(2) Developing and testing potential transmutation fuels;

(3) Evaluating the most effective systems for transmutation of spent nuclear fuel;

(4) Developing a spallation target to provide an effective environment for transmutation;

(5) Establishing and supporting a national university program to re-energize development and training in nuclear-related fields; and

(6) Collaborating in international research efforts with nations involved in evaluating nuclear waste management.

Through these efforts, the AFC Program is defining the key parameters, experiments, analyses, and facilities needed to further develop fuels and separations technologies, and to demonstrate the technical viability of partitioning and transmutation of long-lived nuclear wastes.

II. HIGHLIGHTS

Fuels Development

- The first edition of the AAA Fuels Handbook was issued. The Fuels Handbook contains thermophysical-property correlations based on the best available data for metal and nitride fuels.

- All required actinide-nitride fuel pellets were completed for the ATW-1 test. Final analysis and characterization is in progress.

- Chemical and isotopic analysis and analysis of the microstructures of all metal-alloy fuel compositions to be irradiated in the ATW-1 experiment were completed.

- The thermodynamic modeling of the Pu-PuN pseudo-binary phase diagram was completed.

- We completed modeling the free energy of $PuO_{2-\delta}$ for a calculation of the pressure of oxygen as a function of temperature and composition (sub-stoichiometry).

- Physics analysis for the ATW-1A, -1B, -1C and -1D experiments was completed for the full-residence time of six 50-day irradiation cycles, and as expected, shows that the experiments reach peak ^{239}Pu-burnups of >20% for anticipated reactor operating conditions.

- The letter report Status Report on ATW-3/FUTURIX, detailing the current status and work needed for insertion of the FUTURIX test into Ph nix in late 2005, was submitted as a milestone to the AAA IMS.

Separations Technology

- The electrochemical reduction of a UO_2-PuO_2 oxide fuel containing 5% plutonium was successfully demonstrated, with analysis showing average conversion efficiency for the PuO_2 and AmO_2 of ~98%, and for UO_2 >99%.

- The UREX flowsheet was re-optimized for the hot demonstration run in the SRTC hot cell to provide the best results and meet all process goals.

- Experiments to clarify the behavior of plutonium in the UREX process were performed, revealing an unexpected result that the extraction of plutonium is second order with respect to the TBP (tributyl phosphate).

Transmutation Science

- The final draft of the 10-year research plan for Transmutation Science was submitted to DOE.

- A draft chapter of the Materials Handbook on the properties of HT-9 was issued in July.

- The International Science and Technology Centre (ISTC) LBE target fabricated by the Institute of Physics and Power Engineering (IPPE) in Obninks, Russia, which was delivered to the University of Nevada at Las Vegas (UNLV), was

tested by ISTC scientists with the assistance of personnel from IPPE, successfully determining that there were no leaks in the target.

- The DELTA loop attained reliable operational status, allowing unattended operations.

- Two LANL-made oxygen sensors were approved for export and delivered to a research group at the Royal Institute of Technology (KTH), Sweden.

- Irradiation of the 20-cm and 40-cm diameter LBE targets was completed in July. LBE corrosion experiments were also completed.

- Data collection began for hydrogen and helium production on iron samples.

- The first nuclear data 150-MeV evaluations for actinides were created.

- MCNPX version 2.4.0 was formally released to the Radiation Safety Information Computational Center (RSICC).

- The report, Evaluation of Safety Design Criteria for Application to Accelerator-Driven, Subcritical, Liquid Metal Cooled Nuclear Reactors, was completed.

- An uncertainty estimation procedure was added to the Proliferation Resistance Assessment Methodology developed by the University of Texas at Austin.

- The University of Michigan completed four milestones: a simple dynamic model framework, interim data and results for the T-91 irradiation campaign, a report on LWR transmutation studies, and a status report on LBE spectrum analysis.

Systems Technologies

- A report on the selection of the reference subcritical multiplier core, *Selection of the Reference Accelerator-Driven System Subcritical Multiplier Core Model for Use in Pre-Conceptual Design Development*, along with three other ADS Reference Design documents, were completed and issued.

- Thermo-hydraulic analyses of the nominal ADS LBE target concept, based on the scale up of the ADTF target design, were performed, verifying that design constraints were met.

- A thermal model of the TREAT fuel assembly was developed and used for estimating fuel assembly temperature distributions.

- The preliminary engineering feasibility report for the use of the TREAT reactor in accelerator-driven experiments, *Engineering Feasibility of Proof-of-Principle Testing of Accelerator-Driven Subcritical Reactor Operation Using TREAT*, was completed and issued.

- Testing of the two β=0.175, 2-gap, 350-MHz superconducting spoke resonator cavities was completed, with both cavities exceeding the ADTF requirements.

Systems Studies

- The NFCSim simulation model is successfully simulating past history of nuclear power plant (NPP) deployment and SNF generation in the US, and a workable framework has been established for integration of a range of Tier-1 and Tier-2 technologies.

- The FCOPT optimization is successfully optimizing a broad subset of AFC technologies on the basis of cost, proliferation risk, extensive parametric systems studies, and key constraints.

- Preliminary scaling studies using the YM Emplacement model indicate a potential for significant capacity enhancement of the repository.

University Programs

- UNLV published and distributed the "UNLV Transmutation Research Program Annual Report for Academic Year 2001"˚that highlights infrastructure improvements, student research programs, and growth in interest in nuclear science and engineering.

- UNLV hosted a visit by William Magwood (Director, DOE-NE), and co-hosted an International Molten Metals Advisory Committee/ISTC meeting.

- A neutron-producing target was designed for an ISU-IAC electron linac and MCNPX calculations on the design were completed. The new design is predicted to produce a factor of two increase in neutron yield compared with previous designs.

- The University Research Alliance (URA) initiated the first steps for recruiting applicants for the FY03 AFCI Fellowship Program.

- URA staff identified and selected a second-year master's degree student at the University of Texas who filled a vacated fellowship position.

- The University Projects Leader brought two additional universities into the AFC-AAA program during the fourth quarter.

Blank Page

III. TECHNOLOGY DEVELOPMENT

1.   FUELS DEVELOPMENT

Scope

AFC/AAA Fuels Development activities are directed toward the development and qualification of fuels for safe transmutation of actinides at maximal rates. The objective of the effort is to provide one or more transmutation fuel forms at Technical Readiness Level (TRL) 6 at the time that transmutation technology overall is to begin integral demonstration. Thus far, requirements for such fuels include nonfertile compositions in forms suitable for fast-spectrum transmuters and a homogenous fuel cycle (i.e., all minor actinides would be maintained in the same fuel and processing stream). However, the AFC/AAA transmutation program is considering additional transmuter architectures, the use of which would imply different requirements for fuels; therefore, the fuel development program is evolving as the nature of and approach for the overall transmutation mission evolves.

The specific R&D activities include development of techniques to fabricate transmutation fuels from LWR fuel-derived actinide feed and from actinide feed recycled from transmuters. As-fabricated samples are chemically and microstructurally characterized to evaluate the success of fabrication processes and to better understand the nature of the fuel materials. Evaluation of proposed fuel forms (nitride, oxide, metal, carbide, dispersion, etc.) requires irradiation testing, so near-term irradiation tests are being planned and will be performed through the course of this program. Finally, the understanding of in-service fuel behavior is best demonstrated through the development and validation of fuel behavior models that are eventually incorporated into fuel performance codes. Such models are being developed, concurrent with an effort to develop thermal models that allow calculation of fuel and cladding temperatures in service and during testing.

Highlights

- The first edition of the AAA Fuels Handbook was issued. The Fuels Handbook contains thermophysical-property correlations based on the best available data for metal and nitride fuels.

- All required actinide-nitride fuel pellets were completed for the ATW-1 test. Final analysis and characterization is in progress.

- Chemical and isotopic analysis and analysis of the microstructures of all metal-alloy fuel compositions to be irradiated in the ATW-1 experiment were completed.

- Stress analysis of fuel rodlets and capsules for the ATW-1A, -1B, -1C and -1D metal and nitride irradiation tests was completed for the Advanced Test Reactor 20% overpower condition, showing acceptable experimental performance.

- An integrated design review of the ATW-1 fuel irradiation experiment was conducted jointly with BBWI and ANL, and design review comments are being addressed.

- The thermodynamic modeling of the Pu-PuN pseudo-binary phase diagram was completed.

- We completed modeling the free energy of $PuO_{2-\delta}$ for a calculation of the pressure of oxygen as a function of temperature and composition (sub-stoichiometry).

- Using nano-indentation, hardness was altered by displacement damage in Xe ion-irradiated ZrN, while intrinsic properties such as elastic modulus were found to be relatively unaffected.

- Results from an *ab initio* study of the energetics of different crystal structures of Am were used to parameterize a semi-empirical MEAM (molecular embedded atom method) potential model for Am.

- Assessment of the fracture resistance of ZrN samples indicates that the material has a toughness that is comparable to that of some monolithic ceramics, despite the large amount of porosity present.

- Fractographic studies of the broken ZrN specimens indicate that a variety of fracture mechanisms are active during static cracking of the materials tested.

- Heat treatment of ZrN samples at intermediate temperatures can increase their mechanical properties, possibly via improvement of the fracture resistance of material in between sintered particles.

- Data analysis from solution calculations of Xe onto the cation site in the stochiometric perfect lattice structures of CmN and TiN indicate a strong thermodynamic driving force for the removal of Xe from this site in these materials.

- The actinide lattice CmN has a lower predicted Xe-solution energy than proposed diluent ZrN or TiN materials, which is also apparent when solution is considered in equilibrium; and, if such solution processes are dominant, the solution limit determined from experiments on surrogate materials will provide a clear lower bound to the extent of solution in actinides.

- Differential thermal and thermogravimetric analysis data have been collected for Pu-60Zr, Pu-10Am-10Np-40Zr, Pu-10Np-40Zr, and Pu-12Am-40Zr (all wt.%) alloys. Analysis of this data is partially complete and shows a single-phase transformation corresponding to the expected δ-ϵ phase transformation for Pu-Zr and Pu-Am-Zr alloys.

- Physics analysis for the ATW-1A, -1B, -1C and -1D experiments was completed for the full-residence time of six 50-day irradiation cycles, and as expected, shows that the experiments reach peak [239]Pu-burnups of >20% for anticipated reactor operating conditions.

- The letter report Status Report on ATW-3/FUTURIX, detailing the current status and work needed for insertion of the FUTURIX test into Ph nix in late 2005, was submitted as a milestone to the AAA IMS.

Fabrication Development

Metal Fuel

Microstructure Characterization of Fuel Alloys

The microstructures of Pu-40 wt% Zr fuel pins (two specimens) and Pu-40 wt% Zr-12 wt% Am fuel pins (three specimens) have been analyzed using scanning electron microscopy (SEM) with energy-dispersive and wavelength-dispersive spectrometry (EDS/WDS). The charge materials for both fuel types were alloyed by arc-melting. Fuel rods were cast from the alloys by arc-melting into coated quartz molds. Specimens for examination were transversely sliced from the as-cast rods.

Figure 1 shows a low-magnification backscattered-electron image of the microstructure of a Pu-40Zr specimen. The microstructure is representative of that seen in a Pu-40Zr specimen, taken from another Pu-40Zr rod. Figure 2 shows a Pu-12Am-40Zr sample; the microstructure shown in Fig. 2 is representative of that observed in samples from the two other Pu-12Am-40Zr rods. In general, moving from the center of the samples towards the outer edge, uniform microstructures were observed in all Pu-40Zr and Pu-12Am-40Zr specimens, the most prominent feature being very fine porosity.
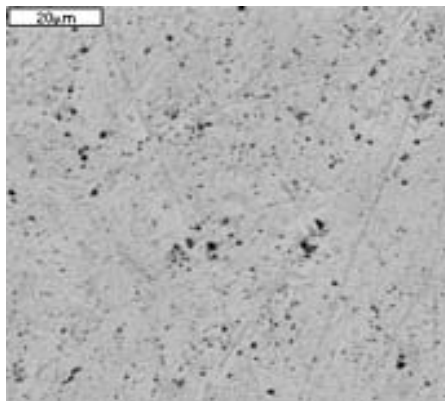

Fig. 1. A backscattered-electron image of the microstructure observed in a Pu-40Zr sample. Dark features are pores.
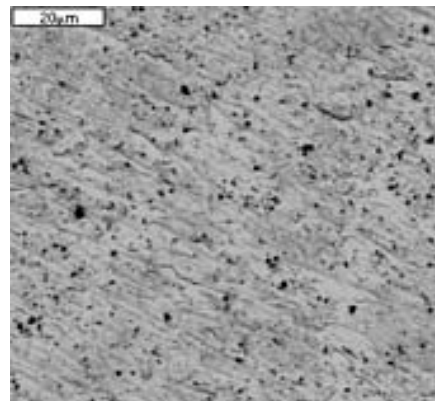
Fig. 2. A backscattered-electron image of the microstructure observed in a Pu-12Am-40Zr sample. Dark features are pores.

At the outer periphery of some of the alloy samples, a non-uniform band ~50–100 μ wide was observed (see Fig. 3). It appears that this change in alloy microstructure is due to the penetration of oxygen and other impurities into the fuel pin from the refractory oxide-coated quartz molds. This feature is typical of metallic-fuel alloys cast into coated-silica molds, and has been shown not to affect fuel performance. Methods for production of large quantities of fuel would eliminate this rind .
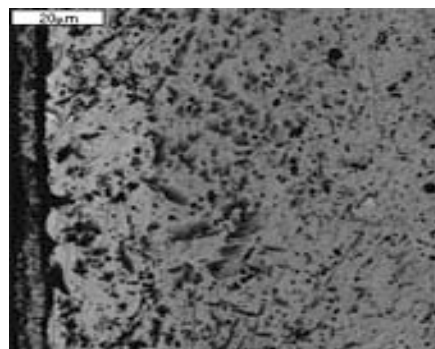

Fig. 3. Backscattered-electron image of the microstructure observed at the outer periphery of a Pu-12Am-40Zr sample. To the far left is a rind left from the casting mold.

Shown in Figs. 4—5 are x-ray dot maps of the elemental distributions of Pu and Zr in a Pu-40Zr alloy, and Pu, Am, and Zr in a typical Pu-12Am-40Zr specimen. Both alloys show even elemental distributions of the actinides and Zr.

X-ray diffraction patterns (Fig. 6) from the Pu-40Zr, and from Pu-12Am-40Zr fuel samples that were examined using SEM, indicate the presence of a single δ-Pu type (face-centered cubic) phase, consistent with the observed single-phase microstructure.

The substitution of 12 wt% Am for Pu does not change the alloy microstructure or the phase array. In this range, the ternary phase array appears to be an extension of the Pu-Am binary, with Am forming a δ-phase solid solution with Pu and Zr.

Fig. 4. (a) Backscattered-electron and (b) secondary-electron images of sample Pu-40Zr, along with x-ray maps for (c) Pu and (d) Zr. Dark areas in images and x-ray maps correspond to areas where pores are located.
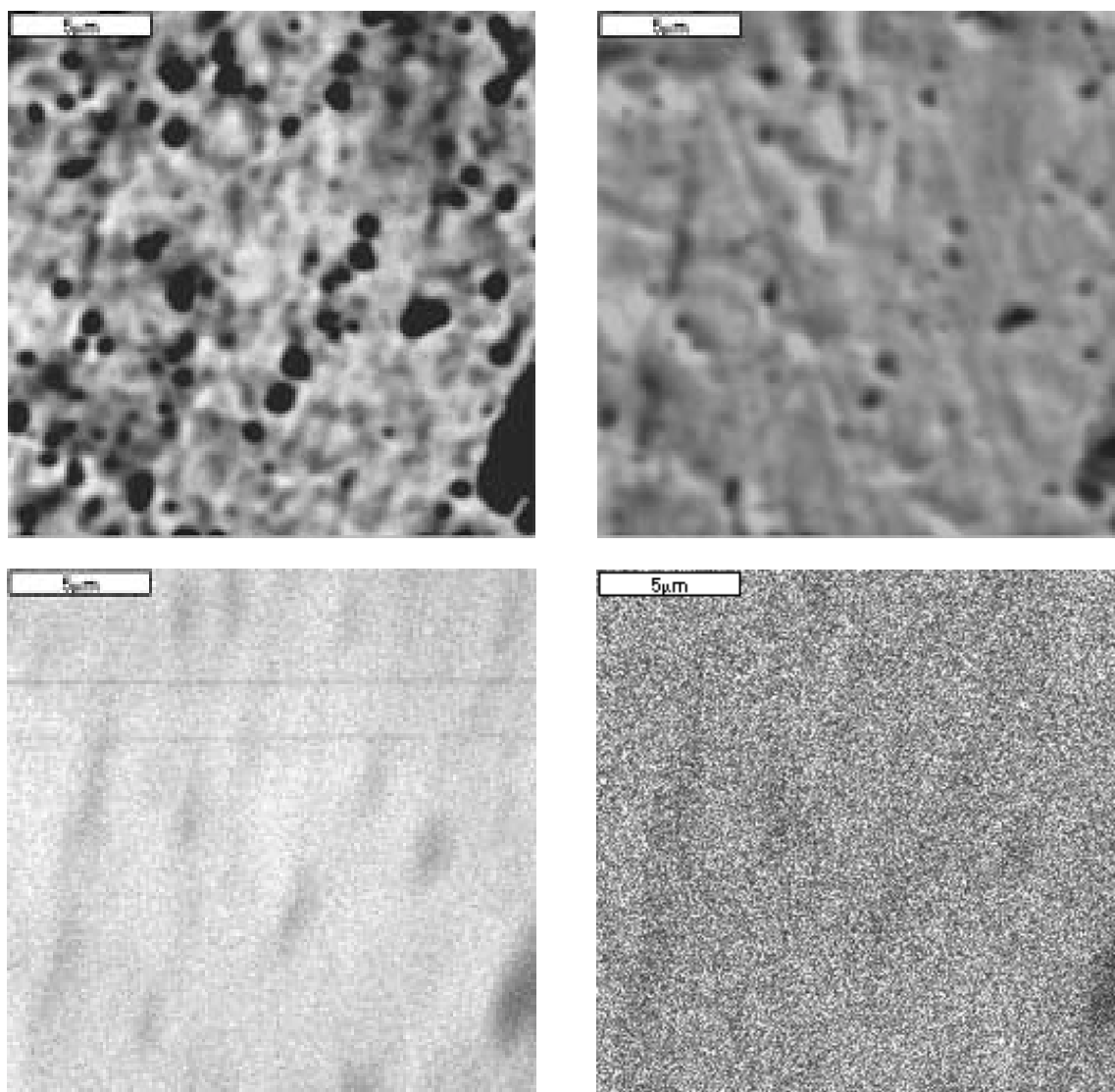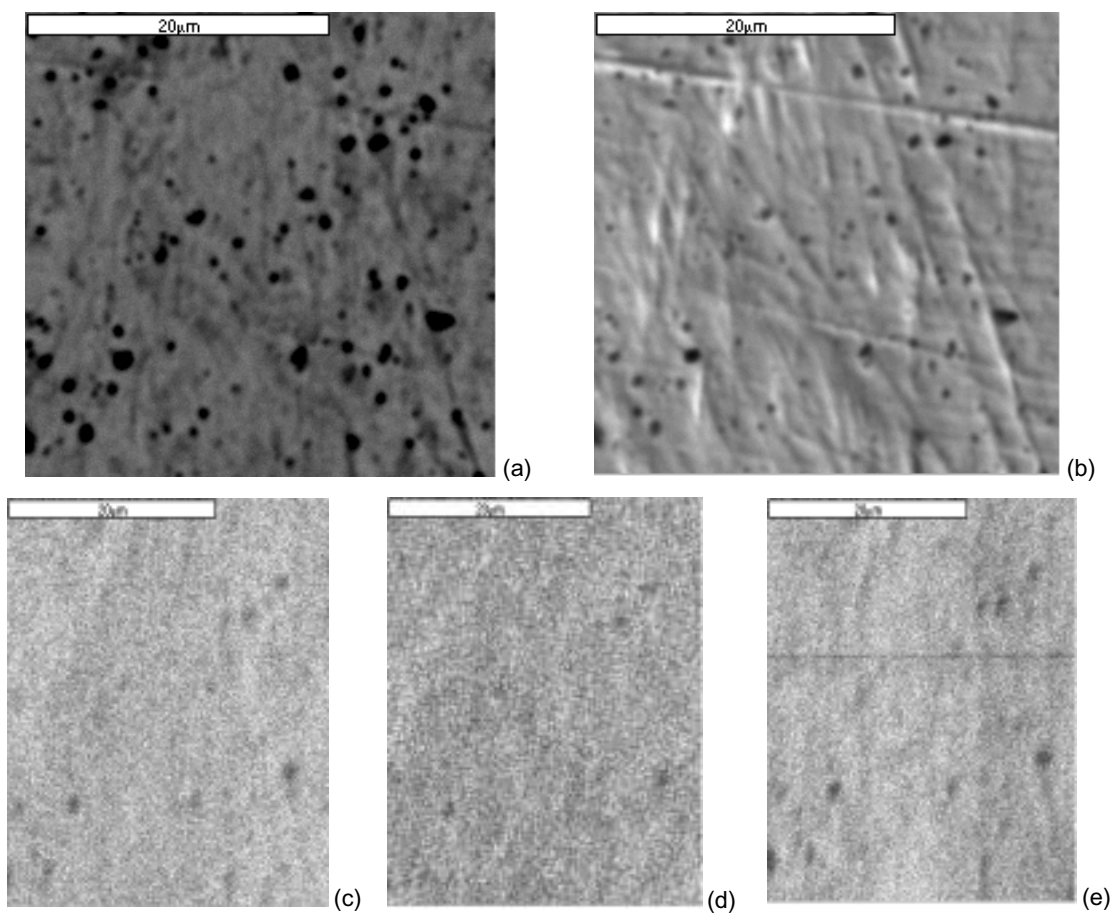
Fig. 5. (a) Backscattered electron and (b) secondary electron images of sample Pu-12Am-40Zr, along with x-ray maps for (c) Pu, (d) Am, and (e) Zr. Dark areas in images are porosity.
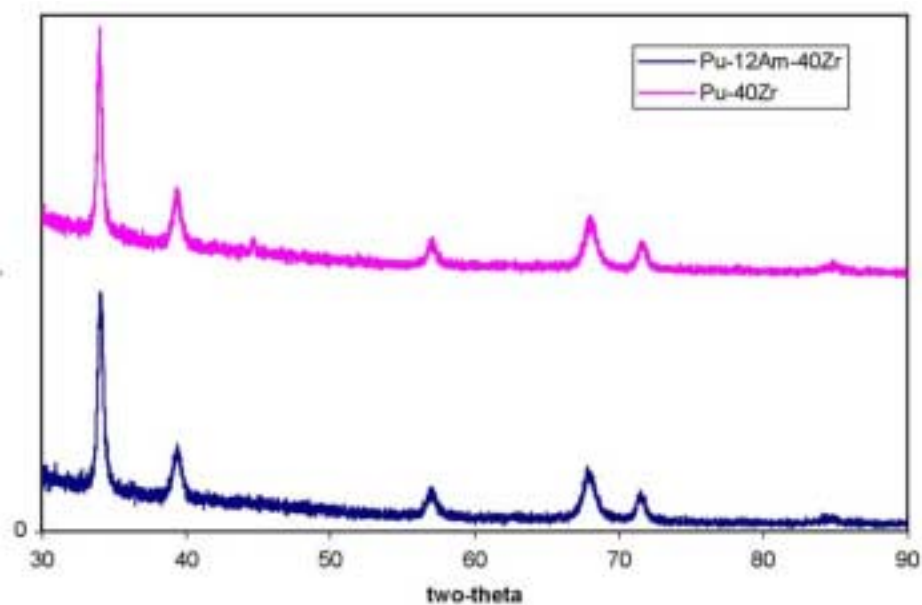

Fig. 6. X-ray diffraction patterns of Pu-40Zr and Pu-12Am-40Zr alloys. Both are single-phase δ-Pu.

Thermal Analysis

Simultaneous Differential Scanning Calorimetry-Thermogravimetric Analysis (DSC-TG) was performed on ATW-1 fuel specimens. This technique allows for the simultaneous recording of mass and energy changes that occur as a function of temperature during heating and cooling.

Data was taken using a Netzsch TG-DTA/DSC apparatus operated in a dry air glovebox. Samples were contained in capped alumina crucibles; argon was used as a purge gas, with heating and cooling rates of 10¡C/min. A complete cycle started at 20¡C, ramped to 1000¡C and then cooled to ~80¡C. Pu-40Zr, Pu-40Zr-10Am-10Np, and Pu-40Zr-12Am specimens were subjected to six complete thermal cycles. Summary data is presented here.

_Pu-40Zr_ - A single transition was observed at T_{onset} between 598¡C and 624¡C with an enthalpy change in the range of -1.9J/g to -2.3 J/g due to the δ-Pu (fcc) to ε-Pu (β-Zr, bcc) transition. The transition was reversible and repeatable during cooling with an onset between 623¡C and 626¡C. Figure 7 shows the DSC-TG data for the second heating/cooling cycle; data from the other five cycles matched the shape of the curve. Over all six cycles, a total mass increase of 2.6 mg (1%) occurred in the sample due to oxidation. The published and assessed Pu-Zr phase diagram also shows a transition from δ-Pu to θ + α-Zr occurring at 267¡C; this was not observed, presumably due to the relatively rapid heating and cooling rates during these measurements.
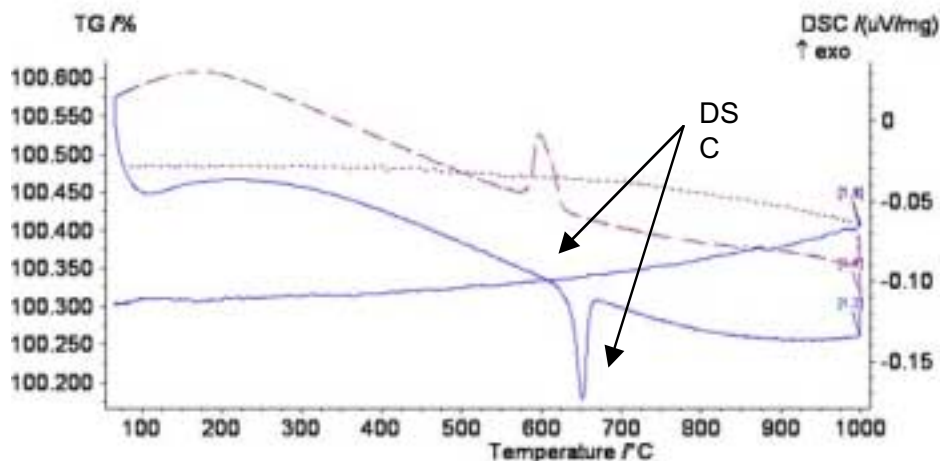
Fig. 7. DSC trace and thermogram of Pu-40Zr on heating (solid line) and cooling (dashed line).

_Pu-40Zr-10Am-10Np_ - Two reversible transitions were observed, as shown in Fig. 8 for the second heating/cooling cycle. The first endotherm had onset temperatures ranging from 505¡C to 514¡C and enthalpy changes ranging from -1.7 to -2.2 J/g. The defining temperature of the second transition is difficult to determine because of the gradual onset, but was estimated to be between 620¡C and 653¡C. Mild oxidation was observed on inspection of the specimen after testing, however, no evidence of melting or dimensional change of the well-defined sample geometry were observed. There was no measurable volatilization of Am. Thermal analysis data from this quaternary alloy are much more difficult to interpret because the phase diagrams of constituent binary alloy systems are not, in general, well studied. There are no phase diagrams for ternary or quaternary alloys within this system. The current literature has conflicting reports on the features of the Np-Zr phase diagram. Because the Zr-Am and Zr-Np phase diagrams are uncertain and incomplete, and

---

due to the complexity of quaternary systems, the nature of the phase transition cannot be ascertained from this data.   Further analysis of this alloy by high-temperature x-ray or neutron diffraction is planned.
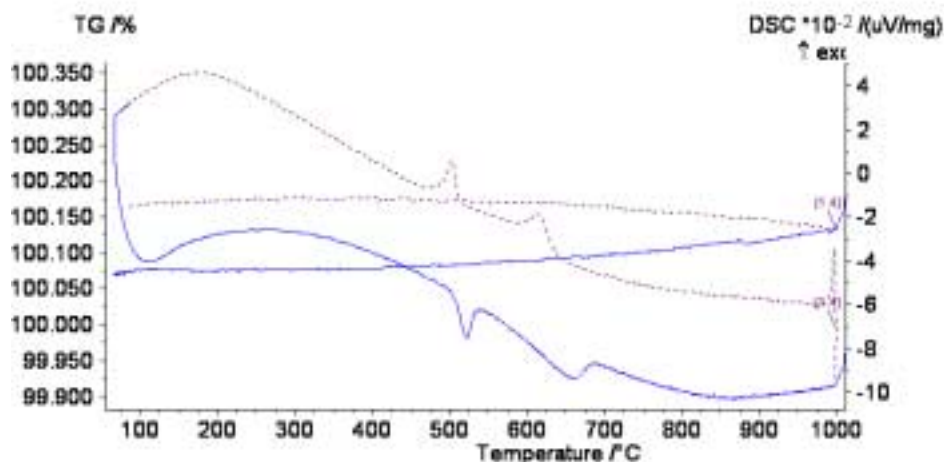
Fig. 8. DSC trace and thermogram of Pu-10Np-10Am-40Zr on heating (solid line), cooling (dashed line).

Pu-12Am-40Zr - Similar to Pu-40Zr, one endotherm was observed on heating at an onset temperature of 691¡C–704¡C, the exotherm representing the reversal of the transition occurred between 665¡C and 669¡C on cooling. The DSC-TG of the second heating cycle is shown in Fig. 9. This observation is consistent with the δ-Pu (fcc) to ε-Pu (β-Zr, bcc) transition, and supports the characterization of this material as a single-phased δ-Pu alloy. The results of these preliminary studies found no measurable volatilization of Am.
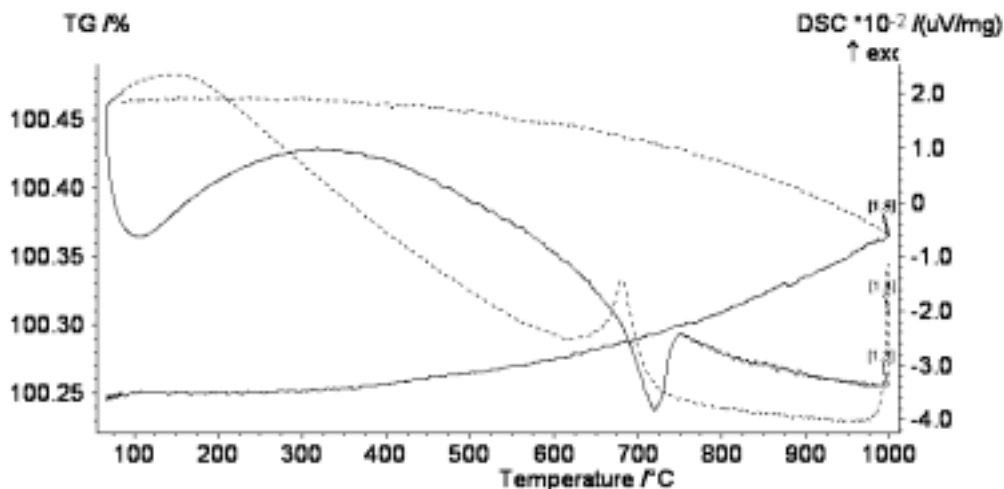

Fig. 9. DSC trace and thermogram of Pu-12Am-40Zr on heating (solid line), cooling (dashed line).

Chemical and Isotopic Analysis

Chemical and isotopic analyses were completed on fuel rod specimens from all five alloys types.   Summary data representing average compositions for each alloy are given in Table

1; there was little variation in major constituents from alloy to alloy. Of note is the fact that very little Am was lost during the casting process used to alloy the metals and cast the fuel rods. Np losses were higher due to the high oxygen impurity levels in the available metal feedstock leading to generation of oxide soot .

Table 1. Summary Chemical Analysis Results for ATW-1 Metal Fuel Rods

°	Units	Pu-60Zr	Pu-40Zr	Pu-12Am-40Zr	Pu-10Np-40Zr	Pu-10Am-10Np-40Zr
Total Pu	wt%	39.5	59.1	48.8	50.1	°40.1
Zr	wt%	60.5	41.0	41.0	41	°41.0
Np-237	wt%	°-	<40	0.23	8.3	9.5
Am-241	wt%	°-	0.32	12.4	-	10.8
O	ppm	664	690	-	295	-
N	ppm	65	6.2	-	<10	-
C	ppm	168	76	-	74	-
Fe	ppm	179	680	-	245	°-
Cu	ppm	118	70	-	<50	°-

Table 2 lists summary isotopic analysis data for the five types of alloy fuel specimens prepared for ATW-1.

Table 2. Summary Isotopic Analysis Results for ATW-1 Metal Fuel Rods

°	Pu-60Zr	Pu-40Zr	Pu-12Am-40Zr	Pu-10Np-40Zr	Pu-10Am-10Np-40Zr
Pu-238	<0.058	<0.057	<0.051	<0.056	°<0.052
Pu-239	82.83	82.83	82.57	82.83	°82.60
Pu-240	16.21	16.22	16.51	16.21	°16.48
Pu-241	0.556	0.545	0.522	0.556	°0.522
Pu-242	0.347	0.348	0.344	0.347	°0.344

Nitride Fuel

ZrN Matrix Processing Tests

ZrN pellets can typically be cold pressed to a green density of ~70%, and additional densification can be achieved with sintering above ~1650¡C for commercially available —325 mesh powders. (TRU)N/ZrN fuel compositions also require such high temperatures for densification of course powders. In order to achieve the desired final density of ~85% for the ATW-1 irradiation fuel pellets, it was necessary to mill the starting nitride powders to reduce the particle size, i.e. increase the driving force for sintering by increasing the surface area of the powder. The milled powders decrease the firing temperature required for significant densification. However, the microstructure of the resulting pellets has not yet been optimized.

The focus of the recent fuel matrix fabrication work has been to provide better understanding of the fundamental processing behavior of ZrN and to survey the characteristics of the sintered microstructure. Initial studies evaluated the effect of sintering temperature on the

relative density of ZrN and the results are shown in Fig. 10. In each run, several pellets were processed under identical conditions then sintered for 10 hours. The data show that temperature provides enough driving force for significant densification only above 1500¡C. Note that due to differences in processing furnaces, the absolute densities do not directly translate to what is achieved in the LANL TA-55 facility; however, the relative density differences in the plots below should be accurate.

ZrN Relative Density vs. Sintering Temperature
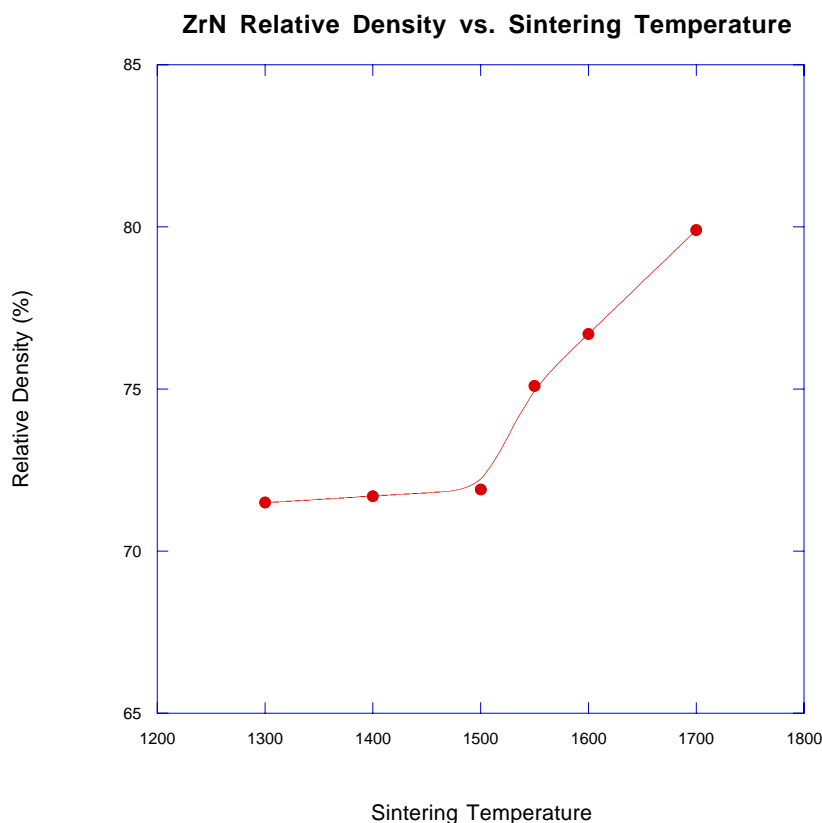
Fig. 10. Density versus sintering temperature for ZrN pellets. Powders were milled for 45 min and pressed into pellets at 300 MPa without binder or powder lubricant. Pellets were fired under flowing Ar.

This temperature dependence of densification is consistent with subsequent experiments that evaluated the change of relative density with time at 1400¡C and 1700¡C (Fig. 11). Although the results for the two temperature series show a similar trend in densification with increasing sintering time, the density increases only by approximately 2% for the lower temperature. The densification is greater in the series run at 1700¡C showing an increase in relative density of approximately 6%. Figure 11 also demonstrates the baseline sintering dwell time of 10 hours used for the ATW-1 nitride fuels. At 10 hours for the 1400¡C and 1700¡C temperatures, the densification has begun to plateau, and further increase in sintering time provides a minimal increase in density. This data is consistent with the behavior of the actinide-nitrides and illustrates the relationship between sintered density and sintering time and temperature and the potential effect on volatile species.

ZrN Rho vs Time @ 1400C and 1700C
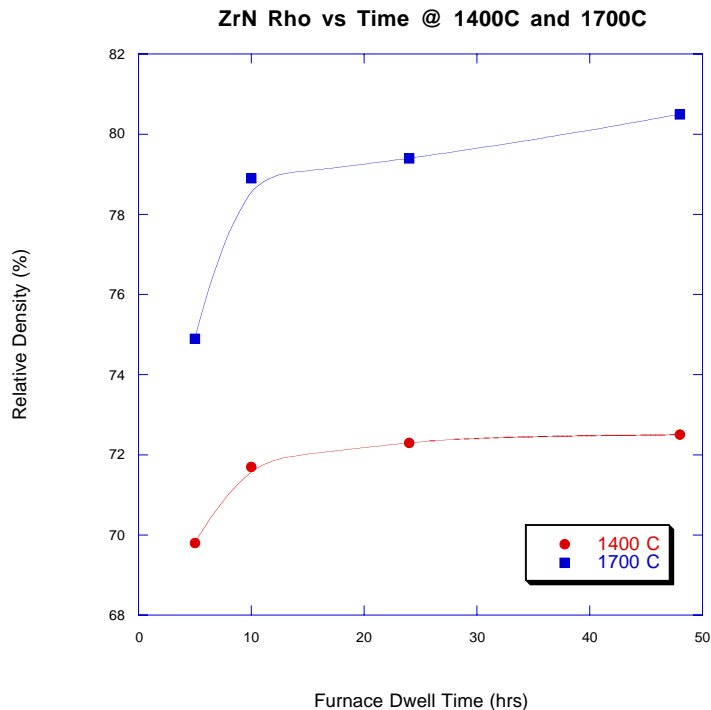
Fig. 11. Relative density vs. sintering dwell time for ZrN pellets fired
under Ar at 1400¡C and at 1700¡C for 10 hours.

This work has also shown that the increase in relative density for ZrN-based matrices fired below ~1550¡C is limited. Optical characterization of sintered pellets also reveals that a substantially heterogeneous microstructure develops during sintering. Fig. 12 shows a polished interior surface of a pellet sintered at 1700¡C for 24 hours.
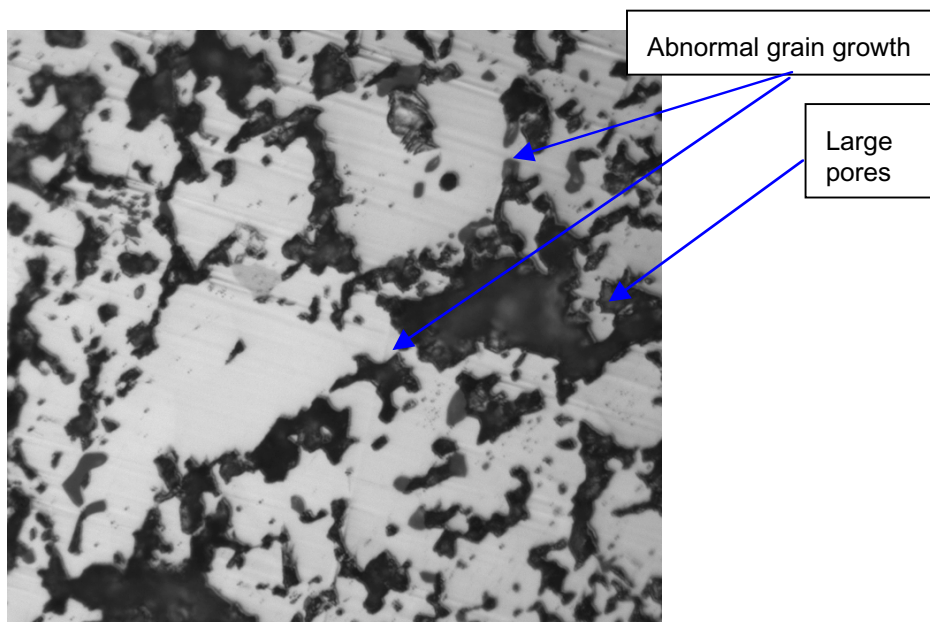
Fig. 12. Optical micrograph showing microstructure of ZrN sintered at 1700¡C for 24 hours.

Exaggerated grain growth is observed with accompanying large pores. Other regions retain a much finer grain size and finer associated porosity. The heterogeneous nature of the microstructure needs to be further characterized as it can impact both irradiation performance and mechanical integrity.

Thermo-Mechanical Characterization of Sintered ZrN Pellets

The fatigue behavior and mechanical properties of sintered ZrN were studied and measured to evaluate the mechanisms that can compromise the structural stability of fuels during transmutation, with emphasis on fatigue and fracture. Vickers hardness (Hv) and fracture toughness were measured using samples from pure ZrN pellets. These pellets were prepared with an improved sintering process, with respect to that used to sinter the material evaluated last quarter (3Q FY02). In addition, the volume fraction of porosity was measured using optical analysis to estimate the relative density. The static mechanical properties were evaluated first, since they provide the guidelines needed to study the fatigue behavior. Microstructural characterization revealed the presence of distributed porosity and microcracking in all samples. Material produced with the improved process was also heat treated at 800¡C for 24˚hours under high purity nitrogen to estimate the effect that temperature might have on the structural stability of the material. The fatigue behavior was studied once the static properties were evaluated and notched samples were tested under four-point bending at different levels of applied stress intensity, ranging from 30% to 87% of the measured fracture toughness. Fatigue lives were measured for these different conditions to evaluate the fatigue resistance.

Cylindrical ZrN pellets (12 mm in diameter and ~12 mm in height) were sintered at LANL using an improved process relative to the material studied last quarter. Samples for metallographic characterization and microhardness testing were cut from these pellets using Wire Electro-Discharge Machining (WEDM). These samples were first polished with SiC paper (600, 800 and 1200 grit) and then finished with 1- m diamond paste. Samples for fracture toughness were also cut using WEDM, in the form of micro-beams with height and thickness of ~1 mm and lengths of about 6-7 mm. Notches with lengths of approximately one half of the height were also made using WEDM. The surfaces of these beams were polished with SiC paper only up to 1200˚grit. Samples for fatigue testing were cut in the form of beams, with height and thickness of ~3 mm and lengths of ~10 mm. Some of the material was heat treated at 800¡C for 24 hours under a nitrogen atmosphere to evaluate the influence of intermediate temperatures and environment on the mechanical properties.

Hardness testing was carried out in a standard microhardness testing apparatus using a Vickers indenter with a load of 500 g. Five indents were made per sample, to obtain average values of the hardness. Fracture toughness testing was performed using a screw-driven loading stage under displacement control following the procedures specified by the standard ASTM E-399. The load resulting in fracture was measured using a 500-lb load cell. Fatigue testing was performed using four-point bending under load control in a servo-hydraulic Instron 1331 load frame. Load amplitudes were set to have a maximum K_l equal to a given fraction of the measured fracture toughness of the material and the minimum load was selected to have a load ratio ($R=L_{min}/L_{max}$) of 0.1. Cracks were nucleated from the notches using compression-compression loading, as described in [2].

Microstructural characterization, measurement of indents for hardness determination, and fractography, were performed using Scanning Electron Microscopy (SEM) with an x-ray detector for Energy Dispersion Spectroscopy (EDS). The relative density was measured by obtaining the volume fraction of porosity via analysis of the microstructure using image analysis software.

Mechanical Properties

Results from the microhardness and the fracture toughness experiments for samples with and without heat treatment are plotted in Fig. 13. Four different sample batches (3 to 6) are shown.

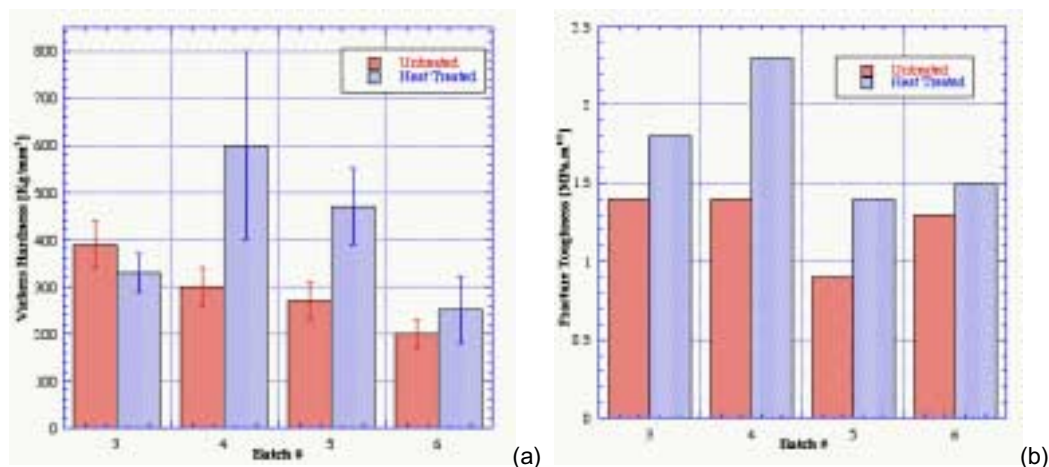(a)   (b)

Fig. 13. (a) Hardness and (b) toughness as functions of the heat treatment.

Note that there is a measurable increase in the mechanical properties of the material in three out of four batches for the hardness and in all cases for the fracture toughness. The values of the mechanical properties for the untreated specimens did not correlate very well with the measured density, as was the case for the samples with Pd additions studied during the last quarter (3Q FY02). The relative densities were 81% for batch 3, 94% for batch 4, 93% for batch 5 and 85% for batch 6. Densities measured via SEM images were about the same after heat treatment. However, note that the increase in properties correlates well with the initial density, i.e., samples with densities that were high initially (batches 4 and 5) have the highest increases on their measured mechanical properties after the heat treatment. This suggests that the new method to sinter the pellets can be optimized even further by using an adequate intermediate temperature for heat treatment after sintering at high temperatures. The fracture surfaces offered some insight about the reason for this increase (Fig. 14).

It seems likely that the heat treatment improved the properties of interfaces between particles, probably by putting nitrogen in solid solution. This could not be verified using EDS in the SEM, since nitrogen is hard to quantify in the available microscope; however, a direct comparison of the fracture surfaces for samples before and after heat treatment offers some indirect evidence pointing along this direction. The comparison of these two fracture surfaces indicates that the crack in the treated sample had to propagate across particles, given the higher fraction of cleaved surfaces that can be observed in Fig. 14b. The fracture surface in the untreated sample shows a lower fraction of cleaved surfaces, indicating that the crack could propagate between particles. This, in turn, points to weaker interfaces in the untreated material. Maximum fracture toughness obtained in the heat-treated specimens is higher than the toughness of pure ZrN that was evaluated in the first part of this work (see Q3FY02 report). However, variability of results, particularly with respect to the densities, indicates that further improvements to the sintering process are required to reduce scatter and improve structural reliability of the material.
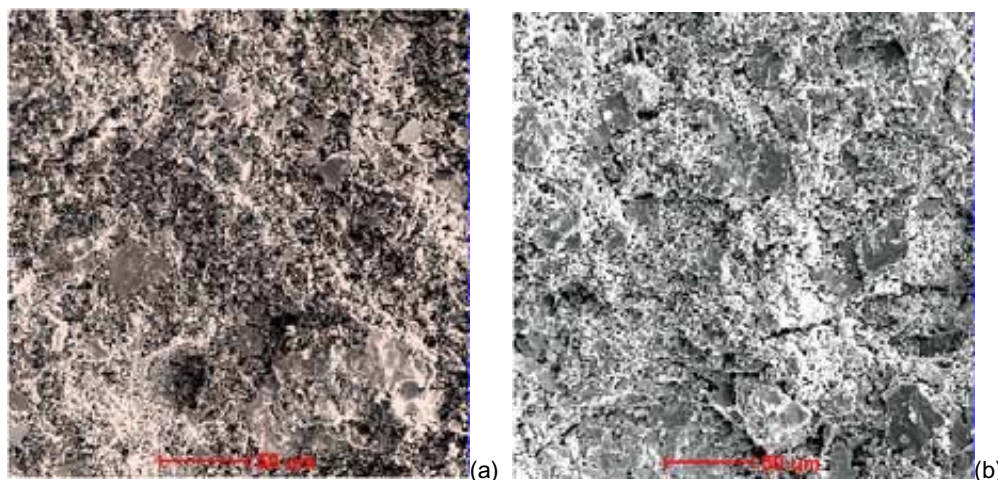
Fig. 14. Fracture surfaces for samples from batch 3; (a) before heat treatment; (b) after treatment.

Fatigue Behavior

Sharp pre-cracks were nucleated from notched specimens in compression-compression fatigue using four-point bending. The setup used for the crack nucleation and the resulting crack are shown in Fig. 15. It was found that load amplitudes of more than 50% of the estimated fracture toughness of the material were required to initiate a crack using compression-compression loading. In addition, cracks did not always nucleate at the tip of the notch. In at least two specimens, sharp cracks nucleated from the side of the notch, just where the radius of the tip begins. However, this is not expected to affect the results since the pre-cracks extended beyond the length of the notch itself, making the tip of the pre-crack the dominant defect. These cracks eventually propagated to total failure. The distribution of stresses around the notch in compression is likely to be responsible for this, since a positive stress could be present at that location.

(a)   (b)

Fig. 15. (a) Setup for nucleation of a crack in compression-compression fatigue. (b) Resulting crack indicated by arrows. The width of the notch is ~0.2 mm in both cases. Load is vertical.

Once a crack of adequate length was nucleated, e.g., one or two times the width of the notch, the sample was flipped over to apply tension to the crack tip and proceed with fatigue test as shown in Fig. 16.

Fig. 16. Four-point bending setup for fatigue crack growth. The width of the notch is ~0.2 mm. Load is vertical.

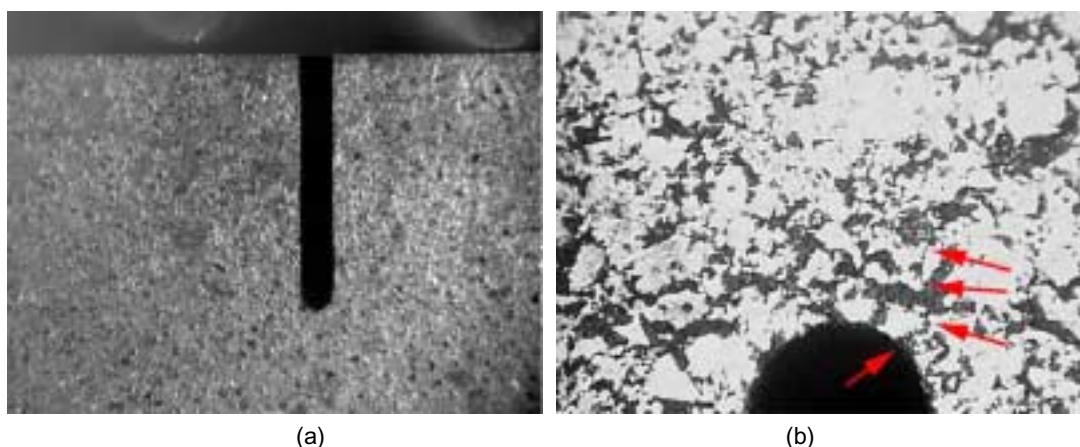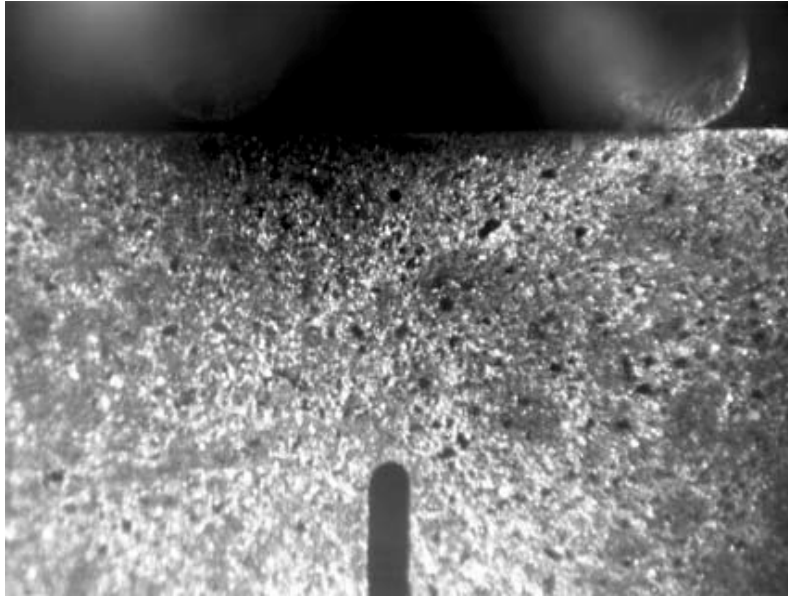Samples for the fatigue test had dimensions consistent with ASTM E-399; however, the four-point bending setup used is not covered by the standard. This setup was chosen to insure a homogeneous loading in the region surrounding the notch, since four-point bending produces a constant moment in the central section of the beam. This, in turn, helps to decrease the scatter in the results. The load amplitudes used were chosen such that the maximum stress intensities applied were 0%, 43%, 58%, 72% and 87% of the maximum fracture toughness measured, which was estimated at 2.4 MPa•m$^{1/2}$ for treated samples. The fatigue lives measured are shown in Table 3.

Table 3. Summary of Fatigue Behavior for the Samples Tested

Test #	Applied Load (% of K_{Ic})	Fatigue Life (cycles)
1	30%	> 250,000
2	43%	⁻ 200,000
3	58%	⁻ 170,000
4	72%	⁻ 120,000
5	87%	⁻ 700

The sample at the lowest load amplitude did not show signs of crack propagation after more than a quarter million cycles. The other samples did finally break, and in most cases the fracture surface was macroscopically perpendicular to the applied load. The one exception is sample five, the one tested at the maximum amplitude, where the crack propagated at an angle and ended on one of the load pins, probably because of local stress concentrations.

The sharp difference in fatigue lives between the 72% and 87% applied load indicates that the fatigue crack propagation in this material is controlled by static deformation modes, at least at room temperature. Note that the fatigue lives fall into the high cycle fatigue regime; however, the applied stress amplitudes are fairly low (the maximum was approximately 2.08˚MPa• m$^{1/2}$). Examinations of the fracture surfaces confirmed these observations. A typical fracture surface is shown in Fig. 17.
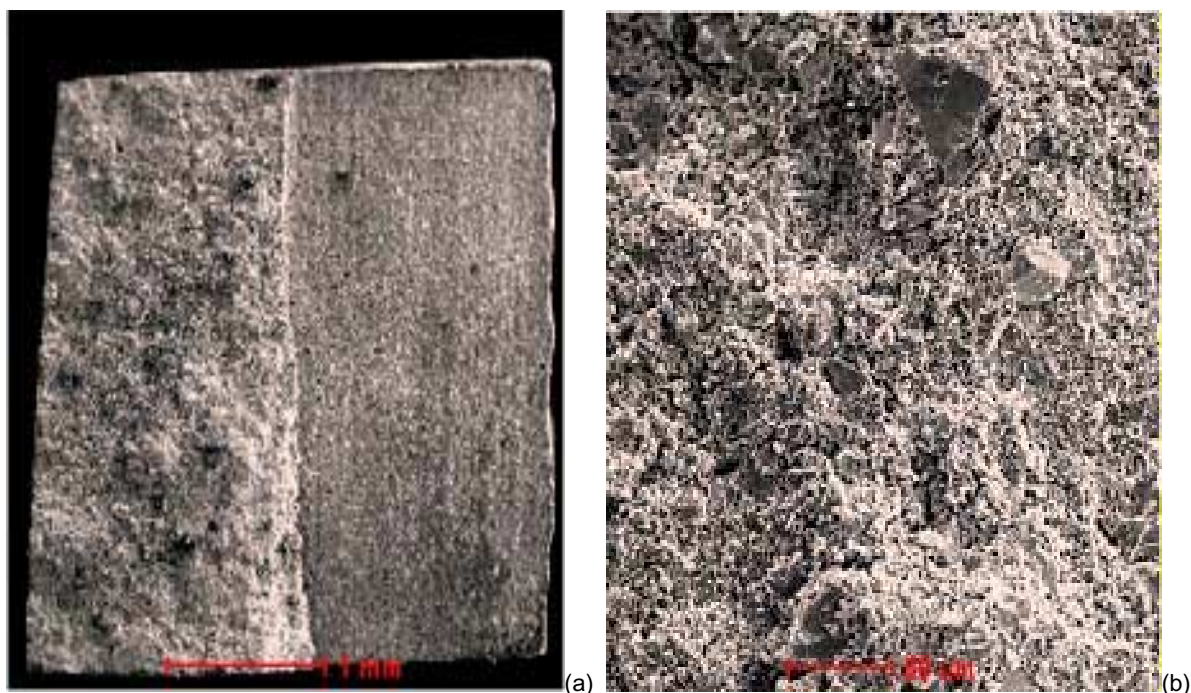
Fig. 17. Fracture surfaces of a sample tested at 72%K_{Ic}. (a) 80x; (b) 400x.

Note from Fig. 17a that there is a noticeable macroscopic roughness of the fracture surface, which is one of the differences observed with respect to fracture under monotonic loading. The aspect of the fracture surface at the microscopic level (Fig. 17b) shows that the same mechanisms observed during static fracture are present, viz., cleavage of particles and linking of microcracks. However, the presence of material debris was observed, which is compatible with rubbing and frictional processes during the growth of rough fatigue cracks in brittle materials. In this sense, the fatigue behavior of the ZrN pellets is consistent with what has been observed in many other ceramic materials, where failure modes can be mostly related to static deformation mechanisms, and the presence of cyclic loading can lead to a resistance to crack growth due to frictional effects and the presence of crack tortuousity [2].

Actinide-Nitride Pellet Fabrication

All six compositions of nitride pellets for the ATW-1 test were fabricated. Table 4 shows the six fuel mixtures with their nominal compositions and sintering conditions. Typically, sintered densities were a function of the Am content. The high Am-bearing materials had to be sintered at lower temperatures because of the boil off of Am. Even with the lower temperatures, the sintered densities were somewhat low. Only for the case of the non-Am-bearing pellets, Compositions 3 and 4, where the sintering temperature was 1700¡C, was the target density of 80%-90% met.

Figures 18 and 19 show the actual actinide nitride fuel pellets of all six compositions. In Fig. 18, the pellets are placed in holders for inspection and in Fig. 19 the pellets are being prepared for measurement.

Fig. 18. Actinide nitride fuel pellets of all six compositions

Table 4. ATW-1 Nitride Fuel Composition Results

	Comp1	Comp2	Comp3	Comp4	Comp5	Comp6
Nominal Composition	(0.2 Pu 0.8 Am)N-36ZrN	(0.8 Pu 0.2 Am)N-36ZrN	(0.5 Pu 0.5 Np)N-36ZrN	(1.0 Pu)N-36ZrN	(0.5 Pu 0.25 Am 0.25 Pu)N-36ZrN	(0.5 Pu 0.5 Am)N-36ZrN
Sint T (¡C)	1550	1650	1700	1700	1650	1550
Sint t (hr.)	10	10	10	10	10	10
Atmosphere	Ar	Ar	Ar	Ar	Ar	Ar
Typical Sintered Density (%)	65-73	75-82	80-87	84-90	72-80	67-71
Target Chemical Composition						
Pu (wt.%)	12.8	51.2	32.0	64.0	32	32
Am (wt.%)	51.2	12.8	32.0	0	16	21.5
Np (wt.%)	0	0	32.0	0	16	0
Measured Chemical Composition						
Pu (wt.%)	13.8	36.3	30.6	50.1	33.0	33.3
Am (wt.%)	tbd	tbd	tbd	tbd	tbd	tbd
Np (wt.%)	tbd	tbd	tbd	tbd	tbd	tbd
Measured Pu Isotopics						
Pu 238 (wt.%)	0.0101	0.0095	0.0118	0.0099	0.0107	0.0100
Pu 239 (wt.%)	93.7975	93.8662	93.8843	93.8729	93.8717	93.8746
Pu 240 (wt.%)	6.0569	5.9905	5.9725	5.9845	5.9833	5.9820
Pu 241 (wt.%)	0.1057	0.1051	0.1035	0.1048	0.1057	0.1050
Pu 242 (wt.%)	0.03	0.0286	0.0278	0.0278	0.0286	0.0284
Pu 242 (wt.%)	n/a	n/a	n/a	n/a	n/a	n/a
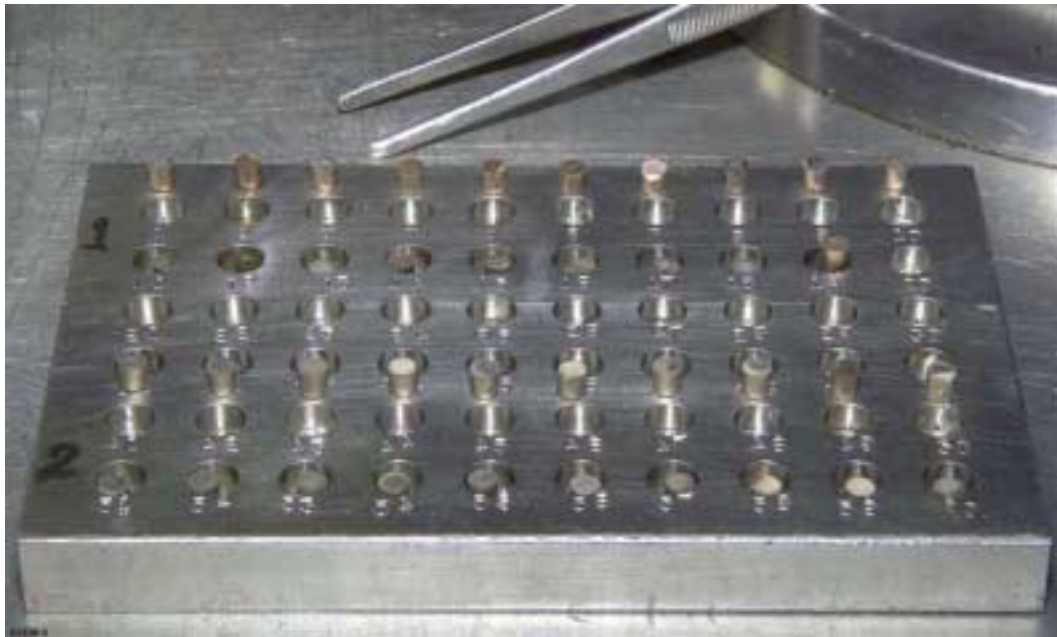
Fig. 19. All the actinide nitride fuel pellets prepared for measurement.

Fig. 20 and 21 show Am loss as a function of starting Am content and sintering temperature respectively. The figure assumes that all the weight loss measured for the sintered pellets was due to Am loss. (Subsequent chemical analyses suggest that some Pu was also lost due to sintering. The details of weight loss are still being analyzed.) The figures suggest Am weight loss is independent (to a first approximation) of starting Am content. Sintering temperature seems to affect Am loss to a much greater extent. However, a different weight loss mechanism seems to be at work for the low-Am pellets (Comp2) v. the higher Am pellets (Comp1, Comp 5, and Comp6).
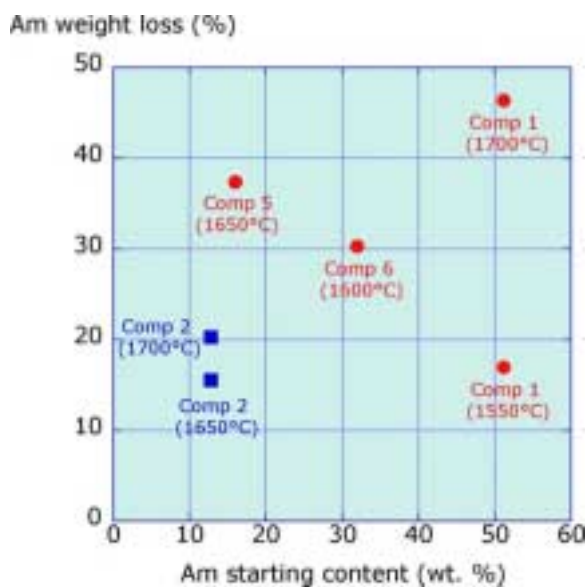
Fig. 20. Am loss vs starting Am content.
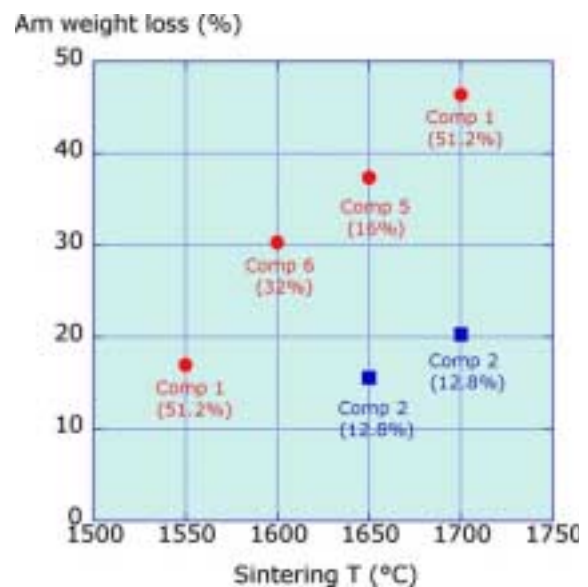
Fig. 21. Am loss versus sintering temperature for each Am composition

Dispersion Fuels

During this report period, many of the remaining components for the fluidized bed-chemical vapor deposition (FB-CVD) apparatus were assembled and have been tested. A photograph of zirconia microspheres fluidized in the CVD side feed apparatus is shown in Fig. 22. The initial operations have demonstrated that particle fluidization is readily achieved; 100- m-diameter zirconia (ZrO_2) and 300- m-diameter hafnia (HfO_2) microspheres were used for this demonstration. The goal of these fluidization experiments was to demonstrate that the FB-CVD apparatus indeed has the capability to fluidize particles as small as 100 m and the capability to fluidize particles with a density comparable to actinide fuels (hafnia ρ=9.68 g/cm^3). Niobium pentachloride, a well-documented precursor for the CVD of niobium, has been received.   Due to the change in program focus, it is not likely that this work will continue into FY03.
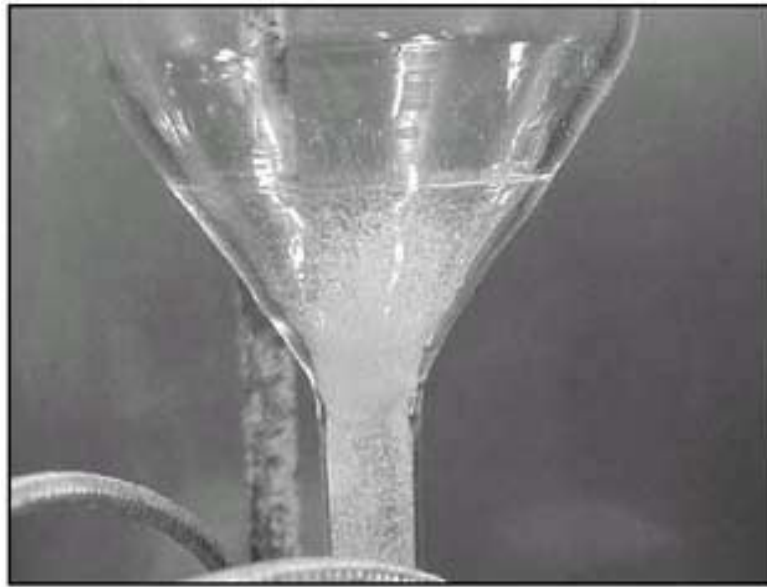

Fig. 22. Photograph of ZrO_2 particles fluidized in FB-CVD coater.

Fuels Irradiation Testing

ATW-1 Irradiation Test in ATR

Physics Analysis

Physics analysis of the ATW-1 Experiment for Cycles 3-6 was performed using INEEL s detailed MCNP full-core model to provide the fuel fission-neutron heat rates in the East flux trap following typical irradiation cycles (50 Effective Full-Power Days—EFPDs) with lobe powers of 17 MW (NW), 17 MW (NE), 25 MW (C), 25 MW (SW), and 25 MW (SE). The Phase-II initial fuel loadings for each rodlet are input from the end of Phase-I irradiation (the Phase-I results for Cycles 1 and 2 were previously reported). The MCWO methodology (Monte-Carlo with ORIGEN), which applies the Monte-Carlo code MCNP coupled with the isotope depletion code ORIGEN-2 is used to calculate burnup and fission heating rate.

The geometry used for these calculations consists of six fuel capsules in each of the six positions of the flux trap outer ring. Each capsule is surrounded by an aluminum shroud containing boron. The shrouds are replaced every two irradiation cycles (~100 EFPDs) in order to maintain the desired linear heating rate. Each test capsule contains 6 fuel rodlets. The correspondence between rodlet number and composition is given in Table 5. In Fig. 23, the metal low- and high-burn capsules are located in positions 1 and 6, respectively. The nitride low- and high-burn capsules are located at positions 2 and 5 (unmarked in Fig. 23). Oxide low- and high-burn capsules were included in positions 3 and 4 to simulate the original test matrix and the possible inclusion of additional ATW-1 test capsules.

We calculated the burnup and LHGR (linear heat generation rate) distributions of the Phase-II (ATW-1 Cycles 3 and 4 with a new Al-B shroud) rodlets vs. EFPDs using the MCNP and ORIGEN-2 codes. Because of the depletion of boron-10 during irradiation, the peak metal-rodlet LHGR increases from 205 w/cm to 278 w/cm, but stays within the target maximum value of 300 W/cm. We also calculated the burnup and linear heat generation rate (LHGR) for phase III (ATW-1 Cycles 5 and 6).
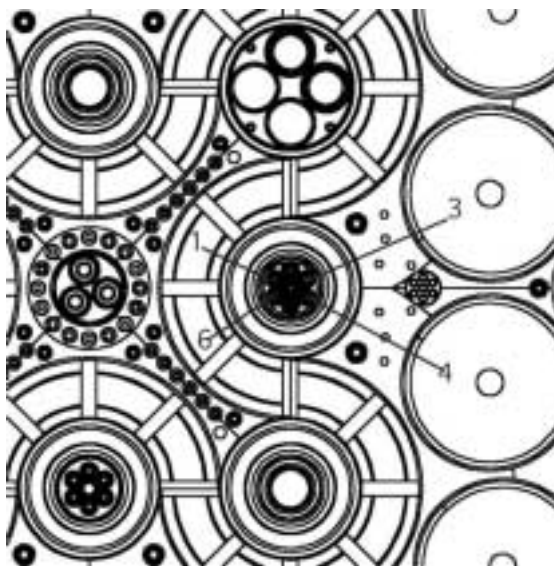
Fig. 23. Location of ATW-1 test capsules in the ATR east flux trap. Serpentine object in the figure is the ATR driver fuel.

Table 5. Correspondence Between Rodlet Number and Composition for Metal and Nitride ATW-1 Capsules.

Nitride (ATW-1A and ATW-1C)	Nominal Composition
Rodlet 1	$(Pu_{0.2}, Am_{0.8})N\text{-}36ZrN$
Rodlet 2	$(Pu_{0.8}, Am_{0.2})N\text{-}36ZrN$
Rodlet 3	$(Pu_{0.5}, Np_{0.5})N\text{-}36ZrN$
Rodlet 4	$PuN\text{-}36ZrN$
Rodlet 5	$(Pu_{0.5}, Am_{0.25}, Np_{0.25})N\text{-}36ZrN$
Rodlet 6	$(Pu_{0.5}, Am_{0.5})N\text{-}36ZrN$
Metal (ATW-1B and ATW-1D)	
Rodlet 1	Pu-12Am-40Zr
Rodlet 2	Pu-10Am-10Np-40Zr
Rodlet 3	Pu-40Zr
Rodlet 4	Pu-12Am-40Zr
Rodlet 5	Pu-10Np-40Zr
Rodlet 6	Pu-60Zr

Fuel Performance Calculations

Fuel performance calculations were completed for ATW-1 metal and nitride fuel specimens under nominal and 20% overpower conditions. Details are available in the ATW-1 Design and Data Package,[1] but summary data are reported here.   The powers of the fuel rodlets increase with time due to depletion of the B-10 absorber in the borated aluminum basket. A maximum basket lifetime has been established to be 110 full-power days of irradiation. For conservatism, the fuel powers used in the following analyses are those at basket end-of-life. Since the two nitride-fuel experiments are identical in design, only the analysis for the high-power, high-burnup ATW-1C experiment will be presented here as a bounding evaluation of both nitride experiments. Similarly, the conditions for the ATW-1D experiment bounds both metallic fuel experiments.

The temperature of each fuel rodlet was calculated using the linear heat generation rates reported above and assuming all power was uniformly deposited in the fuel. The 1-D heat conduction equation was solved in the fuel and bond sodium, and the cladding inner-diameter temperature was specified to be the maximum allowable cladding temperature of 525¡C. These assumptions make the calculated temperatures extremely conservative and overestimate the actual temperatures the rodlet will experience in the reactor for a number of reasons. First, a calculated 1-D temperature will be higher than a realistic, 3-D temperature. Second, the energy deposition will not be uniform in the fuel, but preferentially deposited near the fuel periphery and some even deposited outside of the fuel. Lastly, if the peak cladding temperature in the hottest rodlet is held to 525¡C (near core axial midplane), the other rodlet cladding temperatures will be well below this value; nevertheless, all cladding temperatures were assumed to be at this peak value.

Based on these assumptions, the peak fuel temperature of 831.9¡C in ATW-1C occurs in rodlet 4; this peak fuel temperature is far below the 1400¡C temperature limit established for ATW-1 nitride fuels. The peak fuel temperature of 847.9¡C in ATW-1D occurs in rodlet 3; this peak fuel temperature is well below the conservatively low 900¡C ATW-1 experiment temperature limit established for metallic fuel.

Overpower Analysis

Two changes were made to the input data to calculate response to an ATR overpower condition: (1) the temperature of the inner cladding diameter was set to the off-normal limit of 650¡C, and (2) all fuel powers were multiplied by 1.2 to simulate a 120% overpower condition. This is quite conservative, since a 120% overpower would not raise the peak cladding temperatures from 525¡C to 650¡C; nevertheless, the higher cladding temperature limit was employed. All the additional assumptions leading to very conservative calculated temperatures that were discussed above also apply here.

During overpower conditions, the peak fuel temperature of 1019.7¡C in ATW-1C occurs in rodlet 4; this peak fuel temperature is far below the 2000¡C temperature limit given for nitride fuels during overpower conditions. The peak fuel temperature of 1039.4¡C in ATW-1D occurs in rodlet 3; this peak fuel temperature is well below the 1100¡C overpower temperature limit established for metallic fuels.

Internal Pressure Generation of the Experiment Capsule

Since the primary containment boundary is the stainless steel outer capsule, it has been assumed that all six fuel rodlets fail during irradiation; this would subject the outer capsule to

---

[1] ATW-1 Design and Data Package, ANL Document W7520-0481-ES

the maximum pressurization. The two high-burnup experiments (i.e., ATW-1C and ATW-1D) at 120% overpower conditions establish a bounding scenario. Since gas pressure within the experiment increases monotonically with burnup, evaluation of the high-burnup experiments will bound the corresponding low-burnup experiments. It is assumed that all fuels in these experiments are irradiated to a uniform burnup of 25% of all Pu present in the fabricated fuels; i.e., 25% of all Pu isotopes present in the fuels are assumed to fission, producing fission products. This assumption will be conservative for two reasons: (1) the discharge burnup of many of these fuels will be less than 25% due to the axial dependence of flux within the ATR, and (2) only the fissile isotopes of Pu will readily fission in the ATR thermal neutron spectrum. Furthermore, the fission product yields of the Kr and Xe fission gases are assumed to total 25% of all fission products. Finally, six moles of He are assumed to be produced for every mole of fission gas produced, weighted by the mole fraction of ^{241}Am in the fuel compound or alloy (since this is the isotope chiefly responsible for He production); this assumption was taken from the results of recent minor actinide irradiations in the High Flux Reactor at Petten. Thus, the number of fission gas and He atoms produced in the fuel is calculated as:

$$N_{FG} \ = \ x_{FG} \ \cdot \ B \ \cdot \ \left(\frac{w_{TRU} \ \cdot \ \rho \ \cdot \ N_A}{A} \right) \ \cdot \ V_{fuel} \text{ , and} \tag{1}$$

$$N_{He} \ = \ 6 \ \cdot \ N_{FG} \ \cdot \ w_{Am} \text{ ,} \tag{2}$$

where N_{FG} and N_{He} are the number of atoms of fission gas and He produced in the fuel, respectively, x_{FG} is the yield of gas atoms per fission, B is burnup, w_{TRU} is the weight fraction of actinides in the fuel compound or alloy, ρ is the density of the fuel alloy or compound (g/cm^3), N_A is Avogadro s number (6.023x10^{23} atoms/mole), A is the fuel alloy or compound molecular weight (g/mole), V_{fuel} is the fuel volume (cm^3), and w_{Am} is the weight fraction of actinide content in the fuel that is Am. Results from Eqns. (1) and (2) are used to compute the total gas released to the experiment free volume as:

$$n_{gas} \ = \ \frac{R_{FG} \ \cdot \ N_{FG} \ + \ R_{He} \ \cdot \ N_{He}}{N_A} \text{ ,} \tag{3}$$

where n_{gas} is the total quantity of gas released to the experiment free volume (moles), and R_{FG} and R_{He} are the release fractions for fission gases and He, respectively. For nitride fuel, these release fractions are conservatively assumed to be 0.25 for fission gases and 0.50 for He;[2] for metallic fuel, the release fractions are well established as 0.80 for fission gases and assumed to be 1.00 for He. Finally, pressure on the experiment capsule inner boundary is calculated as:

$$P \ = \ \frac{n_{gas} \ \cdot \ \left(82.056 \ \frac{\text{cm}^3 \ \cdot \ \text{atm}}{\text{mole} \ \cdot \ \text{K}} \right) \cdot \left(14.7 \ \frac{\text{psi}}{\text{atm}} \right) \cdot \ T}{V_{capsule}} \text{ ,} \tag{4}$$

where P is the capsule internal pressure (psi), T is the gas temperature (K), and $V_{capsule}$ is the capsule free volume (cm^3). The gas temperature was assumed to be average of the peak cladding temperature (650¡C) and a maximum conceivable primary coolant temperature (130¡C), since more than half of the internal free volume is contained in the outer capsule

---

[2] Konings et al., 2000 measured 0.05 and 0.20 in oxide fuel

located above the experimental fuel rodlets and exposed to direct cooling by the reactor primary coolant; thus, 0.5*(650¡C+130¡C)+273=663K. Pressures calculated for both ATW-1C and ATW-1D using Eqns. (1) to (4), are given in Table 6, and show that even under the most conservative assumptions of burnup, temperature and gas production/release, the peak internal pressures that could be produced inside the experiment outer capsules (assuming all rodlets breach at end-of-life) will remain well below 235 psi.

Table 6. Maximum Internal Pressure in ATW-1C and ATW-1D.

	ATW-1C (Nitride Fuel)	ATW-1D (Metallic Fuel)
Total Free Volume (cm^3)	17.971	19.665
Total Fissions	7.68E+21	8.00E+21
Total FG Atoms	1.92E+21	2.00E+21
Total He Atoms	2.27E+21	1.13E+21
Gas in Free Volume (mol)	2.68E-03	4.54E-03
Max. Internal Pressure (psi)	**119.3**	**184.6**

FUTURIX/ATW-3 Irradiation Test in Ph nix

Unlike U.S. test reactors such as EBR-II, FFTF or the ATR, the Ph nix reactor safety authorization basis does not specifically include the provision for fueled experiments to be approved for irradiation by a safety authority lower than the national authority. Consequently, a proposal for any Ph nix experiment must be reviewed and approved by the French equivalent of the U.S. Nuclear Regulatory Commission. This requirement is what leads to the time-consuming and lengthy process of experimental approval, which can take up to three years to obtain.

Approval of the experiment requires that the customer, as well as all its subcontractors and suppliers, be qualified by Ph nix. In the proposed collaboration, the CEA Cadarache LTEC Laboratory will act as the customer, and ANL and LANL will be classified as suppliers to CEA. ANL and LANL are required to write a Quality Plan, which must be approved before experiment fabrication begins. The Quality Plan includes references to all documents used in fabrication and analysis of the fuel test specimens. The format of the quality plan is the responsibility of the submitting supplier. Acceptance of the fuel from the DOE Laboratories will require a visit (or multiple visits) from Ph nix personnel to observe aspects of the fabrication process based on the supplied Quality Plan. All nonconformances must be evaluated and approved by the CEA.

Four packages (dossiers) are required for submittal prior to experiment approval. These are, in order of submittal: (1) a presentation report that provides a detailed description and the performance of the experiment; (2) a technical report that provides a complete design and a preliminary safety analysis, including results of experiments designed to answer safety-related questions raised in the Presentation Report; (3) specification files that provide the technical specifications for the experiments; and (4) a final safety report that takes into account the configuration of the as-fabricated experiment, including non-conformances.

A final and (most likely) conceptual design review are required in addition to a safety review. A well-defined path for disposition of scrap-irradiated materials is also required. The approximate schedule for preparation and submittal of these reports is given in Table 7. Due

to the fact that an agreement with the CEA to perform the experiment has not yet been reached, the presentation report has not yet been submitted.

Table 7. Schedule for Required Experiment Approval Documents.

Report or Activity	Start Date	Submittal Date
Presentation Report	February 2002	August 2002
Technical Report	August 2002	July 2004
Specification files	April 2004	September 2004
Safety Report	May 2005	August 2005

It is important that the DOE and the CEA come to an agreement regarding this collaborative fuels experiment as soon as possible so that the needed design and analysis work can proceed and be completed in a timeframe consistent with the proposed schedule. Failure in this could result in a delay in the approval and insertion of the experiment, significantly reducing the maximum burnup attainable in this experiment due to the remaining Ph nix operation lifetime.

To remain on schedule for the irradiation test as proposed, work during FY03 must include submittal of the presentation report, insertion of the ATW-1A, -1B, -1C and -1D irradiation experiments of metallic alloy and nitride fuels in the Advanced Test Reactor, and continued analysis that will support the submittal of the technical report during FY04. Additionally, the issues of supplying Am feed material to the CEA and initiation of arrangements for the international shipping of both fresh and irradiated fuels are also of immediate concern.

Fuel Performance

Assessment of Radiation Tolerance of ZrN

Transmission Electron Microscopy

Various techniques to evaluate radiation damage evolution in ZrN following irradiation with either He ions or heavy ions continued to be explored. Heavy ions such as Xe and Kr were used in order to simulate fission-product damage.

As an example, transmission electron microscopy (TEM) was used to examine samples irradiated with Xe ions. Figure 24 shows a TEM bright-field micrograph obtained from a poly-crystalline plan-view sample of ZrN irradiated with 300 keV Xe ions at cryogenic temperature (~100 K). The fluence used in this irradiation was $1¥10^{16}$ Xe/cm^2, which corresponds to a peak displacement damage level of about 40˚dpa. The presence of implanted Xe gas was confirmed using Rutherford backscattering (RBS) and energy dispersive x-ray spectrometry (EDXS). The TEM image in Fig. 24 reveals the presence of small voids (less than 10 nm in diameter) as well as micro-twins. The grain size is significantly reduced due to the heavy ion irradiation. In the case of 300 keV Xe ion irradiation at a substrate temperature of ~100 K, the grain size decreases by a factor of about 20, from ~2 m to 100 nm diameter. This suggests that rapid recrystallization takes place under irradiation at temperatures as low as 100 K.
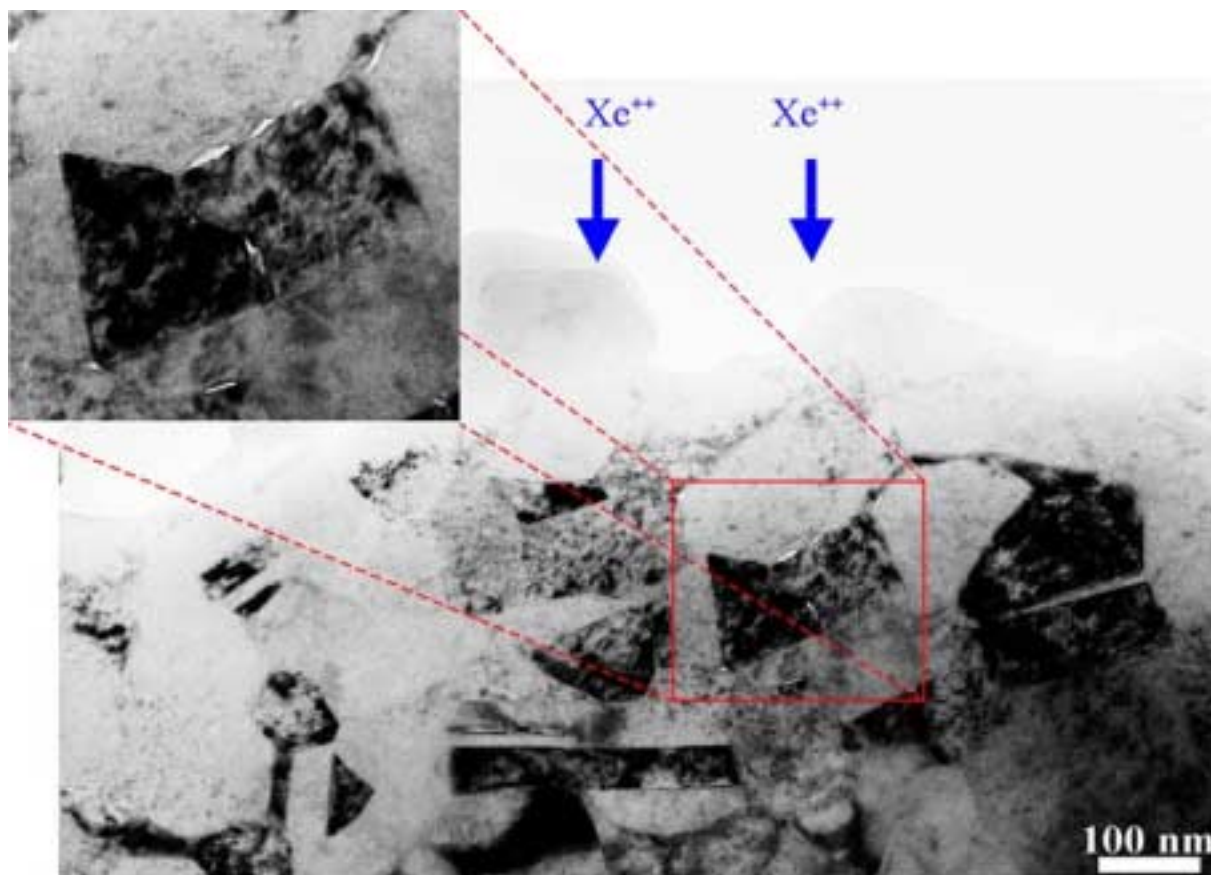
Fig. 24. Voids, micro-twinning, and small grains (~100 nm diameter) produced by Xe ion irradiation of ZrN to a fluence of 10^{16} Xe/cm^2 at 100 K.

Preparations for *in-situ* ion-irradiation experiments on plan-view TEM samples of ZrN also continued. A combined mechanical polishing and ion-milling procedure to produce large areas of electron transparent material in ZrN was developed. It was determined that the samples produced by the new procedure are ideal for *in-situ* ion-irradiation experiments. These plan-view samples will be irradiated using the *in-situ* electron microscopy and ion-irradiation facility at ANL.

Nanoindentation Experiments

In order to assess possible changes in mechanical properties due to ion irradiation, nanoindentation experiments on ion-irradiated ZrN polycrystalline samples were initiated. Nanoindentation was performed on hot-isostatically pressed (HIPed) samples with highly polished surfaces. For nanoindentation experiments, the indention tip is a small triangular diamond point that presses into the sample to depths of ~200 nm. The ZrN samples were irradiated with multiple implants of Xe ions at different energies and using fluences ranging from 10^{14} to 10^{15} Xe/cm^2, in order to produce a fairly uniform shelf of damage over a sample thickness range of ~100 nm. Figures 25a and 25b show results of a Monte Carlo computer simulation of the ion implantation and damage profiles for the different Xe ion implantations used in this experiment.
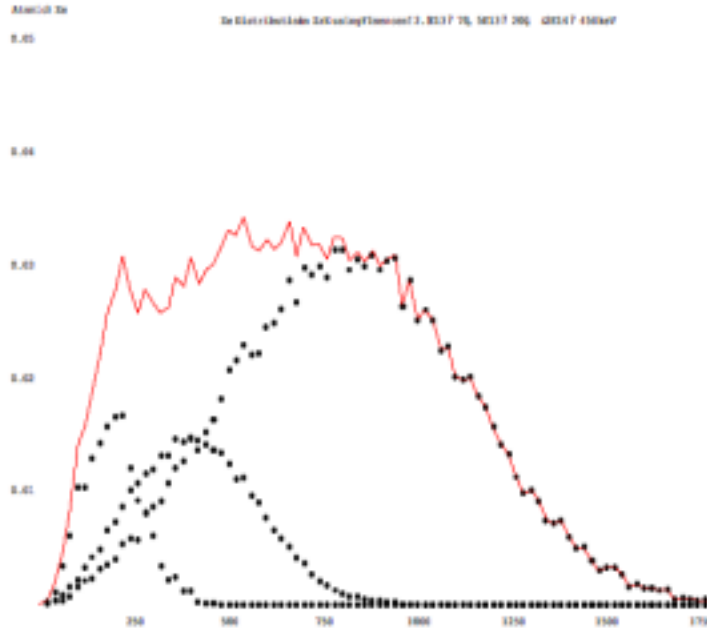
Fig. 25a. Black dot curves show computer simulation results of Xe ion implantation profiles in atomic % Xe (ordinate) vs ZrN target depth in Angstroms (abscissa) for (i) 70 keV Xe to fluence $2.5\yen10^{13}$ Xe/cm^2; (ii) 200 keV Xe to fluence $5.0\yen10^{13}$ Xe/cm^2; and (iii) 450 keV Xe to fluence $2.0\yen10^{14}$ Xe/cm^2 (from shallowest to deepest). The red curve shows the superposition of the three ion implantation profiles.

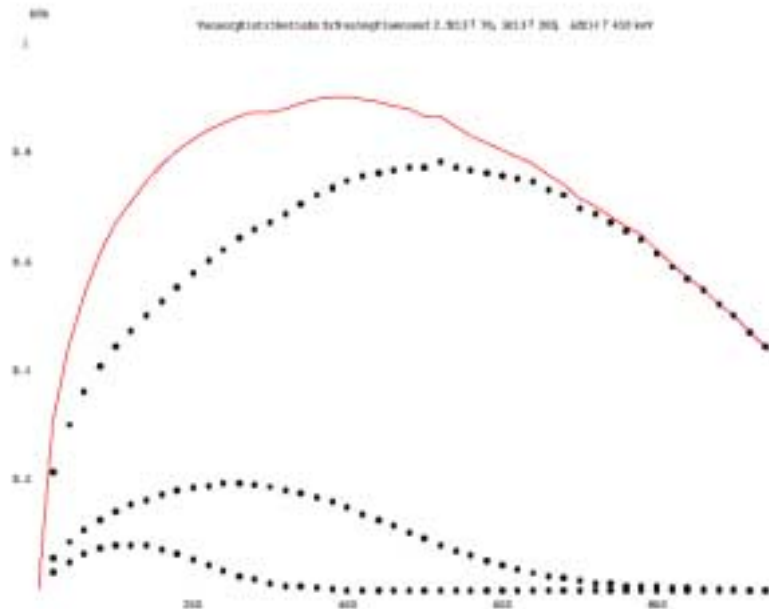Fig. 25b. Black dot curves show computer simulation results of Xe ion-damage profiles in dpa (ordinate) vs ZrN target depth in Angstroms (abscissa) for (i) 70 keV Xe to fluence $2.5\yen10^{13}$ Xe/cm^2; (ii) 200 keV Xe to fluence $5.0\yen10^{13}$ Xe/cm^2; and (iii) 450 keV Xe to fluence $2.0\yen10^{14}$ Xe/cm^2 (from shallowest to deepest). The red curve shows the superposition of the three ion-damage profiles.

A statistical nanoindentation experiment was performed in the sense that numerous indentations were carried out on one sample and the indentation results were averaged. We excluded so-called statistical outliers due to anomalies such as subsurface flaws, grain boundaries, etc. Half of each sample was masked during implantation and this section was tested for direct comparison to the implanted section.

Results (see Fig. 26) showed that there was a statistically significant hardening due to irradiation damage. Hardness values increased by ~13% on a sample with a damage shelf corresponding to an average displacement damage level of ~0.9 dpa.

Nano-hardness of ZrN implanted with Xe
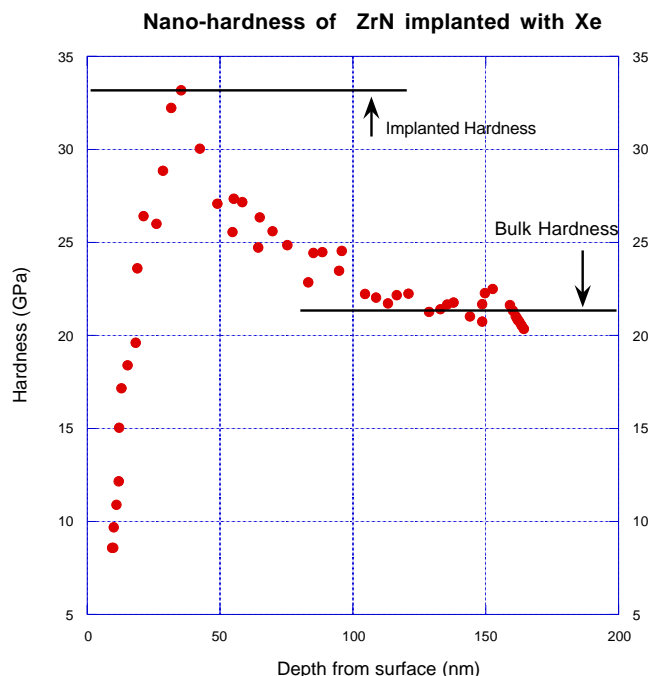
Fig. 26. Nanoindentation measurements showing hardness (H) in GPa as a function of indenter displacement˚(nm). The initial rise in H over the first ~25 nm should be ignored as it is an artifact of the measurement technique. The peak value of 33 GPa at a depth of ~40 nm is significant as it corresponds approximately to the middle of the irradiated layer in the ZrN sample. This value is significantly larger than the hardness of the unirradiated material deeper in the sample (~22-23 GPa, labeled Bulk Hardness in the plot).

However, the elastic (Young s) modulus (E) of the ZrN did not change significantly following irradiation. The value of E was found to be ~370 GPa before and after irradiation, which compares reasonably well with a published value of E=~388 GPa for HIPed ZrN [1]. These results suggest that extrinsic properties such as hardness may be altered by displacement damage in irradiated ZrN, while intrinsic properties such as elastic modulus are relatively unaffected. The increase in hardness can be explained as being due to the accumulation of point defects and their complexes during irradiation. The invariance of the elastic modulus is consistent with the TEM observations showing no change in crystal structure of ZrN with increasing radiation dose.

Fuels Modeling

Continuum Scale Modeling

The thermodynamic modeling of the Pu-PuN pseudo-binary phase diagram was completed (Fig. 27). The assessment was performed using the CALPHAD method and resulted in the Gibbs free-energy values of all phases—important for any calculations of phase equilibrium of multi-component systems that include Pu and N.

The free energy of $PuO_{2-\delta}$ was modeled using a regular solution of PuO_2 and Pu_2O_3 (Figs. 28 and 29). The model was employed for the calculation of the pressure of oxygen as a function of temperature and composition (sub-stoichiometry). The assessment of the phase diagram was possible only in the vicinity of the Pu_2O_3 compound and for temperatures below 2500 K. Coupling of future experimental and thermodynamic modeling results is required to completely determine the phase diagram.

An *ab initio* study of the energetics of different crystal structures of Am was performed based on self-consistent density functional calculations, and these results were then used to parameterize a semi-empirical MEAM (molecular embedded atom method) potential model. The results for bond lengths and bulk modulus compares favorably with experiments (Fig. 30). However, due to the uncertainty with the modeling of the electronic correlation in the narrow 5f band, several alternative approaches should be performed. The MEAM model reproduces the fitting database reasonably well. However, the model will continue to be refined as predictions of defect, thermal, and mechanical properties of Am are attempted. *Ab initio* modeling of the ground state hcp structure of Am is in progress and the computed properties will be used to refine our model. Furthermore, the variation of the results of the large-scale dynamics simulations using the MEAM model will hopefully further guide us to a deeper understanding of the fundamental properties of Am. This will lay a strong foundation for the work on Am-N alloys planned for FY03.
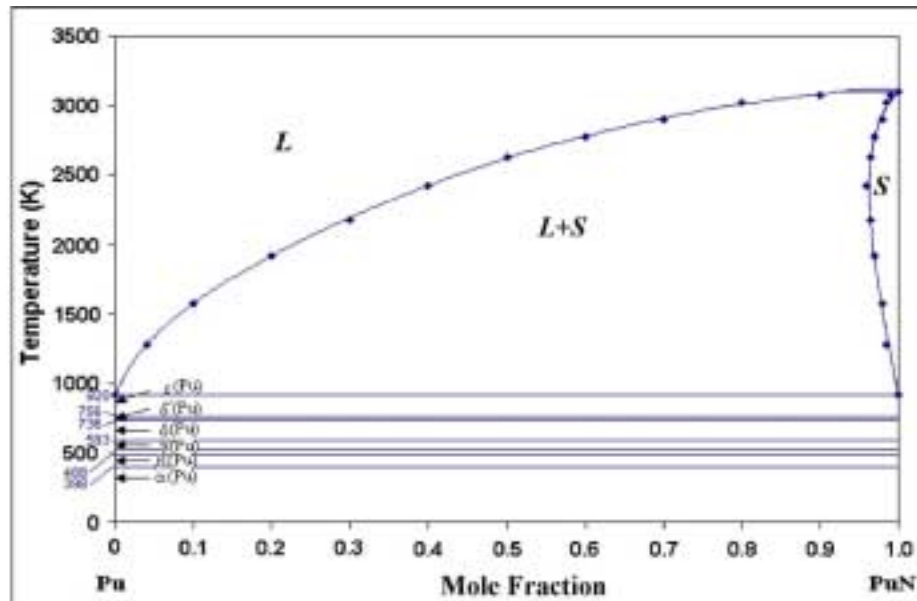
Fig. 27. Comparison of calculated phase diagram and data points from Masalski phase diagram [3].
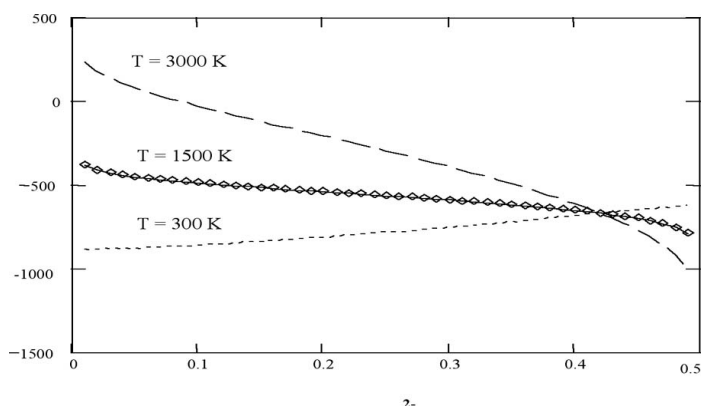
Fig. 28. Calculated partial pressure of oxygen in $PuO_{2-\delta}$. For comparison, the diamonds represent the values reported in [4-6] for T=1500 K.
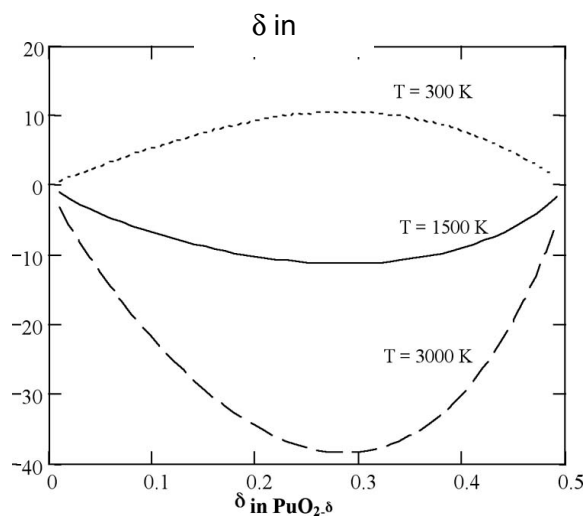

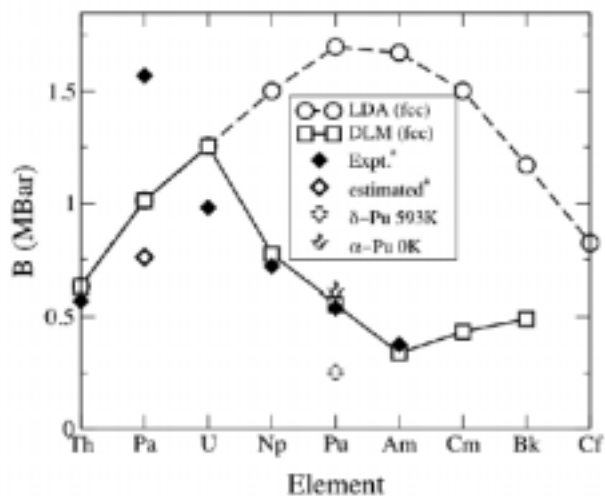Fig. 29. Mixing Gibbs free energy of PuO_{2-d}

Fig. 30. Comparison between the experimental and calculated bulk modulus for the actinide metals. The experimental data are given in Refs. [7] and [8].

Atomistic Simulation

Fission Product Solution Processes

In the previous quarter (3Q FY02), sets of consistent interatomic potentials that describe an extensive range of mononitride lattices were derived. This work has now been extended in that potential parameters that describe the interaction of the fission product Xe with selected mononitride lattices have also been derived. In particular, Xe solution within CmN, TiN and ZrN has been modeled.

If it is assumed that the Xe atoms occupy pre-existing cation vacancy sites, the solution (or incorporation [9]) energies are as given in Table 8:

Table 8. Solution Energies for Xe in Mononitride Materials

	Lattice Parameter ( )	Solution Energy eV	
		Pre-existing Site	In Equilibrium
CmN	5.027	2.35	11.17
ZrN	4.585	4.00	12.56
TiN	4.238	5.49	13.29

As one would expect, in the larger CmN actinide lattice the solution energy is less than in the smaller titanate lattice. Nevertheless, the inert gas atom is large, even in comparison to Cm, and so the solution energies are high in all three materials. As such there is a strong thermodynamic driving force for removal of Xe from these materials.

However, this does not necessarily mean that the Xe gas atoms will all be expelled from the lattice. The activation energy for Xe migration through the rock salt lattice is likely to be high, and as such, Xe could become trapped due to the kinetic or transport barrier. On the other hand, irradiation effects may overcome kinetic barriers and drive the system to thermodynamic equilibrium. Radiation-induced resolution of fission products have long been debated in UO_2 fuels [10].

As the amount of Xe builds up in the system as a whole, the concentration will become such that the equilibrium between the Xe in the trap sites is important. That is, for the Xe atoms to be accommodated in the lattice, cation vacancy sites must be formed. The equilibrium formation energy of a cation vacancy can be derived from;

$$Cm_{cm}^{x} + N_{N}^{x} \; \rightarrow \; V_{Cm}^{///} + V_{N}^{\bullet\bullet\bullet} + CmN \quad \Rightarrow \quad \left[V_{Cm}^{///}\right]\left[V_{N}^{\bullet\bullet\bullet}\right] = \exp(E/kT)$$

Since it has previously been shown that Schottky disorder is dominant, the concentration of cation vacancies will be approximately the same as the concentration of anion vacancies. Thus,

$$\left[V_{Cm}^{///}\right] = \exp(E/2kT)$$

At stoichiometry, the cation vacancy formation energy is therefore half the Schottky energy. The solution energies are thus increased and the equilibrium values are reported in the fourth column of Table 8 above.

Again it is clear that the actinide lattice exhibits a significantly smaller equilibrium solution energy than ZrN or TiN — albeit a large absolute solution energy. Of course, the energies are expected to be overestimates (given the full charge model), but certainly correct relative to

---

each other. It has also been assumed that Xe is accommodated at a cation site (by analogy to the situation in UO_2). Nevertheless, the implication is that the equilibrium solution of Xe in the surrogate/matrix materials ZrN and TiN will be lower than that exhibited in the actinide lattice. <u>Consequently, the value determined from experiments on these materials is expected to provide a clear lower bound to the extent of solution in actinides.</u> That is, the actinide lattice will be able to accommodate more Xe that the matricies/diluants. Unfortunately it seems that the concentration of Xe, as isolated atomic species, is small.

It is a matter of urgency that we consider the accommodation of Xe at other lattice defects such as nitrogen vacancies and larger defect clusters.

Anti-Site Defect Energies

Anti-site defect energies were initially calculated in TiN. Although this study will be extended to other nitrides, it is anticipated that similar conclusions will be forthcoming. At this point, results show that the total formation of single anti-site pairs is a very high-energy process—72.36eV per isolated pair. Despite this, there is a significant reduction in energy for an associated anti-site pair compared to an isolated anti-site pair—23.83eV per clustered pair, i.e. a binding energy that is 67% of the formation energy.

This may have significant implications for recrystallisation after radiation damage in that it alerts us to the possibility of shear plane or other planar defect formation. Clearly, it is necessary to check the energies of such processes by considering larger anti-site cluster formation and possibly planar defect energies. The interface between such larger scale defects and the remaining lattice would provide sites for the accommodation of fission products. It is certainly possible that they would be favorably compared to the high-energy isolated defects modeled above.

Nonstoichiometry of Nitrides

Quantum Mechanical (QM) calculations have been used to predict the variation in lattice parameter with TiN nonstochiometry. These calculations were carried out using the CASTEP code on a limited basis on a borrowed resource. The agreement with experimental data is excellent (see Fig. 31), and as such, we believe that this approach will yield useful results.

The density functional code uses periodic boundary conditions, plane-wave basis functions with pseudo potential cores.

From this initial study it is clear that TiN exhibits a remarkably broad range of nonstoichiometry. This has implications for the solution of Xe since a nonstoichiometric material will provide alternative solution sites.
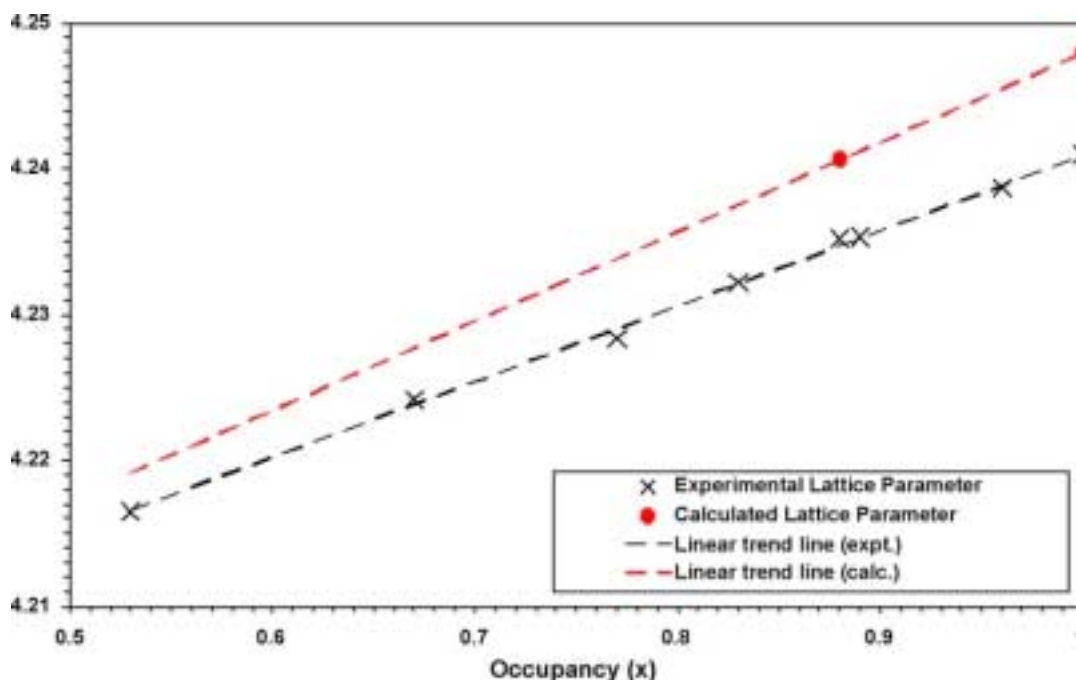
Fig. 31. Relation between lattice parameter and stoichimetry for TiN.

Improvements to the Parameterized Lattice Model

The success of the solution energy calculations was partly facilitated through the derivation of a shell model to simulate ionic polarizability, thus allowing prediction of dielectric properties. This model consists of a mass-less shell of charge Y (electronic charges) connected to a core of charge X though an isotropic harmonic spring of force constant k. Thus, the charge of an ion is (Y+X). As an isolated ion, the polarizability is given by: Y^2/k. Within the lattice, the polarizability of an ion is modified through the short-range parameterized forces that act between the ion s shell and other surrounding ions. As such, the shell model develops a many-body component to the overall lattice model. Here the shell model is specific to the semi-empirical potential set.

Despite this improvement, re-evaluation of the electron gas calculation for the common nitrogen-nitrogen potential suggests that the use of a different mathematical form for the interaction potential may be required. Part of the motivation for this stems from the present quantum mechanical calculations on TiN and previous calculations on AlN [11], which are both consistent with an overall 1-charge state for nitrogen. As such, electron gas calculations will be re-run, assuming a 1-charge state. This will produce another pair potential set, which will be used alongside the existing pair potential sets for comparison. With models based on interatomic potentials, overall conclusions do not alter greatly between the models. Once the quantum mechanical code is working on the local system it will also be a matter of priority to derive a nitrogen-nitrogen pair potential consistently from QM simulations of a nitride lattice. The process used will be equivalent to that described in Reference 12.

2. SEPARATIONS TECHNOLOGY

Scope

The separations technology activity consists of three tasks addressing the various stages in the process of partitioning irradiated fuels for subsequent fissioning of transuranic elements and transmutation of long-lived fission products. The tasks are as follows:

Light-Water Reactor Spent Fuel Treatment

This task involves the development and demonstration of efficient and economic means for the separation of uranium, transuranic elements, specific long-lived fission products, and other fission products from LWR spent fuel. An aqueous partitioning process (UREX) is envisioned for the initial treatment of LWR fuel,°involving the extraction of U for disposal as a low-level waste. A°pyrochemical process (PYRO-A) will follow to separate the transuranic elements from fission products. Pyrochemical processes for the direct treatment of LWR spent fuels are also being developed for possible future use.

Transmutation Fuel Treatment

Fertile or nonfertile fuel that has been irradiated in the transmuter to fission transuranic elements must be processed to recover and recycle the unburned transuranics and to extract newly generated, long-lived fission products for transmutation. This task accomplishes the development and demonstration of the means for processing that blanket fuel. A°pyrochemical process (PYRO-B) is planned for the separation of unburned transuranics and long-lived fission products. Such processes are favored because the reagents are stable under high-radiation fields, and because the processes are normally operated at elevated temperatures with the use of molten salts and can thus accommodate high levels of decay heating. In certain cases, aqueous separations processes may prove appropriate, and methods are being developed that will enable the optimum combination of aqueous and non-aqueous processes.

Waste Form Production

One of the overarching criteria for AFC/AAA separations technology development is the minimization of high-level waste generation. Design of the hybrid LWR fuel-treatment process has been oriented toward the elimination of liquid high-level waste streams, and the pyrochemical processes are similarly being designed to minimize high-level waste volumes. This task involves the development and qualification of durable high-level waste forms to accommodate the two principal waste streams (salt and metal) that emanate from the separations process as well as the waste form for the disposal of the pure U extracted from the spent LWR fuel.

Highlights

- The electrochemical reduction of a UO_2-PuO_2 oxide fuel containing 5% plutonium was successfully demonstrated. Experimental results showed that the electrolytic reduction process is very effective at reducing PuO_2 and AmO_2 in the presence of uranium oxide. Analysis of cathode product samples showed average conversion efficiency for the PuO_2 and AmO_2 was 98%, with that for UO_2 being greater than 99%.

- Analysis of a pyrochemical reduction experiment conducted with an oxide feed containing four phases showed only small yields reduced to metal, indicating that even with chlorine evolution, the reduction of rare-earth oxides is very difficult in a LiCl electrolyte.

- The UREX flowsheet was re-optimized for the hot demonstration run in the SRTC hot cell to provide the best results with the existing SRTC 36-stage centrifugal contactor and to meet all process goals.

- Experiments to clarify the behavior of plutonium in the UREX process were performed, revealing an unexpected result that the extraction of plutonium is second order with respect to the TBP (tributyl phosphate). Work is in progress to resolve this issue.

Oxide Fuel Processing Electrolytic Oxide Reduction (PYROX) Process

Analyses of two reduction experiments were completed during this report period. The first experiment, LRNd-11, was performed with an oxide feed containing four phases: Nd_2O_3, CeO_2, La_2O_3, and $Ce_{0.5}Nd_{0.5}O_{1.75}$. The second experiment, LRNd-14, was performed with Nd_2O_3. The results of LRNd-11 show that 2.2 mol.% of the charged Nd_2O_3, 3.4 mol.% of the charged La_2O_3, and 3.3 mol.% of the charged CeO_2 were reduced to metal. The small yields indicate that even with chlorine evolution, the reduction of rare-earth oxides is very difficult in a LiCl electrolyte. It is also possible that the mixed rare-earth oxide phase in the feed material is more difficult to reduce.

Experiment LRNd-14 was a repeat of an earlier experiment, LRNd-10, with the objective of improving the process yield, as the results of LRNd-10 were promising and indicated significant amounts of Nd metal present in the cathode product. Experiment LRNd-14 was performed at 750…C and designed to increase the amount of chlorine evolution in the cell. The analytical results of the product from LRNd-14 show that excessive chlorine evolution in the cell in combination with carbon from the graphite electrode resulted in the corrosion of the MgO cell container. This, in turn, resulted in the formation of magnesium metal at the cathode. There is evidence of a neodymium species in the magnesium deposits. It is likely that Nd metal was formed at the cathode and alloyed with Mg. The alloying effect is supported by the Mg-Nd binary phase diagram[3], which shows a significant solubility for Nd in Mg at 750…C. However, results suggest that, later in the process, further Nd_2O_3 reduction at the cathode was inhibited by the increased oxide-ion concentration in the electrolyte as a result of MgO corrosion. In summary, the expected higher yields of Nd metal were not realized in the experiment because of interference from Mg metal formation. The results also show that MgO is not a suitable cell container for these experiments with chlorine evolution and especially when a graphite anode is used in the cell.

The electrochemical reduction of a UO_2-PuO_2 oxide fuel containing 5% Pu in a LiCl-1wt% Li_2O electrolyte at 650…C has been demonstrated. Results show that the electrolytic reduction process is very effective at reducing PuO_2 and AmO_2. Chemical analyses on six randomly-selected cathode-product samples showed that the average conversion of the minor oxide components, PuO_2 and AmO_2, in the fuel was 98%, and the average conversion of the major oxide component, UO_2, was >99 %.

The nominal Pu content and the oxygen-to-metal ratio of the oxide fuel were 4.99 wt% and 2, respectively. We used 18.5 g of the oxide fuel (particle size range 0.045—1.2 mm) in the experiment. The cell cathode was a SS screen fuel basket, 1.5 cm dia x 2.5 cm high,

---

[3] Binary Alloy Phase Diagrams, 2nd edition, vol. 3, Ed. T. B. Massalski, ASM International (1990), pp. 2527-29

containing the feed oxide. A 1-mm-dia Pt wire anode, a Ni/NiO reference electrode, and a LiCl-1wt% Li_2O electrolyte were the other major components of the electrochemical cell. The experiment was performed in an argon glovebox with <1 ppm oxygen and nitrogen levels.

The cell was operated under current-control conditions with a secondary limit on cell voltage and periodic current interrupts. A total charge of 12.4 A•h was passed over 13.5 hours of cell operation that spanned two working days. The theoretically required charge for reduction of 18.5 g of UO_2 is 7.3 A•h. So the total charge passed exceeded the theoretically required charge by about 70%. Five salt samples were extracted from the melt (at the start and end of cell run each working day and a final salt sample before the cathode product was pulled out of the cell) for chemical analysis. These salt samples were submitted for chemical analysis to determine the electrolyte Li_2O concentration.

The cell current ranged from 1.5 A at the start of the run to 0.5 A at the end. The cell voltage range was 3.4—3.7 V; the open-circuit cell voltage ranged 2.5—2.8 V. Because the cathode potential is very close to Li potential during most of the run, the instantaneous open-circuit cell voltage represents the anode potential. Thus, throughout this experiment, the anode potential was kept between 2.5—2.8 V a range conducive for oxygen evolution. Minimal (or practically no) chlorine evolution is expected to occur over this potential range. The cathode potential was maintained at or just above the Li deposition potential during most of the run. The cell run was terminated based on the cathode rest potential reading, which indicated that reduction was virtually complete at the end of the run.

At the end of the run, the Pt anode showed no signs of corrosion or degradation. The cathode product consisted of a metal-like phase and a gray phase. Visually, there was no evidence of the starting oxide fuel in the cathode product. Only reduced metal and entrained salt were observed in the cathode product. Six random samples, ~1 g each, were extracted from the cathode product for chemical analysis. As described in Table 9, the samples consisted of a random mixture of large, small, and fine particles from the cathode product. The samples were initially washed with methanol to separate the salt and metal/metal-oxide phases, and then analyzed by the bromine/ethyl acetate method, except for sample Prod-1A which was analyzed by the bromine/methanol method. Both methods have been described in detail in earlier reports, and were developed during this fiscal year for quantitative determination of metal/metal-oxide ratios for a variety of metals including U, TRU, and rare-earths. The elements of interest in this experiment were U, Pu, and Am. More details on the analytical procedure followed in this experiment are described in the following section.

Table 10 shows the results of the chemical analyses. The starting oxide fuel analysis shows that all of the U, Pu, and Am were recovered from the oxide phase, which is insoluble in the bromine/ethyl acetate (or methanol) solvent. These results confirm that oxide dissolution in the solvent is minimal. For the six product samples, the results suggest that the metallic phase is the dominant phase with minimal recoveries of U, Pu, and Am as oxides. The last column in Table 10 shows that a significant amount of the entrained salt remains with the metal phase and that the initial methanol wash is only partly effective at separating the salt phase from the metal/metal-oxide phases. It is likely that some of the entrained electrolyte is inaccessible during the methanol wash because it is trapped inside metal particles.

Table 11 summarizes the conversion data for U, Pu, and Am as well as the amount of entrained electrolyte in the cathode product. For the measurement technique used in this study, the uncertainty is –0.5% for the conversion numbers reported in Table 11. All the samples showed very high conversions of U, Pu, and Am oxide to metals with very small variations between samples. The average conversion for U, 99.4%, was marginally higher than that for Pu and Am, 98%. In addition, Am conversion tracked the Pu conversion very

closely. This is shown graphically in Fig. 32 where the lines for Pu and Am recovery virtually overlap one another. Also shown in Fig. 32 is the Pu content of each sample calculated from the data in Table 10. The Pu content of the starting oxide fuel (the first sample on the graph) is 5.0 and this measurement exactly matches the fuel specification that was given to us. However, the Pu content in the product (the last six points on the graph) ranges between 3.6 and 4.2 and is significantly smaller than that in the fuel. At this stage, we are not sure if this is indicative of some Pu segregation during the reduction process or if it is a measurement anomaly. The U-Pu phase diagram suggests significant Pu solubility in U at 650…C and hence we would expect a homogenous U-Pu solid solution to be formed by reducing a UO_2-PuO_2 fuel with 5% Pu.

As shown in Table 11, an average 17 wt% of the cathode product was entrained electrolyte. This is also consistent with our earlier observations from depleted UO_2 reductions. In all these experiments, the fuel basket is lifted out of the melt at the end of the run and held in the hot zone above the melt for a only a few minutes to drain the molten electrolyte before being completely lifted out of the furnace well. This procedure does not significantly reduce the entrained electrolyte content of the cathode product especially because of the porous nature of the reduced product.

Salt samples extracted from the cell during the reduction run were analyzed by acid-base titration methods for their Li_2O concentration. The results are reported in Table 12. The first sample, taken before the start of the run, contained 0.99 wt% Li_2O, which was the amount of Li_2O added to the LiCl melt. The second and fourth samples, 1B and 1D, were extracted from the cell immediately at the end of the run on days 1 and 2, and they show a small decrease in Li_2O concentration. This is because some lithium deposition occurred at the cathode in addition to oxide reduction during the cell run. The electrolyte Li_2O concentration, however, is restored to the original value (see results for samples 1C and 1E in Table 12) by reacting the excess lithium at the cathode with a new batch of oxide fuel (depleted UO_2 was used in this experiment) during the overnight periods when the cell is not under load.

In summary, the results of the UO_2-PuO_2 reduction experiment are very encouraging. The electrolytic reduction process using a LiCl-1wt% Li_2O electrolyte can easily convert PuO_2 and AmO_2 to metals. The reduction characteristics of the UO_2-PuO_2 fuel with 5% Pu appear to be very similar to those of depleted UO_2. The bromine/ethyl acetate method works very well for U, Pu, and Am, and can provide the feedback necessary for understanding the cell performance and improving the cell design.

Table 9. Description of Samples Analyzed by the Bromine/Ethyl Acetate (or Methanol) Method

Sample ID	Sample Description	Analytical Method Used
Fuel 1A	Very fine black powder	Methanol wash followed by dissolution in bromine/ethyl acetate
Prod 1A	One large piece + some smaller pieces	Methanol wash followed by dissolution in bromine/methanol
Prod 1B	Two larger pieces + some fines	Methanol wash followed by dissolution in bromine/ethyl acetate
Prod 1C	Two larger chunks + 3-4 smaller pieces	Methanol wash followed by dissolution in bromine/ethyl acetate
Prod 1D	10-11 smaller pieces + some fines	Methanol wash followed by dissolution in bromine/ethyl acetate
Prod 1E	1 large chunk + 3-4 smaller pieces	Methanol wash followed by dissolution in bromine/ethyl acetate
Prod Fines	6-7 small pieces + fines	Methanol wash followed by dissolution in bromine/ethyl acetate

Table 10. Results of Chemical Analysis of Oxide Fuel and Cathode Product

Sample ID	Uranium (mg)	Plutonium (mg)	Americium (mg)	Lithium (mg)
Fuel 1A —				
Metal Phase	0.6	0.01	0	
Oxide Phase	835.0	50.6	2.9	
Methanol Wash	0.3	0.04	0	
Prod 1A —				
Metal Phase	714.7	34.0	1.8	18.4
Oxide Phase	1.6	1.4	0.07	0
Methanol Wash	0.2	0	0	6.6
Prod 1B —				
Metal Phase	698.3	29.1	1.5	19.5
Oxide Phase	1.2	0.2	0.01	0
Methanol Wash	0.4	0.01	0	6.2
Prod 1C —				
Metal Phase	798.2	36.9	1.9	12.7
Oxide Phase	2.5	1.1	0.06	0
Methanol Wash	1.3	0.3	0.02	16.2
Prod 1D —				
Metal Phase	789.8	37.5	1.9	16.7
Oxide Phase	10.3	1.1	0.06	0.1
Methanol Wash	1.0	0.03	0	13.2
Prod 1E —				
Metal Phase	736.6	32.7	1.7	15.9
Oxide Phase	2.2	0.6	0.03	0
Methanol Wash	0.4	0.05	0	6.2
Prod Fines —				
Metal Phase	361.1	17.1	0.9	4.0
Oxide Phase	5.2	0.04	0	0
Methanol Wash	0.4	0.02	0	7.7

Table 11. Extent of Conversion and Electrolyte Entrainment During the Electrolytic Reduction of UO_2-PuO_2 Fuel

Sample ID	Uranium Conversion, %	Plutonium Conversion, %	Americium Conversion, %	Entrained Electrolyte, wt%
Prod 1A*	99.8	96.2	96.1	16.8
Prod 1B	99.8	99.2	99.1	17.6
Prod 1C	99.7	97.0	96.8	17.2
Prod 1D	98.7	97.2	97.1	17.8
Prod 1E	99.7	98.2	98.1	14.8
Prod Fines	98.6	99.8	99.8	15.5
	Mean = 99.4	Mean = 97.9	Mean = 97.8	Mean = 16.6

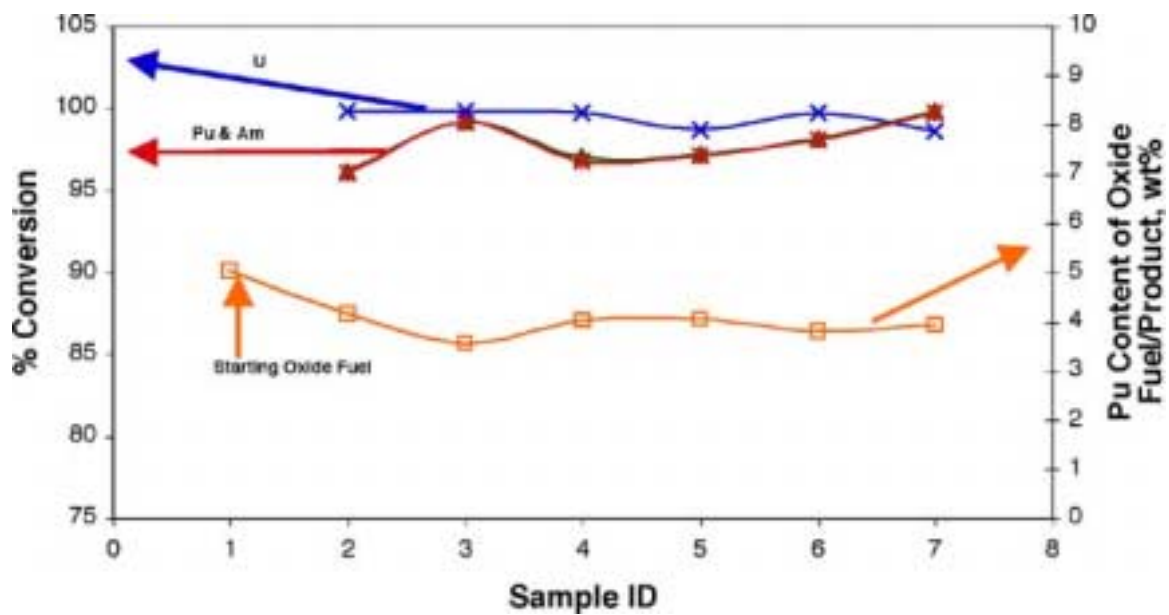* sample analyzed by the bromine/methanol method.

Fig. 32. Analytical results -- % conversion and Pu content of fuel/product.

Table 12. Li₂O Concentration in Electrolyte During the Electrolytic Reduction of UO₂-PuO₂ Fuel

Salt Sample ID	Timing of Sample Extraction	Li₂O, wt%
1A	Start of Run on Day 1	0.99
1B	End of Run on Day 1	0.87
1C	Start of Run on Day 2	0.99
1D	End of Run on Day 2	0.70
1E	Final Electrolyte Composition	0.97

Electro-Refining Process - U/TRU Electrolysis Technology Development

The PYRO-A and PYRO-B fuel specimens prepared by ANL-W, along with the plutonium metal bar stock needed to create the electrolyte for the electrorefining tests, became available during the quarter. The fuel specimens and the bar stock have been inspected and are ready for use.

Production of the $PuCl_3$ electrolyte has been achieved by converting ~82 g of the bar stock by reaction with $CdCl_2$ in LiCl to produce a Pu-rich stock salt that will then be diluted down to the desired 2 mol% by addition of LiCl for the experimentation. The ΔG for reaction of $CdCl_2$ with Pu is about —90 kcal/mol at 650°C, and Cd has a very high vapor pressure at this temperature. Therefore, production of a pure $PuCl_3$/LiCl mixture is possible after reaction and vaporization of the Cd. Of concern, however, is the material used for the crucible, particularly if the Pu is in the liquid state. Initially, based on phase diagrams on hand, the decision to use Ta as the crucible material was made. Ideally, the LiCl matrix salt would be melted first, the $CdCl_2$ added and melted, and subsequently, the Pu bar stock would be added and expected to react vigorously with the $CdCl_2$. The mixture would then be cooked

for a number of hours to distill off the resulting Cd metal, and the product salt would be recovered.

In planning the work, the question arose as to whether Ta metal was stable with respect to $CdCl_2$. Calculations suggested that the ΔG of reaction to produce tantalum dichloride is about —5.5 kcal/mol at 650C, but this result was not definitive based on the references on hand. To test the question of tantalum reactivity, LiCl was melted at 650°C in the tantalum crucible, and salt samples taken at different time intervals. Analysis of the salt samples showed tantalum present at about 0.020 wt%.

In the interests of minimizing Ta content in the electrolyte salt, we decided to perform the chlorinations by first melting the LiCl, adding the Pu bar stock and then, after the temperature stabilized, adding small amounts of $CdCl_2$, knowing that the differences in ΔG values would strongly favor obtaining $PuCl_3$ over $TaCl_2$. Unexpected results were obtained from this approach that have ramifications for the series of planned experiments.

A 23-g piece of Pu bar stock was treated using the above-mentioned chlorination procedure. After adding the $CdCl_2$ and holding at temperature overnight, the crucible was removed from the furnace and allowed to cool. The salt ingot was mechanically removed and observed to have small patches of bright metallic silver coloration. Examination of the crucible showed a bright silvery color, with areas of exfoliating corrosion and some crystal habits. Further examination of the literature revealed Pu-Ta phase diagrams that illustrated a small zone of Ta,Pu solid solution at or near the 100% Ta point. We suspect that prior to $CdCl_2$ addition, the molten Pu in contact with the crucible bottom formed this solid solution. Subsequent reaction of the Pu with the $CdCl_2$ extracted the Pu from this solution and redeposited the Ta back on the crucible bottom. Analysis of the salt showed that complete conversion of Pu to its chloride did occur.

For the next batches, reagent additions were changed back to first proposed order, i.e., LiCl followed by $CdCl_2$, followed by Pu metal addition. Further, the temperature was lowered slightly to 630°C to keep the Pu in the solid state. Three batches of Pu metal (18-23 g/batch) were successfully chlorinated by this method. Analyses of these batches showed complete Pu chlorination and very minimal Ta and Cd contamination (<0.02 and 0.04 wt%, respectively, worst case).

To avoid issues with the Ta,Pu solid solution during electrorefiner operations, the decision was made to replace the Ta foils with a half-shell catch-cup made of Mo. Machining of these pieces has been successfully accomplished. The pieces will be heat-treated to anneal them prior to the experimental runs. In the interim, we are proceeding with the PYRO-B experiments by using two 10-mil-thick Ta liners, knowing that the Pu will be assayed by weight difference and dissolution of the liners. Using the Mo liners will prevent solid solution formation and allow easier recovery of the Pu, particularly in the PYRO-A experimentation, which is expected to generate significant amounts of the metal.

UREX Process Development - LWR Spent Fuel Treatment

Using AMUSE 1.10, we updated the previously optimized flowsheet derived last February for the UREX hot demonstration in the Savannah River Technology Center (SRTC) hot cells. The updated flowsheet that was developed is shown in Fig. 33. The U-strip section of the February flowsheet was not changed. The basis for the design of each section is the same as reported in February and is given below for completeness.

UREX Process Goals
- Achieve >99.9% U extraction for recovery
- Achieve >95% Tc extraction for recovery
- Achieve <0.01% Pu extraction
- Achieve <10% Np extraction
- Achieve uranium loading in the solvent ‡70% to obtain a decontamination factor of 10^4 from fission products[4]
- Set conditions so that a 5% change in flow rate or species concentration or a 5¡C temperature change would not cause an impact on meeting process goals

Given that an existing 36-stage 2-cm centrifugal contactor in the SRTC hot cell is being utilized for the demonstration, we are limited in the options for flowsheet design. The contactor is divided into two tiers, with 20 stages on top and 16 stages on bottom. Because of this break, the extraction/scrub section can only be performed on the top tier, and, more importantly, only 16 stages are available for the Tc-strip section. Uranium stripping must be performed outside the hot cell. Given that the contactor is also being used for demonstration of the Caustic-Side Solvent Extraction (CSSX) process, it is good practice to not use the first stages of the top tier, thus keeping cross-contamination effects to a minimum.

Extraction/Scrub Section

In the extraction section, U and Tc are extracted from the feed, and Np, Pu, and the fission products remain in the aqueous solution and exit the process in the raffinate. The effectiveness of the extraction of U and Tc is primarily influenced by (1) the number of extraction stages, (2) the feed-to-solvent {O/A} flow rate ratio, and (3) the process temperature, which primarily affects pertechnetate, as its extraction has a strong inverse dependency on the process temperature. The uranium loading of the solvent is primarily influenced by the feed-to-solvent O/A ratio, and the flow rate and nitrate concentration of the scrub feed.[5] Increasing the nitrate concentration makes U more extractible and Tc less. The inextractability of Pu(IV) and Np(IV) is primarily affected by the following:

- concentration of acetohydroxamic acid (AHA)
- increases in the concentration of both hydrogen and nitrate, (higher hydrogen and nitrate concentrations increases Pu(IV) and Np(IV) extractability), and
- solvent loading (higher loading reduces the extraction of Pu and Np).

The extraction of Np(V), which will be the major neptunium species in the feed, is increased by increasing the nitrate concentration, but is unaffected by AHA. Under the flowsheet conditions, Np(V) will be more extractible than Np(IV); therefore, only the behavior of Np(V) was followed.

Optimization studies indicate that 9 extraction and 8 scrub stages, maintained at 25¡C, will meet all process goals at the influent flow rates shown in Fig. 33. Figures 34—35 show the percent U and percent Tc in the raffinate, and the percent Pu in the loaded solvent, at a feed flow rate of 5.6 mL/min and as a function of HNO_3 concentration in the feed for the extraction/scrub stage combinations shown. Additional feed conditions are given in Fig. 33.

---

[4] This is a new requirement suggested by Major Thompson based on SRS PUREX-process experience. Because it requires two moles of tributyl phosphate (TBP) to extract one mole of uranyl nitrate, loading to 70% means that the uranium concentration in 30 vol% (1.1 M) TBP should equal (0.7*1.1)/2 = 0.385 M.

[5] Under the low-acid scrub condition required for the UREX process, uranium is pinched in the scrub section, and its highest organic-phase concentration is in the later stages of the scrub section.
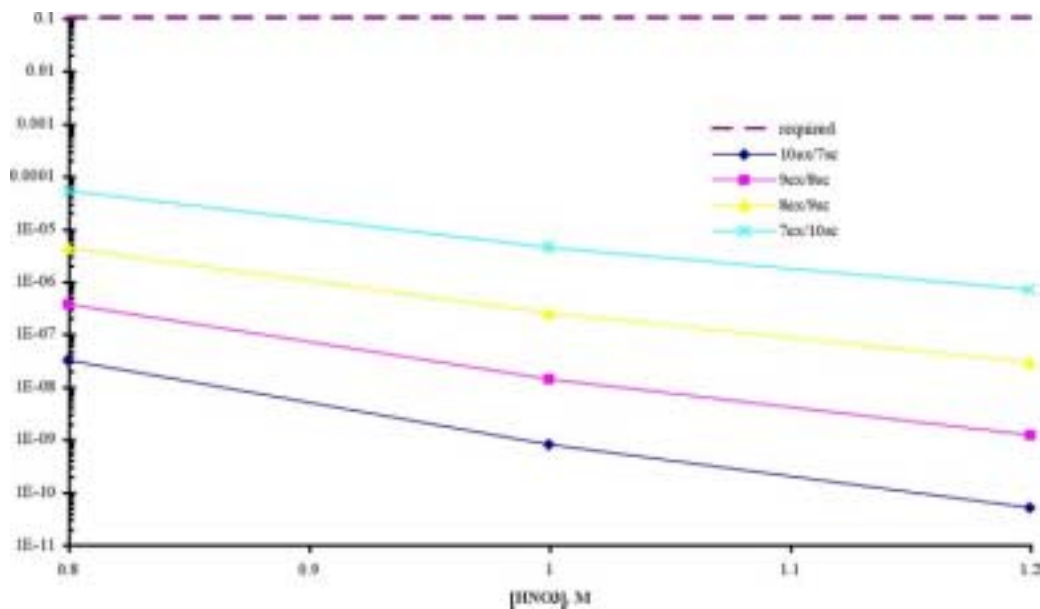

Fig. 34. Percent U in the raffinate as a function of HNO_3 concentration in the feed for shown extraction/scrub stage combinations and a feed flowrate of 5.6 mL/min.

Fig. 35. Percent technetium in the raffinate as a function of HNO_3 concentration in the feed for shown extraction/scrub stage combinations and a feed flowrate of 5.6 mL/min.

Fig. 36. Percent plutonium in the loaded solvent as a function of HNO_3 concentration in the feed for shown extraction/scrub stage combinations and a feed flowrate of 5.6 mL/min.
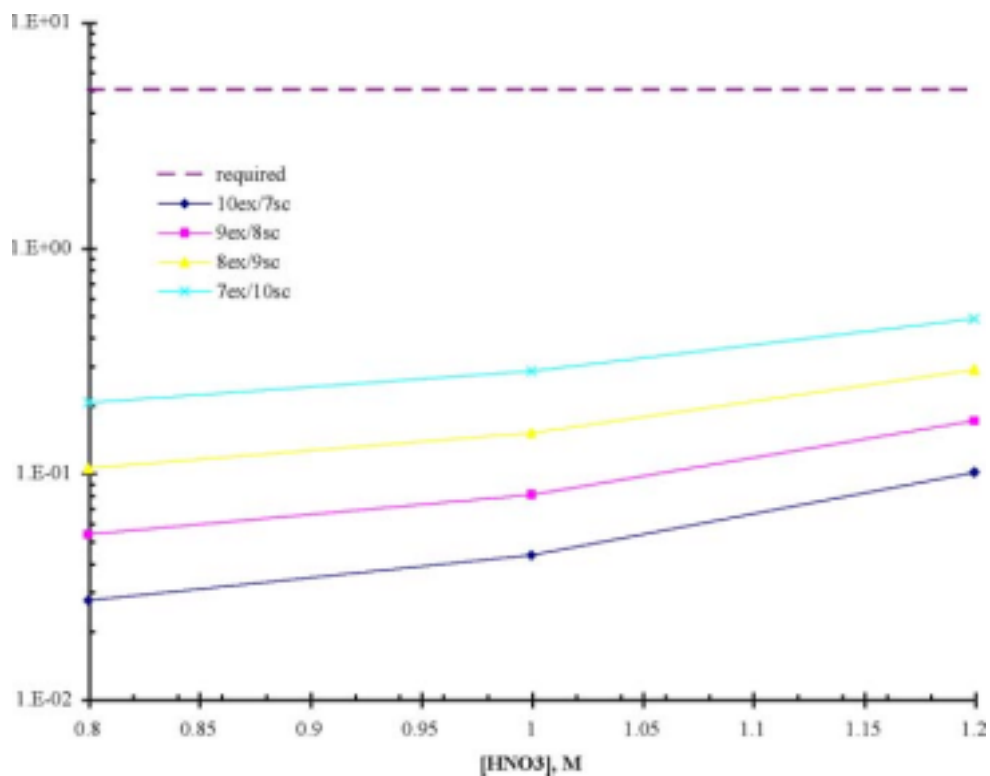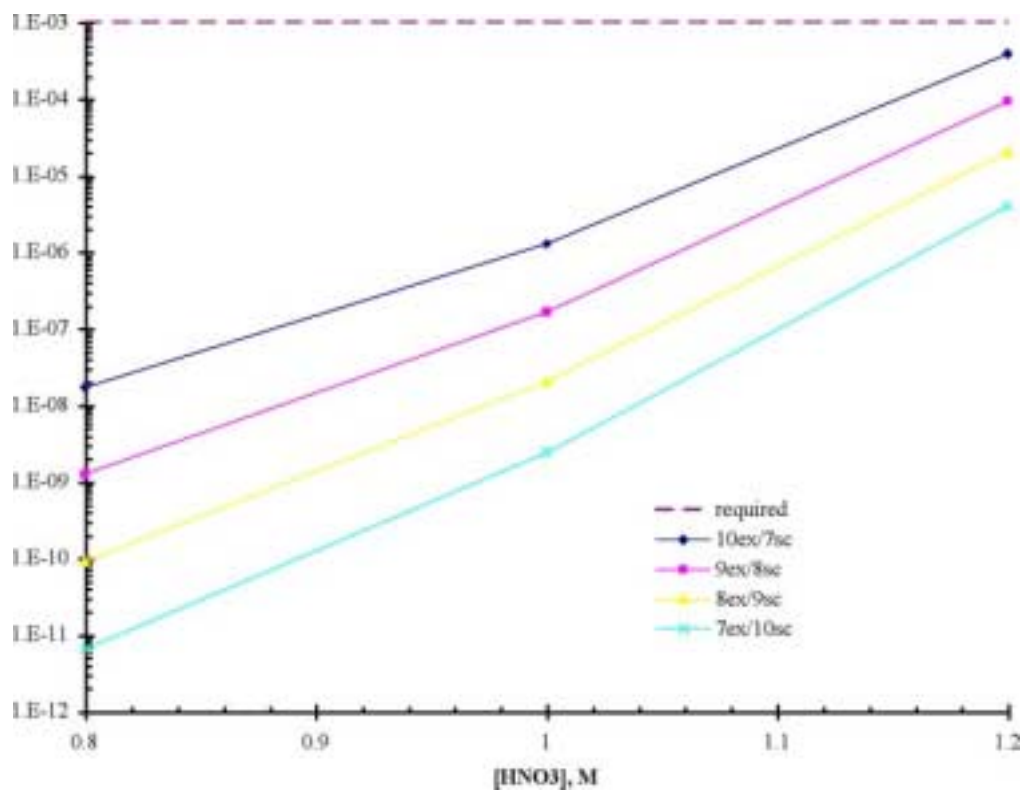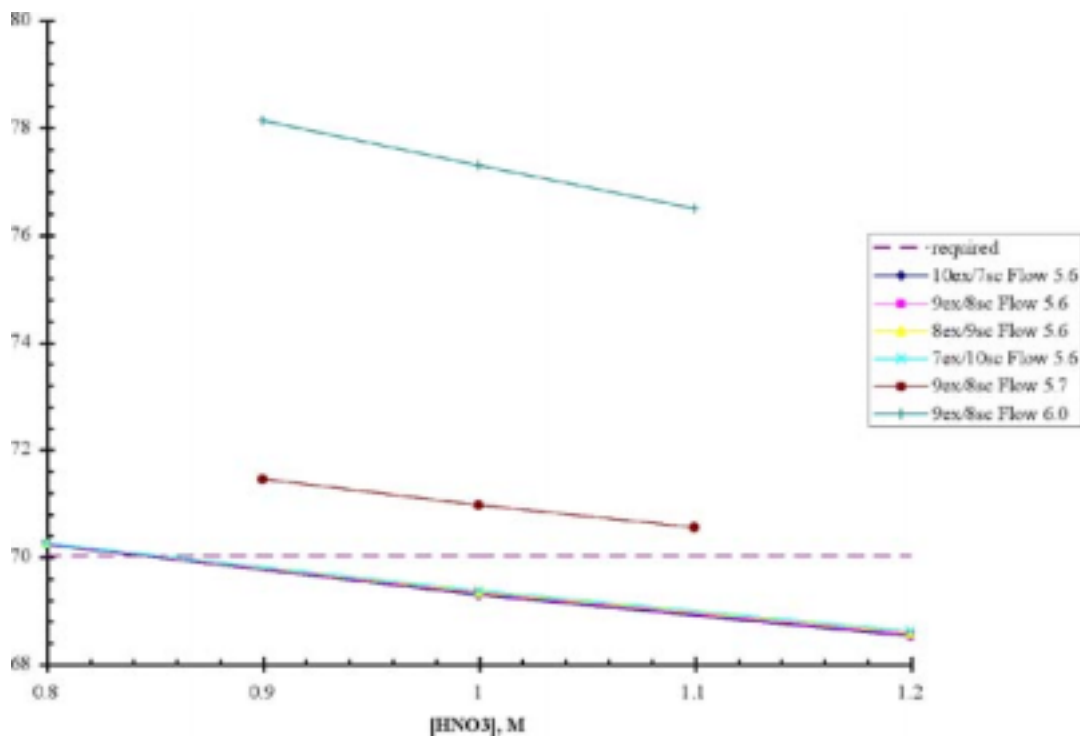

Fig. 37. Percent solvent loading as a function of HNO_3 concentration in the feed for shown extraction/scrub stage combinations and given feed flow rates.

Although all the extraction/scrub combinations shown satisfy the process goals for U, Tc, and Pu, it is clear from Fig. 37 that the solvent loading is greater than 70% only for cases where the HNO_3 concentration is less than 0.85M. Achieving this goal at a feed flow rate of 5.6 mL/min will require large dilutions of the feed. Changing the feed flow rate to 5.7 mL/min would result in a solvent loading greater than 70% at HNO_3 feed concentration ranging from 0.9 to 1.1M. Additional scrub stages have a positive effect on the Pu process goals. Since all process goals could be met by a number of configurations, it was decided that the ease in plumbing the existing contactor for the 9 extraction and 8 scrub stages combination was very desirable, and thus this combination was selected for the flowsheet.

Technetium Strip Section

The Tc-strip section consists of two subsections (See Fig. 33). The loaded solvent from the scrub section (stage 17) enters the contactor at stage 26, where it is stripped of technetium in stages 26-32. By contacting the stripped Tc product with clean solvent, the fraction of uranium nitrate that was also stripped from the loaded solvent is then scrubbed in the uranium re-extraction section (stages 18-25). In the previously optimized flowsheet reported in February, a third acid-scrub section was included to scrub residual acid from the uranium-loaded solvent. Given that more than the available stages are required to optimize the flowsheet this section was eliminated. The effectiveness of the Tc-strip section depends on
- the stage distribution between the two sub-sections,
- the flow rates of clean solvent, loaded solvent, and Tc-strip feed, and
- the HNO_3 concentration in the Tc-strip.

Optimization studies show that 8 uranium re-extract and 7 technetium strip stages, maintained at a temperature between 30¡C—45¡C will meet all process goals at the influent flow rates shown in Fig. 33. Figures 38—39 show the concentration of U in the Tc product and the percent Tc in the U product at an operation temperature of 30¡C as a function of clean solvent flowrate for three uranium re-extract/Tc-strip stage combinations. The other feed conditions are those given in Fig. 33.

Although all U-reextract/Tc-strip combinations shown satisfy the process goals for U and Tc, it can be seen in Fig. 40 how operational temperatures quickly affect these goals. Note that at 8 uranium re-extract and 7 Tc-strip stages process goals are not met at clean organic solvent flowrates of less than 5.5 mL/min if the operating temperature exceeds 35¡C. Given that process temperature can range from 30¡C—45¡C, it is necessary that the flowsheet design be robust at these conditions. A clean organic flowrate of 7 mL/min was selected to satisfy this requirement. The effect of temperature is seen the concentration of U in the Tc product and the percent Tc in the U product. Since the current Tc temperature model is not as accurate as the U model for temperatures above 35¡C, the flowsheet optimization was done using the concentration of U in the Tc product as the decision criteria. A more accurate Tc temperature model will be available at the end of the FY.

Varying the Tc-strip feed-flow rate can minimize the effects of temperature on the concentration of uranium in the technetium product goal. As shown in Fig. 41, reducing this flowrate decreases the uranium in the technetium product, but also makes technetium stripping less effective, increasing the amount of technetium that would be present in the uranium loaded product (not shown).
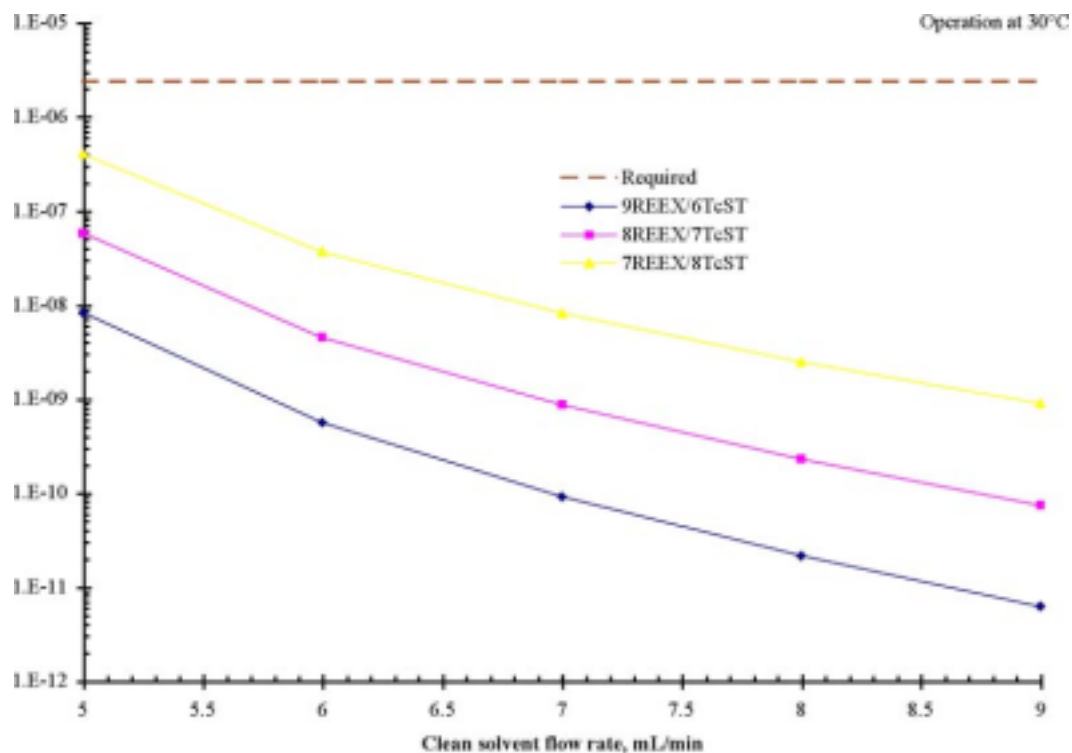
Fig. 38. Concentration of uranium in the technetium product as a function of clean solvent flowrates for shown uranium re-extract/Tc-strip stage combinations at 30¡C.
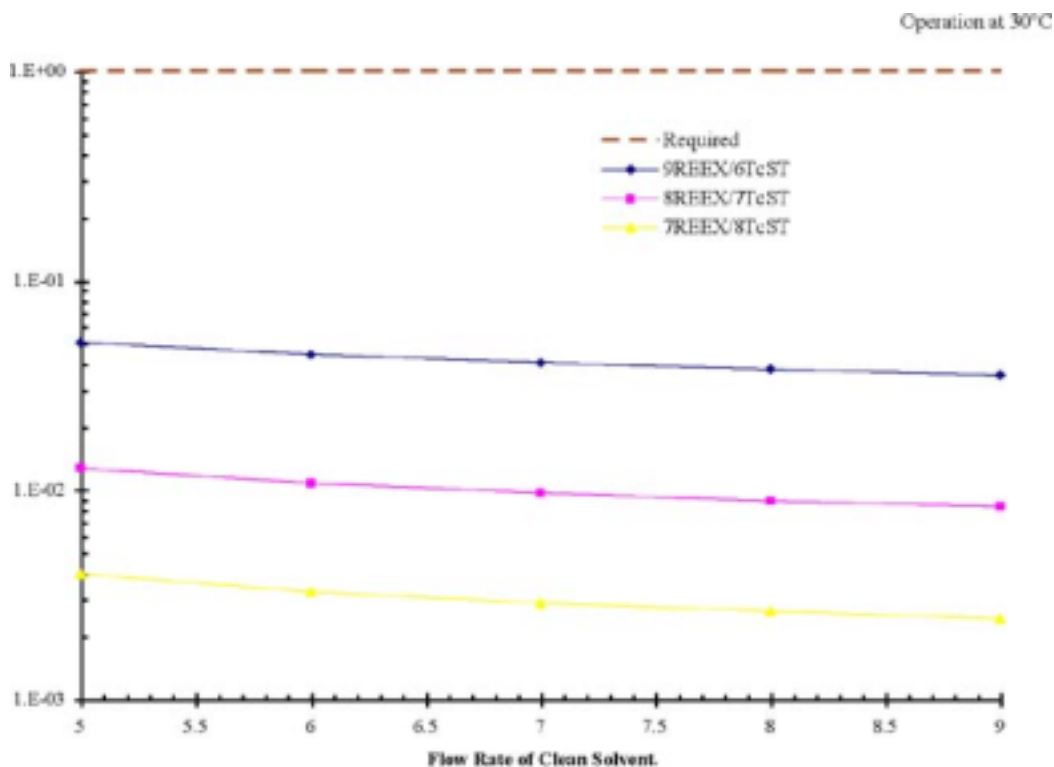
Fig. 39.   Percent technetium in the uranium product as a function of clean solvent flowrates for shown uranium re-extract/Tc-strip stage combinations at 30¡C.

Fig. 40. Concentration of uranium in the technetium product as a function of temperature for shown clean solvent flowrates and 8 uranium re-extract/7 Tc-strip stages.
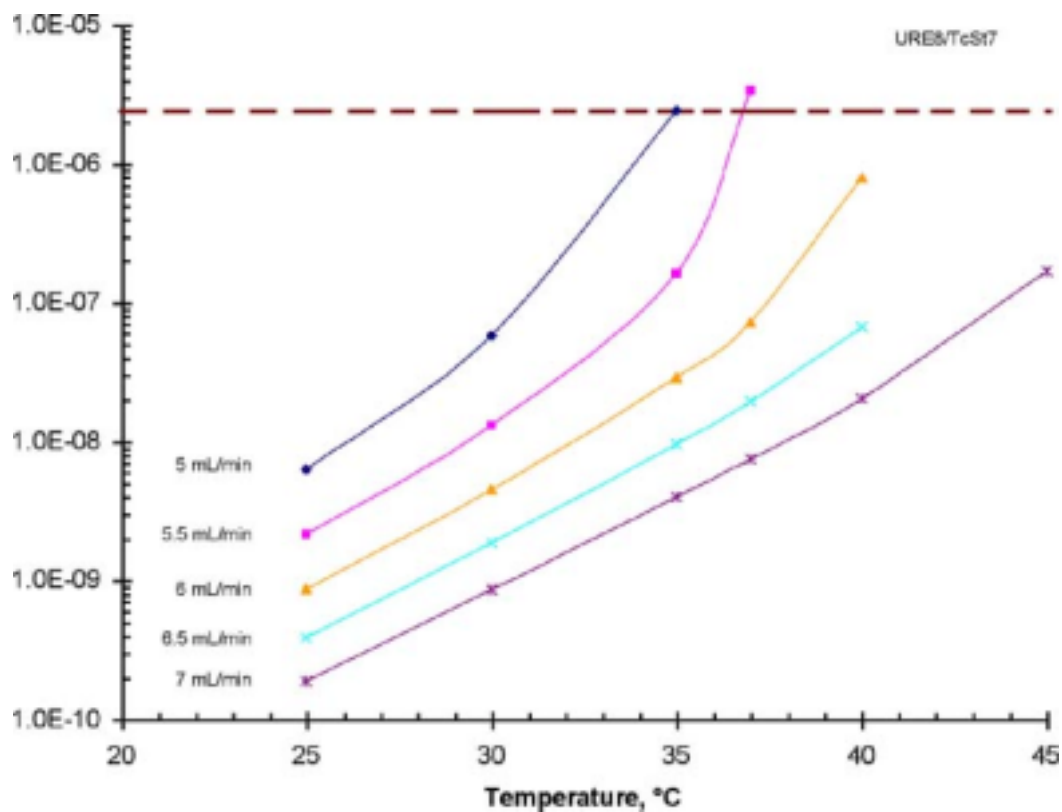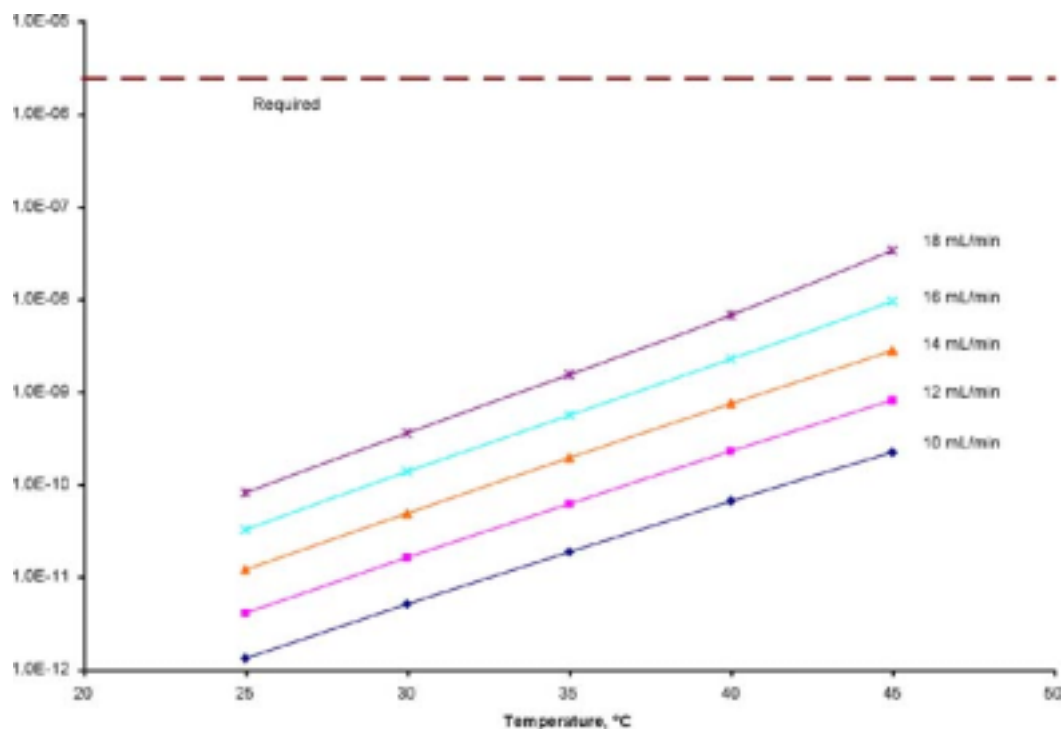

Fig. 41. Concentration of uranium in the technetium product as a function of temperature for a clean solvent flowrate of 7 mL/min for shown Tc-strip flowrates.

To improve the plutonium model in the AMUSE code, a series of tests was conducted to determine the distribution ratio (D) of plutonium between acidic aqueous phases and tributyl phosphate (TBP)-bearing organic phases. The aqueous phases were chosen to test the effect of total acid content and nitrate content. The organic phases chosen were 15 and 30 volume% TBP in n-dodecane. After the tubes were centrifuged to assure complete phase separation, each phase was removed from the tube, placed in a glass shell vial, and sampled for liquid scintillation counting (LSC).

The preliminary data reported here are meant to describe the dependence of D on TBP and nitrate concentration. The data shown in Fig. 42 suggest that the extraction of Pu (IV) is second order with respect to nitrate concentrations using 30% TBP. Data from extractions with 15% TBP are quite scattered and inconclusive, and further experiments are needed. Comparison of the data from 30% TBP and 15% TBP extractions suggest that the extraction is second order with respect to TBP in 1M total acid. The extracted complex is thought to be $Pu(NO_3)_4 \cdot 2TBP$, so the extraction was expected to be fourth order with respect to nitrate and second order with respect to TBP. The second order nitrate dependence of D is unexpected. We are currently conducting a series of experiments that will provide data to allow us to decrease the uncertainty of our results and allow us to propose a chemical mechanism that is consistent with the observed reaction order.
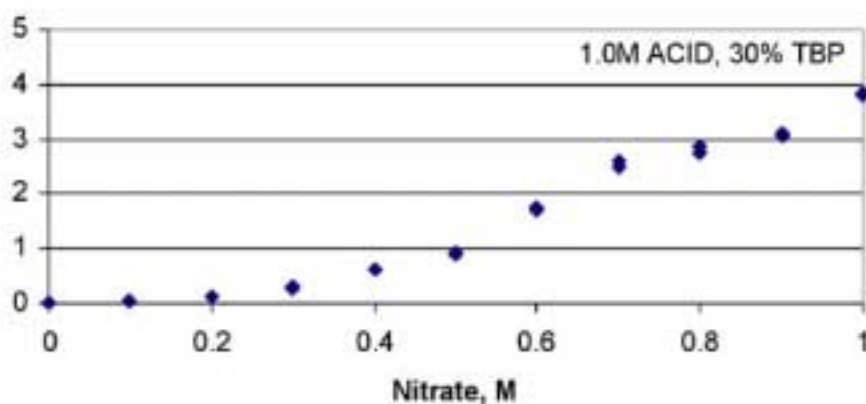

Fig. 42. Distribution ratio of Pu between 1M acid and 30% TBP in n-dodecane as a function of nitrate concentration.

Blank Page

3.   TRANSMUTATION SCIENCE

Transmutation science research is divided among the following major categories:

- Integration and Analytical Support
- Materials
- Lead-Bismuth Eutectic (LBE) Technology
- Irradiation Experiments
- High-Energy Physics
- Reactor Physics
- International Collaborations
- LANL-Sponsored University Projects

The quarterly progress in each area is presented in the subsections that follow.

3.1   Integration and Analytical Support

The major objective of the integration and analytical support activities is to define and implement a consistent research plan for transmutation science.

Scope

Integration and analytical support activities include project management and integration of activities under transmutation science. The specific technical scope includes the following:

- Implement/maintain the 10-year research plan for transmutation science (experiments and supporting analyses);
- Maintain and coordinate international work packages (DOE international coordination agreements) relevant to transmutation science topics;
- Assist AFC Program management in generating other international collaboration work packages in transmutation science; and
- Participate in safety and hazard control plan (HCP) reviews for project experiments.

In general, analytical support tasks involve defining and designing the experiments, defining the test requirements and the data quality objectives, and converting the test data into technology readiness input. Defining and designing experiments involve scaling analyses, assessment of the facility limits and parametric ranges, and comparing those to the technology development needs. During this process, the specific requirements for tests as a function of a Technology Readiness Level (TRL) also are defined in terms of data quality objectives (with emphasis on accuracy requirements). Generated data must be analyzed and assessed in terms of TRL achievements and used to define design parameters or the need for supplementary and complementary tests. Specifically, tasks include:

- Integration of the Weapons Neutron Research (WNR) facility gas production test results with Blue Room neutron-yield results to map out buffering effects;
- Assessment of the data provided through international collaboration in terms of its impact on the TRL and definition of US experiments;

- – Input to international test plans; and
- – Completion of LBE-Na compatibility experiments begun in FY01.

Highlights

- The final draft of the 10-year research plan for Transmutation Science was submitted to DOE. This plan will be revised in FY03 to reflect the changes in the program direction for AFC.

Progress Summary

In integration and analytical support, most activities were programmatic, primarily focused on the preparation of FY03 workscopes. Planning packages were prepared for FY03 and presented to DOE. As part of the presentations, we provided DOE with summary packages of the FY02 accomplishments. The project leader for the transmutation science also participated in the preparation of the AFC program plan based on initial DOE guidance.

3.2   Materials

The major objective of the materials activities is to test and quantify materials properties under proton and neutron irradiation.

Scope

The major activities in this area are continuation of the high-temperature testing of irradiated materials, irradiation test plans, collaborations with the Paul Scherrer Institute (PSI) materials program, and updating and maintaining the *Materials Handbook*. Specifically, testing in hot cells will support the AFC Program by determining the mechanical properties of structural materials at prototypic temperatures after irradiation in a proton beam. This will involve testing some materials irradiated at LANSCE at low temperatures and testing materials irradiated at PSI at high temperatures. The following are the activities in support of this mission:

- – Receive and test irradiated rods from PSI;
- – Order and install a high-temperature furnace for performing mechanical tests on specimens in vacuum or argon at temperatures up to 700¡C;
- – Perform bend tests at 300¡C, 400¡C, and 500¡C on F82H, 9Cr-1Mo, and SS-316L;
- – Perform compression tests on W at 600¡C;
- – Perform mechanical tests on Ta at high temperature;
- – Continue high-temperature testing of 9Cr-1Mo at PNNL;
- – Complete and publish new chapters of the *Materials Handbook,* including 9Cr-1Mo, W, Ta, Hg, LBE, and corrosion on˚various steels;
- – Prepare an irradiation test plan (mostly in reactors) for cladding duct materials; and
- – Review the reactor irradiation database as applicable to transmutation.

Work in the materials area has been curtailed due to budget uncertainties.

Highlights

- Two reports, *Advanced Accelerator Applications Cladding and Duct Review* and *Advanced Fuel Cycle Initiative, Cladding and Duct Irradiation Program*,[6] outlining irradiation needs for transmutation systems, were issued.

- At PNNL, shear-punch tests were performed on unirradiated and irradiated SS-316L as a way to extend the number of specimens available for estimation of tensile properties.

- At LANL, a high-temperature furnace was installed and tested in the hot-cell. This furnace will be used for subsequent high-temperature testing.

- A draft chapter of the Materials Handbook on the properties of HT-9 was issued in July 2002. Additions to the handbook chapter will be proposed for FY03.

- An analysis, Microstructural Characterization of HT-9 Alloy Proton-irradiated to 3.0 dpa at 450 ¡C with 100-appm He implantation was performed. This met the deliverable, Analysis of Proton Irradiated HT-9.   The results are reported below.

PNNL Activities

PNNL activities can be broken up into three categories: materials studies, technique development and support activities, and presentation of research results. For this quarter, the materials studies consisted of TEM on irradiated Mod 9Cr-1Mo and shear- punch tests on SS-316L. The technique development consisted of design, construction, and evaluation of a shear-punch test fixture to be installed at LANL. Support activities were comprised of inventory and shipping of irradiated specimens back to LANL.

Transmission Electron Microscopy (TEM)

As part of a plan to understand the elevated-temperature tensile behavior of irradiated Mod 9Cr-1Mo, TEM was performed on irradiated (1.4 dpa) specimens thermally aged after irradiation at 500¡C for about 1.5 hrs. Estimated He and H content in these samples were estimated to be 87 appm and 737 appm, respectively. It was thought that thermal aging at 500¡C may lead to the formation of small gas-filled bubbles or cause the coarsening of black spot (interstitial loop) damage that may be present. Initial observations performed in the third quarter showed no evidence of any cavities with the understanding that the maximum observable cavity size in TEM is ~1.5 nm. A second set of observations were performed in the fourth quarter to examine the black-spot morphology. Due to oxidation of the sample surfaces and due to the highly magnetic character of Mod 9Cr-1Mo, it was not possible to make any clear observations of black-spot damage.

Shear Punch Testing

Shear-punch tests were performed on unirradiated and irradiated SS-316L as a way to extend the number of specimens available for estimation of tensile properties. All the higher dose SS-316L and SS-304L tensile specimens had been used in tensile tests at temperatures of 164¡C and below. Shear-punch tests on TEM specimens

---

[6] ANL Reports ANL-AAA-025, ANL-AAA-029

provided a means to estimate the tensile properties at 300¡C of SS-316L at higher dose levels. Tests were performed at 300¡C on unirradiated specimens and specimens irradiated to 1.45 dpa and 9.7 dpa. The shear-punch tests traces are shown in Fig. 43. With excellent reproducibility, the tests show an increase in yield strength, a more sharply defined yield point, and an increase in ultimate shear strength with increasing dose. The shear yield and shear ultimate as a function of dose are shown in Fig. 44. As expected from examination of the test traces, shear yield and shear ultimate strength both increase with increasing dose. Using previously derived linear correlations between shear-punch test properties and uniaxial tensile properties, uniaxial yield strength, uniaxial ultimate strength, and true uniform elongation were estimated from the shear-punch properties and are shown in Fig. 45 along with actual measured tensile properties obtained from tensile tests at 300¡C on unirradiated SS-316L specimens and SS-316L specimens irradiated to 2.5 dpa. The predicted tensile properties from shear-punch tests are in generally good agreement with the observed tensile properties at 0 dpa and 2.5 dpa. The shear-punch tests predict that after 10 dpa at 35¡-67¡C, the uniaxial yield strength will be approximately equal to the uniaxial ultimate strength, and the uniform elongation will drop to approximately zero. These predicted tensile properties at 300¡C are similar to the available data in the open literature on tensile properties of SS-316L irradiated and tensile tested near 300¡C [1-3]. As the AAA specimens were irradiated near room temperature, the estimated tensile properties support the idea that tensile test temperature has a strong effect on tensile properties of SS-316L at these moderate mechanical property test temperatures.
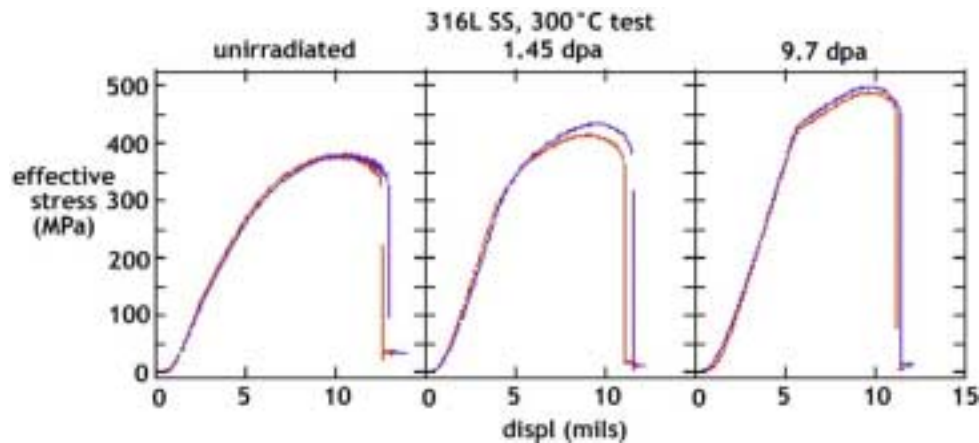
Fig. 43. Effective shear stress vs. crosshead displacement traces of shear punch tests performed at 300¡C on SS-316L.

The correlations used for estimation of tensile properties from shear punch properties were derived from a series of shear-punch tests and tensile tests performed on a variety of unirradiated materials [4, 5]. The correlations used here for predicting uniaxial yield and uniaxial ultimate strength were not those published in Ref. 4. Rather than using the more complicated method in Ref. 4 for grouping the data for the correlations, the data were simply taken as is , and a single straight line through the origin was fitted to all the data. The resulting correlations were:

$$\sigma_y = 1.95\,\tau_y \tag{1}$$

$$\sigma_m = 1.48\,\tau_m \tag{2}$$

The correlation used for estimating true uniform elongation was the one published in Ref. 5 and is:

$$\varepsilon_u = 2.26n_\tau - 0.15 \qquad (3)$$

where n_t is as described in Ref. 5.

Fig. 44. Shear yield strength and ultimate shear strength plotted as a function of dose for SS-316L shear punch tested at 300¡C.
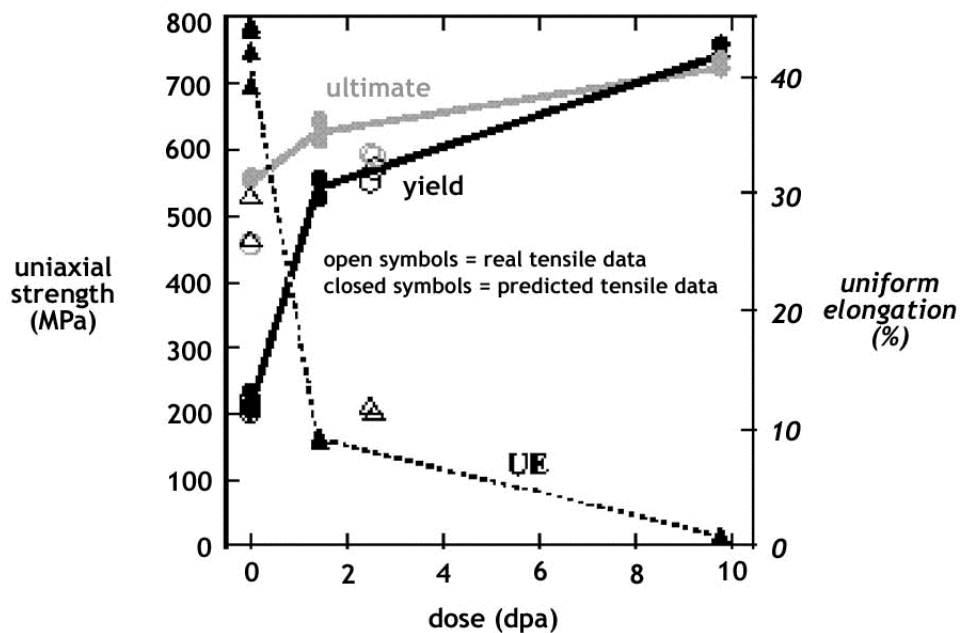
Fig. 45. Observed tensile properties and tensile properties predicted from shear punch tests for tests performed at 300¡C on SS-316L.

Technology Transfer

The technology transfer activities consisted of redesign, construction, and evaluation of a shear-punch test fixture to be used at LANL. Based on past experience doing shear-punch tests, modifications were made to the design of the shear-p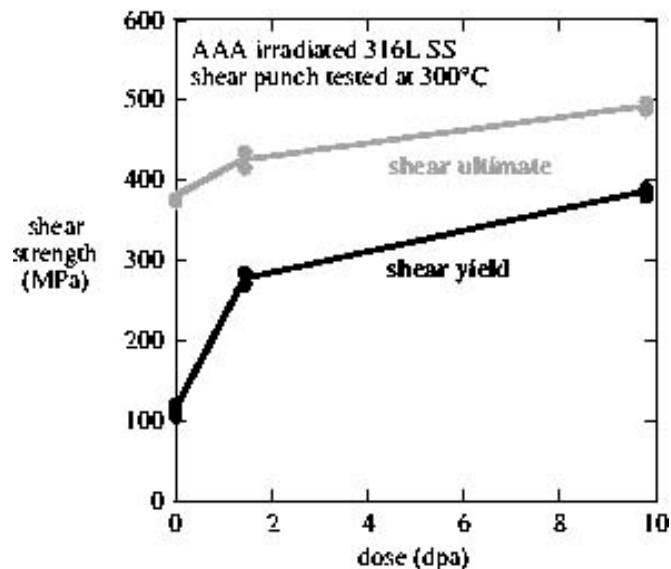unch test fixture with the intention of improving the consistency of the shear yield strength data obtained from it. A cross-sectional view of the improved fixture design is shown in Fig. 46. The fixture for LANL was constructed by JW Industries (located in Albuquerque, NM) and sent to PNNL for evaluation. In the course of evaluation, it was found to be necessary to increase the clearance on some of the bolt holes and chase the threads on several of the threaded holes to improve usability of the fixture. Honing of two pieces was also found to be necessary to allow for smooth motion of fixture during testing. Final evaluation is currently underway.
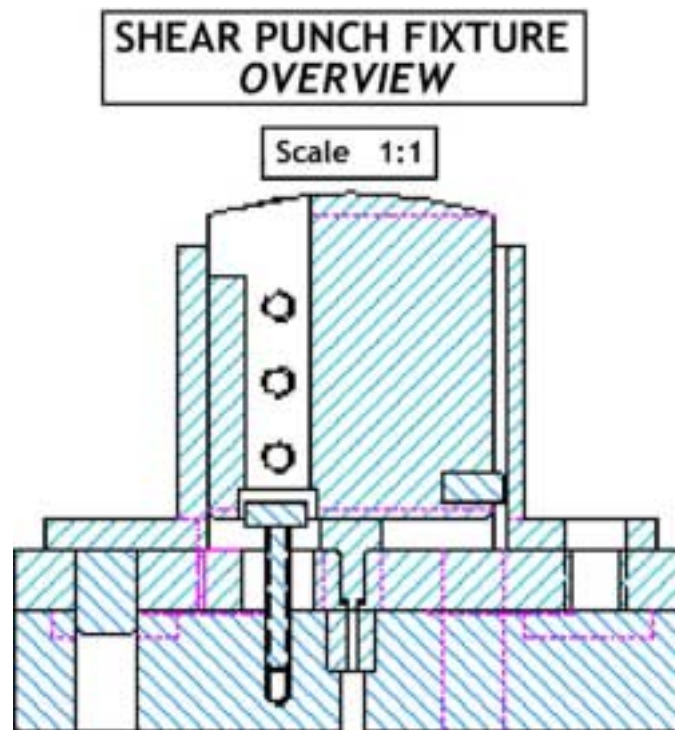
Fig. 46. Cross-sectional view of the shear punch design for LANL.

ANL Activities

Proton Irradiation of HT-9

The microstructural characterization of the unirradiated martensitic steel HT-9 was summarized in a previous report. The same materials with the identical thermal mechanical treatment were irradiated with 2.0 MeV protons at an irradiation temperature of 450…C to doses of 3, 7 and 10 dpa either with or without He-implantation of 100 appm. The profile of He distribution along with the displacement damage of 2 MeV protons in HT-9 is shown in Fig. 47. The chemical composition provided by Carpenter Technology Co., the manufacturer for the HT-9 bars, is listed below in Table 13.

Table 13. Chemical Composition of HT-9 bars (wt%)

C	Mn	Si	P	S	Cr	Ni	Mo	Al	V	W	Co	Fe
0.21	0.70	0.30	0.012	0.003	11.73	0.61	1.00	0.002	0.31	0.50	<0.02	Bal.

TEM Sample Preparation for Proton-Irradiated HT-9

The irradiated HT-9 coupon has a geometry of 2x20x0.5 mm as rectangular bar. The samples were mechanically wet-polished from the unirradiated side using SiC papers of 240-600 grit. At a thickness around 150 mm, a 2.3-mm-diameter disc punch was used to cut 2-3 discs from the irradiated area. The discs were further ground from the unirradiated side down to ~70 mm using 600 grit SiC paper. Due to the narrow width of the He implantation as shown in Fig. 47, the thin area of the foil for microstructure examination should be controlled to a depth of 2-3 mm below the irradiated surface. A jet-polishing solution of 5% perchoric acid in methanol at a temperature of —40…C was used. Through the jet-polishing of a test disc of unirradiated HT-9, it was estimated a 4-sec flash polishing on the irradiated side would remove a ~2.5 μm thick layer. Samples with and without He-implantation were jet-polished for 4 sec on the irradiated side and then back-thinned until perforation. The disc samples after jet-polishing were mounted using epoxy to a 3-mm-diameter copper washer (50 μm thick) having a 1-mm hole in the center. This sample preparation has proven successful in cutting down a magnetic field interference with the electron beam in the electron microscope.

Microstructure Characterization

Two TEM samples were prepared, one with and one without He-implantation, both irradiated to a dose of 3 dpa. Results of the microstructural analysis from the He-implanted sample were available for this report.

The overall microstructure for the He-implanted sample irradiated to 3 dpa at 450…C is very similar to the unirradiated HT-9 except the presence of dislocation loops. The sample consisted of low-density dislocation loops, high-density dislocations, dislocation cell boundaries, precipitates, and lath structure. No voids were found. The dense dislocation structure in the irradiated HT-9 is similar to that in the unirradiated HT-9, shown in Fig. 48. The irradiation-created dislocation loops in HT-9 are shown in Fig. 49 under three different diffraction conditions. These loops have a Burgers vector of the type **b**=**a**[100]. The average loop size is 10.8 nm with a number density of 1.2×10^{21} m^{-3}.

The precipitate structure in the irradiated HT-9 (3 dpa at 450…C, He-implanted) is similar to that in the unirradiated HT-9. No irradiation-induced phases were identified. The analysis of diffraction spots and x-rays from the precipitates revealed that the precipitates have an FCC structure with a lattice constant about 1.09 nm and a composition in atomic fraction of 29%Fe+64%Cr+3.9%Mo+1.3%V and 0.8%W. This is in close match to $M_{23}C_6$. Figure 50 shows the images of precipitates under both bright field and dark field imaging conditions. The diffraction patterns from both HT-9 matrix and the precipitates are shown in Fig. 51 where the bright spots are from the matrix near the [001] zone and the weak spots are from $M_{23}C_6$ precipitates with a much larger lattice constant.

Comparison to Other s Work

Comparing the result to the Gelles and Kohyama reference[7], voids were not found in HT-9 irradiated in EBR-II to 70 dpa in the temperature range of 400…C—450…C, although helium bubbles were formed at temperatures as low as 400…C. The result from the proton irradiated HT-9 is consistent with neutron result. Although the implantation of 100 appm He may assist the void development, the dose of 3 dpa may be still too low to form the cavity. The dislocation loops examined in the work by Gelles were also identified as a<100> type. The type of the loops identified in the proton irradiated HT-9 is also in agreement with the reference.
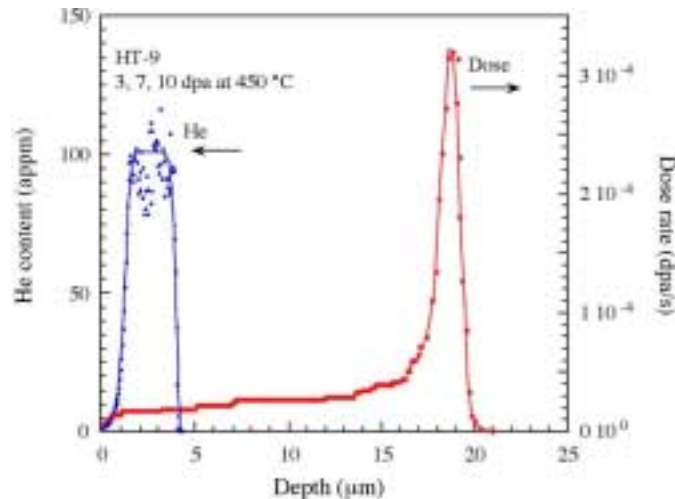
Fig. 47. He distribution profile and the 2 MeV proton damage profile for HT-9 irradiated with protons to doses of 3, 7 and 10 dpa at 450…C.
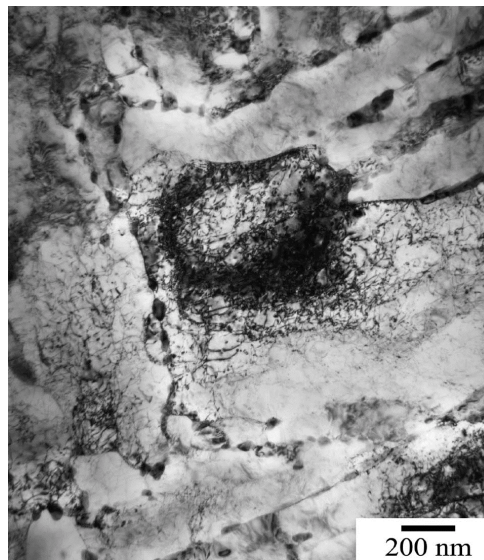
Fig. 48. Overview of the microstructure for HT-9 implanted with 100 appm He followed by proton irradiation at 450…C to a dose of 3 dpa.   The microstructure consisted of low density and small dislocation loops, dense dislocation structure, precipitates and lath structure. No voids were found.

---

[7] D. S. Gelles and Akira Kohyama, DOE/ER-0313/6, 1989
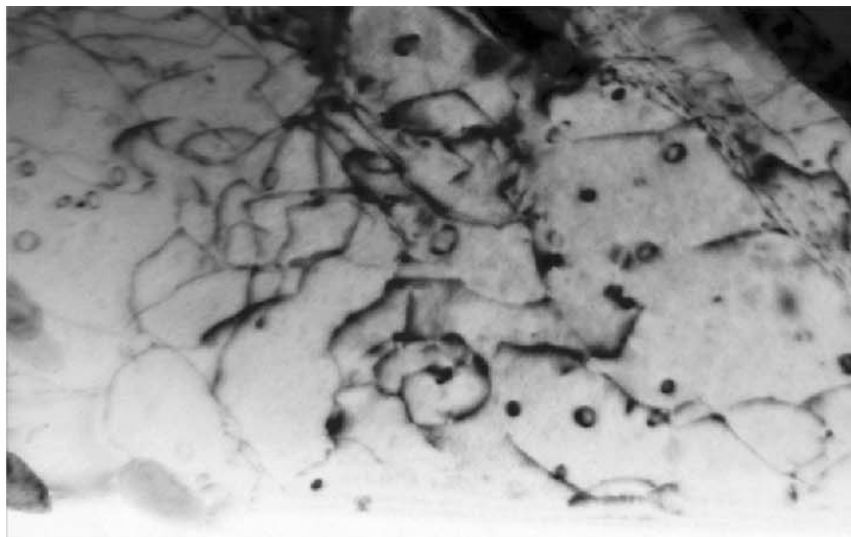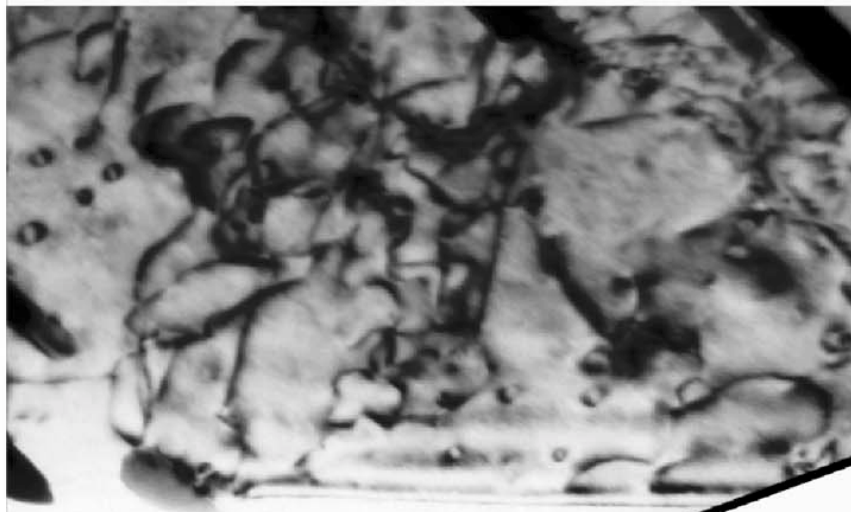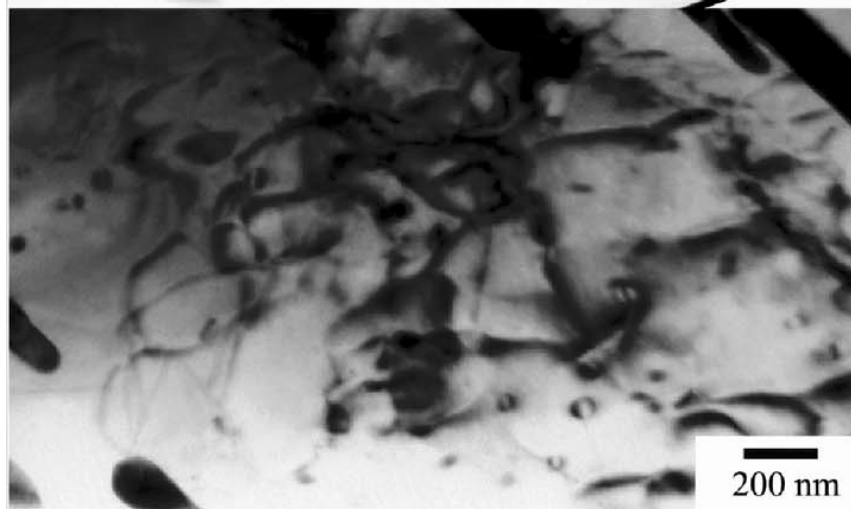
Fig. 49. Dislocation loops in HT-9 implanted with 100 appm He followed by proton irradiation at 450…C to a dose of 3 dpa. All loops have a Burgers vector of **b**=**a**[100] type. The average loop size is 10.8 nm with a number density of 1.2×10^{21} m^{-3}. The diffraction conditions for images of the same area are (a) g=10-1, (b) g=1-10 and (c) g=2-1-1.
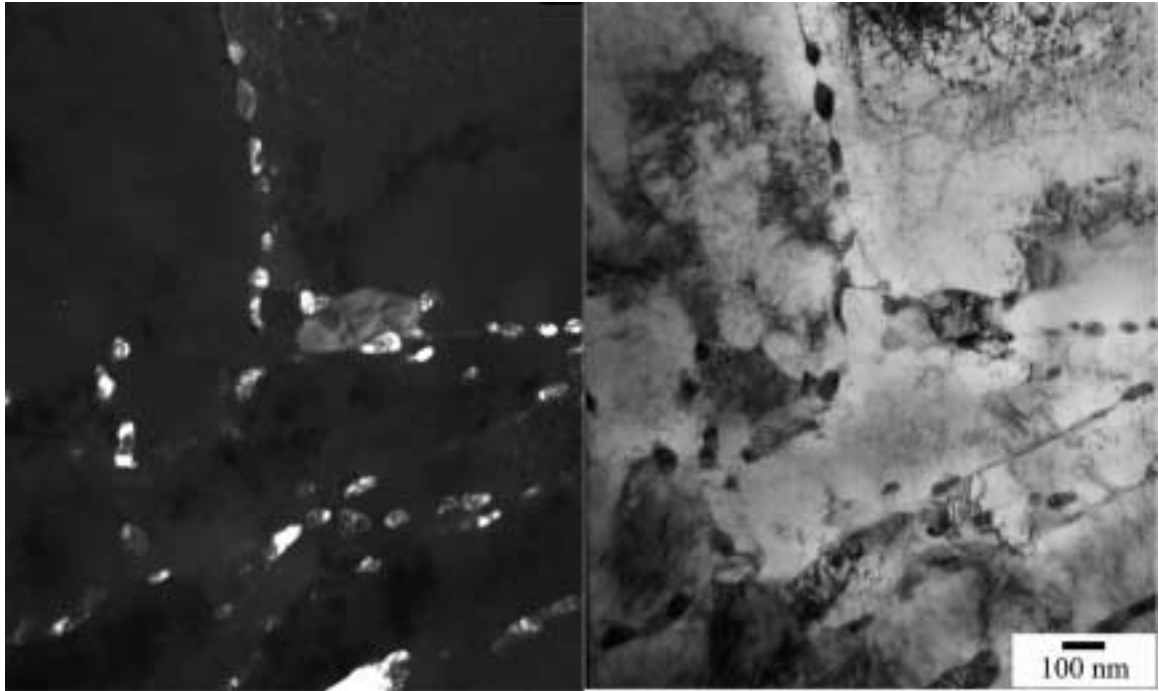
Fig. 50. Images of precipitates in HT-9 implanted with 100 appm He and irradiated with protons at 450…C to a dose of 3 dpa. The dark filed image on the left was taken using the diffraction spot from the precipitates. The image on the right was from the same area using bright filed imaging condition.
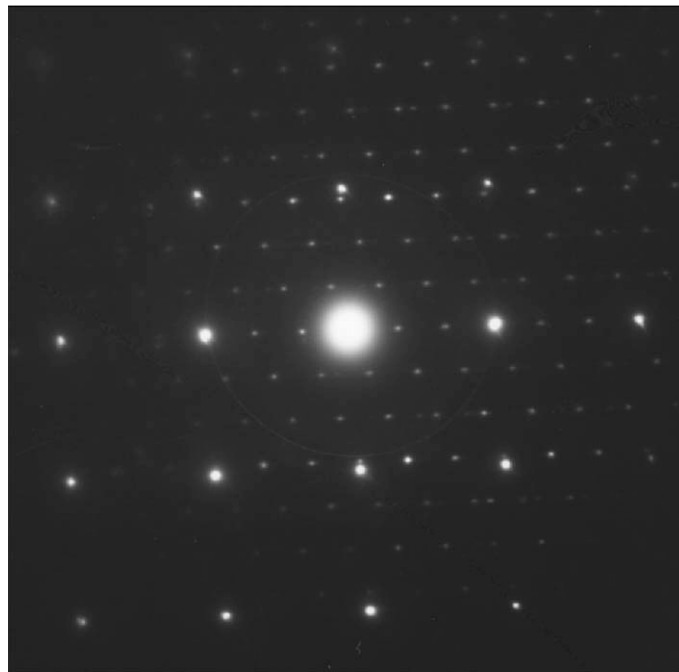
Fig. 51. Diffraction spots from the HT-9 matrix (bright spots) near zone [001] and from precipitates (weak spots) near zone [011].

LANL Hot-Cell Work

A high temperature furnace designed by MRF furnaces was set-up, tested, then installed in a hot cell with cooling lines, thermocouples and power leads routed through the hot-cell wall. A final and successful test was performed in the hot cell on the furnace heated to 700¡C in argon.

Tantalum disks were retrieved from envelopes that were irradiated for 6 months at LANSCE. Shear-punch tests will be performed on these disks at room temperature, 250…C, and 500…C. Bend specimens sliced from the STIP-1 irradiated SS-316L and Mod9Cr-1Mo rods will also be tested at room temperature, 250…C and 500…C.

Materials Handbook

A second draft of Materials Handbook Chapter 19 (T-91 [9Cr-1MoV] Ferritic/Martensitic Steel) was completed and reviewed, and final formatting initiated. The second draft of Materials Handbook Chapter 22 (Pb-Bi Eutectic) was also completed and final formatting initiated.

Reviews of revisions made to two sections of Chapter 7 (Tungsten), Effects of Irradiation on Yield Strength and Corrosion were completed and the sections finalized.

A second round of revisions was made to the corrosion sections in Chapter 2 (Alloy 718), Chapter 3 (SS-316L), and Chapter 4 (Al-6061-T6), and final formatting is in progress. Also, a detailed review was performed for a draft chapter on HT-9 steel.

Meetings/Conferences/Workshops

Two technical papers were completed one paper was submitted to Practical Failure Analysis entitled, Failure Analysis of a Radio-activated Accelerator Component, and the other was submitted to J. of Nuclear Materials entitled, Comparison of Fission Neutron and Proton/Spallation Neutron Irradiation Effects on the Tensile Behavior of Type 316 and 304 Stainless Steel.

3.3   Lead-Bismuth Eutectic Technology

The major objective of LBE research activities is to develop a fundamental understanding of LBE performance parameters and measurement techniques when used as a nuclear coolant, with primary emphasis on spallation-target applications.

Scope

LBE Technology Development

The safe and reliable implementation of the LBE technology requires additional developments for the oxygen sensors. Development of other nonintrusive flow measurement and online corrosion measurements would significantly improve the reliable operations of an LBE target. The development will be carried out in collaboration with international partners (e.g., CEA and FZK) under DOE agreements. By collaborative testing, the objective is to achieve in 3—4 years a TRL-4 level where

a parametric (velocity, temperature, materials, thermal gradients, etc.) is developed to Pb into the spallation-target conceptual design.

The scope of this work package involves developing new sensor technologies and corrosion data analyses with the long-term objectives noted above. Some of the actual tests will be performed in the DELTA Loop (Materials Test Loop) at LANL, and testing must be closely coordinated with loop-operation work-package activities. The FY02 activities are as follows:

- Fabricate oxygen probes to be tested in the DELTA Loop;
- Develop a calibration standard in conjunction with international partners;
- Cross-calibrate oxygen sensors;
- Develop gas and solid-phase oxygen control methodology;
- Develop concepts for low-temperature oxygen probes;
- Develop ultrasonic laser velocimetry technique;
- Analyze corrosion data;
- Develop and design components for FY03 testing (with international collaboration); and
- Revise the DELTA Loop test plan according to international collaboration work packages.

DELTA Loop Operations

The DELTA Loop will be operated to validate key Russian LBE nuclear-coolant technology, to perform corrosion and thermal-hydraulic testing, and to develop diagnostics and probes for application in a high-powered spallation-target system. Again, the tests will be carried out in collaboration with international partners.

The scope of this work package involves operating, maintaining, and upgrading the DELTA Loop in accordance with the long-term objectives mentioned above. The actual test plans will be developed under the LBE technology work package, and operations must be closely coordinated with activities under that work package. The FY02 activities are as follows:

- Completing construction for operational and instrumentation testing;
- Addressing all post-start findings;
- Performing operational tests;
- Testing oxygen control techniques and procedures;
- Updating data acquisition and control (DAC) system and hazard control plans for unmanned operations;
- Installing new instruments (e.g., improved oxygen sensors and ultrasonic velocimetry) as delivered from the LBE technology team; and
- Performing 1000-hr corrosion tests (two different materials and/or two different velocities).

Highlights

- The DELTA loop attained reliable operational status, allowing unattended operations.

- Two LANL-made oxygen sensors were approved for export and delivered to a research group at the Royal Institute of Technology (KTH), Sweden.

- One study was submitted to the Journal of Nuclear Materials: Parametric Study of a Corrosion Model Applied to Lead-Bismuth Flow Systems.

- Two reports were issued: Adaptation of Ultrasonic Doppler Velocimetry (UDV) to Measurement of LBE Flows, and Low Temperature Oxygen Sensors for LBE Systems.

LBE Technology Development

Several significant technical objectives were achieved during this quarter. The oxygen sensor (OS) development had a breakthrough in achieving the control system stability necessary for calibration at the extremely low oxygen concentration levels. The majority of the corrosion test specimens were fabricated and received. The LBE corrosion model was expanded to include time dependence, simple corrosion-product reaction in fluids, and multi-branch multi-section variable cross-section loop systems.

The oxygen-sensor calibration system has achieved the stringent system tightness requirement needed for the calibrations. A series of calibration curves are shown in Fig. 52 for two sensors.

The LBE in the rocking U-tube calibration apparatus was cleaned by a 6% H_2/He mixture at a temperature between 440¡C—500¡C to a desired oxygen level as indicated by the OS, after which the gas supply was terminated and the system shut off. After some time, the temperature of the LBE gradually decreased while the OS output is continuously reported the corresponding temperature.

The OS voltage-vs-temperature curves obtained so far are for constant oxygen concentrations. After initial transients, the curves display the linear trend with slopes very close to theoretical values as illustrated in Fig. 52. As was confirmed in the experiment, when the LBE temperature reaches the point where the oxygen becomes saturated, the voltage no longer follows the constant-concentration curve but instead tracks the saturation-limit curve.

There are two experimental difficulties: (1) Because there is residual hydrogen left in the cover gas after the system is closed, the oxygen concentration is slightly reduced and is perhaps the reason behind the flatter calibration curves near the start of the runs; and (2) When oxygen reaches the saturation limit as temperature decreases, the excess oxygen comes out in the form of precipitated lead oxide a phase transition process involving nucleation, mass transport and precipitation and is difficult to measure. Overall, it is very difficult to maintain the necessary system tightness for more than two days.

Preparation of the oxygen sensors, especially with the addition of sufficient bismuth oxide and the cleaning of the ceramic surface, was improved during the experiments for more consistent sensor response and the ability to measure the extremely low oxygen concentration at the magnetite dissociation limit (oxygen concentration in that range is below ppb and approaching 10^{-12}).

The next phase of the investigation will focus on more systematic calibration runs, improvement of sensor design and assembly, tabulation of calibration curves with uncertainty and variability bounds, and increasing the partial pressure of hydrogen-and-water steam mixture for measuring the partial pressure of oxygen.
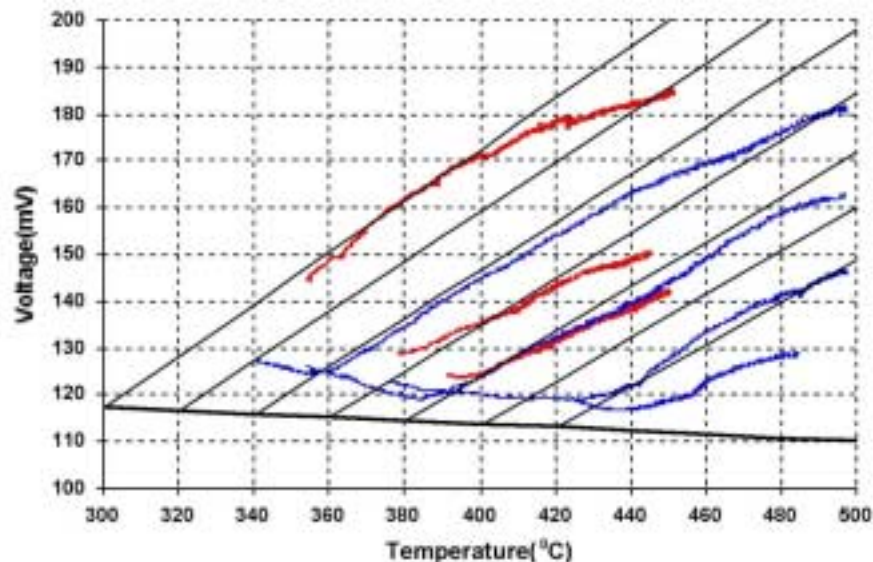
Fig. 52. Oxygen sensor calibration curves for two sensors (red and blue). The solid lines are theoretical values for constant oxygen concentrations (not computed for the OS data), and the bold solid line is at the oxygen saturation limit in LBE.

Low Temperature Oxygen Sensors for LBE Systems [8] was completed and issued, summarizing needs, requirements, and existing literature results on low temperature oxygen sensors, examining the preliminary experimental results of YSZ-based sensors in that temperature range, and presenting a path forward for future development.

In several experiments performed in the DELTA Loop and the oxygen sensor calibration apparatus, the behavior of such sensors at temperatures below 350¡C can be determined, although a more systematic study will be needed to quantitatively characterize sensor response.

From Fig. 53, we find that the oxygen sensor has very low output voltage (close to zero) before the reference electrode Bi (saturated with oxygen) is melted. Once the Bi is molten, the output voltage increases to a level corresponding to oxygen saturation in LBE as expected since the LBE in the DELTA Loop has not been cleaned with hydrogen. As the temperature rises, the dependence of the output voltage of the oxygen sensor on temperature follows a linear trend. This trend can be calculated from the thermodynamic data and the oxygen solubility in LBE. The experimental results agree well with the theoretical prediction, indicating that the LANL-developed YSZ | B/Bi_2O_3 sensors may follow the Nernst equation down to the melting point of Bi. Even if it deviates from this ideal relationship, this type of sensor may be calibrated to give proper reading of the oxygen activity in LBE down to 270°C if the reliability and consistency can be proved.

Two LANL-made oxygen sensors were approved for export and delivered to a research group in the Royal Institute of Technology (KTH), Sweden (see Fig. 54). The sensors will be installed into a LBE natural convection loop studying reactor core cooling. Sensor specifications were also sent to the MEGAPIE project.

---

[8] LANL Report, LA-UR-02-6428
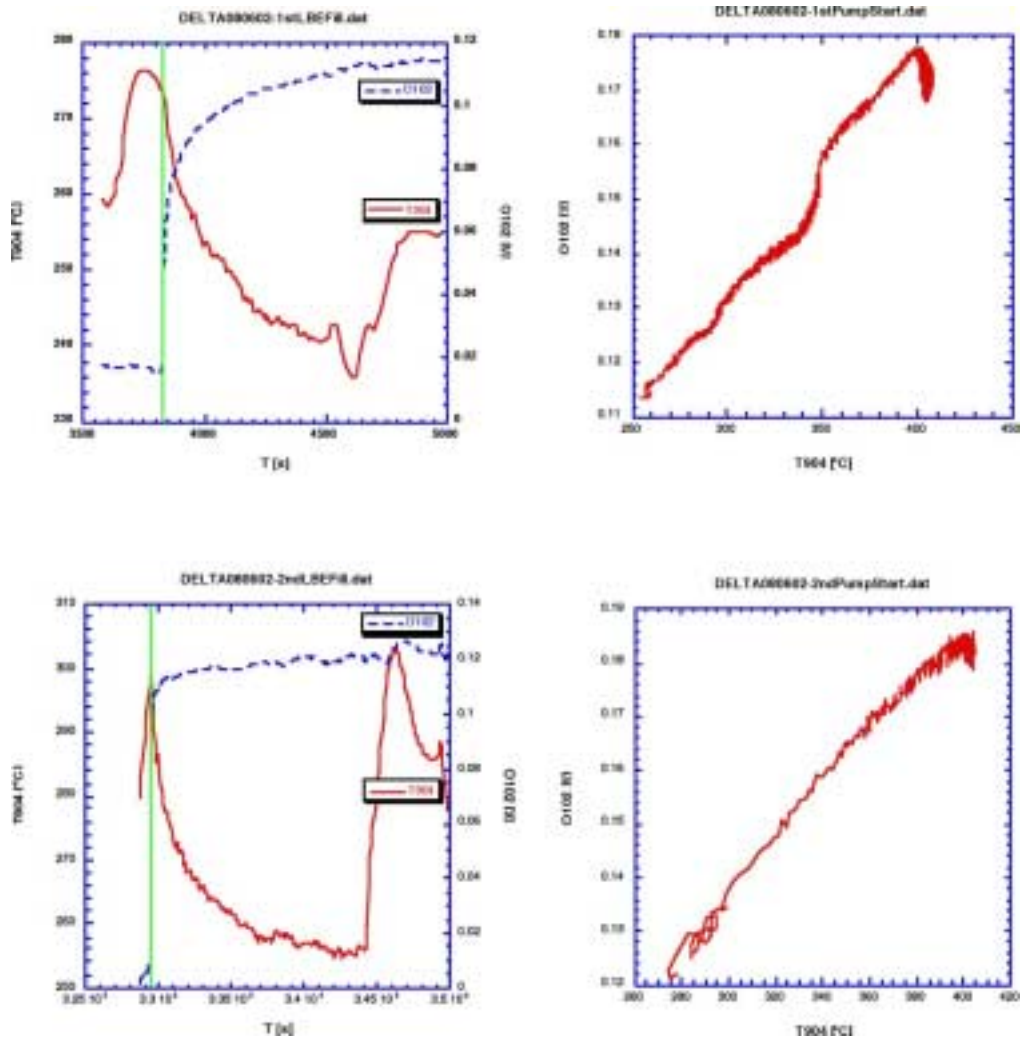
Fig. 53. YSZ | B/Bi$_2$O$_3$ oxygen sensor response to temperature changes in DELTA Loop
(08/06/2002 operation data).

Fig. 54. Two LANL-developed YSZ | B/Bi$_2$O$_3$ oxygen sensors delivered to KTH, Sweden.

The corrosion test specimens, including 12 different materials and welds (T-91-316L) were fabricated and received for DELTA Loop tests. The specimens have been separated into corrosion test bar specimens and dog-bone type miniature tensile test specimens, and are awaiting final surface treatment. The sample holder design was finalized and a fabrication contract awarded.

The system corrosion modeling continues to make significant progress. We have expanded the model to include multi-branch, multi-section variable cross-section loop systems, time evolution toward steady state, simple corrosion product reactions in the fluid, and other effects. This work has significantly improved the capability to predict the corrosion rates in oxygen-controlled LBE systems, and the ability to interpret and extend the use of corrosion test results. The system model, with analytical solutions in many instances, and numerical solutions for the more general cases, is used to parametrically study the corrosion and precipitation distributions in LBE systems, and to improve the system designs to accelerate corrosion in test systems and minimize corrosion in engineering applications. "Parametric Study of a Corrosion Model Applied to Lead-Bismuth Flow Systems [9] was submitted to the *Journal of Nuclear Materials*. Two more journal papers are under preparation.

The report, Adaptation of Ultrasonic Doppler Velocimetry (UDV) to Measurement of LBE Flows, was issued, summarizing the working principles of UDV, the selection of US probe parameters, the coupling and transmission of US through container walls into fluids, and the reported experience in the literature. It will establish the needs, the requirements and a technical path forward for the LBE technology development.

To adapt ultrasonic (US) transducers to the working temperature of LBE systems requires careful extension and coupling considerations. One of them is to minimize the transmission loss through interface steel structures for the high signal levels needed for UDV. Due the acoustic mismatch between steel and LBE, it is found that the thickness of the steel interface plate should be multiples of half the half-wavelength, or the loss could amount to more than 15% (Fig. 55).

Fig. 55. Transmission coefficient of a US beam through a stainless steel plate into LBE.

[9] LANL Report, LA-UR-02-5416

The TRAC model for the DELTA Loop was completed. The initial runs showed reasonable agreement with the experimental data with some adjustment for the LBE heat-transfer coefficient.
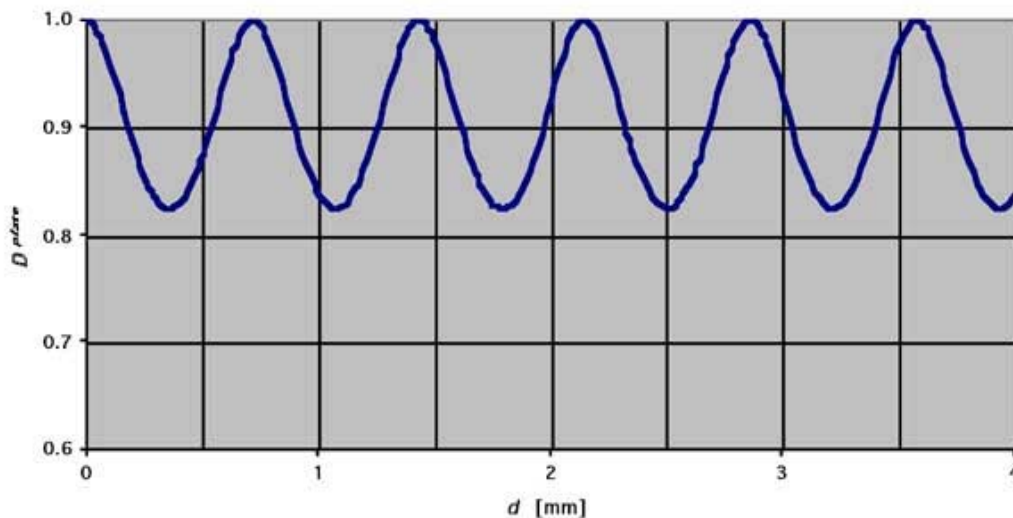
We participated in the International Molten Metal Target Advisory Committee meeting at UNLV to chart the path forward for the delivered Russian LBE test-target loop. Staff and postdoc personnel made several visits to UNLV for continued interaction with the faculty members and students working on LBE-related R&D.

A contract with the University of Illinois, Urbana-Champagne, for research and development of online active corrosion probes based on electric impedance spectroscopy was approved.

Finally, Thermal Experiments in the ADS Target Model will be published in the proceedings of FMTM-2001, Japan. This paper presents the heat transfer experiment performed at IPPE (Institute of Physics and Power Engineering, Russia) on the target window. The measurements show significant temperature fluctuations at the window surface, suggesting that care must be taken to account for this effect in the strength and fatigue analysis for liquid metal target windows.

DELTA Loop Operations

In the fourth quarter of FY02, the DELTA loop was brought to a reliable operational status that allowed unattended operations.

The DELTA Data Acquisition and Control (DAC) system includes automatic controls for temperature and gas pressure distributions in the loop. It also handles all of the different shutdown conditions such as high temperature or high pressure. In case of a shutdown condition, the DAC program automatically opens drain valves and allows the liquid lead-bismuth to drain into the drain tank. All of the DAC functions were tested and tuned for best operations.

Automatic cleaning gas control was also included into the main DAC program. All oxygen sensors were connected to the DAC system and the readings were consistent. The oxygen control system was operated successfully. The freeze plug in the venturi used for gas injection was melted and the liquid-metal level was maintained by balancing its pressure with the cleaning gas pressure.

DELTA loop was operated during the fourth quarter to test systems for unmanned operations. Total run time reached 120 hours. The first continuous 48-hour-long DELTA loop run was executed without problems. We ran at ~4.8m^3/hr flow rate and 60°C temperature gradient with minimum temperature of 345°C. The water-cooled heat exchanger was engaged during the entire run and performed consistently well. The Magnetic Flow Meter, however, did not function well during this run. The measurement was unstable and appeared to change with time. The decision was made to replace it with a more reliable venturi flow meter, and subsequent runs with the venturi flow meter proved successful. The readings were consistent with the theoretical predictions.

Pressure measurement in LBE proved difficult. Two kinds of pressure transducers failed after only several hours of operation. Investigation showed that solidifying liquid metal might damage the transducers diaphragms. The high temperature may also affect the electronics. We purchased more sophisticated and more robust pressure transducers made for higher temperature applications. We also devised a

gas blow off system that sends a jet of gas at the transducers diaphragms blowing off the liquid metal and thus preventing it from solidifying on the diaphragm. The gas system was installed and linked to the DAC. We have already operated it and are working on tuning the valves dynamics to ensure the best results.

In addition to repairing the liquid-metal pressure-measuring system, we had to repair or replace several other items on the loop:

- All oxygen sensors fittings welded to the loop piping had to be replaced. This was a preventative measure after a weld inside one of them failed.
- A new fitting for the gas injection inlet was designed and installed.
- The heat exchanger had to be disassembled to find cause of a water leak. A small error in manufacturing tolerance caused a bad seal at the location of the leak. The defect was fixed and the heat exchanger reassembled. No water leaks have been observed since the repair.
- We relocated and replaced several trace heaters and thermocouples for more uniform temperature distribution and control.
- National Instruments hardware used for Data Acquisition and Control (DAC) malfunctioned. New data acquisition modules were installed, thereby resolving the DAC hardware error.

As a result of the extensive work described above DELTA loop can be operated reliably unattended for long periods of time (hundreds of hours). The DELTA loop will be ready for the first materials test at the beginning of November. We are planning on 333-hour, 666-hour and 1000-hour tests with materials samples inside the test section.

The DELTA loop status was presented at the Third International Workshop of Utilization and Reliability of High Power Proton Accelerators in May 2002, held in Santa Fe, New Mexico. The report, Results from the Initial Operation of the LANL DELTA Loop, is part of the workshop proceedings. DELTA loop status was presented at a Molten Metal Target Advisory Committee meeting at University of Nevada Las Vegas (UNLV) in August, 2002, and DELTA loop team members also participated in meetings and teleconferences with the UNLV faculty aimed to advise them on the best use of their LBE system based on the target built by IPPE, Russia.

3.4   LANSCE Irradiation Experiments

The major objective of the LANSCE irradiation experiments is to advance the TRL for°transmutation in various areas up to TRL 6 by performing small-scale proton and neutron irradiation of materials to investigate various phenomena. Specific experiments to be performed in FY02 are as follows:

- Sodium activation tests;
- Neutron yield and spectrum tests;
- Helium and hydrogen production tests; and
- Corrosion studies.

Scope

Sodium Activation Tests

If a Na-cooled spallation target is used, accurate prediction of coolant activation is important for operational and safety reasons. In the summer of FY01, we performed a series of activation tests using an 800-MeV beam. Subsequent tests at other energies were postponed because of budget reduction. The FY02 activity is limited to completing the final data report.

Neutron Yield and Spectrum Tests

Spallation neutron sources create high-energy neutrons whose energies extend up to the incident proton-energy. In the design of accelerator-driven waste transmuters, the high-energy neutrons that leak from the spallation target have three practical implications:

- They dominate the shield design because they have long attenuation lengths (18 cm in steel);
- They lead to the production of source neutrons in the fuel region, which generates a spatially dependent neutron source that influences the power density distribution in the blanket; and
- They dominate the production of helium and hydrogen atoms in the steel structural elements that reside in the multiplier region near the target, while gas production limits the lifetime of structural materials near the target.

As a means of reducing gas production in structural materials in the multiplier region, a buffer region consisting of high-atomic-mass material may be placed between the target and the multiplier. This buffer attenuates˚high-energy neutrons that leak from the target into the multiplier. Additionally, the configuration of the buffer and the associated beam rastering parameters are variables available to the ADTF designer for adjusting the multiplier power distribution. The objective of these experiments is to provide benchmark data for the analysis tools. The data from these tests will be combined with the gas-production test results and structural-properties test results to optimize the target and buffer design (which impacts the multiplier design). To evaluate the effectiveness of a buffer in reducing the leakage of high-energy neutrons, we propose making these measurements of high-energy neutron distributions a function of target radius.

Helium and Hydrogen Production Tests

Currently, considerable uncertainty exists in predicting the helium and hydrogen production at high energies. The objective of these experiments is to provide data to˚improve helium and hydrogen production cross-sections in materials near the spallation target. The data from these tests will be combined with data from spectrum tests and structural properties tests to optimize the target and buffer design (which impacts the multiplier design). Optimizing the design with large uncertainty in the design tool is not adequate and will result in a waste of time and money in the long run. Hydrogen and helium production on materials proposed for the AFC Program in the neutron-energy range up to 100 MeV will be measured. Measurements of the double differential cross-sections for proton and alpha-particle emission will provide not only data for the total hydrogen and helium production by neutrons in these

materials, but also data for transport of these elements by recoil into or out of zones of different composition in AAA/AFC designs. We will take the measurements for iron (Fe). As an integral test and to provide data quickly, an alloy of stainless steel such as SS-316 will also be studied.

Corrosion Studies

Liquid-metal corrosion is the major issue when LBE is used as a nuclear coolant or as a spallation target. If oxygen control is used to control the corrosion, it must be shown that stable oxide layers can be developed and maintained on the surfaces. This is affected by the initial conditioning of the surfaces, as well as changes in thermodynamic conditions during operations. For spallation target applications, we must also˚show that direct proton irradiation does not cause a drastic change in oxide layer properties adversely affecting corrosion rates. Finally, a more reliable operation is possible if a capability for online corrosion monitoring during actual operations can be˚developed for the loops. By collaborative testing, the objective is to achieve in 3-to-4 years a TRL 4, where a parametric is developed to lead into the spallation target conceptual design. The scope of this work involves oxide film characterization, Blue Room irradiation of oxidized surfaces, and conceptual design of corrosion probes to be used in the test loop.

Highlights

- The 40-cm-diameter target was irradiated in July, and the 20-cm diameter target (previously irradiated in December) was once again irradiated to sample data along time-of-flight (TOF) beamlines, which were unavailable earlier.

- Data collection for hydrogen and helium production on iron samples as a function of neutron energy was begun at WNR.

- LBE corrosion experiments were performed in the Blue-Room.

- A conceptual design report for an on-line corrosion probe was completed.

LBE Target Experiments

The second phase of the Blue Room Neutron Yield Experiment was performed in July. A 40-cm diameter LBE target was irradiated and the neutron yield and spectra analyzed by a combination of TOF spectroscopy and activation analysis. Additionally, the 20-cm diameter target previously irradiated last December, was irradiated once again to sample data along TOF beamlines which had been previously unavailable.

For the 40-cm target, TOF data were taken from 4 beamlines around the target, at 7.5°, 30°, 60°, and 150° from the target (and proton beam) axis. Activation foils were placed at intervals along the axial length of the target and at 45° radial intervals at the z=15 and z=40 cm axial locations. A picture of the target positioned in the Blue Room is shown in Fig. 56.

The activation foils were removed and a counting program initiated to sample the gamma spectra to determine the isotopes created. Each foil was counted at least twice, but in some cases 3 or 4 times to determine both the short and long-lived isotopes present.

Fig. 56. 40-cm diameter target in the Blue Room.

After this sequence of irradiations, the 40-cm target was removed and the 20-cm target placed in position. No activation foil analyses were performed, but TOF measurements were made for the purpose of gathering data at the 60° and 150° angles that had not been used with the previous irradiation of this target.

In August, the counting program continued, with many of the foils being sent to TA-48 for counting by the LANL C-INC group. A paper was prepared for presentation at the 11th International Reactor Dosimetry Symposium.[10]

A preliminary report of the July irradiation experiment has been drafted and is currently under review. The preliminary report for the December (2001) irradiation Neutron Leakage from a Lead-Bismuth Target (Diameter=20 cm, Length=50 cm) [11] was completed and issued.

Initial analysis of the results from the 40-cm target irradiation has focused on the Bi foils. An analysis of three different gamma energies from the decay of ^{204}Bi is given in Figs. 57—58. These results show a slight asymmetry, most likely from small misalignment of the proton beam with the target axis. The shape of the neutron flux has also been analyzed from the Bi data. Further analysis of the activation foils data will be undertaken to examine the neutron spectra at various locations in detail.

---

[10] LANL Paper and Presentation, LA-UR-02-5046 and LA-UR-02-5047
[11] LANL Reeport LAUR-02-5552
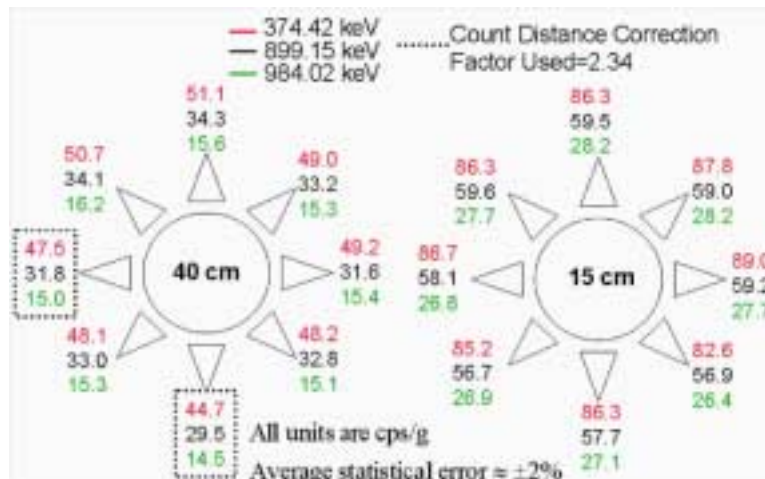
Fig. 57. Radial asymmetry ion the Bi-204 decay.
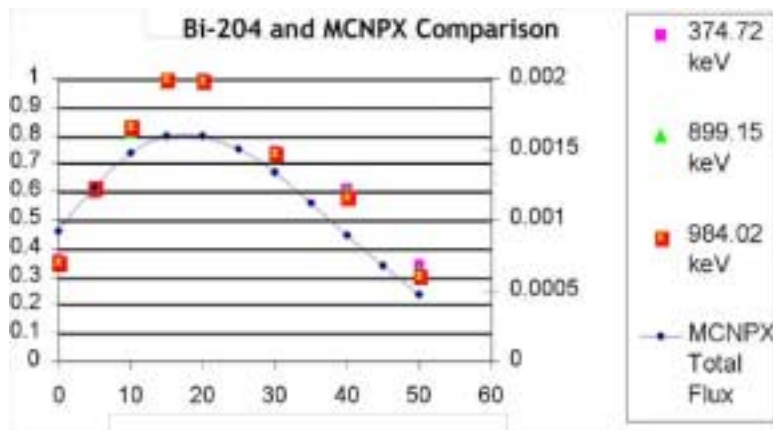
Fig. 58. Neutron intensity as a function of axial position from Bi-204 results.

Helium and Hydrogen Production Tests

During this quarter, we improved the experimental setup for the helium and hydrogen production tests and collected gas-production data on iron. These gases are produced initially as energetic protons, deuterons and alpha particles from nuclear reactions. When these charged particles slow down and stop (with ranges of mm to cm), they acquire electrons from the material and become hydrogen (protons and deuterons) or helium (alpha particles).

We are able to measure the charged particles with d_____ __stems at four angles concurrently, and can move the detector systems to investigate new sets of angles. A total of 8 angles is sufficient for determining the angle-integrated production cross sections. Each detector system consists of 2 or 3 detectors in coincidence, arranged so the charged particles pass through the first detector and stop in the second or third. This is done to be able to identify the protons, deuterons, and alpha particles separately as well as a small number of tritons and ^{3}He.

Major activities this quarter included the following:

- conducting experiments to measure proton, deuteron and alpha particle production for neutrons on iron over the energy range from threshold to 100 MeV;
- reducing experimental data to obtain preliminary results;
- purchasing a thick chromium sample, which could be used to estimate gas production in chromium;
- exploring the possibilities for preparing thin chromium foils generally not available commercially which are necessary for detailed measurements of gas production by neutrons in chromium; and
- preparing the report for the end of the fiscal year.

Preliminary results for the production of protons with energies above 14 MeV on iron are shown in Fig. 59 as a function of incident neutron energy. Lower energy protons were also detected and we will be able to give total proton production (which is most of the hydrogen production) when the data analysis is completed. The relative cross section for producing protons with energies above 14 MeV by neutrons incident on iron is plotted for four of the observed angles and given as a function of incident neutron energy. The forward-angle production is clearly dominant and appears to grow monotonically with incident neutron energy.
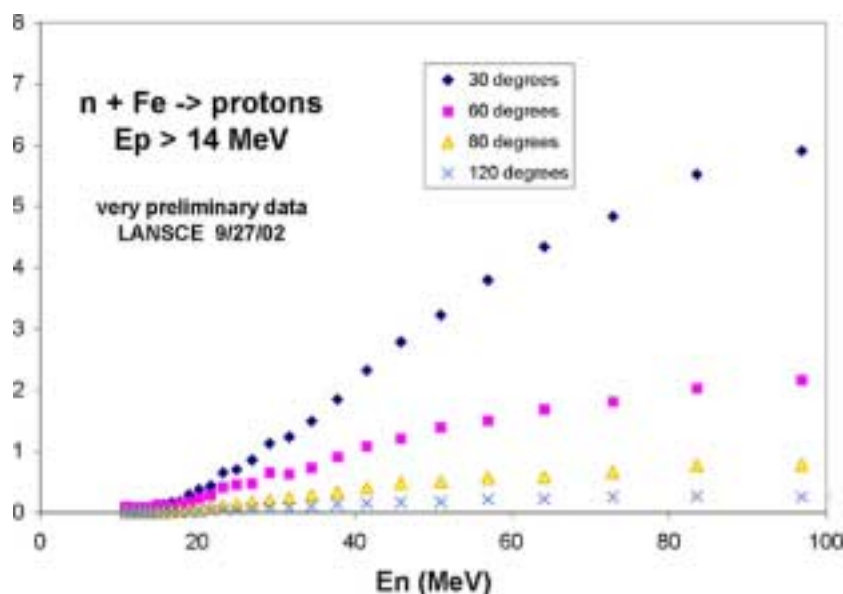
Fig. 59. Preliminary results from recent experiment of proton emission from neutron reactions with iron.

Corrosion Studies

WNR (Blue Room) Experiments

LBE corrosion experiments were performed in the furnace shown in Fig. 60. Similar to our laboratory experiments, this furnace was made from off-the-shelf 1.5" O.D. SS-304L tubing (ultra high vacuum tubing). Heating was supplied by a 700-W band heater (1-inch x 2-inch-diam.) and regulated to within 3°C of the setpoint with an

Omega controller and a type-K thermocouple. To avoid excessive oxidation of the LBE melt, the furnace was continuously flushed with Ar during the course of the experiments. To minimize exposure to radiation as a result of proton activation of the LBE, a lead wall was constructed to separate workers from the furnace. The sample to be tested in the furnace assembly was welded to the end of a piece of SS-304 tubing. At the opposite end the tubing was welded to a kf-type electrical feed, electrically isolating the sample from the SS furnace.
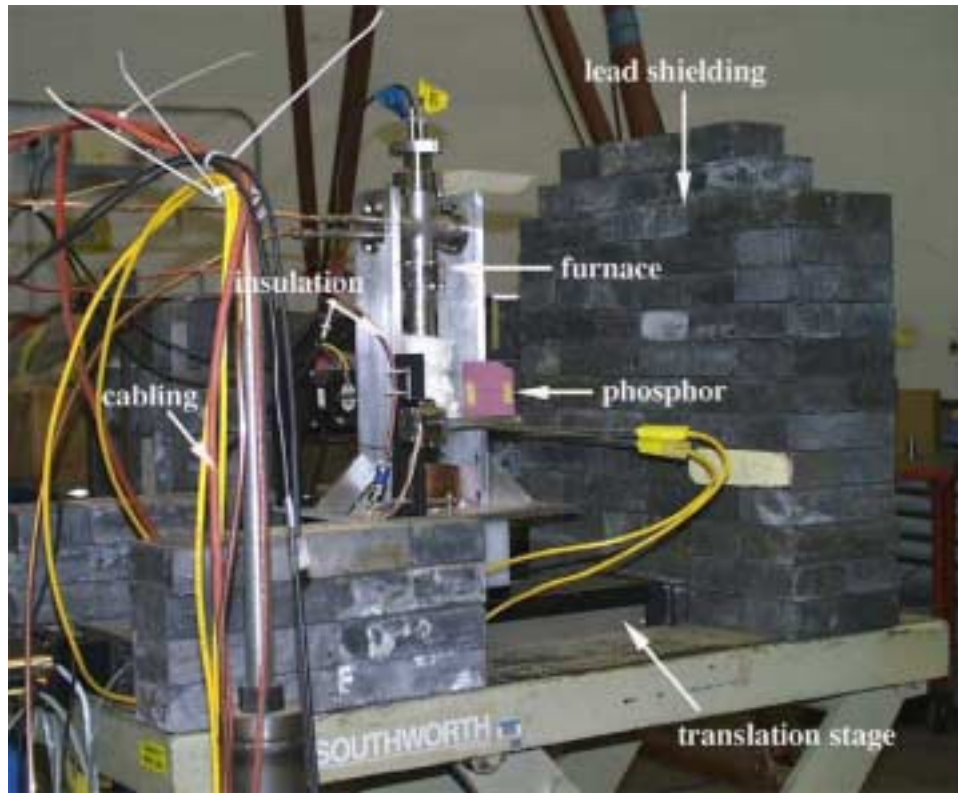
Fig. 60. Photo of the furnace at WNR used for in-beam experiments.

The flux of the incident proton beam had a Gaussian distribution of σ ⁻0.7 cm. The energy of this particle beam was 800 MeV. The pulsed beam was characterized by a gate length (macropulse) of 100 ms, a macropulse repetition rate of 100 Hz, and a fixed peak current of 16 mA (Fig. 61). These duty cycle parameters yielded an average proton beam current of 63 nA. Both HT-9 and SS-316L were tested in the WNR experiments. These samples were prepared by polishing to 4000 p and sequentially cleaning in acetone, ethanol, and DI water. This was followed by oxidation in moist air at 800°C for 48 hrs for HT-9 and 70 hrs. for SS-316L. Following grinding, cleaning, and preoxidation, the samples were subsequently immersed in LBE (no irradiation) for up to 72 hrs.

Impedance data (R_{ox}) for an HT-9 sample as a function of immersion time in the WNR furnace is presented in Fig. 62. Prior to irradiation with protons, R_{ox} increased steadily and appeared to be nearing a plateau value of ~10^4 W·cm^2. After 247 min of immersion, the proton beam was turned. Correspondingly, R_{ox} was observed to decrease. After ~28 minutes of irradiation, the proton beam was turned off. For ~60˚minutes after the proton beam was turned off, R_{ox} continued to decrease at a rate

similar to that observed during irradiation. After this period, both high and low values of R_{ox} were observed indicating the sample impedance was unstable. While we are not prepared to speculate as to why these trends were observed during/after proton irradiation, the behavior was reproducible. Therefore, it appears for these experimental conditions, mixed radiation fields may adversely influence oxide properties. A full analysis of the data is planned for FY03.
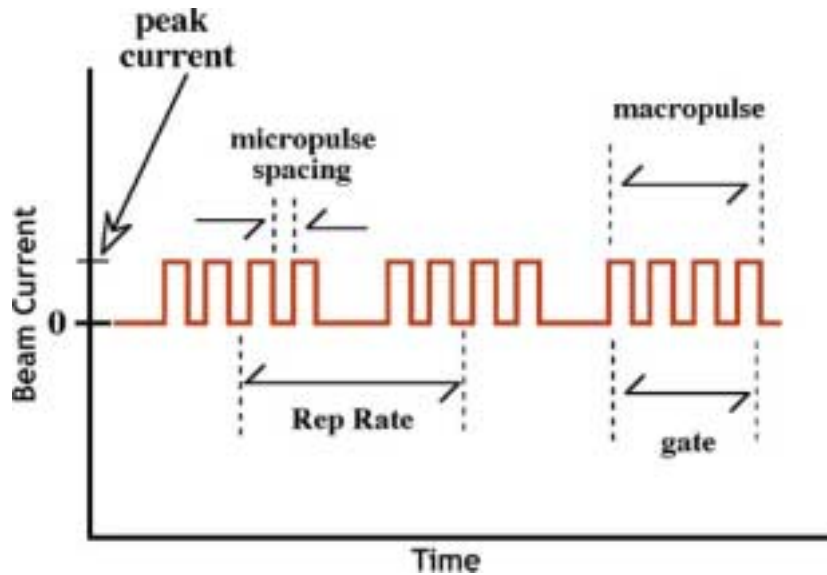
Fig. 61. A diagram depicting the proton beam current time relationships and nomenclature.
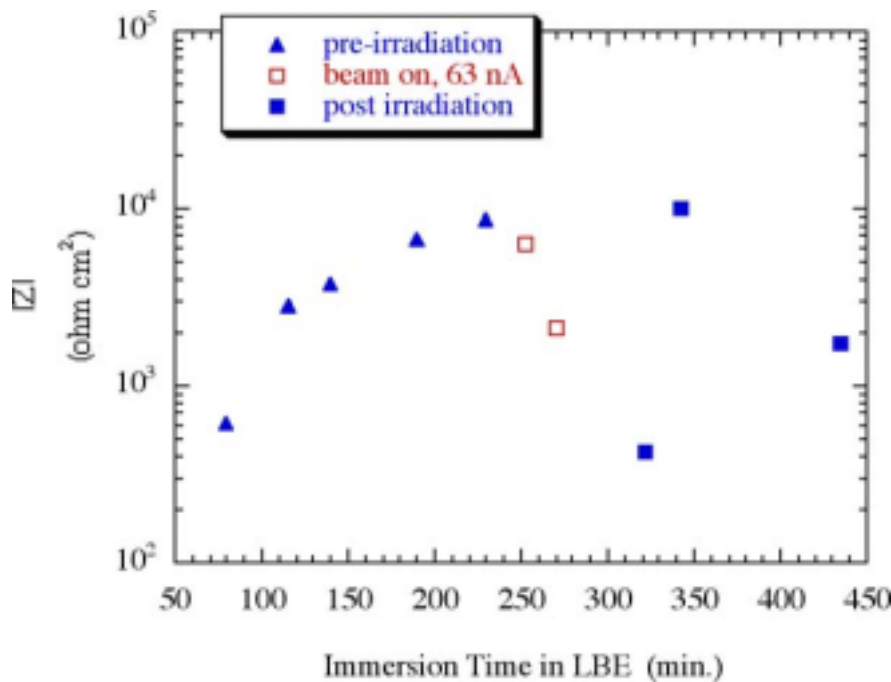
Fig. 62. Oxide impedance as a function of immersion time in LBE. Sample was preoxidized in moist air at 800°C for 48 hrs. prior to immersion. △ represents pre-irradiation data, □ represents data taken with the beam on, and ■ represents post-irradiation data (beam off).

Corrosion Probes - Conceptual Design

Analogous with the science of aqueous corrosion and its real-time measuring techniques, a corrosion probe for a molten lead-bismuth eutectic (LBE) system would measure in real-time the dielectric properties of the protective oxides. From these data we can obtain information such as oxide thickness, which is proportional to corrosion rate. Laboratory studies on candidate materials are in progress to determine the relation between the dielectric properties of the protective oxide layers (which are typically semiconductors) and the metallographic characterization of those oxides in other words, to understand the kinetics of metal corrosion in LBE. It is anticipated that the DELTA Loop will figure prominently in the determination of the relation between the properties of the oxide layers and measurable metal corrosion because long exposures are under controlled oxygen, flow, and temperature. Furthermore, the DELTA Loop could become an ideal laboratory for the kinetics studies provided that corrosion probes can be successfully introduced.

In laboratory studies, metals samples are partially immersed in LBE with air or a gas covering the LBE. An LBE corrosion probe suitable for use in the DELTA Loop must have the following characteristics:

- It must be electrically isolated from the loop piping in order to measure the dielectric properties of the oxide surface.
- The insulator and the metal-to-insulator joint must withstand the pressure, fluid forces, temperature, and the corrosive effects of the LBE.

Although several designs have been proposed in our end-of-year report, we will only discuss the tapered fit in transverse configuration, as we believe it will be the most successful from an operational standpoint (although it may be somewhat complicated to manufacture). Figure 63 shows the tapered fit probe (preferred 3° taper) in a full flow region, constrained by a bolt from escaping into the fluid. The upper insulator seal is among the best presented in the end-of-year report. The aspect ratio of the insulator is adjusted to accept very high axial loads during the pressing of the upper and lower joints. A most important improvement calls for a ceramic with a larger coefficient of thermal expansion, and there is frequent mention of zirconia in the range of $10.5 \times 10^{-6}/°C$, which is excellent for use with HT-9 and adequate for T-91. With a press fit on such a ceramic, differential expansion uses up only 20% of the elastic strain of HT-9 and, less favorably, 38% of the elastic strain of T-91.

A second design condition is that stress relaxation (related to creep) not loosen the joint. For T-91, the creep rate is 1×10^{-7} per hour at 270 Mpa and 755K. For 1000 hours at temperature, the creep strain is 7% of the elastic strain, which is quite acceptable. It might be assumed that only 7% of the elastic stress will relax at zero strain under the same conditions (note also that the stress quoted is 70% of the yield stress in order to obtain the low creep rate). The high temperatures materials are thus able to maintain high compression on the seal and the sealing surfaces during temperature cycles.

Thoughts are that the optimum condition for the metals is the annealed state prior to the final press. Work hardening is minimized in this way, which helps also with minimizing stress relaxation.
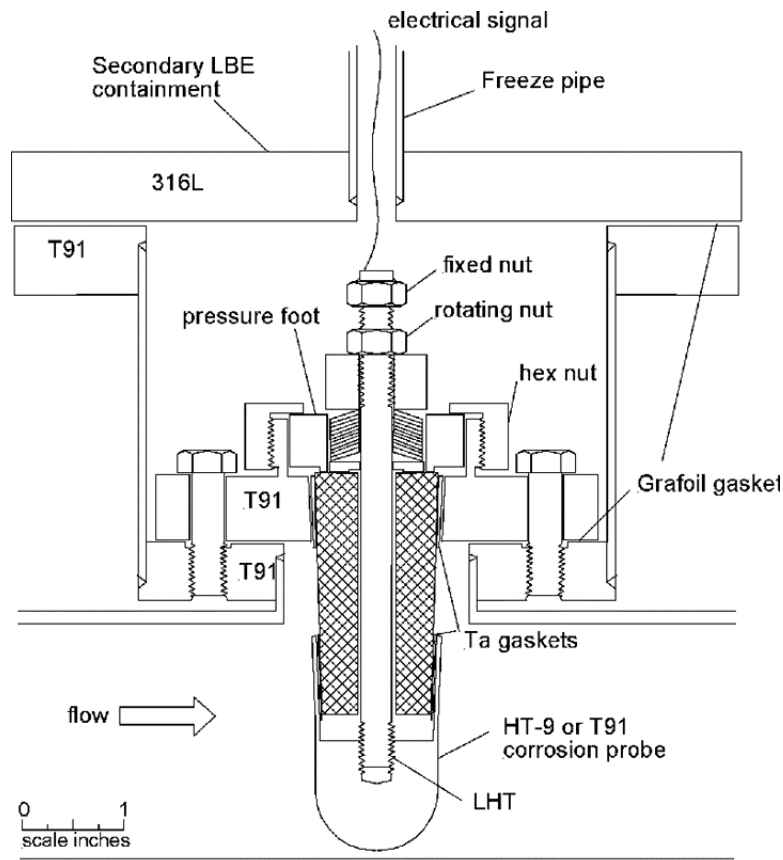
Fig. 63. Cross section through a Ta-sealed press-fit assembly. Uses 3° taper for upper and lower joints.

The retainer nut is not expected to drive the cone into the flange; its purpose is to align the pressing foot, to start the joint with good alignment[12] and to help maintain alignment as pressing proceeds. The corrosion probe seal is pressed next and is likewise not constrained. Hence, the probe wall thickness should be the maximum that still permits the probe to press onto the insulator without breaking it. In this way large pressures can be generated in the tantalum (at 200°C) to extrude it into the cracks and scratches and to form a crevice-free seal at the top edge. Fixturing is possible where the center bolt can be tightened as pressing proceeds. Here again, the bolt is intended to start the pressing with good alignment and to maintain the alignment. And then, particularly for T-91 probes, it ensures that the joint stays tight during thermal cycles.

As expressed earlier, the potential for this design is the highest: It is the most robust of the free standing probes; the joint has the potential to form a helium-leak seal; if necessary, it could work without tantalum (and has); and may even simplify to a version without threaded retainers. The biggest detractor is inability to accommodate SS-316L.

---

[12] The pressure face must be exactly parallel to the thread for there to be any alignment benefit.

3.5   High-Energy Physics

The major objective of high-energy physics activities is to improve and maintain the computer codes used in the analyses of accelerator-driven transmutation systems. As part of the improvement, the nuclear data accuracy will be reevaluated to match the desired objectives.

Scope

MCNPX Code Development

MCNPX code development consists of the following activities:

- Development of the "mix and match capability within MCNPX, which requires production of a version of MCNPX in which evaluated data libraries with different upper-energy limits may be used within the same MCNPX run. This will allow the new LA150n data tables to be used simultaneously with the standard 20-MeV data tables for those isotopes that do not appear in LA150n. (LA150n refers to Los Alamos-generated nuclear data library, extending up to 150 MeV.)

- Incorporation of the Cugnon intranuclear cascade and Schmidt evaporation models into MCNPX, which will be carried out in collaboration with CEA-Saclay under the CEA-AFC collaboration framework. CEA will install the models in MCNPX, with LANL oversight. LANL will perform a quality check of this work and incorporate the code changes into the official release.

- MCNPX maintenance and beta testing, which involves maintaining an approved list of beta testers for the code and fixing bugs as beta testers report them. Regular releases of MCNPX will be transmitted to the Radiation Safety Information Computational Center (RSICC) as significant improvements to the code are made.

Nuclear Data Evaluations

The nuclear data activities include production of new neutron fission and capture ENDF (Evaluated Nuclear Data File) evaluations to 150 MeV for two actinide isotopes of highest priority. This involves the following:

- Calculating fission barrier and nu-bar[13] data to 150 MeV;

- Using the results of GNASH (nuclear reaction code) to generate model-based cross-sections; and

- Using advanced statistical methods to combine discrepant experimental data in the adjustment of the GNASH-generated results to produce new evaluated cross-sections.

As part of these activities, NJOY data processing of new ENDF evaluations and generation of data files of the new ENDF evaluations using the NJOY code will be performed.

---

[13] Average number of neutrons released per fission.

The nuclear data tasks also include improving ^{208}Pb inelastic scattering ENDF cross-section and production of a new version of ENDF ^{208}Pb neutron cross-section that improves the inelastic scattering in the few MeV energy regions.

Highlights

- The first nuclear data 150-MeV evaluations for actinides were created.

- MCNPX version 2.4.0 was formally released to the Radiation Safety Information Computational Center (RSICC).

MCNPX Code Development

MCNPX New Physics and Capabilities

MCNPX version 2.4.0 was formally released to the Radiation Safety Information Computational Center (RSICC), and several useful capabilities in the next version of the code were added. We also posted the first release of a code version with the 'Mix and Match' capability. This version fully updates MCNPX to MCNP4C, and also rewrites the entire code in Fortran-90. An automated build system was released with the code, which uses the 'config' utility to query the hardware directly as to what operating system, compiler, and run-time libraries are available. The build system eliminates the need to issue separate versions of the code for different platforms. An updated MCNPX 2.4.0 User's Manual was also prepared, and the notice of the 2.4.0 code release is was posted in the October 2002 RSICC newsletter. User support to the AAA collaborators continued, through direct interaction, beta test-team activities, and formal classes.

The 'Mix and Match' capability essentially has two parts: (1) the ability to designate different libraries for the various particles (isotope mixing), and (2) the ability to use different energy limits between nuclear data table and physics models (energy matching). The isotope-mixing problem was solved, and the user can now choose any library desired for neutron, proton and photonuclear interactions. For example, the user can designate natural carbon for neutrons, and carbon-12 for protons. MCNPX 2.5.a also has the latest CEM2k implementation, which includes a complete energy match solution for the photonuclear component. Thus, different transition energy limits may be specified for each isotope chosen for photonuclear reactions in the same problem. A photonuclear physics model is also included for all isotopes, so the user now has access to photonuclear physics at all energies for all isotopes. Previously, we were limited to the 12 available nuclear data libraries. Based on the photonuclear implementation of energy matching, the same capability was added for neutrons in version 2.5.a. Proton energy matching will be available in November, thus completing the solution to the longstanding 'Mix and Match' problem.

The MCNPX cross-section plotter was revised in order to plot proton and photonuclear cross sections. In addition, the FM card was updated so that Proton and PN cross-sections can be folded into track-length tallies. The source capability in the code was upgraded so that positrons can now be used as source particles. An improved version of the CEM2k code was also added, which also includes physics models for photonuclear interactions, and also greatly improves our modeling of residual nuclei.

Several corrections were made to the code including:

- Number of collisions not incremented for terminal collisions
- Particle mean free path not incremented in model energy region.
- Multigroup adjoint energies not printed correctly.
- Corrected time-dependent weight-window generator bug
- Integrated several photonuclear corrections in the physics region.

The computer test farm was enhanced by the addition of 6 donated used HP machines, which will allow us to test multiprocessing on a regular basis. Nightly regression testing on the code is performed to make sure the day's code development efforts do not affect the code when run on different platforms. We also attempted adaptation our TCOV test problem coverage utility to the new F90 code. This utility tells us which specific lines of the code are exercised when the test problems are run. Although the TCOV utility runs well for F77 code, it has trouble with the F90, and we will be looking at alternative utilities. We have discussed our test farm, TCOV and automated build system systems with code developers at the NRC, and they are most interested in applying these to other codes, since they have no comparable capability.

We taught an MCNPX class at the Santa Fe Community College in July with 15 registered students. Another class was taught in San Diego in September with 12 students. A class co-sponsored with SCK-CEN in Belgium was announced for the week of November 18th. This class will be co-sponsored with NEA, RSICC and KTH in Sweden. As of October 1st, there are 911 registered MCNPX beta testers at 201 institutions internationally. The code is now making important contributions in areas outside of our traditional AAA/AFC applications. A major paper was published in the July 5th issue of Science Magazine, which used the code to analyze backscatter spectra from cosmic ray impacts on the Martian surface. The result was the discovery of water on Mars.

Nuclear Data

LA150 Actinide Cross Section Evaluations

We have almost completed the ENDF formatting of our new ^{239}Pu and ^{238}U evaluations. This required merging the prior ENDF/B-VI file up to 20 MeV incident energy with new sections/subsections obtained up to 150 MeV. Some codes developed for the creation of the LA150 library were used for our present purpose. However, the previous evaluations concerned only non-fissile nuclei, and the associated codes were therefore not intended to be used for fissile ones. As part of our current work, we have developed various additional tools (mostly in the Perl programming language) to deal with this particular situation and others. In doing this ENDF formatting, we went through various steps regarding the physics of the final evaluation. First of all, we modified the calculated (n,tot) cross section to better agree with available accurate experimental total cross-section data (from Lisowski at LANSCE). We then had to renormalize the elastic subsection (MF3 MT2 in ENDF parlance) in the ENDF file to reflect the change in the total cross section (MF3 MT1). Because of the presence of fission, no recoils were included (since the fission fragments dominate recoil energy deposition). We performed a regridding of the entire energy grid above 20˚MeV and up to 150 MeV. The elastic scattering angular

distribution (MF=4,MT=2) was taken directly from our ECIS optical model calculations. The energy-angle distributions for the reaction products were taken from the GNASH output. Finally, the neutrons emitted from the fission fragments were calculated with the CEM/Furihata code. We have tested successfully our final ENDF formatted file using different standard checking codes.

Additional checking and validation work for these new actinide LA150 high-energy evaluations will include: (1) Performance in MCNPX; (2) Comparisons with some recent Russian cross-section work that supports ADS applications in Europe, Japan, and Russia; and (3) Comparison with thin- and thick-target measurements where available.

The aforementioned evaluations for neutrons on ^{239}Pu and ^{238}U up to 150 MeV were based on GNASH nuclear model calculations as well as CEM calculations to obtain the fission neutron spectra information. The ^{238}U nucleus is valuable to study because of the larger amount of experimental data available, compared to other actinides. The LANL total cross-section data (Abfalterer, Dietrich et all, funded by APT, and Lisowski), together with absorption and elastic scattering data, enabled us to develop a new relativistic high-energy optical potential for ^{238}U and ^{239}Pu. This was important for allowing us to model and evaluate (n,fission) as well as (n,xn) neutron production cross sections.

3.6   Reactor Physics

The reactor physics task involves the codes and methods used to assess the transmutation process. The objective also includes defining and designing long-term experiments needed to advance the TRL in this area.

Scope

Experiment and Safety Analysis

This task consists of analyzing physics experiments and developing a safety analysis strategy applicable to accelerator-driven system (ADS) design. Part of the physics experimental work consists of providing high-quality experimental data; and for this purpose, ANL personnel will participate in collaboration with CEA to perform the critical and subcritical experiments of the MUSE4 configuration. To validate data and methods for the neutronic design of an ADS, an analysis of the experimental results obtained in the MUSE4 program will be performed using both deterministic and stochastic codes with different data files (e.g., JEF2 and ENDF/B-VI). Additionally, the irradiation experiments PROFIL-1 and -2 will be analyzed, in which samples of actinide isotopes were irradiated in the French Phenix reactor. The objectives for safety analysis are to develop the conceptual safety design basis and criteria for ADS reactors, to develop and verify the computational safety analysis methods and computer codes necessary for safety assessment of ADS reactors, and to perform initial scoping analyses of design basis and bounding accident sequences for an ADS reactor conceptual design.

Physics Needs and Methods Development

Physics needs will be assessed by performing uncertainty evaluations and developing new capabilities for computational tools used for the neutronic analysis of ADS. Work will be performed to define physics needs and needs related to cross-section data uncertainties. In a first phase, sensitivity and uncertainty analyses will be performed for minor-actinide-dominated fuel compositions. A significant effort will be devoted to extend the present field of applicability of deterministic tools to energies >20 MeV, taking into account phenomena (e.g., gas productions) that can be affected by uncertainties in this energy range. Code and methods upgrades are needed to improve our capability to correctly calculate coupled systems with deterministic tools. The iteration strategies for equilibrium concentrations in the REBUS-3 burnup code will be modified to eliminate instabilities observed for subcritical and deep burnup conditions. Implementation of multivariate cross-section fitting capability will also be performed. Coupling with high-energy (spallation) source calculation has to be extended to the 3-D geometries (Cartesian and hexagonal) and needs to be implemented in a more flexible manner. Considerations will also be given to the possibility of developing an entirely deterministic coupled calculation (i.e., spallation and high-energy charged-particle transport treated deterministically).

Physics Experiment Planning

To simulate the physics and dynamic behavior of accelerator-driven systems and to support their design, an action will be taken to investigate the possibility of using the Transient Reactor Test Facility (TREAT) and the Zero Power Physics Reactor (ZPPR) facilities located at ANL-W. The information coming from the potential experiments performed at these facilities will play a critical role in validating data, codes, and methods needed for reducing uncertainties and margins for the design of an ADS. Experiments will be planned to complement existing and future experimental programs (e.g., MUSE, TRIGA) carried out by foreign partners. The scope is to provide an experimental plan, to perform sensitivity analysis for justification of the program, and to define the objectives and feasibility of experiments.

Highlights

- A report entitled Evaluation of Safety Design Criteria for Application to Accelerator-Driven, Subcritical, Liquid Metal Cooled Nuclear Reactors was completed.

MUSE Analysis

Twenty million neutron histories have been accumulated for the COSMO critical configuration, for the MUSE-4 1112-cell critical configuration, and for the MUSE-4 976 cells subcritical configuration. ENDF/B-VI data were used. K_{eff} results are shown in Table 14. Prompt neutron lifetime and beta-effective were calculated.

For the D-T pulse neutron simulation, total neutron histories of 500,000 have been accumulated. Flux monitors were used for tallies at the specified locations and channels to obtain various reaction rates and neutron spectra (see Fig. 64). More neutron histories are needed to improve statistics and better understanding of the time tally will be pursued.

**Table 14. MCNP-4C Results for K-effective Values
Based on 20 Million Neutron Histories**

Configuration	COSMO	MUSE-1112	MUSE-976
k-effective	1.00651	1.00613	0.97408
1-sigma	0.00039	0.00028	0.00031
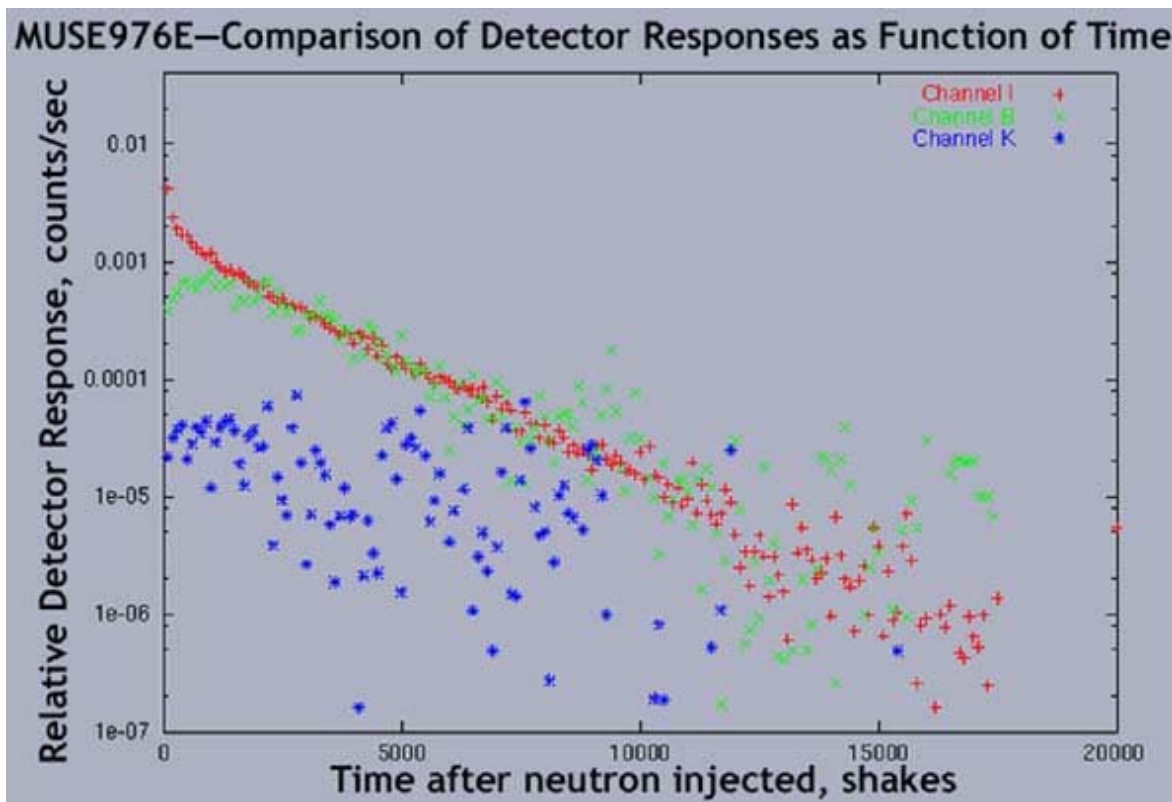
Fig. 64. Relative detector response as function of time (1Shake = 10^{-8} sec) for 3 detectors at different locations in a source-driven MUSE-4 976-cell subcritical configuration. Channel I is near the source at core center, Channel B is near the outer edge of the radial reflector, and Channel K is on the outer edge of the radial shield.

In addition, some deterministic calculations also were performed. The ^{235}U fission rate for several detectors as a function of the time for the deuteron-tritium source pulse was calculated. The deuteron beam was assumed to have a time structure of 1˚μs pulses repeated at 1 kHz. The time step and range were 1˚μs and 500˚μs, respectively. Calculations were performed for pulse #1 and for the pulse after equilibrium ($n˚ \rightarrow ˚\infty$).

In Fig. 65 we show time dependent rates using the direct method for the solution of the kinetic neutronic equations. No significant differences were observed when the quasi-static method was used.
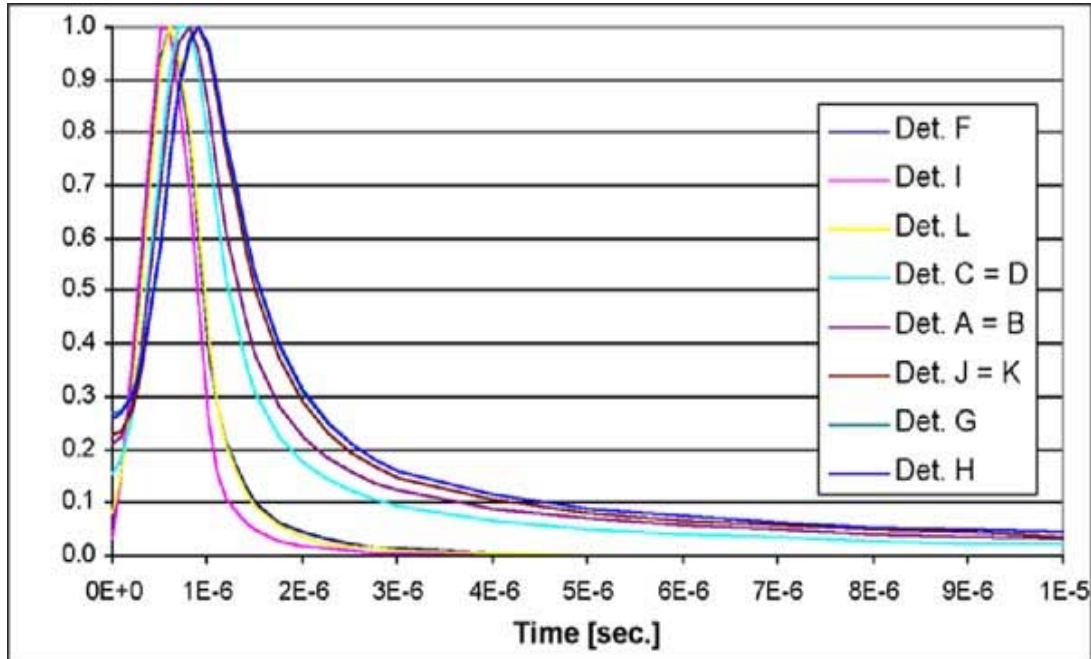
Fig. 65. Direct method time dependent rates.

Significant spatial effects were observed. The more distance the detectors were from the external source (from detectors A,B,C and D in the reflector to the detectors H,J,K and G in the shielding), the more extended in time was the answer. Also, the maximum value was reached at a different time.

Work also continued to understand the discrepancy of the results obtained by MC^2-2 when compared with those obtained by ECCO or Monte Carlo codes. First, we tried to correct the long-standing deficiency in MC^2-2 ultra-fine-group (ufg) scattering cross sections for Fe, Ni, Cr, Mn, and Pb, due to their resonance-like structures above the resolved resonance cutoff energies. The correction was necessary to account for a self-shielding effect. Corrections were negligible (less than 100 pcm.) for JEF2.2 and ENDF/B-VI data and ~200 pcm. for ENDF/B-V.   The discrepancy was finally resolved by using the total cross section weighted by the current. This effect is very important for structural material in a reflector medium. When this correction was made, results of MC^2-2 agreed with those of ECCO and Monte Carlo codes.

PROFIL Experiment

The analysis of the PROFIL-1 experiment using JEF2.2, ENDF/B.V and ENDF/B.VI data was completed. A sensitivity and uncertainty study on the impact of cross-section data and decay constants on the calculated isotope densities was also performed. Results of the three cross-section libraries and associated uncertainties are shown in Table 15. The results obtained indicate the relevance of the PROFIL experiments in order to reduce current uncertainties via, e.g., a statistical adjustment procedure.

Table 15. Uncertainties Associated to the C/E Values Relative to the PROFIL-1 Experiment.

Data Type	C/E			Total Uncertainty[14]		
	JEF2.2	ENDF/B-V	ENDF/B-VI	NEC	PEC	TEC
σ_{capt} U-235	0.95–1.7 %[15]	0.99–1.7 %	0.95–1.7 %	3.4 %	6.5 %	7.6 %
σ_{capt} U-238	0.98–2.3 %	1.02–2.3 %	0.98–2.3 %	1.7 %	2.2 %	3.1 %
σ_{capt} Pu-238	0.98–4.0 %	1.30–4.0 %	1.69–4.0 %	23.6 %	32.3 %	48.0 %
σ_{capt} Pu-239	0.99–3.0 %	0.96–3.0 %	0.94–3.0 %	5.8 %	7.2 %	10.6 %
σ_{capt} Pu-240	1.14–2.2 %	1.07–2.2 %	0.99–2.2 %	12.3 %	16.4 %	23.7 %
σ_{capt} Pu-241	1.24–4.1 %	1.03–4.1 %	0.88–4.1 %	14.2 %	21.1 %	27.4 %
σ_{capt} Pu-242	1.19–3.5 %	1.11–3.5 %	1.06–3.5 %	13.3 %	17.8 %	24.9 %
σ_{capt} Am-241	1.02–1.7 %	0.87–1.7 %	0.83–1.7 %	10.6 %	13.8 %	20.6 %

Safety Analysis

A report entitled Evaluation of Safety Design Criteria for Application to Accelerator-Driven, Subcritical, Liquid-Metal-Cooled Nuclear Reactors was written and submitted to AAA Program Management, meeting a milestone. The report provides a survey of safety design criteria applicable to accelerator-driven, subcritical, liquid-metal-cooled nuclear reactors. Criteria selected for consideration include 1) generalized design criteria specified by Title 10, Part 50, Appendix A of the Code of Federal Regulations for application to light water nuclear power reactors, 2) American National Standard general safety design criteria for a liquid metal reactor nuclear power plant, and 3) U.S. Department of Energy nuclear reactor safety design criteria. Considerations of design criteria by U.S. Nuclear Regulatory Commission in licensing and safety evaluation of proposed liquid-metal-cooled nuclear power reactor designs were reviewed. Applicability of the selected set of design criteria to accelerator-driven, subcritical plant design features and operational characteristics were discussed. Recommendations were made for modifications to existing safety design criteria for relevance to accelerator-driven, subcritical system designs. A set of point-kinetics analyses was also performed for inclusion in AAA Program documentation. The 840-MW accelerator-driven reactor design was subjected to unprotected reactivity-insertion accident assumptions, starting from initial reactivities of -3.81$, -1.74$, and -0.72$.   For each initial condition, reactivity insertions of 0.5$ and 0.1$ over 2 seconds were analyzed, with and without reactivity feedbacks.

Uncertainty Assessment

The investigation of the ADS with minor-actinide-dominated fuel continued this quarter. A depletion study was performed.   The calculations were first devoted to the determination of the K_{eff}, and K_s, and fuel composition change during the cycle. Then a perturbation study was performed to find the main contribution, by isotope and cross section type, to the reactivity loss during the cycle. Then, an uncertainty

---

[14] Total Uncertainty Associated to the basic data knowledge (NEC = No Energy Correlation, PEC = Partial Energy Correlation, TEC = Total Energy Correlation).

[15] Uncertainty associated to the experimental measurement.

analysis was performed on transmutation rates and reactivity loss during the cycle. Finally; a target accuracy definition study was completed. The following is shown in Table 16:

- the initial uncertainties on the chosen integral parameters;
- the part of uncertainty accounted for by the selected cross-sections;
- the uncertainties resulting from the new required uncertainties on data; and
- the imposed target accuracies on the select integral parameters, as given above.

The results are very encouraging, since all the integral parameters uncertainties (except for the power peaking) can be brought within the target accuracy. The case of the power peaking (i.e. resulting uncertainty of ~–8% vs the –5% target value) does not seem to be of major concern. As far as the required cross-section uncertainties, all the values are very reasonable and do not require unrealistic uncertainty reductions. In particular, the required level of uncertainty for the capture, fission and inelastic cross-sections of the minor actinides (MA), is comparable to the level of the uncertainties that have been achieved for major actinides in the past.

Table 16. Selected Integral Parameters: Uncertainty due to all the Original Data Uncertainties ($\breve{I}_{initial}$); Uncertainty due to Selected Cross Sections; Target Accuracies; Resulting Uncertainty

	K_{eff}	_*	Power Peak	Max dpa	Max He Production	Max H Production	Max He-Prod/dpa
$\breve{I}_{initial}$	–2.77	–2.74	–20.50	–29.90	–43.60	–28.50	–45.50
$\_I_{selected}$	–2.63	–2.63	–19.45	–28.44	–43.43	–27.51	–45.18
$\breve{I}_{required}$	–1%	–2%	–5%	–15%	–15%	–15%	–15%
$\_I_{resulting}$	–1.1%	–1.0%	–8.2%	–13.0%	–14.8%	–13.7%	–15.3%

Method Development

The work to develop a general source-coupling interface code between high-energy Monte Carlo and low-energy deterministic calculations was completed. A method to generate higher order angular and/or spatial source moments for deterministic neutronics calculations from an MCNPX log file was developed and implemented into a computer code named FIXSOR. Using the low-energy neutron sources produced by the high-energy MCNPX calculation, this code creates the FIXSRC CCCC interface file for general 3-D geometries in a flexible manner to be consistent with the deterministic codes such as DIF3D, REBUS-3, VARIANT, and TWODANT. For VARIANT and TWODANT, it generates the higher order angular and/or spatial source moments.

The work to estimate the feasibility of developing a full deterministic coupled-calculation system for accelerator-driven systems in conjunction with the variational nodal transport code VARIANT was completed. The important particles to be considered for ADS neutronics analyses were first identified and the high-energy cross sections of these particles investigated using the MCNPX code and its post-

processing code XSEX3. Based on these results, the feasibility of generating multi-group cross-section libraries with MCNPX was evaluated.

TREAT-Coupling Experiments

We completed a study of the validity of the pulsed-source method with a point-kinetics model for TREAT incorporating the appropriate feedback effects of the reactor, and the composition of the experimental program for TREACS experiments. This included consideration of how representative the experiments are, the reference core configuration, and the types of experiments to be performed. A transient analysis of TREACS source-excursion and control-rod experiments in TREAT was completed and documented. Both spatial and point kinetics analyses, with and without fuel temperature feedback reactivity, were computed. The results indicate that point kinetics, with verification by spatial kinetics, is an adequate experiment design-analysis method, if the power, temperature, and reactivity feedbacks are calculated with a spatially-distributed model. A point model in which a single, average core temperature is used to calculate reactivity feedback for point kinetics, was found to be significantly inaccurate for some transients.

3.7   International Support

International support and collaboration is a strong part of the research conducted under transmutation science. A major collaborator is CEA in France. However, this collaboration is defined at the basic research level, and there are no tasks specifically conducted or funded in support of CEA s efforts. All the tasks discussed in Sections 3.1—3.6 directly or indirectly benefit this collaboration.

Some tasks are specifically funded in support of the MEGAPIE Project at Paul Scherrer Institute (PSI) in Switzerland, as well as the import of the Russian IPPE (Institute of Physics and Power Engineering) LBE target. Those tasks are discussed below.

Scope

MEGAPIE is a 1-MW LBE spallation target experiment being set up at PSI in Switzerland. DOE signed a partnership agreement on the MEGAPIE Project that includes having a US engineer participate in the MEGAPIE design and analyses on change-of-station at PSI. The objective is to provide technical support to the MEGAPIE Project and to transfer knowledge gained and related research on the project to US laboratories to advance the TRL for the US LBE target development.

The IPPE LBE target was designed and built in Russia with the initial objective of irradiating it at LANSCE (LANL). However, because of the unavailability of the irradiation facility, the target will be used as another LBE loop for basic research. Currently, the objective is to bring the target to the US, to deliver it to UNLV, and to set it up as another research loop.

Highlights

- The International Science and Technology Centre (ISTC) LBE target fabricated by the Institute of Physics and Power Engineering (IPPE) in Obninks, Russia, was delivered to the University of Nevada at Las Vegas (UNLV).

- AFC team member E. Pitcher completed his assignment at the Paul Scherrer Institute (PSI) in Switzerland to support the MEGAPIE neutronics analyses. AFC team member K. Woloshun returned to PSI to continue the engineering support task for MEGAPIE in FY03.

IPPE Target

The ISTC LBE target built in IPPE (Russia) was delivered to UNLV in June 2002 (see Fig. 66). LANL engineers participated in the initial inspection of the target upon receipt at UNLV. A meeting of the International Advisory group was held at UNLV to provide an initial set of recommendations to UNLV for target testing. Based on these recommendations, UNLV will develop the final test plan and start testing the target to support the international effort in LBE technology development. With participation of the Russian engineers, the target-cover gas pressure was tested and it was determined that there are no leaks in the target.

Fig. 66. ISTC target being unloaded at UNLV.

MEGAPIE Support

MEGAPIE Status

The MEGAPIE Project has made significant progress toward the goal of irradiation in 2005. A brief summary of major events and milestones for MEGAPIE in FY02 (fourth quarter) is given below.

The target system design was essentially completed. Although there remains a list of details that must be resolved, drawing packages and documentation are now being finalized. A bid solicitation was issued and a vendor tentatively selected. The vendor requires a complete specification of the design by December, 2002 to insure delivery by the end of CY03.

The ancillary system designs are complete. Some documents are still in review. Drawing packages, instrumentation specifications, procurement specifications, and operating procedures, are essentially complete.

The prototype pump and flow meter were fabricated and tested at IPUL. These tests showed pump performance slightly better than required. Flow meters were operating successfully, but improvements and more testing, with improved instrumentation, are required. Cavitation is no longer an issue since no cavitation has been observed even with overpressures as low as 3 mBar.

Initial LISOR tests began, but have been problematic. The first test was stopped because of an amplifier failure, and the second test failed, most likely due to cyclic fatigue, caused by a highly focused beam (2.5 mA/cm2) that wobbled at too low a frequency (1x14 Hz over a rectangular beam footprint). Material tests will resume in October with new beam parameters. A potentially significant observation is that while the bulk of the T-91 sample remained unwetted by LBE after irradiation, the portion of the sample in the beam-spot was wetted.

Efforts are ongoing to minimize the complexity of the ancillary systems. Most notably, the fill-and-drain system may be replaced with a fill-only system. The LBE would be allowed to freeze inside the target to be drained later in a hot cell. Detailed studies of the LBE expansion after freezing, due to recrystalization of the solid, are being conducted to see if the target can be frozen without breaking the target window. Another possible simplification of ancillary systems is the minimization of the cover gas system. The current system, which includes a decay tank and a sampling capability, could be replaced with a sealed system if it can be shown that the gasses generated during irradiation can be contained at low enough pressure in the available volume.

DOE Contribution

MCNPX Model of the MEGAPIE Target

A new MCNPX model of the MEGAPIE target has been developed based on the latest design drawings. The model extends out to the light-water jacket that surrounds the heavy-water moderator tank. Figure 67 shows a vertical cut through this geometry. The model has high fidelity in faithfully representing the actual geometry of the target and safety hull in the vicinity of proton beam interaction. This includes the bypass flow tube, and target catcher that is designed to protect the safety hull should the Pb-Bi target container fail for some reason.

The proton beam profile used in the MCNPX calculations is based on simulations carried out by Urs Rohrer. The x- and y-profiles are assumed to be separable, that is, $P(x,y) = p(x) q(y)$, where $p(x)$ and $q(y)$ are the y- and x-integrated profiles given in the spot20.dat output in Rohrer s note. Figure 68 shows his calculated x-y profile and the profile used in the MCNPX calculations. Rohrer s calculations predict a peak current density at the center of the beam of 29.6 mA/cm^2 per mA of beam current, whereas the profile used in the MCNPX calculations has a peak current density of 30.3 mA/cm^2 per mA. The proton energy is taken to be 575 MeV.
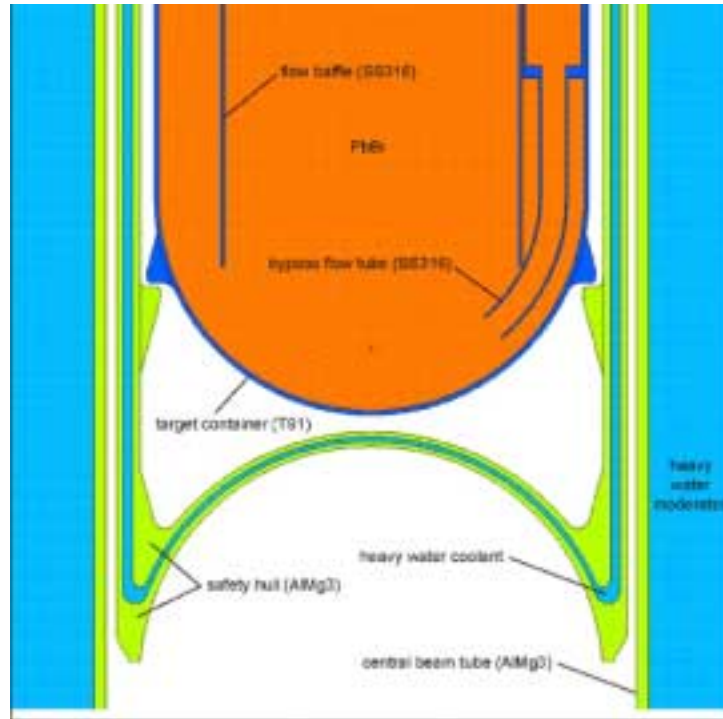
Fig. 67. Vertical slice through the MCNPX model of the MEGAPIE target.

(a)

(b)
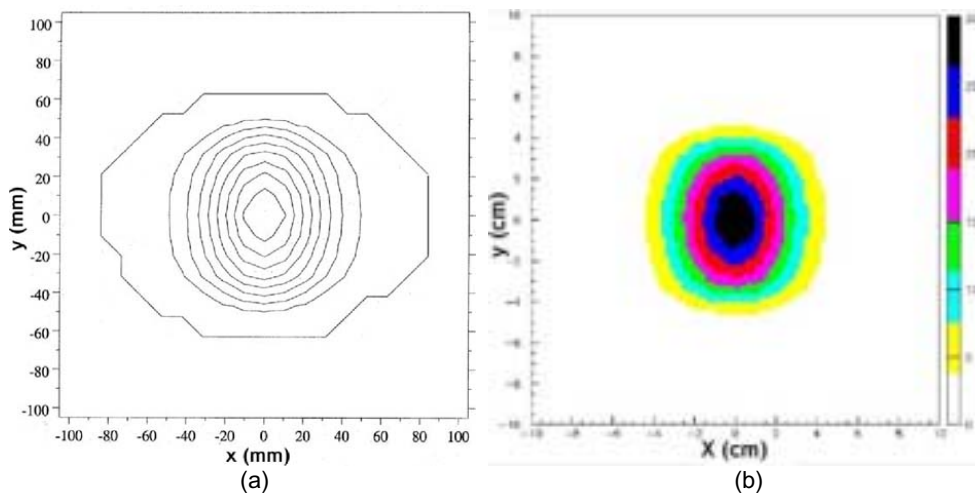
Fig. 68. MEGAPIE beam spot contours: (a) Rohrer s prediction contour lines are 10% integrals;
(b) MCNPX source units on the color bar are mA/cm^2 .

MEGAPIE Fluxes

Proton and neutron fluxes in the MEGAPIE target have been calculated. The proton flux is shown in Fig. 69. The 575-MeV protons range out after traversing about 27 cm of Pb-Bi. Peak proton flux on the central beam tube (zentralrohr) is ~3x10^{11} p/cm^2/s. Neutron flux plots are shown in Fig. 70. The neutron flux is highest in the center of Pb-Bi target, at a depth of ~6 cm from the front face. Peak neutron flux at this point is about 1.1x10^{15} n/cm^2/s. The thermal (<0.625 eV) flux peaks in the heavy water at a

distance of about 21 cm from the proton beam centerline, with a peak flux near 1.5×10^{14} n/cm^2/s.
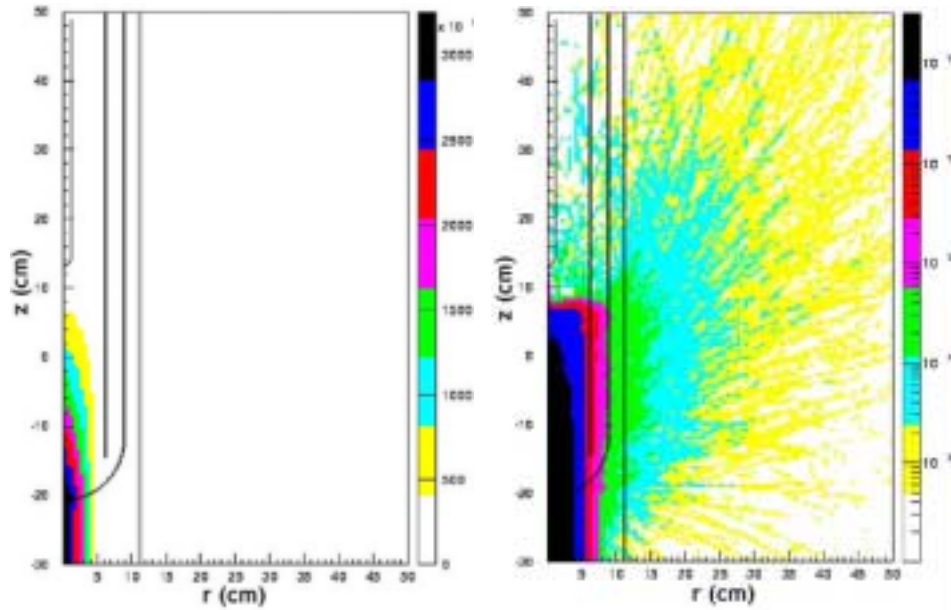
Fig. 69. Proton flux at 1.74 mA beam current: (a) linear scale; (b) logarithmic scale.
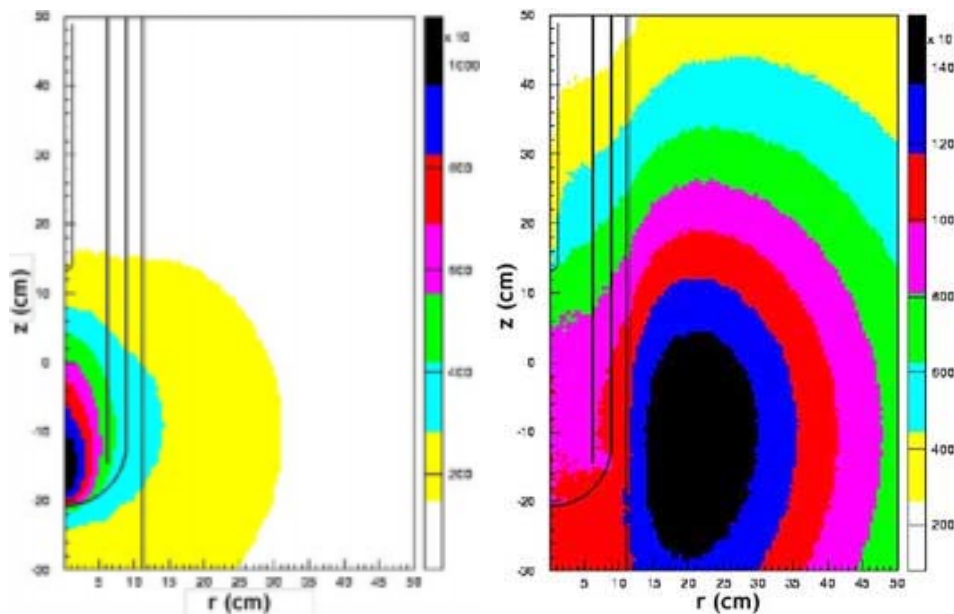
Fig. 70. Neutron fluxes at 1.74 mA beam current: (a) total flux; (b) thermal flux.

Pb-Bi Radionuclide Inventory

The build-up of radionuclides in the Pb-Bi during the anticipated operation of the MEGAPIE target was calculated using the MCNPX and CINDER 90 codes. Spallation-product generation rates and low-energy (<25 MeV) neutron fluxes were calculated by MCNPX, and these data passed to CINDER 90, which was used to

calculate time-dependent nuclide inventories during and after a 200-day irradiation at 1.74 mA beam current (8.35 A•h). The activities of some notable radioisotopes, after 6 A•h of operation at 1.74 mA beam current, are listed in Table 17. The total radioactivity of the Pb-Bi during 200 days of irradiation at 1.74 mA followed by 30 days of cooldown is shown in Fig. 71. Six A•h of operation produces 5.3 liters of hydrogen and 1.1 liters of helium at standard temperature and pressure (293 K and 0.1013 MPa). After 200 days of continuous operation at 1.74 mA (that is, 8.35 A•h of charge), the volumetric decay heat ($\beta+\gamma$) in the Pb-Bi is calculated to be 0.060 W/cm^3, which gives a total decay power of 4.9 kW within the 82-liter volume of Pb-Bi in the loop.

Table 17. Activities of Some Notable Isomers in the Pb-Bi after 6 AÆh of Operation.

Isomer	Half-life (s)	Activity (Ci)
H-3	3.89×10^8	310
Ar-41	6.58×10^3	0.0088
Kr-79	1.26×10^5	69
Kr-83m	6.59×10^3	240
Kr-85	3.38×10^8	2.0
Kr-85m	1.61×10^4	160
Kr-87	4.58×10^3	140
Xe-127	3.15×10^6	69
Xe-129m	7.68×10^5	8.0
Xe-131m	1.03×10^6	4.5
Po-210	1.20×10^7	5060
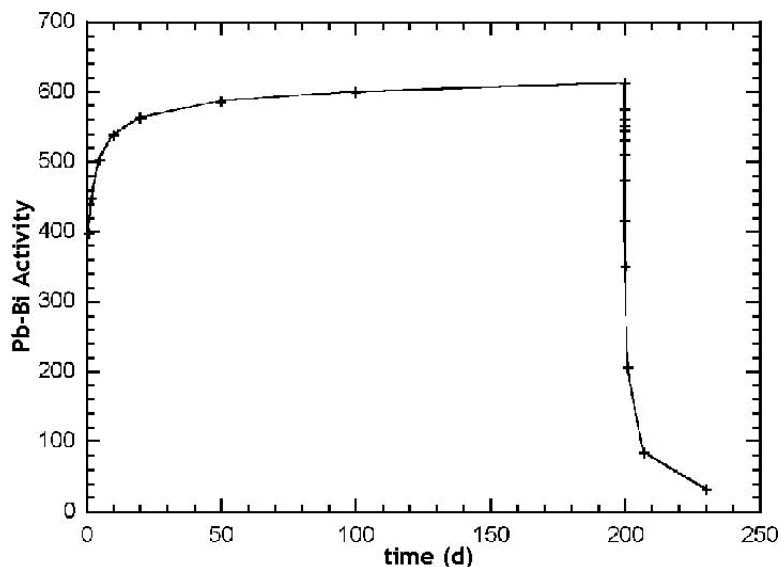
Fig. 71. Pb-Bi radioactivity during and after a 200-day irradiation at 1.74 mA.

Radiation Dose to the Diphyl Oil in the MEGAPIE Primary Heat Exchanger

We performed a neutronics analysis of the dose rate to which the THT oil (the working fluid in the secondary loop of the MEGAPIE Pb-Bi cooling system) is subjected during operation. Three sources of radiation exposure were evaluated:

- activated heavy water that cools the safety hull,
- activated Pb-Bi,
- prompt radiation.

Of these sources, the activated Pb-Bi dominates the dose received by the oil. The Pb-Bi activity was divided into two terms: a short-lived component, and a long-lived component. The short-lived component represents short-lived radionuclides that are not diluted in the Pb-Bi volume because they decay away before mixing. The activity of the short-lived component varies strongly with position in the loop (e.g., highest at the bottom of the target, lowest in the downcomer region of the target). The long-lived component does not vary significantly with position in the loop.

The depletion code CINDER 90 provides a decay-gamma source term in 25 energy groups at user-specified times during and after irradiation. The source term of the short-lived component is calculated by subtracting the Pb-Bi activity following a long decay period (e.g., 300 s) from the activity after a short (e.g., 10 s) decay period. The short period represents the transit time from the point of Pb-Bi activation (bottom of the target) to the primary heat exchanger, while the long decay period represents the time needed to assure the residual radioactivity is evenly distributed throughout the 82-liter Pb-Bi volume. The two decay gamma source terms (short and long) so derived were then transported in a MCNPX model of the primary heat exchanger, shown in Fig. 72. Various permutations of short and long decay periods were used to gauge the sensitivity of the absorbed dose on these parameters. For short decay periods ranging from 3—30 s and long decay periods ranging from 100—1000 s, the calculated absorbed dose to the oil in the heat exchanger varied by —6%/+11% from the mean value of 4.4 W, assuming a beam current of 1.74 mA. When averaged over the 77-kg inventory of oil in the secondary loop, this amounts to an absorbed dose of 0.20 WÆh/g after 6 AÆh of operation.

Oil-LBE Interaction Experiments

A set of experiments was conducted to study an oil-LBE interaction that would result in the event of a heat exchanger leak. Specifically of interest are the gas generation rates and the pressures that will result, possibly leading to more serious mechanical failures. Oil at nominally 150…C and at a pressure greater than the LBE pressure in the target, would leak into the nominally 300…C, with a 350…C peak temperature.

A control experiment was conducted first, heating only the oil up to 350…C and holding for several hours with a slight Ar overpressure. Cover-gas pressure was measured as a function on time and temperature. The cover gas pressure was consistent with the sum of the Ar overpressure and the vapor pressure expected from the suppliers vapor pressure curve. The test was then repeated with both oil and LBE in the autoclave. The result was the same, indicating no oil-LBE interaction. A slight net pressure rise after the system has returned to room temperature indicates that there may be a small amount of noncondensible gas generation. Since the time scale for cooling the target following an accident of this sort is within a few hours, this gas generation will not contribute to any pressure buildup that might compound the accident. Additional tests are being prepared to collect and analyze gas byproducts.
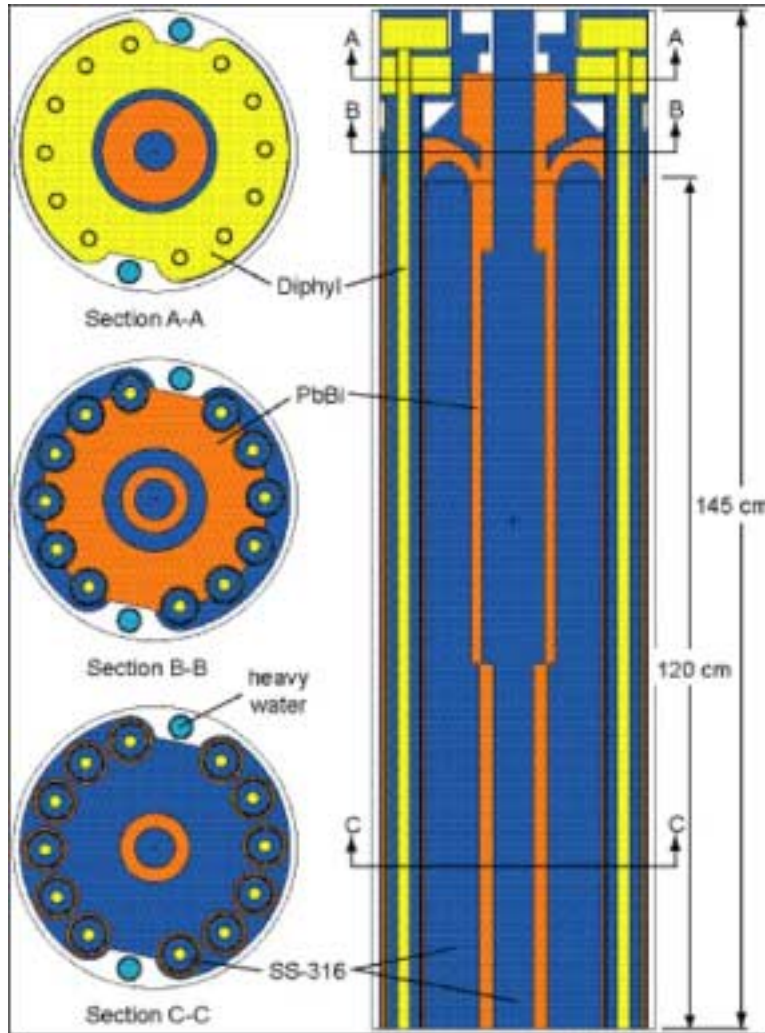
Fig. 72. Horizontal and vertical cross-sectional views of the MCNPX primary heat exchanger model.

TRAC Model

A TRAC model of the MEGAPIE 3-loop system is being set up to evaluate the system transient performance during operation in SINQ as well as during reduced power tests in the integral test stand. This modeling effort began in the last weeks of this fiscal year and will be continued into FY03.

At this time, a partial model of the LBE side of MEGAPIE is operational, with beam heating and transient analysis capability. Heat dump is to a simplified secondary system. This TRAC model will follow as closely as possible the RELAP5 model developed by Ansaldo for the heat removal system design basis. The TRAC model will be used to evaluate the steady state and transient test conditions for the integral testing, and for the development of the controls system.

Integral Test Stand

A major activity in FY03 will be the preparation of the integral test stand for out-of-beam testing. We are working with the PSI team to define the test matrix and a

---

heater configuration to simulate beam heating at reduced power. These heater tests will be used to establish the transient response of MEGAPIE as an aid in development of the control system. The current heater concept a dummy outer target container equipped with electrical heaters (estimated 200 kW) will replace the target window during these integral tests. Commercially available cartridge heaters could provide about 200 kW, 1/3 of the thermal operating load of MEGAPIE. Details of the heater selection, mounting, variable power supply, and test matrix are being resolved at this time.

Absorber Tests

Tests of the hydrogen absorbers over the oil and LBE cover gases are now in the planning and analysis stage. In the case of the oil system, the hydrogen produced by radiolysis is about 3 liters (STP), so proper absorber operation is essential to controlling the system pressure. In the LBE cover gas, hydrogen must be absorbed to keep the pressure low and minimize the number of dumps to the decay tank. However, the configuration of the absorber is constrained by the space available. The resulting arrangement of absorber must be tested. The design of these tests is now underway.

Material Data

LANL provided irradiated and unirradiated SS-316L material property data as the baseline data for MEGAPIE. These data were generated and compiled for the Accelerator Production of Tritium Project, representing Chapter 3 of the APT Materials Handbook.

Oxygen Sensor Design

LANL provided to MEGAPIE the detail design drawings of the oxygen sensors in use on the DELTA loop. These sensors may be used on the MEGAPIE integral test stand, and in the actual MEGAPIE test.

3.8   LANL-Sponsored Directed-Research University Programs

Scope

University support is an important part of the AFC Program. In addition to the general University programs run by the DOE-HQ, a number of universities are supported directly by the programmatic funds to provide technical assistance to the AFC Program. The directly supported universities include University of Michigan, UC-Berkeley, UT-Austin, and North Carolina State University.

University of California — Berkeley

Provide technical support to the Systems Analyses and Transmutation science teams via specific tasks defined and coordinated through the AFC Program leads, including:
- Benchmark of the simple model for fuel cycle analysis;
- Resolve the discrepancy with ANL on actinide built-up with cycles;
- Apply fuel-cycle analysis methods to compare design alaternatives;
- Compare Na vs. LBE-cooled ATW;

- ATW performance assessment using molten salt and alternative;
- ATW assessment during approach to equilibrium using molten salt; and
- Perform optimization and analyses of pebble-bed ATW.

University of Michigan

Provide technical support to the Systems Analyses and Transmutation science teams via specific tasks defined and coordinated through the AFC Program leads, including:

- Analysis of coupled accelerator core dynamics with emphasis on k_{eff} predictions and control;
- LWR-based reactor transmutation studies for equilibrium cycles;
- Assessment of LBE slowing down spectrum and the associated cross-sections;
- In collaboration with technical staff at LANL, use proton irradiation to simulate spallation neutron radiation damage in accelerator-driven systems. This work is to investigate the effect of higher gas production at significant doses (several dpa) to lay a foundation for a full-scale radiation campaign;
- Develop a detailed description of the irradiation campaign (temperatures, dose rates, doses, and He-implantation levels); and
- Conduct a single irradiation campaign (~240 hours of irradiation) on SS-T-91 at three dpa levels.

University of Texas — Austin

Provide technical support to the Systems Analyses and Transmutation Science teams via specific tasks defined and coordinated through the AFC Program leads, including:

- Participation in the helium and hydrogen production experiments in LANL/Blue Room (Summer 2002);
- Development of a test plan, and post-test analyses for spallation product benchmark experiments for targets (emphasis on LBE);
- Time-dependence incorporation on the proliferation metrics development and analysis; and
- Development of the uncertainty analysis methodology for the proliferation metrics, providing results to the Systems Analysis Team.

North Carolina State University

Calculate radiation damage (production of displacements, helium, hydrogen, and heavier transmutation products) and energy deposition in the target materials, containment structures, and entrance windows of the target assemblies for the SINQ spallation neutron sources that are under design and development at the Paul Scherrer Institute (PSI). These targets include the Mark II and Mark III designs. The Monte Carlo code MCNPX will be the primary computational tool, but other codes such as SPECTER and SRIM (or TRIM) and cross-section information sources such as ENDF and LA150 will be used. The calculations are two-fold in nature:

- (1) a detailed simulation model will be constructed incorporating the materials and geometry of the spallation-neutron-source targets by means of which the spatial variance of proton and neutron fluxes will be determined;

- (2) cross section sets for the production of the damaging entities (displacements, helium, etc.) will be created to cover the full applicable energy range of protons and neutrons in each of the affected materials. The damage production rates will then be determined by folding the radiation fluxes into the cross sections.

In addition to the direct production of displacements due to incident and secondary protons and due to spallation neutrons, the scope includes cognizance of less obvious (and less well studied) mechanisms for the transfer of energy to the irradiated materials and hence the production of displacements. These mechanisms include recoil-atom damage and n-gamma capture damage. These mechanisms could be important in special cases. Furthermore, the scope includes consideration of the spectrum of transmutation products upon spallation and their possible effects on corrosion properties.

The effects of the calculated radiation damage on mechanical and other property changes will be analyzed, and reasonable and safe lifetimes for the radiation-damaged components will be assessed.

Highlights

- UC-Berkeley issued a status report on fuel cycle model and actinide built-up cycles. Also, four status reports on Na vs LBE ATW, Molten Salt ATW, and Pebble Bed ATW were completed.

- The University of Michigan completed the following milestones:
  - Framework for a Simple Dynamic Model
  - Interim Data and Results for the T-91 Irradiation Campaign
  - Report on LWR Transmutation Studies
  - Status Report on LBE Spectrum Analysis

- An uncertainty estimation procedure was added to the Proliferation Resistance Assessment Methodology developed by the University of Texas at Austin.

University of California — Berkeley

A study was initiated to examine the feasibility of transmuting in a molten salt (MS) transmuting reactor using $LiF-BeF_2$ salt rather than $NaF-ZrF_4$ salt. Preliminary results for a MS reactor using $LiF-BeF_2$ salt were very promising: equilibrium k_{eff} was close to 1.0 with the actinide concentration below the solubility limit and fractional transmutation of ~98% in one pass! The solubility limit in $LiF-BeF_2$ salt is significantly lower than in the $NaF-ZrF_4$ salt studied earlier. The set of coupled nuclide density equations was expanded to include U and Np isotopes, and the sensitivity of the reactor performance to the feed composition was studied. The extension of the number of nuclides considered has a small but positive effect on the equilibrium k_{eff}, whereas the inclusion of small amounts of U in the feed has a small negative effect on the equilibrium k_{eff}. Our general conclusions concerning the promise of the MS reactor as a transmuter did not change. Sensitivity analysis of the MS transmuting reactor is showing extremely large sensitivity of the equilibrium concentration to the feed concentration this unexpected high sensitivity is being examined. The overall leakage probability from a MS transmuting reactor has been estimated. For an

equilibrium k_{eff} value of 0.98, the core should be ~4.5 m high and 4.9 m in diameter. The resulting core power is in the 8 GWth range.

The development of a simple interpolation procedure for effective one-group cross sections to be used for simplified fuel-cycle analyses was completed successfully. The fuel cycle in LM-cooled transmuters can now reliably be simulated.

The agreement between the predictions of UC Berkeley s simplified fuel-cycle model WACOM and that of the coupled transport-depletion code MOCUP has been improved. WACOM was successfully used for finding the fuel composition in the equilibrium cycle.

The methodology to be used for the revised comparison between a lead-bismuth cooled transmuter and a sodium-cooled transmuter has been formulated. The comparison is underway.

University of Michigan

LWR Reactor Transmutation Studies

We performed assembly-level lattice physics calculations with the CASMO-3 code to evaluate the efficiency of multiple recycling of Pu in pressurized water reactors (PWRs). Global fuel depletion calculations are approximated by CASMO-3 calculations using a linear reactivity model. The CASMO-3 calculations are combined with an extrapolation algorithm to estimate the equilibrium cycle of two configurations: (1) heterogeneous assembly configuration that contains both UO_2 and mixed oxide (MOX) fuel pins, and (2) homogeneous configuration comprising a 2x2 colorset arrangement of MOX and UO_2 assemblies. We also studied two recycling methods. Method 1 recycles self-generated Pu only, so that, after reactor discharge, the Pu remaining in the spent MOX fuel and the Pu in the spent UO_2 fuel is reprocessed and blended with natural U to fabricate the reload MOX fuel for the subsequent recycle. In method 2, the ^{235}U enrichment in the UO_2 rods remains fixed for each recycle. Method 1 recycling calculations suggest that regardless of the MOX arrangement in a PWR core, a net Pu depletion is not feasible at any point during multiple recycles (including quasi-equilibrium), and that the stabilization of the Pu inventory occurs at the expense of an increased overall Pu inventory. Method 2 calculations indicate that a whole-core loading of heterogeneous assemblies in a PWR core would allow a substantial rate of net Pu depletion from a spent-fuel stockpile. A homogeneous configuration or partial loading of MOX assemblies could also reduce the Pu stockpile, although the depletion rate would be slower and the equilibrium inventory would be larger. Key results of the study will be presented at the ANS meeting in November.

Fast Neutron Moderation Analysis

We previously reported on the unusual features of neutron slowing-down spectra in Pb and Bi moderators. Above the inelastic scatter threshold, a subtle interplay of elastic and non-elastic scattering can cause very deep flux depressions in the spectrum of 14 MeV neutrons slowing down in heavy moderators. In the case of pure ^{208}Pb, this flux depression can be 16 orders of magnitude deep between the flux peak at 14 MeV and the bottom of the depression at about 11.6 MeV. This depression is caused by the non-elastic removal of particles from just below the source energy; its

depth is very sensitive to the elastic to non-elastic scatter ratio, and its width and other detailed features, are dictated by the energies of the low lying nuclear states in the scatterer. Below the flux depression, the flux rises abruptly due to the influx of particles from non-elastic scattering events. We have used MCNP4c and MCNPX to provide benchmark computations of the slowing-down spectrum. To complete our task of validating the community s fast-spectrum computational capability, we have used a fast-reactor spectrum code, MC^2, to model the slowing down of 14 MeV neutrons in natural Pb. Although MC^2 correctly computed the gross features of the flux depression and subsequent flux rise, we note differences from MCNP results, which are likely due to differences in the energy levels used to model the inelastic scatter and also due to slight differences in the lead isotopics used. Overall, it was seen that the MC^2 fine-group method with the inconsistent P_1 method could properly model the fast neutron spectrum for 14 MeV neutrons slowing down in heavy moderators. The results of this study will be presented at the November ANS meeting.

Space-Time Analysis of Coupled Accelerator-Core Dynamics

We continued our effort to develop dynamic models for simulating multiple pulses of spallation neutron sources and methods for determining the reactivity in accelerator-driven subcritical (ADS) systems, with a focus on space-time models that can accurately represent the localized nature of spallation sources. Subject to thermal-hydraulic feedback and source transients, it is important to ensure that the system remains sufficiently subcritical throughout any transients and throughout a fuel cycle. The reactivity determined either through the solution of the inverse point-kinetics equations or other semi-analytic point-kinetics methods is, however, subject to considerable variations, depending on the relative separation between the detector and localized source locations. To overcome this difficulty, we have developed a method, within the quasi-static formulation of the FX2-TH code, which can account for the spatial dependence of reactivity measurements in pulsed-source experiments. Our focus to date has been for the case where multiple-source pulses are introduced into an initially zero power configuration. Using pulsed source data simulated with the FX2-TH code, we are able to show that our quasi-static method could essentially remove the space-time effects, provided we determine the shape function with sufficient accuracy.   The results of this space-time ADS study will be presented at the ANS meeting in November. Effort has been also made to perform MCNP simulations of the French MUSE and TRADE (TRIGA Accelerator Driven Experiment) data.

Target Irradiation Experiments

We completed the initial irradiation program for alloys HT-9 and T-91. A total of twelve samples were irradiated at 450¡C: six HT-9 and six T-91 samples. Six samples (three HT-9 and three T-91) were implanted with He to a dose of 100 appm prior to irradiation. The other six were irradiated in the as-received condition. Irradiations were conducted to three doses: 3, 7 and 10 dpa. At each dose were two HT-9 samples (one with and one without He) and two T-91 samples (one with and one without He). Irradiations were conducted in two separate batches with an average dose rate of $\sim 1.5 \times 10^5$ dpa/s. The total irradiation time for the full compliment of twelve samples was ~180 hours.

University of Texas-Austin

An uncertainty estimation procedure was added to the proliferation-resistance assessment methodology developed by the University of Texas at Austin. The details of the assessment methodology and the uncertainty assessment have been documented. The assessment methodology is based on the Multi-Attribute Utility Analysis method. It was developed to allow for relative comparisons of proliferation resistance for different fuel cycles and facilities. This method uses a variety of intrinsic and extrinsic attributes in determining its measures including (though not limited to) the following:

- Attractiveness Level of the material
- Heating rate from Pu in the material
- Weight fraction of even Pu isotopes
- Concentration in material (in SQs/MT)
- Radiation dose rates (in rem/hr at 1-meter distance)
- Material pH level
- Material stability in air
- Size/weight of material items
- Frequency of measurement
- Measurement uncertainty
- Separability
- Physical barriers (vaults, canyons, etc.)
- Total facility inventory
- Facility fuel loading type (continuous or batch)
- Percentage of processing steps that use item accounting

Each of these attributes has some input data associated with it. Derived utility functions operate on this input data and the results from these utility functions are combined in a weighted average to produce the relative proliferation-resistance score for any process step. These proliferation-resistance scores are then aggregated into a total nuclear security measure for a complete cycle as follows:

$$NS = \frac{\sum_{i=1}^{I} m_i \cdot \Delta t_i \cdot PR_i}{M \cdot T} \qquad (1)$$

where m_i is the amount of material in process i, Dt_i is the time the material is in process i at the static proliferation resistance value of PR_i for process i, M is the total amount of material evaluated in the cycle (e.g., 1000 kg), and T is the time frame over which the assessment is performed (e.g., 100 years).

The weighting factors in this averaging procedure were developed by soliciting opinions from 24 different experts in the field. The uncertainty analysis performed on this methodology consisted of an error estimation procedure and a propagation of these errors through the analysis methodology. Error estimates were produced for all of the input data used in this analysis, including the weights for each attribute and the input values for each process step. The uncertainties in the weighting factors were produced using the standard deviation of the results compiled from the

questionnaires. The uncertainties in the input values were estimated based on expert knowledge of the variability of these parameters. In some cases, the input data is binary in nature and an uncertainty of zero was estimated for the data. These error values were then propagated through the utility functions and averaging procedure to produce an estimate of the uncertainty at any process step. Lastly the uncertainties were propagated through the nuclear-security measure-aggregation procedure to allow for an understanding of how the uncertainties evolve with time.

North Carolina State University

Target 5 of the Spallation Neutron Source at Paul Scherrer Institute (SINQ) in Switzerland was the primary focus of our attention during the fourth quarter of FY02. Target 5 is the irradiation facility for the SINQ Target Irradiation Program STIP III. As for the earlier STIP I and II irradiations, STIP III represents a collaboration that includes CEA, FZJ, JAERI, LANL, ORNL, and PSI. Approximately 700 test samples are being exposed in the STIP III irradiation, which is scheduled to end in December 2003. During this quarter, we completed calculations to provide proton and neutron fluxes and energy deposition at various locations in Target 5 and to determine production rates for displacements, helium, and hydrogen in various materials. Analysis of the calculations is underway.

We revised the Target 4 input file significantly \to reflect the changes in going from Target 4 to 5. In particular, this included specifications of test samples and rod geometries. In addition, we introduced modeling of the entrance window.

Two source proton beams were described: Beam 1, determined experimentally, and Beam 2, calculated using a truncated double-Gaussian proton-current density distribution. Resulting peak-current density for Beam 1 was 1.94×10^{14} protons/cm^{2}s per mA, which is 21% greater than for Beam 2. Results cited below refer to Beam 1. The peak neutron flux for Target 5 was determined to be 2.6×10^{14} neutrons/cm^{2}s per mA and it occurs at Rod 7, which is at the center of the seventh layer of rods. For the same source beam and incident energy (~570 MeV), we find that the peak neutron flux for Target 5 is 1.3 times that for Target 3 (which was used for STIP I). A major difference in the two targets is that the spallation target material for Target 5 is Pb, whereas it was Zircaloy-2 for Target 3. The question arises as to whether the increased n/p yield for Pb over Zr can account for the 30% difference. We ran MCNPX to get the n/p yields for a particular geometry of Pb and Zr and found the n/p yield ratio, Pb to Zr, to be ~2, and thus more than enough to account for the 1.3 ratio in the neutron fluxes. Nevertheless, there appears to be more at play with regard to the neutron flux than just the n/p yield, and the question is being further analyzed.

Cross sections for Al, SS-316, 9Cr-1Mo, and Zircaloy-4 were folded into the proton and neutron fluxes to yield production rates for displacements, He, and H, at various locations of the entrance window and within the array of target rods of Target 5. Table 18 shows the defect production information for Al at the center of the entrance window (point of maximum proton flux) and at Rod 7 (point of maximum neutron flux) in terms of the defect concentrations for an exposure of 10 A•h. For displacement damage at the entrance window, ~70% is due to protons, whereas for Rod 7, ~70% is due to neutrons. Also, about twice as many displacements are produced at Rod 7 than at the entrance window due to greater neutron flux. In addition, almost all of the He and H is produced by protons. Because of the greater proton flux at the entrance window, He and H concentrations are significantly greater there than at Rod 7.

Table 18. Defect Concentration in Aluminum at the Entrance Window (Maximum Proton Flux) and at Rod 7 (Maximum Neutron Flux) for 570-MeV-Proton Exposure of 10 A•h at Target 5.

		WINDOW	ROD 7
DISPLACEMENTS, dpa (% dpa)	Neutrons	2.3 (29%)	11.2 (72%)
	Protons	5.6 (71%)	4.3 (28%)
	Total	7.9 (100%)	15.5 (100%)
HELIUM, appm He (% appm He)	Neutrons	33 (2%)	121 (9%)
	Protons	1980 (98%)	1200 (91%)
	Total	2010 (100%)	1320 (100%)
HYDROGEN, appm H (% appm H)	Neutrons	128 (3%)	460 (14%)
	Protons	3950 (97%)	2750 (86%)
	Total	4080 (100%)	3210 (100%)

4.   SYSTEMS TECHNOLOGIES

Scope

The scope of Systems Technologies is to coordinate all technical elements to define requirements, perform system-level evaluations, develop preconceptual designs, and establishing technology development activities in a comprehensive R&D proof-of-principle (POP) effort. Overall system objectives, system performance requirements, and POP requirements are used to correlate R&D needs, data quality objectives, experimental facilities, resources, and materials. System-level modeling evaluates the performance of multi-strata options in establishing a technically feasible spent nuclear fuel management program, especially with regard to proliferation, economics, environment, safety, and institutional issues. Likewise, pre-conceptual designs serve as fundamental bases in defining critical R&D and focusing POP testing. Woven together, System and Technology Integration activities can provide a solid foundation for focused and coordinated AFC research and development.

Accelerator-Driven Test Facility (ADTF)

The preconceptual and conceptual design phases of the Accelerator-Driven Test Facility (ADTF) includes the Target and Materials Test (TMT) Station, the Subcritical Multiplier (SCM), the accelerator, and the balance of facility segments. The work performed in connection with the ADTF design must be documented, including the reference preconceptual designs of the TMT and the Na-cooled SCM-100, with a Pb-Bi reference target, and the studies of alternative engineering design solutions considered. The scope also includes collaboration with CEA. The following specifics are included:

  − Completion of the ADTF preconceptual design documentation;

- Development of an ADS reference design US will work on liquid-metal-cooled designs (Na, LBE) and CEA will work on a gas-cooled design;
- Proof-of-performance coupling tests a plan for experimental POP coupling between an accelerator and a multiplier will be developed; and
- POP for accelerator reliability and accelerator development.

Integration activities include:
- Development of functional and performance requirements for ADTF;
- Definition of design interfaces between major facility segments;
- Coordination of internal and external design reviews;
- Technical risk assessment; and
- Cost estimating.

ADS Reference Design

The purpose of this task at ANL is to develop a preconceptual design for a Na-cooled, accelerator-driven system. LANL will lead the reference design for a Pb-Bi-cooled system. This work involves development of a preconceptual design for a large-scale (~800˚MWth) ADS with liquid-Na cooling and a Pb-Bi eutectic target. The focus is on defining a set of top-level requirements for the ADS engineering design concept for the facility as a whole, including:
- Identifying the containment structure with ingress and egress routes for personnel, services, and radioactive and nonradioactive equipment;
- Routing and shielding of the accelerator beam;
- Configuring the subcritical multiplier, the vessel in which it is housed and its cover, and all other in- and ex-vessel ancillary components and systems; and
- Handling schemes for all of the above.

The ADS design will be used to update, as necessary, requirements developed for the ADTF.

Micro Accelerator-Driven Coupling Proof-of-Principle Experiments

Coupling Experiments — This task will investigate the use of an experimental facility such as the Transient Reactor Test (TREAT) facility, located at ANL-W, for the study of accelerator-driven-system control issues related to the coupling of a multiplier to an external source. The feasibility of using the TREAT reactor coupled with an accelerator-driven external source to be part of a POP for ADS will be assessed. The dynamic behavior of the experimental coupled system will provide useful information for simulation of operation of an actual ADS power system.

Fuels and Materials Experiments — The main deliverable for this year is to develop a preconceptual design, cost estimate and schedule for the implementation of an irradiation experiment (Fuel and Materials Test Station — FMTS) in the high power beam at LANSCE.

Advanced Cavity Development — The main effort is the procurement and testing of two β=0.175, 2-gap, 350-MHz superconducting spoke resonator cavities and the completion of the design of the power coupler for these cavities. Scope also includes the continuation of the DOE/CEA/CNRS technical collaboration on accelerators for waste transmutation.

Highlights

ADS Reference Design

- A report on the selection of the reference subcritical multiplier core, *Selection of the Reference Accelerator-Driven System Subcritical Multiplier Core Model for Use in Pre-Conceptual Design Development*, was completed and issued.

- Thermo-hydraulic analyses of the nominal ADS LBE target concept, based on the scale up of the ADTF target design, were performed to verify that design constraints were met.

- Hydraulic analyses of the inlet plenum of the ADS subcritical multiplier were performed to assess the effect on flow and pressure distributions caused by the asymmetrical placement of the primary sodium pumps.

- A thermal model of the TREAT fuel assembly was developed and used for estimating fuel assembly temperature distributions.

- The following final documents for the ADS Reference Design were prepared and issued:

  - *Final Report on the Pre-Conceptual Design of a Reference Accelerator-Driven System for Transmutation of Spent Nuclear Fuel Materials*

  - *Spallation Neutron Source Target Concepts for the Subcritical Multiplier of the Reference-Design Accelerator-Driven System*

  - *Preliminary Thermohydraulic Insights for the 840-MW$_{th}$ Sodium-Cooled Accelerator-Driven System*

Coupling Experiments

- The preliminary engineering feasibility report for the use of the TREAT reactor in accelerator-driven experiments, *Engineering Feasibility of Proof-of-Principle Testing of Accelerator-Driven Subcritical Reactor Operation Using TREAT*, was completed and issued.

- Two reports, *Preliminary Safety Assessment of Simulating Accelerator-Driven Subcritical Operation in TREAT* and *Engineering Feasibility Study of Accelerator-Multiplier Coupling Experiments Using the TREAT Reactor* were completed and issued.

Advanced Cavity Development

- The two β=0.175, 2-gap, 350-MHz superconducting spoke resonator cavities were delivered during the first week of the quarter, about a month ahead of schedule.

- Testing of the two β=0.175, 2-gap, 350-MHz superconducting spoke resonator cavities was completed, with both cavities exceeding the ADTF requirements.

- Two technical papers were submitted to LINAC 2002 held in Seoul, Korea, August, 2002: T. Tajima, et al., Test Results of the LANL β = 0.175 2-Gap Spoke Resonator , and R. Garnett, et al., RF-Focused Spoke Resonator.

ADS Reference Design

Sodium-Cooled Engineering Design

Revision of the layout of the ADS subcritical multiplier (SCM) to accommodate previously identified geometric discrepancies continued. In addition, the intermediate heat exchangers (IHXs) were modified for passive safety reasons. The new configuration allows for natural circulation through the IHXs even in the event of primary tank failure. The new IHX design has an inlet that is below the faulted sodium level. The outlet is maintained at a height above the core outlet sufficient to allow the necessary natural circulation head by shortening the IHX. To maintain the requisite heat rejection capability in the shorter envelope, its diameter was increased. The main effect of these revisions is to increase the diameter of the primary tank from 12.8 m to 14.3 m. The depth is still 15.5 m.

The diameters of both rotating plugs were increased slightly. The enlargement of the small rotating plug was enough to allow symmetric placement of the neutron absorber assemblies being considered for burnup compensation instead of the asymmetric configuration previously reported. This reduced the engineering complexity of the asymmetric arrangement as well as the modeling complexity necessary to analyze it.

Work on the equipment layout on the top cover of the SCM primary tank and on the containment operating floor also continued. This has led to a complete re-evaluation of the spatial relationships between various components and systems. Routing of the secondary sodium piping through the personnel and equipment access tunnel was chosen to avoid the necessity for separate piping tunnels. There is already adequate space for maintenance of the piping in the access tunnel. To accommodate this modification, the location of the target-assembly handling-cask laydown area, the orientation of the SCM tank, and the distribution of IHXs and pumps are being changed. Also, the containment structure will be enlarged by ~5 m to accommodate cask handling and fuel unloading.

The report, *Selection of the Reference Accelerator-Driven System Subcritical Multiplier Core Model for Use in Pre-Conceptual Design Development*, documents the selection of the SCM core model used in the ADS reference design activity, presents the criteria for selection, and describes the model taken from the sodium-cooled point design developed by the Nuclear Systems and Materials Analysis Department of RAE at ANL, under the direction of R. N. Hill.[16] The conclusions of that report are reproduced below.

Report Conclusions

The core model developed under the auspices of the DOE ATW Program appears to be adequate for modeling the SCM core for the purposes of the current ADS pre-conceptual reference design activities. Although it does not meet all the functional and design criteria outlined for an ADS, mostly changes involving fuel composition and control strategy are anticipated, and these should not appreciably affect the core size and shape, which are the major factors in facility size and configuration. It clearly would not have been practical to redo the lengthy physics necessary to characterize the point design of another SCM core when the definition of the mission to be served

---

[16] Reported in *Compendium of Initial System Point Designs for Accelerator Transmutation of Radioactive Waste*, LA-UR-01-1817, by D. Bennett, et al., February, 2001.

by an ADS has only been improved marginally since the original point design was completed.

The model is already being used with the MCNPX code to estimate the response of the SCM to a 600-MeV proton beam and a more realistic target, rather than what was used in the original physics point design.

The model has also been used to address the control strategy issue. Estimates have been made of the worth of absorber assemblies, which can be used for burnup compensation during a fuel cycle campaign, in various positions in the core. It will also be used to determine the effect of including a small amount of fertile material in the core as another means of reducing the swing in k_{eff} during a burnup cycle. The question of burnup swing is an important one since it determines the requirement for variability of accelerator beam current. A change in current by a factor of 2-3 may be unacceptable for safety reasons, and a reduction in this requirement to perhaps 1.1 (i.e., 10%) could lead to a major reduction in accelerator cost and have major safety implications.

The set of layout drawings with the final configuration of the preconceptual design of the reference ADS was completed in preparation for terminating this activity at the end of FY02. The preconceptual design for the ADS reference is the point design as of the end of August. It incorporates the latest geometry changes, with a slightly larger primary sodium tank and symmetric placement of the burnup compensation rods.

The report for this activity, *Final Report on the Pre-Conceptual Design of a Reference Accelerator-Driven System for Transmutation of Spent Nuclear Fuel Materials,* was completed and is in final review. It will be issued in early October.

Target Assembly

The nominal target design for the reference ADS is based on the ADTF target concept scaled up to the power levels of the ADS, matching the current density of the proton beam. This nominal ADS target is large and imposes heavy requirements in circulating large masses of lead-bismuth eutectic (LBE.) Recent work, therefore, focused on alternative target concepts rather than on the optimization of the reference target design. The evaluation of the nominal ADS target in a more quantitative manner has been completed during this quarter. An axisymmetric computational fluid-dynamics (CFD) model of the system was developed using the commercial software package Star-CD.

The model consists of 64,520 hexahedral and prismatic volume elements with both the liquid and solid components of the target concept. The volumetric heating of the target is simulated by a user subroutine based upon the heat deposition curve calculated for the ADTF target concept. Since this curve is not a function of the beam current and all other beam parameters remain unchanged, the curve is also valid for the ADS application. A constant inlet velocity condition of 2 m/s and uniform outlet pressure condition are specified in these calculations.

The model uses the nominal target dimensions reported in the target design description.[17] The nominal wall thickness is 5 mm, but the thickness is reduced to 3.5˚mm in the beam window region to insure that the peak internal and surface

---

[17] ANL Report AAA-014

temperatures do not exceed 600¡C. As in the ADTF target, a control fairing based upon the recommendations of Idelchik s *Handbook of Hydraulic Resistance* is employed at the end of the central turning vane to reduce the instability of the flow field in the bulk target channel. It is assumed that all target components included in the model are constructed of HT-9 steel.

The steady-state temperature profile for the liquid and solid components in the heated region of the target module are shown in Fig. 73. The peak temperatures in the beam window and central flow baffles are 533.5¡C and 528.0¡C, respectively. The peak surface temperatures in the beam window and central flow baffle regions are 365.2¡C and 451.55¡C, respectively. The peak temperature constraint is satisfied by this design.
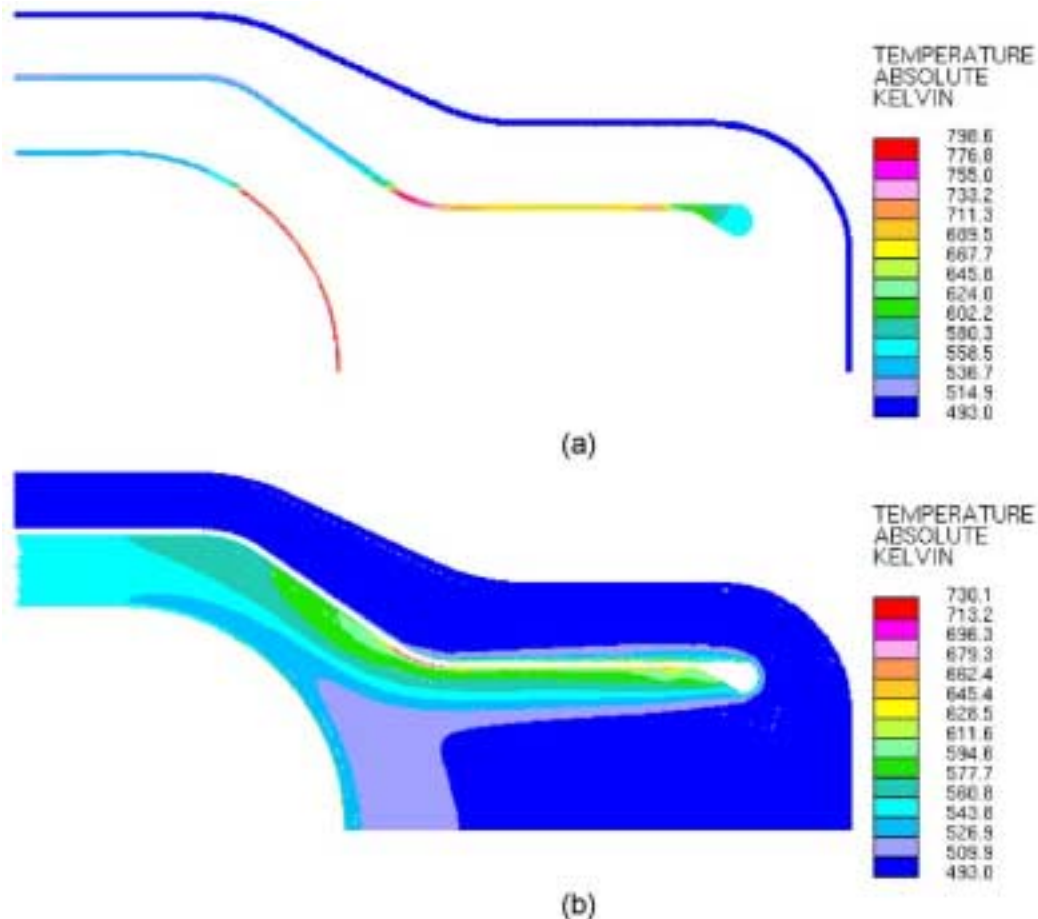
Fig. 73. Steady-state axisymmetric temperature profiles for (a) solid and (b) liquid components in the heated region of the nominal ADS liquid LBE target.

The steady-state velocity profile in the heated region of the target module is shown in Fig. 74. The simulation results clearly show the development of a small recirculation zone upstream of the flow control fairing; however it is well beyond the high power region of the target and should not lead to localized high temperatures. Furthermore, the prediction of a recirculation zone in an axisymmetric simulation is typically indicative of an unstable recirculation phenomenon in the real geometry. The velocity

profile indicates that high velocity flow regions can be anticipated near the surface of the control fairing. Until the erosive characteristics of LBE are better quantified, it should be assumed that erosion of this surface will impact the expected lifetime of the target.
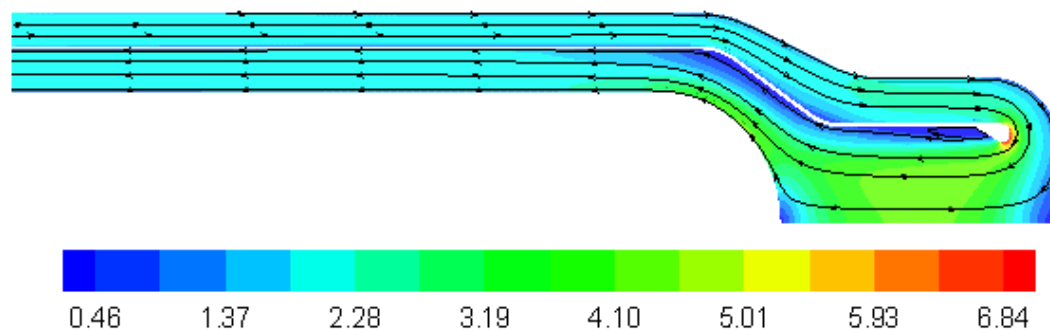

Fig. 74. Steady-state axisymmetric velocity profiles and streamlines for the nominal ADS liquid LBE target.

A paper describing the optimization of the annular channel lead-bismuth target concept was presented at the 2002 ASME joint US-European Fluids Engineering Division Meeting. Following the session in which the paper was presented, the possibility of establishing a forum at a future FED meeting for the discussion of thermal hydraulic optimization and simulation challenges in heavy liquid metal applications was discussed with several attendees.

The report*, Spallation Neutron Source Target Concepts for the Sub-Critical Multiplier of the Reference-Design Accelerator-Driven System,*[18] which was completed this quarter, documents the detailed target design work and covers the following:

- The nominal LBE target design, based on a scale up model of the ADTF target designed the previous year.

- An alternative target concept based on a helical coil containing LBE, (partially) cooled by multiplier sodium and requiring smaller external LBE circulation pipes than the nominal target.

- An alternative target concept based on a fixed packed bed of spheres containing LBE or solid tungsten, cooled with multiplier sodium.

Alternative Target Designs

An updated analysis of the spherical pebble-bed target concept was completed following adjustments in the calculation of the material thickness of a set of three layers of balls arranged in a fixed hexagonal lattice. In the updated calculations, fewer layers are needed to fully stop the proton beam. However, the correction results in an increase in the thickness of a single three-layer set, so the change in the total target height resulting from the correction is very small. The correction in the

---

[18] ANL AAA-051 (D. Pointer et al.)

geometric calculation also results in a slight increase in the surface and peak internal temperatures over previous results.

Based upon these studies, a nominal pebble-bed concept has been selected for further evaluation. The nominal case is the LBE-filled target with a pebble radius of 2˚cm and without spacers between the three layer sets. This nominal concept has a pressure drop of ~23 psi and an average surface temperature of 657¡C. More complex evaluations using computational fluid dynamics will need to be completed in the future to evaluate local temperature peaks within the lattice that result from the complex flow structure.

Multiplier Primary System Thermo-Hydraulics

The physics of the subcritical multiplier (SCM) of the ADS is based upon the ATW system point design using a sodium-cooled blanket. The primary sodium system design is largely parallel to the AFR-300 concept since the systems share similar design requirements and size. The main design differences between the ADS and the AFR-300 result from the inclusion of the target systems in the ADS design. The consideration of a realistic target system requires the removal of several rows of fuel elements from the point design core, which will likely lead to significant core differences between the ADS design and the point design. As a result, a systematic analysis of the thermo-hydraulic behavior of the system is premature. However, the physical dimensions of the SCM components and fuel subassemblies are unlikely to change as a result of future development, and the evaluation of purely hydraulic characteristics can be pursued.

Differences in the subassembly dimensions of the two systems limit the applicability of the AFR-300 hydraulic optimization efforts to the development of the ADS concept. To establish the degree of similarity between the ADS SCM and the AFR-300 core, the pressure drop through an un-orificed driver fuel assembly was evaluated as a function of flow rate for each system. For simplicity, it was assumed that the upper and lower shielding elements had the same diameter and arrangement as the fuel pins themselves. All other dimensions were taken directly from ATW point design and AFR-300 design documentation. The results indicated that the pressure drop through the point design fuel subassemblies used in the ADS design was ~30% higher than in the AFR case over the range of mass flow rates considered. As a result, lower flow rates and higher temperatures would be expected in the ADS than in the AFR-300 if all other system parameters remained identical between the two systems.

Based upon the pressure drop data, the hydraulic force acting on the fuel subassembly was evaluated as a function of mass flow rate for each subassembly type. This calculation considered the local forces resulting from each change in cross-sectional area, the thrust resulting from the release of the fluid to the outlet plenum, and the gravitational force acting on the subassembly.

The three primary coolant pumps in the ADS are placed in the primary tank so that they are separated by only 45¡ rather than 90¡. As in the AFR-300 design, a distribution ring is used to correct the asymmetry of the flow distribution in the inlet plenum of the multiplier. In order to evaluate the effects of further skewing the flow distribution within the inlet plenum, a simplified CFD model of the inlet plenum and distribution ring concept was developed.

Four cases were considered in the evaluation of the hydraulic characteristics of the inlet plenum of the ADS. The first case considered the 45¡ pump arrangement with twelve 10-inch diameter outlets between the distribution ring and the inlet plenum. The second case considered the 45¡ pump arrangement but with twenty-four 7-inch diameter outlets. The third and fourth cases both considered the 90¡ pump arrangement, with a 12-outlet distribution ring and a 24-outlet distribution ring, respectively.

The results of these studies indicate that the arrangement of the pumps at 45¡ angles rather than 90¡ angles does not lead to a significantly asymmetric pressure distribution within the core. As in previous AFR-300 studies, the use of twenty-four 7-inch outlets between the inlet plenum and the distribution ring rather than twelve 10-inch outlets results in smoother pressure profiles and is likely to reduce flow instability within the inlet plenum of the SCM. As a result of the approximate nature of this model, these *results should be considered qualitative rather than quantitative*.

These preliminary hydraulics and safety assessments applicable to the ADS have been documented in *Preliminary Thermohydraulics Insights for the 840 MW$_{th}$ Sodium-Cooled Accelerator-Driven System,*[19] a report completed this quarter.

Micro Accelerator-Driven System (ADS) Proof-of-Principle (POP)

Accelerator-TREAT Coupling Experiments

Characterizing and modeling the thermal behavior of the TREAT reactor is a significant undertaking. A review of past experiments and analyses was conducted with emphasis on significance to TREAT/ADS applications.

A new 3-D SINDA/G thermal model of a TREAT fuel assembly was developed. New modeling is needed to (1) better characterize reactor performance, (2) potentially extend programmatic capabilities, and (3) support and refine safety analyses. This effort extends and modernizes work undertaken in the 1958-1960 time frame, when the reactor was first placed into service. Illustrative calculations representative of both steady state and transient temperature profiles have been performed using mainly design parameters and nominal test conditions. Results compare favorably with measurements made using instrumented fuel assemblies.

Early modeling and experimentation showed that heat transport within the TREAT core is predominantly axial and largely controlled by the axial flow of cooling air. Air gaps designed within and in between fuel assemblies provide a significant impediment to cooling in the absence of airflow. Under these conditions radial and axial temperature profiles in the core (as determined by fission energy deposition) remain virtually unchanged for ~1 hour after a power pulse. However, airflow forced axially downward through the gaps designed between assemblies at the corners (and to a lesser extent along the sides) is effective in removing heat from the assembly by forced convection. Once airflow is introduced, measured temperature profiles respond within minutes. We thus conclude that the overall characteristics of heat transport in TREAT may be built up from analyses of single assemblies cooled from the outside by flowing air. Neighboring fuel assemblies are thermally connected mainly by sharing airflow channels as common boundaries.

---

[19] ANL Report AAA-050 (D. Pointer et al.)

New thermal calculations use nominal dimensions to explicitly model a 10-cm square, 244-cm-long TREAT fuel assembly, including (1) fuel and reflector axial regions, (2) zircalloy and aluminum cladding, and (3) downward forced airflow on the outside of the cladding at both corner and side locations. Heat transfer within bulk fuel and reflector is by conduction in three dimensions. Heat transfer across the air-gaps between fuel/reflector and cladding and between fuel and reflector regions considers both conduction and radiation. Axial airflow at corner and side locations was modeled assuming independent flow channels. Balancing turbulent flow pressure drops implies a mass flow division between corners and sides of ~19 to 1 (based on nominal dimensions).

Figures 75 and 76 show illustrative calculations of temperature profiles in a centrally located TREAT fuel assembly in two cases where actual temperature measurements were made using instrumented assemblies.[20] These cases span the wide range of TREAT s thermal performance. Figure 75 shows the transient response to a power pulse with air cooling started after a delay of 87 minutes. Figure°76 shows a steady-state condition at low power operation with cooling air.

Nominal reactor airflow was assumed equally divided among all TREAT fuel assemblies. Nominal parameters and test conditions were used in both calculations with two exceptions: (1) the ratio of power generated in a central assembly to that of the whole reactor and the axial power shape were plausibly adjusted to yield the *measured* temperature rise profile following an adiabatic power pulse, and (2) heat transfer across the air gap between fuel and reflector was plausibly enhanced to better match measured steady-state axial profiles (to account for difficult-to-model high-conductivity zircalloy spacers). The same adjustments were used in both reported calculations.
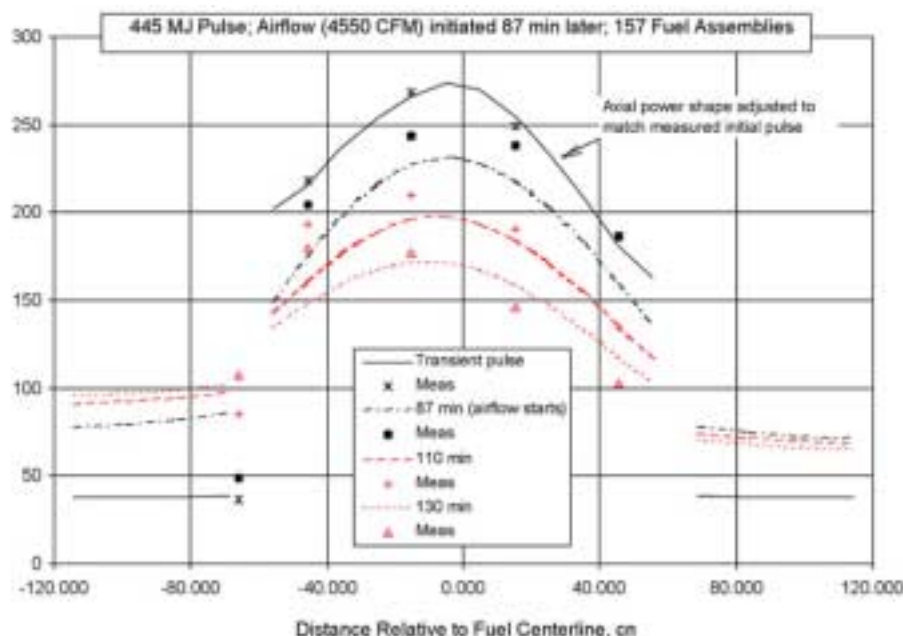

Fig. 75. Computed and measured transient fuel/reflector temperature profiles in a central fuel assembly
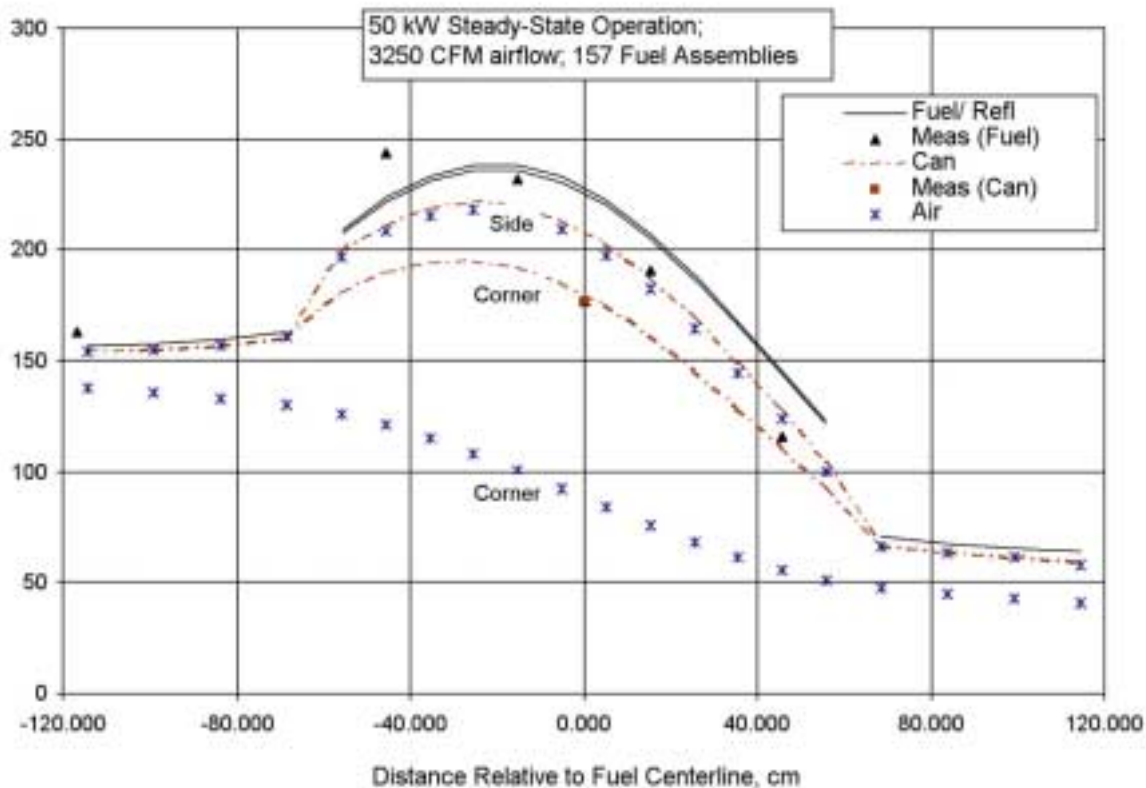
---

[20] ANL-6034, Appendix B, 1960

Fig. 76. Computed and measured steady-state temperature profiles *(units)* in a central fuel assembly

Both measured and calculated results shown in Fig. 75 serve to underline the importance of forced airflow for transient heat removal. As noted earlier, the initial axial temperature profile was adjusted by the calculation to agree with measurements. The difference between calculations and measurement at the time downward airflow begins (87 minutes) may in part be due to *upward* natural convection airflow, a phenomenon not included in the calculations. However, once the downward airflow begins, the subsequent time-dependence of measured fuel/reflector temperatures is plausibly represented by the calculations. However, relative to the calculations, measurements in the fuel seem skewed high toward the bottom half of the core.

Figure 76 shows representative steady-state temperature profiles for the fuel/reflector regions, cladding, and cooling air channels. Hottest and coldest values at side and corner locations are also shown. The high thermal resistance air-gap between fuel and cladding results in significant temperature drops between fuel and cladding but very small temperature differences across a radial slice of the fuel itself. As expected from the assumed 19:1 mass-flow ratio, large temperature differences were computed between corner and side locations of cladding and downward-flowing cooling air. There is generally reasonable agreement of calculated fuel/reflector temperatures with measurements. However, as noted in Fig. 75, measurements in the fuel also seem skewed high relative to calculations toward the bottom half of the core.

TREAT/ADS Preliminary Engineering Feasibility Report

The report, *Engineering Feasibility of Proof-of-Principle Testing of Accelerator-Driven Subcritical Reactor Operation Using TREAT,*[21] was completed, documenting the preliminary assessment of the engineering feasibility of implementing the TREACS (TREAT Experiment for ACcelerator-Driven Systems) Program. Although this is a preliminary report, it is believed that the following conclusions may be drawn regarding the engineering feasibility of TREACS:

- Source-driven behavior of the TREAT reactor is sufficiently representative of a fast-spectrum ADS operating at power to provide a useful simulation of the latter in a small- scale existing facility;
- The achievable neutron source strength of ~5×10^{13} n/sec is sufficient for program purposes;
- An accelerator already available at the Idaho State University s Idaho Accelerator Center can be used with only moderate modifications to drive the neutron source for the TREACS Program;
- Installation of the accelerator in the TREAT Facility appears to require little new hardware and only minor relocation of existing equipment and building modifications;
- Design and installation of shielding around the high-energy beam transport section leading from the end of the accelerator into and through the TREAT biological shielding should be a simple matter;
- A target made of available EBR-II blanket rods appears to be feasible, provided that the compatibility issue regarding the blanket rod-sodium bond and the cooling water can be resolved or avoided;
- A simple reflux-type water-boiler target cooling-system concept appears to be adequate, and a back-up flowing system presents no severe engineering challenges;
- A timetable that would have data available in 2005 to support the TRADE (an experiment in Rome that will couple a proton cyclotron with a TRIGA reactor) licensing process appears to be achievable, provided that restart activities begin promptly at the beginning of FY03 and are funded sufficiently to allow expeditious completion.

A preliminary assessment of the safety aspects of the proposed TREAT-accelerator coupling experiments has also been conducted and documented. The report, *Preliminary Safety Assessment of Simulating Accelerator-Driven Subcritical Operation in TREAT,*[22] has been prepared, is in review, and will be issued in October.

The final engineering feasibility report for the accelerator-driven subcritical operation in TREAT has been prepared, primarily drawing from the reports that have recently been prepared regarding the proposed TREACS experiments (physics reports, preliminary engineering feasibility report, safety report, cost estimate and schedule documentation). The report, *Engineering Feasibility Study of Accelerator-Multiplier Coupling Experiments Using the TREAT Reactor,*[23] is in final review and will be issued in October.

---

[21] ANL Report AAA-021 (J. E. Herceg, et al)

[22] ANL Report AAA-045 (T. Bauer, A. Wright, D. Naberejnev)

[23] ANL Report AAA-031 (J. Herceg et al.)

Transmutation Technology Development Plan

A complete draft of the Transmutation Technology Development Plan (TTDP) was issued for review. Because of the changing scope of the Program in transitioning from AAA to AFC and the changing Program strategy, the TTDP will be left in Final Draft form this year.

Fuels and Materials Experiments

The LANSCE Fuels and Materials Test Station (FMTS) provides the capability for testing, under prototypic ADS irradiation and coolant conditions, fuels and materials proposed for consideration in the AFC Program. The testing station will be located within the LANSCE Area A target facility. The preconceptual design team has advanced the maturity of several aspects of the station s design including physics and thermal-hydraulic performance, mechanical design, target stalk, surrounding shielding, and cost and schedule estimates.

Neutronics studies have been performed on lead-bismuth eutectic (LBE) targets, LBE cooled U-10Mo targets, and light-water-cooled tungsten targets in the U-shaped geometry. Targets were designed to be 11 cm in height, 3 cm wide, and 50 cm long. Axially, 95% of the total proton and neutron fluxes occurs within the first 10 cm of the target region, where test fuel to be irradiated will be placed. At 50 cm, the target essentially becomes a beamstop for protons and neutrons.

Energy spectra for U, LBE, and W were compared within the target at the center and edge where test fuels would be located. At higher energies (E>10 MeV), neutron fluences are an order of magnitude higher and softer at 5 cm into the target than at 0˚cm, suggesting that test fuels be placed more downstream than upstream of the target region.

Until now, peak and total neutron fluxes for test-fuel locations were calculated using target volume fractions of 65% target material and 35% coolant. By increasing the target volume fraction to 80%, the total and peak neutron fluxes in the test fuels increase by 10%, yielding peak neutron fluxes of 1.1×10^{15} $n/cm^2/s/mA$ for LBE-cooled U-10Mo and 8.5×10^{14} $n/cm^2/s/mA$ for light-water-cooled tungsten.

The overall decay heat of tungsten and tantalum (potential target materials) is about the same over a period of nine weeks after a 4-month irradiation at 1 mA. However, the photon contribution to decay heat for tantalum is twice that of tungsten for the same period of time. Spallation of tungsten produces 15% more neutrons than tantalum. Tantalum could be a potential cladding material for tungsten plates. It is currently being used as cladding at ISIS (Rutherford) and KENS (KEK).

For water-cooled clad-tungsten-plate targets, plate thicknesses were calculated as a function of position in the beam. Each plate is clad with 0.0127-cm-thick SS-316L. The beam switches between two sets of targets, spaced to permit a central fuel region between them and on both sides. The 800 MeV beam has a current of 1˚mA. The beam profile on each set of targets is 1.02 cm wide by 7 cm high, so the beam current density is 70 A/cm ^{2}. The peak power density of 2232 W/cm^3 occurs 1 cm into the targets. As the beam penetrates further into the targets, the power deposition decreases. Plate thicknesses were calculated at 5 cm increments into the targets to give peak surface temperatures that are 40¡C below the exit saturation temperature. Table 19 shows the results with thicknesses varying from 0.25 cm at the peak power density location to 4.71 cm at a depth of 26 cm into the target.

**Table 19. Plate Thicknesses and Tungsten Volume Fractions
vs Position in Target**

Position in Target (cm)	1	6	11	16	21	26
Fraction of Pk Pwr Density	1.000	0.729	0.390	0.192	0.102	0.057
Power Density (W/cm^3)	2232	1627	870	429	228	127
Plate Thickness (cm)	0.25	0.35	0.67	1.38	2.62	4.71
Peak Plate Temp (¡C)	180	185	201	237	299	403
Tungsten Volume Fraction	0.665	0.735	0.841	0.916	0.954	0.974

For LBE-cooled clad U-10Mo targets, plate thicknesses were calculated as a function of position in the beam. Each plate is clad with 0.0127-cm-thick HT-9. The same beam parameters were used as for the clad tungsten targets. The peak power density of 2576 W/cm^3 occurs 1 cm into the targets. Again, as the beam penetrates further into the targets, the power deposition decreases. Plate thicknesses were calculated at 5˚cm increments into the targets to give peak plate temperatures of 1000¡C and peak surface temperatures that were less than the 550¡C needed for oxygen control. Table 20 shows the results with thicknesses varying from 0.60 cm at the peak power density location to 3.21 cm at a depth of 26 cm into the target.

**Table 20. Plate Thicknesses and U-10Mo Volume Fractions
vs Position in Target**

Position in Target (cm)	1	6	11	16	21	26
Fraction of Pk Pwr Density	1.000	0.713	0.356	0.172	0.080	0.051
Power Density (W/cm^3)	2576	1837	917	443	206	131
Plate Thickness (cm)	0.60	0.74	1.11	1.67	2.53	3.21
Peak Clad Surf Temp (¡C)	540	510	457	414	380	365
Tungsten Volume Fraction	0.825	0.853	0.897	0.929	0.952	0.962

Calculations were done for the highest power rod of the 14 rods in the central fuel module located between the two sets of targets. Cases were done with either LBE or light water used to cool the targets and fuel.

Preconceptual layouts were created for the stalk and vessel design and bids obtained from two commercial vendors for the vacuum vessel. Illustrations were prepared that helped determine the size of the largest stalk expected. The largest stalk utilizes separate LBE cooling systems for the target and the samples. Scoping calculations were performed for helium cooling of the target and samples, and air cooling of a sodium secondary system. These showed that the LBE stalk was large enough to accommodate either helium or sodium cooling.

Based on the ASME Boiler & Pressure Vessel code, we determined that a 4.9-m-dia. stainless-steel flat-head design requires a minimum thickness of 9.65 cm. The calculations were compared with a DesignStar finite-element model which yielded stress concentrations well below the yield for stainless. This head concept along with the penetration in the head for the stalk was iterated and analyzed several times to minimize stress concentrations. An analysis utilizing supports under the head to lessen the load applied by the hanging stalk was also performed. The current design

is sufficiently robust to allow the stalk, with an estimated weight of 16,000 kg, to be hung from the head with or without supports.

The FMTS project will be implemented in two phases: (1) cleanout of the LANSCE A-1 target region, and (2) installation of the FMTS. These separate phases have different ES&H concerns and require separate analyses. Project Activity Notification Descriptions were prepared and submitted to LANSCE.

Several facility-planning activities were completed. Building construction drawings and a tour of the LANSCE Area-A were given to personnel who will make CAD models of the hot-cell area to aid in planning the FMTS facility. Limits of the LANSCE Area-A cranes were determined for coupled and uncoupled operation, as this information is needed to place equipment for efficient handling. The locations of the support equipment and storage pits were defined within the FMTS external shielding. A PERT exercise was undertaken to help better understand the work that must be performed and the resources required to produce the FMTS.

Advanced Cavity Development

The fabrication of two of β=0.175, 2-gap, 350-MHz superconducting spoke resonator cavities was completed one month ahead of schedule. One of the cavities is shown Fig. 77.

Fig. 77. AAA β=0.175 2-gap 350-MHz superconducting spoke resonator cavity

Following delivery of the two LANL/AAA β=0.175 spoke cavities, testing commenced immediately in the LANSCE-1 Superconducting Laboratory. The results were excellent and are shown in Figs. 78 and 79. Both cavities exceeded the AAA design

specification of Q_o >$5x10^8$ at E_{acc} >7.5 Mvolt/meter. The only post-manufacture processing of these cavities was buffered chemical polishing (BCP) and high-pressure water spray. Mechanical testing of the cavities verified the predictions of cavity stiffness and tuning sensitivity.
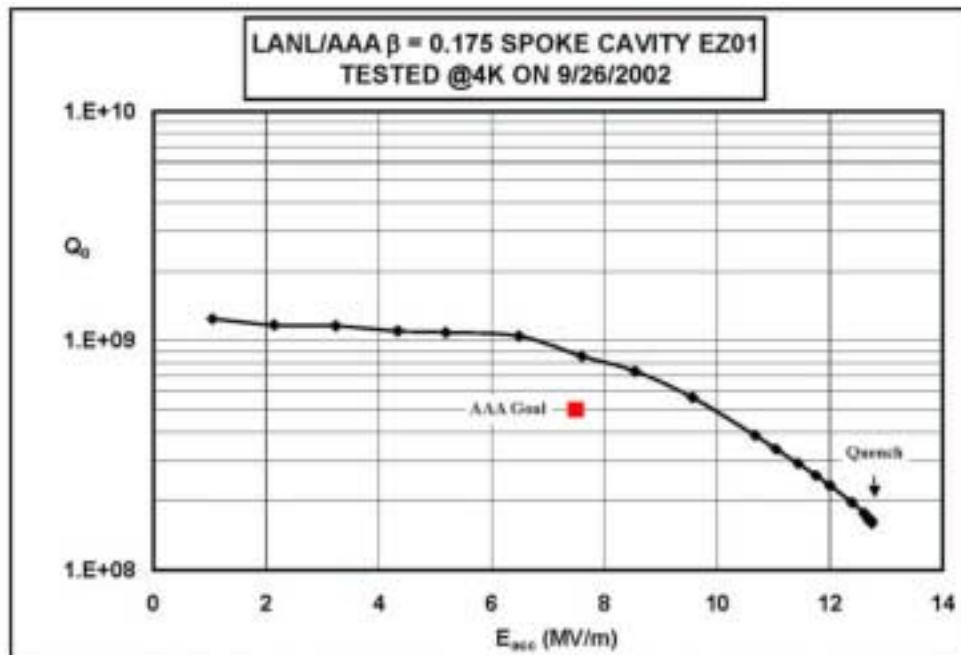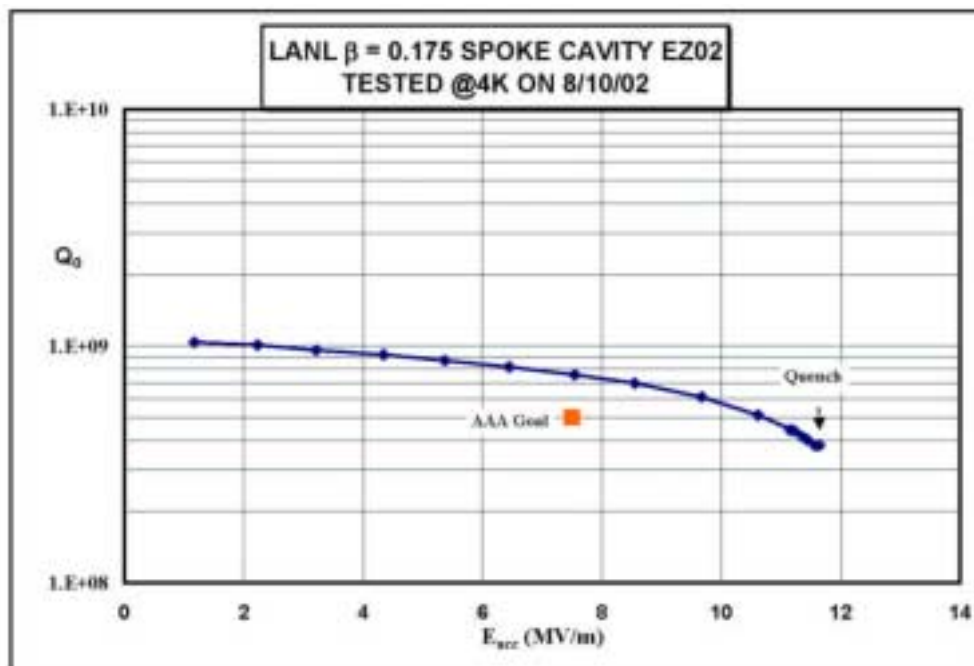

Fig. 78. Test of LANL/AAA β=01.75 spoke cavity EZ01

Fig. 79. Test of LANL/AAA β=01.75 spoke cavity EZ02

Design Of The Spoke Cavity Power Coupler

The objective for FY02 was to complete the design and procurement package for prototype power couplers for the spoke cavities. While some progress was made, inadequate funding did not allow this work to be completed.

DOE/CEA/CNRS Collaboration

There was progress on the DOE/CEA/CNRS collaboration for the Cooperation in Research, Development, and Applications for Accelerator Driven Technology. Work continued on the development of two work packages: study of elliptical cavities and study of spoke resonators.

5.   PROJECT INTEGRATION

5.1   Systems Studies

Scope

Transmutation System Selection Studies

The FY02 AAA/AFCI Systems Studies focused on model development and subsequent analyses to support selection between the multi-tier transmutation system approaches. The shift in NFC modeling emphasis from the equilibrium models to time-dependent simulation and optimization models includes substantial model development. Options will be evaluated to achieve deeper burn-up in the Tier-1 thermal system and the refinement of systems evaluation techniques (*e.g.,* include cost comparisons and more robust fuel cycle consequence analysis using the aforementioned time-dependent models). To this end, proliferation-resistant and conventional ALWR fuel cycles are being evaluated to clarify and assess the practical limits for Tier-1 partial destruction of the transuranic materials (TRU). FY01 studies showed that partial burning of the TRU in a first-tier thermal-spectrum system can substantially impact the performance of the second-tier, fast-spectrum transmuter. Hence, the impact on Tier-2 fast-spectrum system performance for economic, waste-mitigation, and proliferation metrics must be self-consistently considered. LLFP transmutation is also being evaluated, because if the TRU content in repository-directed materials can be reduced, the repository licensing dose rates of the long-lived fission products (LLFP) may dominate. Finally, interest has grown over the last few months in assessing repository savings (*e.g.,* capacity enhancement, dose-limit reductions) that may accrue through a range of SNF preconditioning operations that include uranium separation, heat-producing elements (*e.g.,* cesium and strontium fission products), and/or sources of long-lived dose (*e.g.,* technetium, transuranics). Hence, scoping studies of these SNF-intercept or repository business models also form a growing component the systems studies scope; to this end, the development of a Yucca Mountain (YM) Emplacement model was begun.

The current scope of Systems Studies can be briefly summarized as follows:

- – assess practical limits for Tier-1 partial destruction of TRU;
- – consider the impact on Tier-2 fast-spectrum system performance;

- evaluate the potential for LLFP transmutation;
- begin development of a YM Emplacement model to scale the impacts on repository capacity of reducing the heat load of emplaced materials relative to the canonical SNF direct-deposit scenario.

Report To Congress

The Department of Energy was directed to prepare a report for Congress by May 1, 2002 identifying the benefit of alternative nuclear fuel cycles employing transmutation and addressing a specific list of questions. These questions included (1) comparison of processing techniques, (2) comparison of transmutation approaches, (3) resulting waste streams, (4) life-cycle costs, (5) proliferation resistance, and (6) strategy for facility siting. Technical support was provided by the Systems Analysis team in support and fulfillment of these six charges. This support was underpinned using an equilibrium NFC parametric model that provided scenario-dependent economic, waste-mitigation, and proliferation metrics with which a range of multi-tiered NFC approaches were compared and assessed (within the limitations of the aggregated, equilibrium NFC model—e.g., the question looms of whether such equilibria can in fact be achieved, and on what time scale, and at what cost in terms of dollars and added waste generation).

Highlights

- The NFCSim simulation model is successfully simulating past history of nuclear power plant (NPP) deployment and SNF generation in the US, and a workable framework has been established for integration of a range of Tier-1 and Tier-2 technologies; this simulation mode is ready for benchmarking with both the complementary FCOPT optimization model as well as comparable simulation models used by other institutions.

- The FCOPT optimization is successfully optimizing a broad subset of AFC technologies on the basis of cost, proliferation risk, extensive parametric systems studies, and tuning of key constraints; but further work is needed to understand and better align the projections emerging from this complex optimization model.

- Preliminary scaling studies using the YM Emplacement model indicate a potential for significant capacity enhancement of the repository, but the costs relative to SNF direct disposal can be large.

Integrated Modeling Systems

The major effort in Systems Analysis this past quarter has been directed at the development of a detailed time-dependent NFC simulation model (NFCSim) and a somewhat less-detailed optimization model (FCOPT). Both computer models are operative (NFCSim is JAVA-based, FCOPT is GAMS-based); both models have achieved a level of development[24] where benchmarking between these two complementary approaches to dynamic NFC analyses can begin in FY03. Significant progress in the development of both has been made, and preliminary results from

---

[24] Includes process expansion and integration of both neutronics and costing methods in NFCSim, as well as parametric testing under a range of constraint limits and additional controlling formulary in FCOPT

both have been reported in a comprehensive end-of-year report. In addition, the NFCSim has reached a level of accomplishment and detail to permit benchmarking with a comparable simulation modeling effort at CEA/Cadarache.[25] In addition, preliminary scaled results from the YM Emplacement model are emerging; indications are that significant cost savings for the repository can result from removal of heat-load elements, but the cost of achieving such heat-load reductions can exceed the unit cost of SNF direct disposal by factors of 2-4.

The System Studies scope is being fulfilled in the context of detailed time-dependent AFC simulation and optimization models using an array of economic, waste-mitigation and proliferation metrics. The key analysis tools under development—NFCSim and FCOPT—combine with the earlier equilibrium NFC model DELTA (Krakowski, 2002), the neutronics models Monteburns (Trellue, 1998; Poston, 1999) and ORIGEN (Croff, 1980), and the aforementioned YM Emplacement model to evolve into a modeling system that can address key AFC issues. The modeling system being evolved is illustrated in Fig. 80.

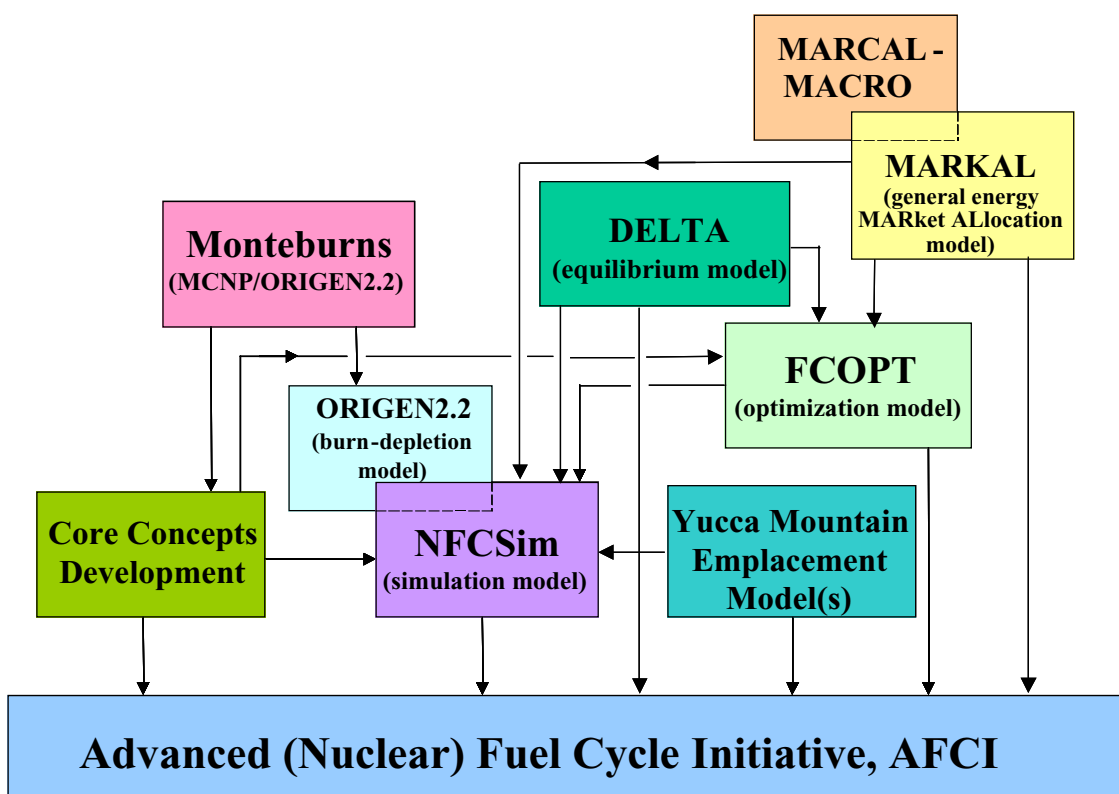Fig. 80. An integrated modeling approach for nuclear fuel cycle assessments.

Combining this modeling system with a means to project actual nuclear-energy demands that might describe a future in which this technology competes with other electrical-generation and liquid-fuel technologies,[26] completes this integrated modeling.

---

[25] The COSI model, (Grouiller, 1991)

[26] *e.g.,* MARKAL (Fishbone, 1981)

Approach and Direction

The aim of Systems Studies in the AAA/AFC Program is to provide quantitative, scenario-based guidance to policy and decision makers in the selection of nuclear fuel cycles (NFCs) that maximize *economic* (mainly energy costs, including fuel resource utilization), *ecological* (mainly short- and long-term waste and repository environmental and dose impacts), and *societal* (primarily proliferation risk) benefits of nuclear energy. Together, these three attributes characterize the *sustainability* of a given Advanced Nuclear Fuel Cycle (ANFC) approach, and in this context, Systems Studies aim to quantify the sustainability of nuclear energy.

Early studies (VanTuyle, 2001) focused primarily on scenario-based analyses of a range of multi-tier transmutation ANFC strategies and the mass-balances related thereto. The addition of a top-level proliferation-risk metric, along with Cost-of-Electricity (COE) estimates, to the neutronics-driven steady-state material balances that define a given scenario, allow each of the above-listed sustainability metrics to be quantitatively evaluated for a range of NFC scenarios. The equilibrium model, DELTA (Fig. 80), provided a technical basis for the Department of Energy Report to Congress (USDOE, 2002) on the economic, proliferation, and waste-mitigation potential of a range of selected, multi-tiered NFCs. Since DELTA is based on the assumption of steady-state, equilibrium (per-TWeh) analyses, with the attendant problems and propensity to mislead, the focus of AAA/AFCI systems studies since the end of the second quarter FY02 and into the third and fourth quarters of FY02 has been the development of a capability for time-dependent NFC scenario analyses to address the short-comings of equilibrium analyses (e.g., important impacts of scheduling and lag-time constraints, transportation issues, time-value of capital and operating expenditure, waste inventory build up incurred during realistically constrained technology development and deployment scenarios, etc.).

Figure 81 illustrates the model options and inter-relationships available to assess ANFC sustainability for a range of scenarios under both static (equilibrium) and time-dependent conditions. The focus of AAA/AFCI systems studies both past (Krakowski, 2002) and present has been only on the NFC leg depicted in Fig. 80, without investigation of nuclear energy in a broader energy context, as possible with the ERB econometrics-based (top-down) model (Krakowski, 1999) or the technology-based (bottom-up) MARKAL (Fishbone, 1981) model.

Systems-studies efforts for this and the previous two FY02 quarters have focused on the development of dynamic models that divide into either *simulation* or *optimization* models. Two approaches are being pursued for the former (NFCSim and an EXTEND™-based simulation, with the focus in this fourth quarter being placed on the NFCSim model); the FCOPT optimization model is developed as a guide to the simulation models. The development (including the buildup of the databases needed for their operation) of both dynamic models is nearly complete, and preliminary results have been generated from each. Ultimately, a reduced set of ANFC scenarios that have been distilled from the earlier equilibrium/static analyses (Krakowski, 2002) will be subjected to dynamic analyses. Figure 82 illustrates candidate scenarios (Salvatores, 2002) evolved from the equilibrium analyses that are slated to be examined using the time-dependent models.
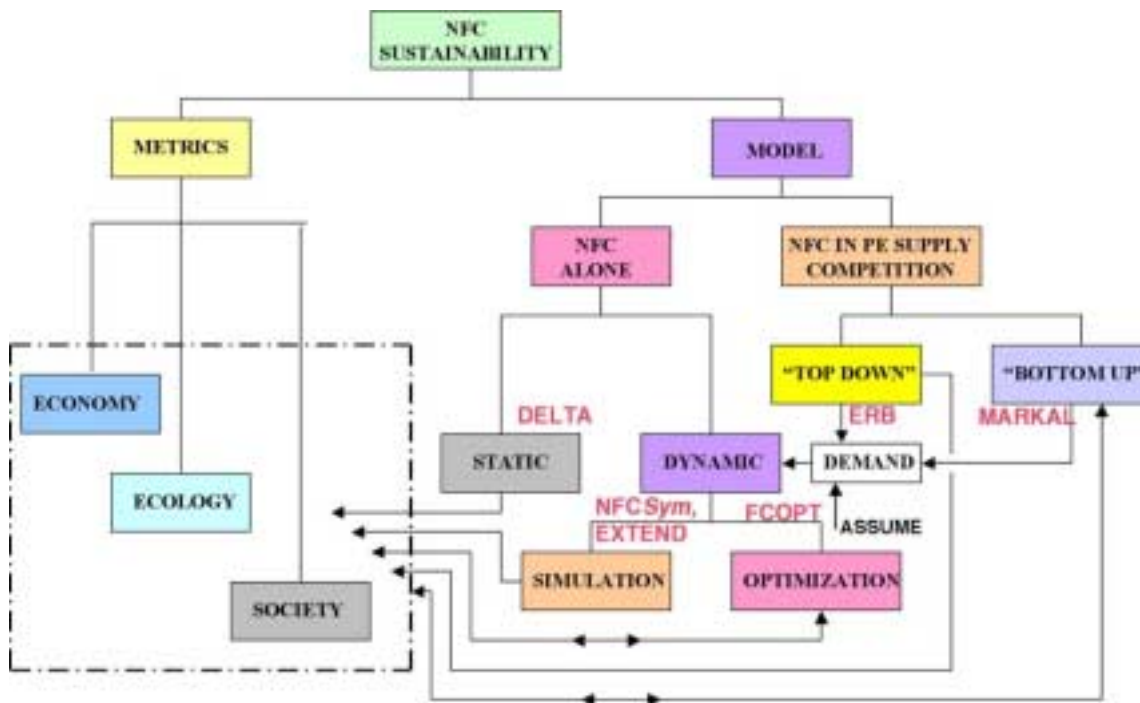
Fig. 81. Nuclear Fuel Cycle modeling relationships, scope, and options, as applied to time-dependent scenario analyses.
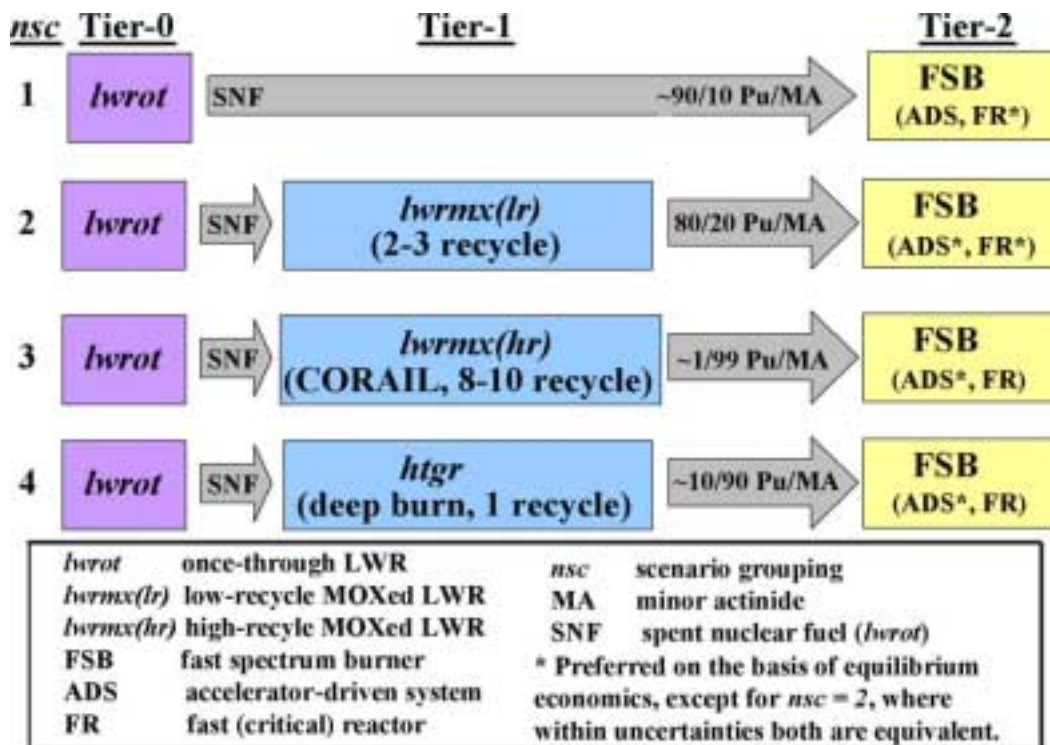

Fig. 82. Top-level scenarios evolved from earlier equilibrium analyses being examined using dynamic simulation models (Figs. 80 and 81).

Sample (Interim) Results from FCOPT Optimization Model

The FCOPT model uses Linear Programming (LP) methods to optimize a comprehensive set of nuclear fuel cycle (NFC) options. Within the context of LP models, FCOPT is time-dependent (*t*) and tracks a range of (*m=20*) nuclear materials and (*p=55*) related processes. Process material flows (*kg/yr*) and inventory (*kg*) are represented by the vectors *x(m,p,t)*, which are followed over a 2000-2100 time frame in one-year increments. The model is driven by an exogenous demand for nuclear-electric energy, which ultimately should be derived from a model like MARKAL-MACRO (Fishbone, 1982). Using this exogenous nuclear-energy demand, the FCOPT model expands the nuclear-energy option, and in the version reported herein, follows six (electricity) generation technologies that include one subcritical accelerator-driven transmuter and one critical fast-spectrum transmuter, along with four commercial nuclear power plant (NPP) options. Multiple processing/reprocessing and repository/depository options can be modeled, as well as a range of uranium-enrichment technologies, but the simplified version developed as part of the FY02 effort aggregates these technology options for enrichment and disposition into one each, except for processing/reprocessing, wherein separations are defined as the purview of the transmuting technologies and reprocessing is associated with the commercial power-producing technologies. Figure 83 depicts a generalized mass/power flow diagram around which the FCOPT model is built. While the use of LP optimization models is not new to the NFC, past work,[27]has focused on a much higher level of NFC aggregation.

Fig. 83. Generalized NFC mass/power-flow diagram around which the FCOPT optimization model is built.

---

[27] Pavelescu, 1982; Ursu, 1986, 1990
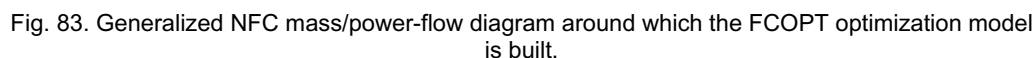
As noted above, the FCOPT model is driven by an exogenous demand for nuclear energy. The projected demand used over the period 2000-2100 is based on an assumption of a US growth rate of *dgrowth = 0.01/yr*. There is a more complete listing of other base-case NFC characteristics used to generate the interim FCOPT results reported herein.[28] In concert with the exploratory nature of this interim evaluation of the FCOPT model, the focus of parametric studies reported to date is the understanding of the trade-off between cost and proliferation risk, as measured by the two objective functions OBJ_{COST} and OBJ_{PROL}, as key capacity limits related primarily to repository disposal (*dd*), interim SNF storage (*is*), reprocessing (*rp*), and separated-plutonium storage (*pus*).

Related to understanding the cost and proliferation impacts of the above-listed technology, capacity constraints are the relative costs attendant to each of the key storage elements in the NFC; the impacts of changes in unit costs associated with each are subsequently explored. Unit Total Cost, *UTC($/We)*, associated with selected generation technologies[29] serves as consensus-generated (OECD, 2002) nominal or point-of-departure (POD) values for key cost estimating relationships (CER). More extensive parametric-systems analyses of unit-cost and capacity impacts on energy-cost and proliferation-risk tradeoffs have been reported.[30]

Two objective functions were evaluated; OBJ_{COST}: the present value of all (nuclear) energy costs over the period 2000-2100; and OBJ_{PROL}: the *AL*-weighted [*AL* = proliferation Attractiveness Level (USDOE, 1999)] exposure (*kg-yr*) evaluated at the terminus year (2100). As described below, the ratio of OBJ_{COST} to the total discounted generation over the optimization period (2000-2100) results in an average cost of energy as follows:

$$< COE > (mill/kWeh) = OBJ_{COST} / \int_{2000}^{2100} \frac{gen(t)}{(1\_dr)^{t-2000}} dt / hpy \qquad (5.1\text{-}1)$$

where *hpy = 8760 h/yr*.

When conducting parametric variations of unit costs or capacity limits, a base case is identified, and results are presented in terms of *<COE>* and *pri* = OBJ_{PROL} values that are normalized to that base or point-of-departure case; these relative economic and proliferation metrics are labeled *rcoe* and *rpri*, respectively.

The following expression indicates a simple means to combine the cost and proliferation objective functions by means of a linear coupling coefficient *pro($/kgPu/yr)*, which assigns a dollar cost associated with a given level of integrated and *AL*-weighted exposure of plutonium in its various forms and inventories throughout the NFC to the risk of theft or diversion.

$$OBJ = OBJ_{COST} + pro * OBJ_{PROL} \qquad (5.1\text{-}2)$$

For small values of *pro*, capital and operating costs dominate the optimization process; for large values of *pro*, the effective cost of proliferation or the risks related

---

[28] Bathke, 2002

[29] Details of the capital costs for the six generation technologies examined with the FCOPT model are given in (Bathke, 2002)

[30] Bathke, 2002

thereto dominate the objective function as the FCOPT model searches for the feasible set of $x(m,p,t)$ vectors that in terms of material (m) and process (p) selection for all times (t) within the time frame of the optimization would minimize the objective function. More so than for any of the other single-point parameter studies made to date with the FCOPT model (Bathke, 2002), the selection of the POD case from which such a parametric study departs determines the trends that result. For this parametric variation of the cost-proliferation coupling coefficient, *pro*, the selected POD case is characterized by a large final repository capacity (number of 70,000 tons SNF Yucca Mountain equivalents, *ym = 10*), and an equally large (eventual) deployment of reprocessing capability (*rpcapf*); the ultimate level of interim storage capacity is also large (*bnisrx = 70 reactor-core-equivalents*), and reprocessing charges are moderate-to-high (*ucrp = 1,500 $/kgSNF*), and the direct disposal charges by any standard are low (*ucdd = 500 $/kgSNF*), at least for moderately sized repositories. Finally, the base *pri* that results from these configuration-determining economic and capacity inputs, along with the *AL* weightings given to each *(m,p,t)* coordinate of the NFC undergoing optimization, determine the dependencies of *rcoe* and *rpri* on *pro* reported in the example depicted in Figs. 84a and b.

Although a strong negative correlation of relative proliferation risk with relative energy cost is revealed in Figs. 84a and b (*e.g.*, reduced proliferation risk is accompanied by an increase in energy cost), these cost increases and (particularly) proliferation-risk reductions are small. Again, this behavior is dependent on the POD chosen for these parametric analyses. More importantly, however, is the strongly non-linear, almost discontinuous interaction between cost and proliferation metrics as the relative importance of each in optimizing a given NFC configuration; initial reductions in *rpri* can be achieved for only minor relative cost increases, but beyond a threshold reduction in *rpri*, the relative costs increase rapidly. Lastly, although not explicitly shown, the generation mix for all cases examined undergoes relatively little change; most of the variations occurring as the cost-proliferation centrum is shifted by increasing or decreasing *pro* occur within the NFC with relatively little dependence on the generation technologies used to meet the exogenous demand. Figure 85 gives a typical evolution of the generation mix for the cases forming the basis of Fig. 84; for the cases shown, the optimal mix tends to be dominated by once-through and MOX-fueled LWRs, with minor contribution from HTGR and FBR technologies in the out years.

Fig. 84a. Comparative dependence of the relative cost and relative proliferation *risk, rcoe*, and *rpri* on the cost-proliferation coupling coefficient *pro*.
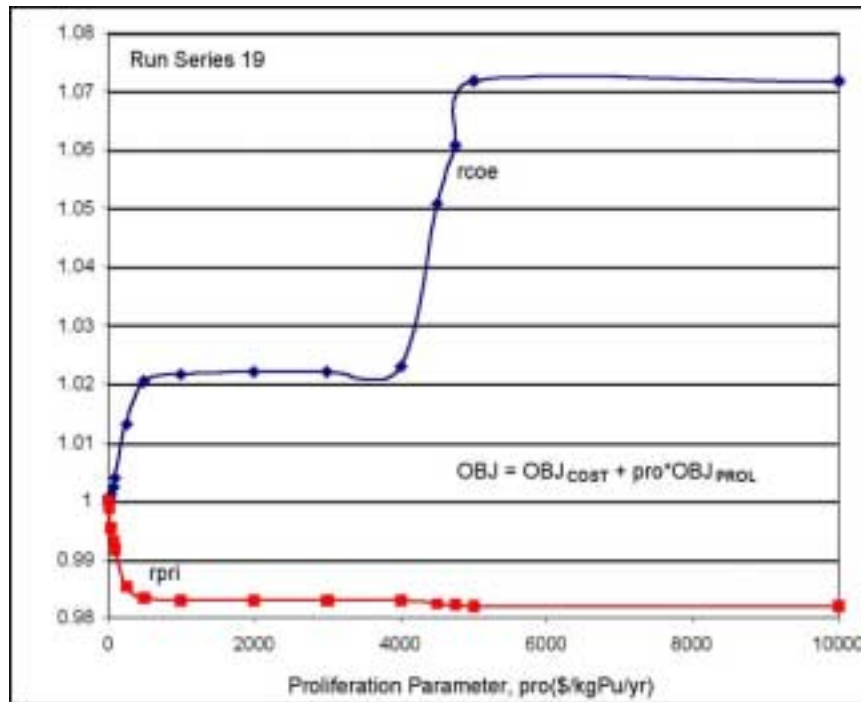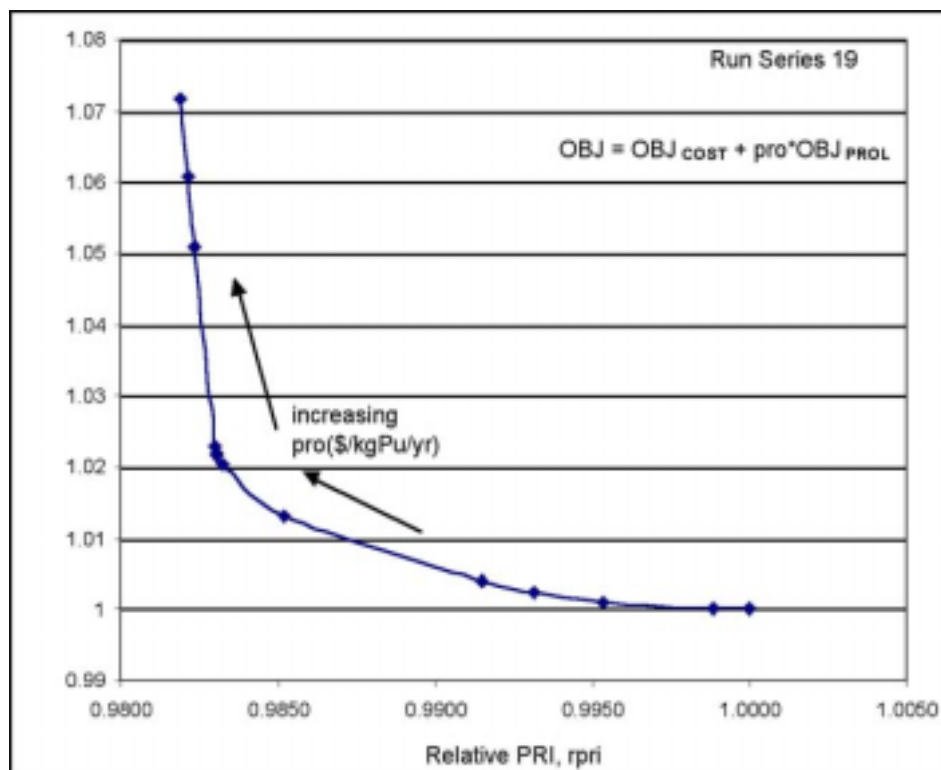

Fig. 84b. Correlative dependence of the relative cost and relative proliferation risk*, rcoe,* and *rpri* on the cost-proliferation coupling coefficient *pro*.
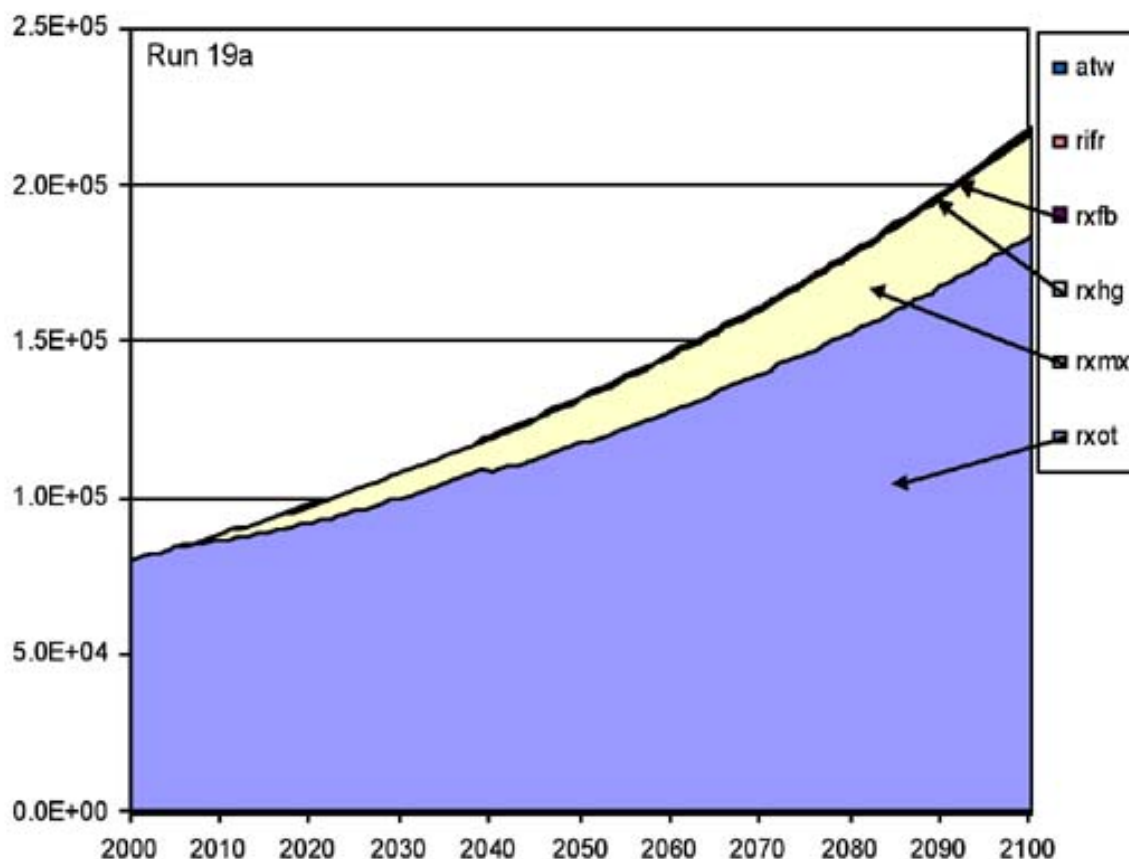
Fig. 85. Typical generation mix for the cases represented in Fig. 84.

Sample (Interim) Results from NFCSim Simulation Model

NFCSim capabilities have been expanded. The primary new capabilities are being able to impose an exogenous demand and to model the front end. Consequently, only the results of a single NFCSim simulation are presented herein to illustrate these capabilities.

Figure 86 shows results from an NFCSim simulation wherein an exogenous demand for nuclear power is met by installing new ALWRs. The demand at time *t* is assumed to be of the form:

$$D(t) = P(t_0)[1 + growth]^{Y(t)},$$

where *P(t₀)* is the installed capacity at the time t_0 when the demand is first applied, *growth* is the rate at which demand changes, and $Y(t) = t - t_o$ is the real number of years since time t_0. In Fig. 86, the demand increases at 1% per annum beginning September 1, 2012. Small deviations of the installed capacity from the demand curve are observable for short periods of time. The reasons for these deviations are multifold. Inherent to the NFCSim model is the assumption that no response is instantaneous (*i.e.*, new capacity only appears after some delay for installation and/or

other reasons). Consequently, NFCSim looks at the demand appropriately shifted into the future. Similarly, NFCSim projects the amount of installed capacity that will still be operating at the appropriate time in the future plus any capacity that has been ordered but not yet installed. The difference between the projected demand and the projected installed capacity yields the capacity deficit that needs to be ordered immediately to meet a future demand. Then NFCSim simulates ordering of the largest integer number of reactors that will not exceed the projected demand. Consequently, NFCSim will always slightly undershoot any demand curve. Nevertheless, these deviations from the demand curve are small compared to the instantaneous-power fluctuations, which can be as large as 30% of the installed capacity.

The reactor capital costs dominate the annual charges, as is also shown in Fig. 86. The associated cooling-storage cost rises linearly between 2000 and 2010, when the capacity is constant. This rise is the result of adopting the DELTA costing model in which the annual cost for cooling storage is charged at 60 $/kg/yr, as if the cooling storage facility were charging a rental fee. A more accurate costing model would charge a levelized cost based primarily on capacity. In 2012 the cooling-storage cost decreases linearly as SNF is moved from cooling storage into a repository.

Although the cost of transporting nuclear material throughout the NFC is relatively inexpensive (*i.e.*, 50 $/kg), the transportation costs are nearly $2.3B in 2000. This large transportation cost arises from the large masses that must be transported between the mine and the converter and between the converter and the enrichment plant. The transportation cost starts to rise after 2012 primarily because of the transport of uranium before enrichment occurs that is associated with the fueling requirements of the new ALWRs being brought online.

The repository cost ramps up starting in 2010, as expected, but sharply drops in 2042 when repository shipments finally eliminate the backlog of SNF that is older than seven years and sitting in cooling storage. The annual enrichment, mining and milling, fuel fabrication, and conversion costs are small compared to the other costs.

The SNF waste generated by all reactors, also plotted in Fig. 86, increases nearly linearly, and reaches a maximum of 146,000 metric tons in 2050. The mass in cooling storage appears to bottom out in 2042, because the backlog of SNF in cooling storage that is seven years old or older has been eliminated and the demand growth is small.

The instantaneous, undiscounted *COE* is approximately constant over the 50-yr simulation period. The constancy of the *COE* is the result of the annual charges being dominated by the reactor cost, which also track the energy production (*COE* is the ratio of cost to energy production). A discounted *COE* for the 50-yr simulation period is 45.5 mill/kWeh, in agreement with the DELTA and FCOPT models.
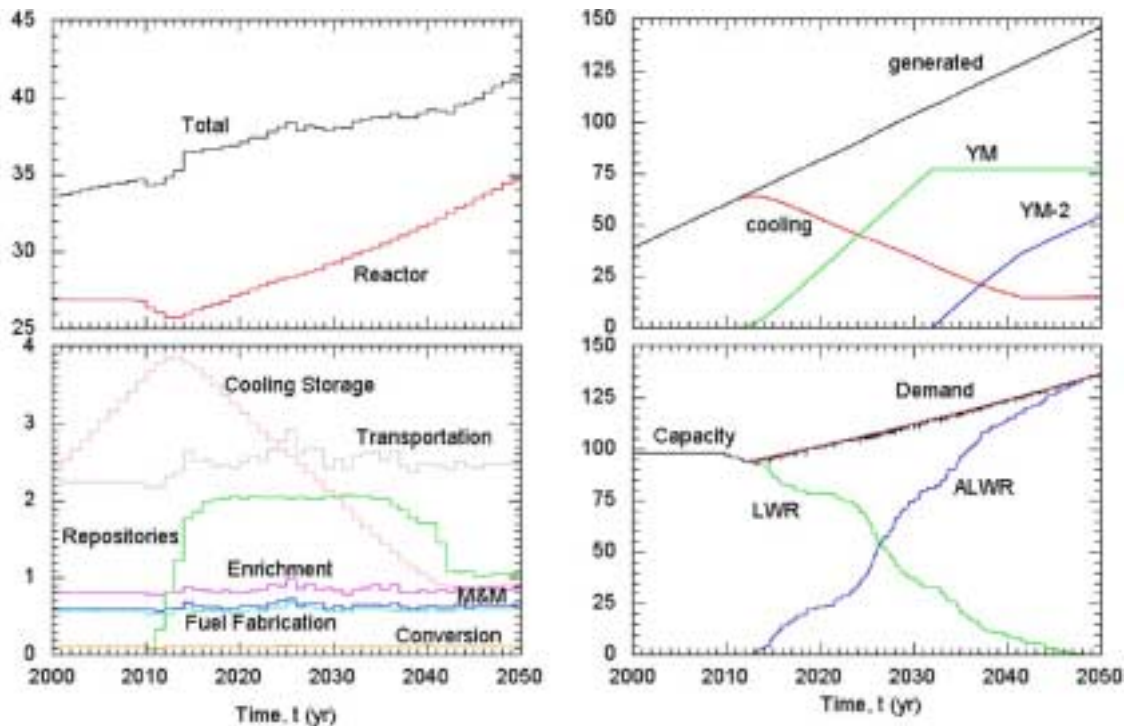
Fig. 86. The annual costs are shown on the left. The mass of SNF generated, stored in cooling ponds, and interred in Yucca Mountain and a second repository are shown in the upper right. The installed capacity, exogenous demand, and reactor mix are plotted as a function of time in the lower right.

Yucca Mountain Emplacement Model

By separating certain components of spent nuclear fuel (SNF), it may be possible to increase the capacity of a long-term geological repository (*e.g.,* Yucca Mountain, YM or its successor, called herein YM2) by a factor of ~10 or more. Additionally, retrievable storage is required for the separated components (cladding, uranium, high-heat-load fission products, transuranic elements), and transmutation of transuranic (TRU) elements would be required for a permanent solution. Only the heat load of repository waste and its volume are herein considered to be design constraints. Specifically, the statutory limit of YM capacity (70,000 tons of SNF and defense waste, prior to opening YM2) is ignored; indeed, it is the goal of this study to investigate ways to exceed that capacity and thereby delay the need for YM2.

While analyses leading to the present repository design (USDOE, 1988) have all assumed that the SNF would remain intact inside its original fuel and waste packages, a number of authors[31] have recognized that certain isotopes contribute to the majority of the heat released from SNF. As shown in Fig. 87, for times less than ~65 yr after irradiation, the major contributors to decay heat are isotopes of Cs and Sr (^{137}Cs with half-life $t_{1/2}$=30.2 yr, and ^{90}Sr with half-life $t_{1/2}$=29 yr), and their short-lived decay products. After this time, the major heat releases come from the actinides, primarily the various isotopes of the TRU elements Pu, Cu, and Am. The remaining

---

[31] Croff, 1994; WHC, 1990; Forsberg, 2000

isotopes in SNF contribute ~3.7% to the heat load at 10 yrs after irradiation. Removing those isotopes from SNF would greatly reduce the decay heat of the waste and, therefore, in principle greatly increase the capacity of a geological repository (*e.g.,* YM or YM2). The separated components would be handled separately.

In examining the impact on YM or YM2 of removing various constituents from the SNF, seven cases or scenarios are being considered for different levels of cleanup, as is listed in Table 21. Scenarios II-VII investigate removal of the actinides U, Pu, and the minor actinides MA = Cm + Am. Scenarios III, IV, and VII also consider the removal of the high heat release (HHR) fission products ^{137}Cs and ^{90}Sr. It is noted that Scenario VII describes the most complete cleanup, and the base case Scenario I has no cleanup and, therefore, represents the present emplacement plan. Table 21 uses the acronyms HHR, LHR, and VLHR for high, low, and very low heat release fractions, as suggested by Croff (1994). In the present analysis, it is assumed that fission products other than those listed here are not removed, except that any reprocessing step (*i.e.,* Scenarios II-VII, Table 21) will necessarily release the volatile fission products (*e.g.,* tritium, carbon, krypton, xenon, bromine, and iodine). These volatile elements can be trapped and processed separately, and, as shown in Fig. 87, they represent only a small fraction of the total decay heat.
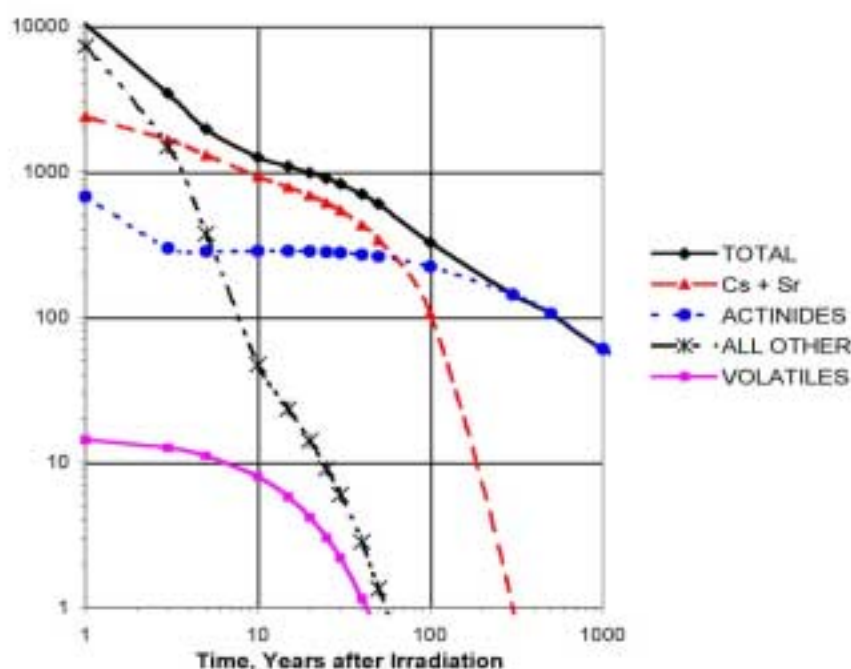
Fig. 87. Spent Nuclear Fuel decay heat, light water reactor at burn-up of 38 GWd/tonneIHM.

The calculated repository capacity ratios for the Standard LWR fuel are presented in Table 22. For each reprocessing scenario, Scenarios II-VII (Table 21) increased packing densities (expressed as a ratio to that of un-reprocessed SNF, Scenario I) are calculated for the short-term integrated, long-term integrated, and instantaneous (10 yr after irradiation) conditions. The fourth column in Table 22 gives the density limit imposed by the waste fraction in VHLW (assumed 25%); this value varies directly with the mass of the remaining fission products after the separation process is performed. The fifth column repeats the lowest (limiting) value of the four constraints.

These capacity ratios will be used to estimate cost impacts of the kinds of SNF preconditioning operations embodied in the Scenarios listed in Table 21.

Table 21. Summary Description of Seven Scenarios Based on Different Degrees of Activation and Fission-Product Removal

	Short Description	Elaborated Description of Disposed Mat I Form	Presumed Advantage of Scenario
I	Base Case	Direct disposal of SNF fuel assemblies	Base- or Point-of-Departure (POD) case: direct disposal of SNF fuel assemblies, including VFPs.
II	I — U(ranium)	Vitrified [MA+Pu+NVFP]	Reduce mass but must deal with full short- and long-term heat load, which establishes limits on the degree to which the volume of the waste form can be reduced.
III	II — {Cs,Sr}	Vitrified [MA+Pu+VLHR = LHR]	Reduce mass, as well as short-term heat load associated with HHRs, but with full (TRU = Pu + MA) long-term heat load and proliferation risk.
IV	III - Pu	Vitrified [1-U-HHR-Pu = MA+VLHR = LHR]	Similar to *nsc = III*, with some reduction in long-term heat load through the removal of Pu (and reduced long-term proliferation risk).
V	II - Pu	Vitrified [1-U-Pu = MA+NVFP]	Not unlike *nsc = II,* but with some reduction in long-term heat load resulting from Pu removal (and reduced long-term proliferation risk).
VI	V - MA	Vitrified [1-U-Pu-MA = NVFP]	Reduce mass with full short-term heat load, but with significantly reduced long-term heat load.
VII	IV - MA	Vitrified [1-U-HHR-Pu-MA = VLHR]	The best it gets; volume & mass reduction along with reductions in both short-term and long-term heat loads

MA = minor actinides Np,Cm, Am　　　　NVRP = non-volatile fission products
VFP = volatile fission products　　　　　　HHR = high heat release radionuclides
LHR = Low heat release radionuclides　　VLHR = very low heat release radionuclides
TRU = MA + Pu

Table 22. Repository Capacity Ratios Calculated on the Basis of Scenario-Dependent Heat Loads.

Scenario *nsc*	Standard LWR				
	Short-Term Benefit[a]	Long-Term Benefit[b]	Waste Package Limit[c]	Waste Fraction Limit[d]	Least Limit[e]
II	1.00	1.00	1.01	6.8	1.00
III	2.99	1.71	3.82	7.4	1.71
IV	4.82	2.51	6.09	9.6	2.51
V	1.15	1.23	1.12	8.6	1.12
VI	1.48	2.7	1.30	9.00	1.30
VII	82.2	218	26.9	10.1	10.1

[a] Short-Term Benefit: Ratio of heat releases for Scenario I compared to Scenario *nsc*, integrated over first 40 years after separation/emplacement.
[b] Long Term Benefit: Ratio of heat releases for Scenario 1 compared to Scenario *nsc*, integrated over first 290 years after separation/emplacement.
[c] Waste Package Limit: Ratio of heat releases for Scenario 1 compared to Scenario *nsc*; instantaneous heat release controlling waste package centerline temperature for vitrified HLW.
[d] Weight Fraction Limit: Limit assuming VHLW is no more than 25% HLW by weight.
[e] Lesser of first four values

Neutronics Support

In addition to providing significant integrating support to both NFCSim and the YM Emplacement models, the core-concept development component of the neutronics task has elucidated the benefits to the nuclear performance of the fast-spectrum Tier-2 technologies of high/deep burn-up in the LWR-based Tier-1 technology.

Mixed (Pu,U) oxide (MOX) fuel used in Tier-1 and an ADS burning the remainder of the material in Tier-2 has been examined with the Monteburns code (Trellue, 1998; Poston, 1999). Multiple recycles of the Pu are required to achieve even 60-70% Pu depletion.° By recycling the Pu in full cores of MOX fuel with an enriched uranium support, after three recycles in the Tier-1 LWR, the resulting material mixture sent to the fast-spectrum Tier-2 ADS was found to reduce the 6-month reactivity swing from 0.07 to 0.03. This reduction results in only halving that which is currently required by the ADS during an operating cycle, significantly decreasing costs.° This behavior results because so many minor actinides remain and are built into the MOX fuel that Pu comprises less than half of the material going to the ADS.

An additional neutronics effort was devoted to developing a way to incorporate neutronics calculations into the real-time NFCSim simulation code. The proposed technique involves taking detailed cross sections calculated using the Monte Carlo burn-up code Monteburns for a particular system (*e.g.,* second recycle in a Pu-burning LWR) and using the depletion/decay code ORIGEN2.2 in NFCSim to calculate material inventories for a given burn-up using these general cross sections. Incorporating such a capability will make NFCSim a more robust code in terms of neutronics compatibility and modeling realism, making the combined system comparable to that used in other industrial strength simulation models [COSI, Grouiller, 1991)]. This melding of neutronics with the detailed NFCSim simulation model is expected to be accomplished early into FY03, in time for a benchmarking exercise with COSI.

5.2   University Programs

Scope

University Programs consists of four major aspects: the University of Nevada-Las Vegas (UNLV) Transmutation Research Program (UNLV TRP), AFC Program at the Idaho Accelerator Center (IAC) of Idaho State University (ISU), University Fellowships Program (UFP), and AFC Directed University Research within the Transmutation Sciences technical area. In addition, the scope of this effort involves coordination between other AFC activities and academia. The Scope, Highlights, and Technical Progress for AFC-Directed LANL-supported university research were reported earlier under Transmutation Sciences.

UNLV AFC University Participation Program

The University of Nevada supports the AFC Program through research and development of technologies for economic and environmentally sound refinement of

spent nuclear fuel [32] The UNLV Program has four components: student-based research, infrastructure, international collaborations, and support.

Idaho Accelerator Center

The IAC at Idaho State University (ISU) will develop a long-term plan and a research program to conduct a variety of investigations that depend on high-energy electron accelerators.

University Fellowships Program

The University Research Alliance (URA, formerly ANRC–the Amarillo National Research Center) acts as the executive agency for the AFC Program to select, award, and administer fellowships for ten graduate students who were selected in FY01 and ten more selected in FY02.

AFC-Directed University Research

Other universities currently support R&D and technology development. LANL has ongoing support contracts with the University of Michigan, the University of California-Berkeley, and the University of Texas-Austin. North Carolina State University and the University of Illinois at Urbana Champaign are being added to support LANL s research responsibilities. ANL is in the process of contracting with U of Michigan and MIT.

Highlights

UNLV Transmutation Research Program

- UNLV published and distributed the "UNLV Transmutation Research Program Annual Report for Academic Year 2001"˚that highlights infrastructure improvements, student research programs, and growth in interest in nuclear science and engineering

- The ISTC Target Complex TC-1 received earlier this year was temporarily moved to a large˚laboratory bay at UNLV and tested by ISTC scientists with the assistance of personnel from IPPE (Obninsk, Russia), successfully determining that there were no leaks in the target. UNLV is currently designing an LBE Loop Facility to house the ISTC target complex.

- UNLV completed the purchase of a Transmission Electron Microscope (TEM) to enhance their materials science capabilities, and are designing a new TEM User Facility to house it.

- UNLV hosted a visit by William Magwood (Director, DOE-NE), and co-hosted an International Molten Metals Advisory Committee/ISTC meeting at which representatives from six countries gave presentations on current molten metal activities and developed recommendations for a plan for conducting research with the ISTC Target at UNLV that will contribute to national and international efforts.

---

[32] ref. H.R. 5483, P.L. 106-377

- Two new transmutation research projects were approved following a peer-review process: Immobilization of Fission Iodine with collaborators from LBNL, ANL, and the Khlopin Radium Institute (Russia), and "Evaluation of Fluorapatite as a Waste-Form Material," with collaborators from ANL and the Khlopin Radium Institute.

Idaho State University — Idaho Accelerator Center

- ISU-IAC initiated research on three projects: positron-annihilation spectroscopy (to make in-situ measurements of residual stresses in materials); computation of dose conversion coefficients for the hundreds of radio-isotopes that will be generated in high-energy proton spallation targets; and development of concepts for coupled accelerator/reactor neutronics experiments.

- ISU-IAC hired a research faculty member to strengthen the positron materials effort. Positron-annihilation stress measurements on UNLV-supplied Zr samples were completed.

- A neutron-producing target was designed for an ISU-IAC electron linac and MCNPX calculations on the design were completed. The new design is predicted to produce a factor of two increase in neutron yield compared with previous designs. The new target has been fabricated and experimental runs begun to verify neutronics modeling projections.

- The first round of Dose Conversion Coefficients inter-comparisons have been completed and data are being analyzed.˚ Software for the DCC analysis was upgraded.

- Transfer of funds to FSU collaborators (University of Georgia in Tiblisi and Khlopin Radium Institute, St. Petersburg) was initiated through the GAP organization.

University Research Alliance

- URA staff identified and selected a second-year master's degree student (Mike Gregson) at the University of Texas to fill a fellowship position vacated by a Fellow who realized his research interests were no longer aligned with the AAA Program.

- A second-year Fellow finished preliminary modeling and has begun writing a thesis on the feasibility of using a fluoride volatility process to extract technetium from post-transmuted ATW fuel. Experiments begin in October.

- A second-year Fellow is modeling the target/cooling blanket of a specific ATW concept from Russia by using a program called CFX, which has produced good results on a laminar-flow test case.

- The URA has initiated the first steps for recruiting applicants for the FY03 AFCI Fellowship Program.

University Project Leader

- The University Projects Leader brought additional universities into the AFC-AAA program during the fourth quarter:
  - A contract was initiated to begin a research project at the University of Illinois at Urbana-Champaign titled "Impedance Spectroscopy as a

Feasible Method of Measuring Lead-Bismuth Corrosion" (includes building a small LBE test loop to investigate the use of impedance spectroscopy to measure the effects and rates of corrosion on structural materials.

– Another contract was completed for North Carolina State University to provide support for PSI-SINQ radiation effects studies.

- Purchase Requests were submitted for the University of Florida to study "The Influence of Radiation on Passivating High Temperature Oxides" for LBE systems and for the Georgia Institute of Technology to consult on the AAA Dose Conversion Coefficients Project (a UNLV-led intercollegiate collaboration that includes LANL, ISU, Texas A&M, and ORNL/U of Tennessee.

- The University Projects Leader was appointed co-PI on UNLV TRP Task 6 "Neutron Multiplicity Measurements" to facilitate experiments at LANSCE and other locations as well as to advise students in modeling of radiation measurements and effects.

- A visit was made to the ISU-IAC to review progress on the Program and to plan future work. Other visits included the University of Minnesota, McAlester College, ANL-W, LANL, and INEEL to discuss research projects and opportunities, and to present seminars on the ATW and AFCI.

Technical Progress

Technical progress of ongoing investigations by direct university research projects is reported under appropriate technical areas (e.g., Transmutation Science). Some technical progress made under the UNLV program has been reported separately (viz., quarterly progress reports by primary investigators).

REFERENCES

Fuels

1. N. Alexandre, M. Desmaison-Brut, F. Valin and M. Boncoeur, "Mechanical Properties of Hot Isostatically Pressed Zirconium Nitride Materials," J. Mater. Sci. **28** (1993) 2385-2390).

2. S. Suresh, *Fatigue of Materials*. 2nd ed. 1998, Cambridge. Cambridge University Press.

3. H. A. Wriedt, The N-Pu Phase diagram in Phase Diagrams of Alloys , Editor T. B. Massalski, ASM International, 1970.

4. T. M. Besmann, J. Nuc. Mater. <u>144</u>, (1987) 141-150.

5. T. M. Besmann and T. B. Lindemer, J. Nucl. Mat., 130 (1985) 489-504.

6. T. M. Besmann and T. B. Lindemer, Trans. Amer. Nucl. Soc., 45 (1983) 280-281.

7. M. S. S. Brooks, H. L. Skriver, and B. Johansson, in A. J. Freeman, G. H. Landers (Eds.), Handbook on the Physics and Chemistry of the Actinides, North-Hollands, Amsterdam, 1984.

8. D. C. Wallace, Phys. Rev. B 58, 15 433 (1998).

9. Grimes R. W. & Catlow C. R. A., The stability of fission products in uranium dioxide *Phil. Trans. R. Soc. Lond. A,* **335**, 609 (1991).

10. Rest J. & Hofman G. L., Kinetics of recrystalization and fission-gas-induced swelling in high burnup UO_2 and U_3Si_2 nuclear fules *Fundamental Aspects of Inert Gases in Solids*, NATO ASI series B, Vol. 297 p443.

11. Grimes R. W., Variations in the properties of ceramic nano-clusters *Phil. Mag. B,* **79**, 407 (1999).

12. Jentys A. & Grimes R. W., Embedding nano-clusters in siliceous Faujasite *J. Chem. Soc. Faraday Trans.* **92**, 2093 (1996).

Transmutation Science

1. J.E. Pawel, A.F. Rowcliffe, D.J. Alexander, M.L. Grossbeck, K. Shiba, Effects of low-temperature irradiation on deformation behavior of austenitic stainless steels, *Journal of Nuclear Materials*, 233-237, 1996, pp. 202-206.

2. G.E. Lucas, M. Billone, J.E. Pawel, M.L. Hamilton, Implications of radiation-induced reductions in ductility to the design of austenitic stainless steel structures, *Journal of Nuclear Materials*, 233-237, 1996, pp. 207-212.

3. N. Hashimoto, S.J. Zinkle, A.F. Rowcliffe, J.P. Robertson, S. Jitsukawa, Deformation mechanisms in 316 stainless steel irradiated at 60¡C and 330¡C, *Journal of Nuclear Materials*, 283-287, 2000, pp. 528-534.

4. M.L. Hamilton, M.B. Toloczko, and G.E. Lucas; "Recent progress in shear punch testing," *Proceeding of the workshop on Miniaturized Specimens for Testing of*

Irradiated Materials, IEA International Symposium, Julich, Germany, published January 1995, pp. 46-58.

5. M.B. Toloczko, M.L. Hamilton, and G.E. Lucas, Ductility Correlations Between Shear Punch and Uniaxial Tensile Test Data, *Proceeding of the 9th International Conference on Fusion Reactor Materials*, October 10-15, 1999, Colorado Springs, CO, Journal of Nuclear Materials, Vols. 283-287, 2000, pp.˚987-991.

6. MCNPX User's Manual, version 2.4.0, September, 2002, LA-CP-02-408

7. D-10:JSH-02-115, D-10 memo from John Hendrix, 'Mix and Match"

8. W. V. Boynton, et. al., "Distribution of Hydrogen in the Near Surface of Mars: Evidence for subsurface Ice Deposits"

Systems Studies

Bathke, C. G., R. A. Krakowski , H. R. Trellue, A. M. Spearing, and C. M. Lovejoy (2002), Advanced Nuclear Fuel Cycle (ANFC) Systems Analyses for FY 2002 , Los Alamos National Laboratory document LA-UR-02-xxxx (in preparation, October, 2002)

Croff, A. G. (1980) A User s Manual for ORIGEN2 Computer Code, ORNL/TM-7175, Oak Ridge National Laboratory (July 1980). (Also known as RSICC code number C00371).

Croff, A.G. (1994), A Concept for Increasing the Effective Capacity of a Unit Area of a Geologic Repository , Radioactive Waste Management and Environmental Restoration, **18**,. 155-180 (1994).

Fishbone L. G. (1981) and H. Abilock,   MARKAL, A Linear-Programming Model for Energy Systems Analysis: Technical Description of the BNL Version, Energy Research 5, 353-375 (1981) [for more resent versions and application, please refer to the Energy Technology Systems Analysis Program at www.ecn.nl/unit_bs/etsap/].

Forsberg, C.W. (2000), Rethinking High-Level Waste Disposal: Separate Disposal of High-Heat Radionuclides (^{90}Sr and ^{137}Cs). Nuclear Technology, Volume 131, pps. 252-268, (2000).

Krakowski, R. A, (1999), Los Alamos Contribution to the IAEA Overall Comparative Assessment of Different Energy Systems and Their Potential Role in Long-Term Sustainable Energy Mixes, Los Alamos National Laboratory document LA-UR-99-627 (February 3, 1999).

Krakowski, R. A. and C. G. Bathke (2002), Method for Quantitative Assessment of Cost and Proliferation Risks Associated with the Civilian Nuclear Fuel Cycle as Applied to the Advanced Accelerator Applications (AAA) Program, Los Alamos National Laboratory document LA-UR-02-2369 (April 26, 2002).

Grouiller, J.-P., G. Flamenbaum, B. Sicard, M. Mus, J. Martin, J. G. Devezeaux de Lavergne, and O. Comellini, COSI, A Simulation Software for a Pool of Reactors and Fuel Cycle Plands: Application to the Study of the Deloyment of Fast Breeder Reactors, Symposium on Fast Reactors (??), Kyoto, Japan (1991).

OECD (2002), Accelerator-driven Systems (ADS) and Fast Reactors (FR) in Advanced Nuclear Fuel Cycles: A Comparative Study, Organization for Economic Co-operation and Development / Nuclear Energy Agency report (2002).

Pavelescu, M and I. Ursu (1982), A Decision Problem Under Uncertainty for Nuclear Power System Development, Energy Research, **6**, 47 (1982).

Poston, D. I. and H.R. Trellue, (1999) User s Manual, Version 2.0, for MONTEBURNS, Version 1.0, LA-UR-99-4999, Los Alamos National Laboratory (September 1999). Also known as RSICC code number P00455.

Salvatores, M., and P. Finck (2002), personal communication, Argonne National Laboratory (Cadarache, France; July, 2002).

Trellue, H.R. (1998), Development of Monteburns: A Code That Links MCNP and ORIGEN2 in an Automated Fashion for Burnup Calculations, Los Alamos National Laboratory report LA-13514-T (December 1998).

Ursu, I., M. Pavelescu, and M. Tuturici (1986), A Deterministic Approach in the Optimization of a Nuclear Power System form Fuel Resource Point of View, Energy Research, **10**, 11 (1986).

Ursu, I., M. Pavelescu, and G. Mociornita (1990), Conditiond Minimization of Fuel Feed Rate for a CANDU-600 MWe Reactor, Energy Research, **14**, 275 (1990).

USDOE (1988), Viability Assessment of a Repository at Yucca Mountain , U.S. Department of Energy report DOE/RW-0508 (December, 1988).

USDOE (1999), United States Department of Energy, Manual for Control and Accountability of Nuclear Materials, United States Department of Energy document DOE M 474.1-1 (August 11, 1999).

USDOE (2002), Report to Congress on the Advanced Accelerator Applications Program, U.S. Department of Energy, Office of Nuclear Energy, Science, and Technology (in preparation, September 1, 2002).

Van Tuyle, G. J. (2001), Candidate Approaches for an Integrated Nuclear Waste management Strategy — Scoping Evaluation, Los Alamos National Laboratory document LA-UR-01-5572 (November, 2001).

WHC (1990), CURE: Clean Use of Reactor Energy , Westinghouse Hanford Company, Document WHC-EP-0268. Prepared under DOE contract DE-AC-87RL10930 (May, 1990).